Université Paris 7
et
Institut de Physique du Globe de Paris

Mémoire

présenté par

Julien AUBERT

pour obtenir

L'Habilitation à Diriger des Recherches

Spécialité : **Sciences de la Terre, de l'Environnement et des Planètes**

Comprendre et interpréter le signal magnétique : Résultats et perspectives géophysiques de la modélisation numérique de l'effet dynamo.

Date de soutenance : xxxx

Composition du jury :

xxx xxx

Table des matières

Résumé sur l'originalité des recherches

Je m'intéresse à l'interprétation du signal magnétique en provenance de l'intérieur de la Terre et des planètes du système solaire. Sur une gamme d'échelles de temps très large, les données magnétiques nous renseignent sur la structure et la dynamique interne de ces planètes. L'outil principal de ma recherche est la modélisation numérique directe du processus dynamo, par lequel l'énergie cinétique des mouvements de convection du fluide conducteur (le fer liquide au sein du noyau externe, dans le cas de la Terre) est convertie en énergie magnétique. Le maintien d'une dynamo contraint sévèrement le bilan thermique global des planètes, ainsi que le couplage de la couche dynamo avec les couches supérieures (manteau, croûte, dans le cas des planètes telluriques). À travers ceci, c'est toute l'histoire des planètes qui nous est contée, jusqu'à plusieurs milliards d'années en arrière. Mon activité a été centrée sur l'étude de la Terre et de sa géodynamo, pour lesquelles nous disposons d'observations géophysiques riches et variées. Cependant, il est intéressant de transposer les connaissances acquises vers les autres planètes, pour lesquelles le signal magnétique s'est beaucoup enrichi dans le passé récent (Mars), ou va s'enrichir dans le futur proche (Mercure, mission Messenger).

Ce domaine de recherche assez jeune s'est fortement développé au cours des deux dernières décennies. Le but et l'originalité de mon recrutement au CNRS étaient de renforcer la présence de cette spécialité dans la recherche française. Au cours des quatre années précédentes, j'ai défini une méthode de travail originale reposant sur l'utilisation conjointe du signal magnétique avec d'autres types d'observables géophysiques (principalement thermodynamiques et sismologiques), et leur interaction avec la modélisation numérique, dont le pouvoir prédictif a pu être renforcé par la mise au point de méthodes d'extrapolation basées sur des lois d'échelle et l'établissement de diagrammes de phase. Ceci a permis une intégration naturelle de ma recherche au sein du laboratoire de Dynamique des Fluides Géologiques de l'institut de Physique du Globe de Paris, qui défend ce type d'approche. J'ai bien sûr maintenu une collaboration permanente avec l'équipe de Géomagnétisme, dont le caractère fructueux ne s'est pas seulement limité à la consolidation de mes connais-

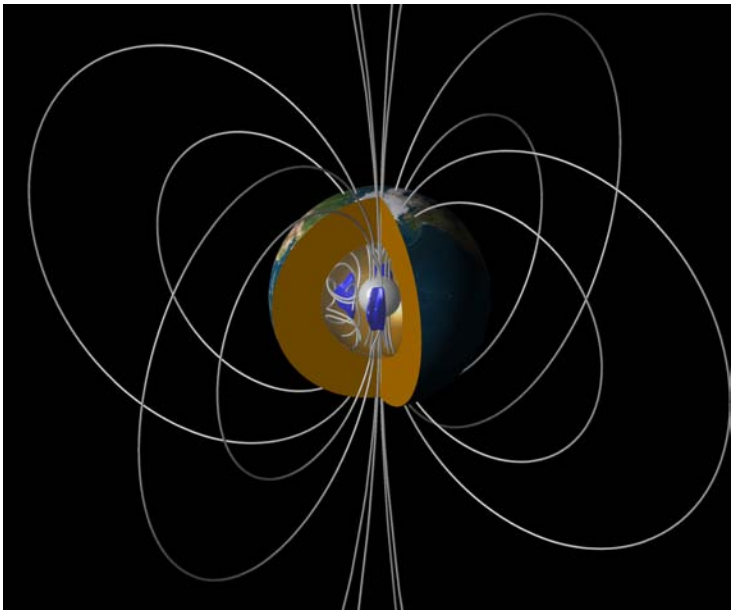

FIG. 1 – Vue tridimensionnelle de l'intérieur de la Terre (le manteau rocheux et solide est en orangé, le noyau externe est transparent, la graine est en gris au centre du noyau externe), comprenant une visualisation d'un modèle numérique de la dynamo terrestre (géodynamo). Les mouvements cycloniques de fluide (en bleu dans le noyau externe) entretiennent, par étirement des lignes magnétiques, le champ magnétique global de la planète, ici représenté par ses lignes de forces grises (Image Julien Aubert, IPGP)

sances générales des données magnétiques.

Je peux dégager quatre contributions importantes dans mon activité récente :

- La formulation d'une théorie d'échelle qui unifie le mécanisme de la génération des champs magnétiques des planètes du système solaire, et la mise en évidence de lois d'échelle permettant de prédire l'amplitude de leurs mouvements convectifs et de leur champ magnétique,
- La production des premiers modèles synthétiques pour l'évolution des principales observables de la géodynamo, depuis la formation du noyau de la Terre jusqu'à nos jours,
- La mise en évidence, sur Terre, du couplage à l'échelle globale (depuis la tectonique des plaques jusqu'à la structure de la graine),
- La visualisation numérique directe (par l'intermédiaire du concept de dynamique des lignes de champ, ou *Dynamical Magnetic Fieldline Imaging (DMFI)* des processus dynamo, permettant de relier les observations magnétiques de surface à la dynamique interne, et d'élucider le mécanisme des inversions de polarité magnétique.

De plus, mon activité a suscité le développement de plusieurs codes numériques librement disponibles pour la communauté scientifique :

– le code PARODY-JA, branchement du code PARODY développé par Emmanuel Dormy et moi-même,
– le code d'imagerie numérique DMFI.

Le potentiel de croissance de mon activité pour le futur se mesure à l'aune des observations thermiques, géochimiques, gravimétriques, sismologiques que je n'ai pas encore fait interagir avec le signal magnétique dans le cadre de mon approche. Leur nombre et leur qualité sont en augmentation régulière, et suscitent des besoins de modélisation nouveaux auxquels j'espère pouvoir répondre dans la suite de mes recherches, afin d'augmenter notre compréhension des couplages dynamiques entre les différentes couches de la Terre et des planètes du système solaire. Parallèlement, mes recherches se développent vers un second axe consacré à l'étude de la prédictibilité du signal magnétique. Nous avons démarré une thèse sur le sujet (Florian Lhuillier, IPGP), que je co-encadre. Ce type d'étude est un préliminaire nécessaire aux démarches d'assimilation des données, qui constitueront la pierre angulaire des modèles numériques dynamo de la prochaine génération.

Chapitre 1

Exposé synthétique des recherches

1.1 Cadre théorique général

Le noyau métallique liquide de la Terre, essentiellement constitué de Fer, occupe l'espace d'une coquille sphérique d'environ $D = 2260$ km de largeur, entre la graine (rayon actuel $r_i = 1220$ km) et la frontière noyau-manteau (rayon $r_o = 3480$ km) (voir par exemple Dziewonski et Anderson, 1981). La dynamique de cette couche s'étudie en général dans le cadre de la mécanique des fluides newtoniens, homogènes, incompressibles et isotropes. Comme dans toutes les couches fluides de la Terre, la rotation joue un rôle prépondérant, et nous considérons donc que la coquille sphérique est en rotation à la vitesse angulaire constante $\mathbf{\Omega}$ autour d'un axe $\mathbf{e}_z$. Du fait de la faible compressibilité du fluide (environ 20%), les phénomènes de convection sont décrits dans le cadre de l'approximation de Boussinesq. Les deux sources de poussée potentielle (voir par exemple Lister et Buffett, 1995) sont le refroidissement de la planète, et la libération d'éléments chimiques légers (tels que le soufre, l'oxygène) consécutive à la cristallisation de la partie solide du noyau, la graine. Si on définit le champ de température T' par rapport à un état de base isentropique, et le champ de concentration ξ' par rapport à un état de base homogène, les deux sources de poussées peuvent être décrites (Braginsky et Roberts, 1995) par le biais d'un seul champ, la co-densité C définie par :

$$C = \alpha\rho T' + \Delta\rho\xi' \tag{1.1}$$

Ici α est le coefficient d'expansion thermique du fluide, ρ est sa densité, et $\Delta\rho$ est la différence de densité entre le Fer liquide pur et les éléments légers. Le système d'équations que nous cherchons à résoudre est donc formé de l'équation de Navier-Stokes, l'équation d'induction éléctromagnétique, l'équation de la chaleur, et les équations de continuité, les champs inconnus étant le champ de vitesse $\mathbf{u}$, le champ

magnétique $\mathbf{B}$ et la co-densité C (voir par exemple Braginsky et Roberts, 1995) :

$$\frac{\partial \mathbf{u}}{\partial t} + \mathbf{u}\cdot\nabla\mathbf{u} + 2\,\boldsymbol{\Omega}\times\mathbf{u} + \frac{\nabla P}{\rho} = \frac{g_o}{\rho}\frac{\mathbf{r}}{r_o}C + \frac{1}{\rho\mu}(\nabla\times\mathbf{B})\times\mathbf{B} + \nu\nabla^2\mathbf{u} \tag{1.2}$$

$$\frac{\partial \mathbf{B}}{\partial t} = \nabla\times(\mathbf{u}\times\mathbf{B}) + \lambda\nabla^2\mathbf{B} \tag{1.3}$$

$$\frac{\partial C}{\partial t} + \mathbf{u}\cdot\nabla C = \kappa\nabla^2 C + S_{T/\xi} \tag{1.4}$$

$$\nabla\cdot\mathbf{u} = 0, \nabla\cdot\mathbf{B} = 0 \tag{1.5}$$

Les symboles non encore définis sont les suivants : P est le champ de pression du fluide, $\mathbf{r}$ est le rayon-vecteur, g_o est la valeur du champ de gravité à $r = r_o$ (la gravité est centripète radiale, décrite par le vecteur $\mathbf{g} = -g_o\mathbf{r}/r_o$), μ est la perméabilité magnétique du vide, ν est la viscosité du fluide, λ sa diffusivité, et κ sa diffusivité thermique et chimique. Afin de simplifier le traitement de la co-densité, nous supposons en effet que les deux sources de poussées sont sujettes à la même diffusivité. Cette simplification peut être justifiée par l'existence, dans le noyau de la Terre, d'une turbulence très développée (nombre de Reynolds typique de 10^8, voir par exemple Christensen et Aubert, 2006). Dans l'equation de la co-densité, le terme $S_{T/\xi}$ représente un terme source volumétrique permettant de décrire respectivement le refroidissement séculaire de l'état de base, et son enrichissement en éléments légers.

Les conditions aux limites sont de type rigide pour le champ de vitesse. Pour le champ magnétique, on prescrit le raccordement à un isolant au manteau, et à un conducteur à la graine. De nombreuses simulations prescrivent cependant un isolant au manteau et à la graine, car il a été montré (Wicht, 2002) que la conductivité de la graine avait une influence marginale sur le processus dynamo. Les conditions aux limites pour la co-densité sont sensiblement plus compliquées. J'ai montré (Aubert et al., 2008) qu'il est plus réaliste, d'un point de vue géophysique, de prescrire le flux de co-densité $F = \int -\kappa\partial C/\partial r\, dS$ à la frontière noyau-manteau, et de prescrire la co-densité elle-même à la frontière de la graine.

Comme dans tout problème en mécanique des fluides, nous procédons à une phase d'adimensionnement des équations. Les échelles retenues pour cette phase sont : longueur D, temps $1/\Omega$, vitesse ΩD, champ magnétique $(\rho\mu)^{1/2}\Omega D$, co-densité $F/4\pi D^3\Omega$. Les équations résultantes sont :

$$\frac{\partial \mathbf{u}}{\partial t} + \mathbf{u}\cdot\nabla\mathbf{u} + 2\,\mathbf{e}_z\times\mathbf{u} + \nabla P = Ra_Q\,\frac{\mathbf{r}}{r_o}C + (\nabla\times\mathbf{B})\times\mathbf{B} + E\nabla^2\mathbf{u} \tag{1.6}$$

$$\frac{\partial \mathbf{B}}{\partial t} = \nabla\times(\mathbf{u}\times\mathbf{B}) + \frac{E}{Pm}\nabla^2\mathbf{B} \tag{1.7}$$

$$\frac{\partial C}{\partial t} + \mathbf{u}\cdot\nabla C = \frac{E}{Pr}\nabla^2 C + S_{T/\xi} \tag{1.8}$$

$$\nabla\cdot\mathbf{u} = 0, \nabla\cdot\mathbf{B} = 0 \tag{1.9}$$

Ici les nombres sans dimension introduits sont les nombres d'Ekman E, de Prandtl

Paramètre d'entrée	Définition	Signification	Modèles	Terre
Ekman	$E = \frac{\nu}{\Omega D^2}$	forces visqueuses / force de Coriolis	3.10^{-4} – 3.10^{-6}	10^{-14}
Rayleigh modifié	$Ra_Q = \frac{g_o F}{4\pi\rho\Omega^3 D^4}$	flux de co-densité	10^{-9} – 10^{-3}	10^{-13}
Prandtl magnétique	$Pm = \frac{\nu}{\lambda}$	viscosité / diffusivité magnétique	0.1 – 10	10^{-6}
Prandtl	$Pr = \frac{\nu}{\kappa}$	viscosité / diffusivité de la poussée	0.1 – 10	?
rapport d'aspect	$\chi = r_i/r_o$	géometrie du problème	0 – 0.35	0.35 à présent

Tab. 1.1 – Nombres sans dimensions du problème. Les nombres pour lesquels les paramètres simulés sont loin de la réalité sont reportés en rouge, ceux pour lesquels la simulation atteint un domaine réaliste sont représentés en vert. Les estimations des quantités terrestres peuvent être trouvées par exemple dans Christensen et Aubert (2006).

Pr, de Prandtl magnétique Pm et de Rayleigh (basé sur le flux de co-densité) Ra_Q, dont les définitions et valeurs se trouvent dans le tableau 1.1.

Le nombre de Rayleigh Ra_Q mesure le flux de co-densité traversant le modèle. Nous avons aussi montré (Christensen et Aubert, 2006) qu'il représente, à une constante multiplicative près (qui dépend de la géométrie), la puissance mise à disposition pour le système convectif. Le nombre d'Ekman représente l'importance relative de la viscosité et de la force de Coriolis. Les deux nombres de Prandtl représentent les rapports des trois diffusivités. Si on compare les paramètres habituellement simulés dans les modèles numériques aux valeurs attendues pour la Terre (tableau 1.1), on voit que seul le nombre de Rayleigh s'approche raisonnablement des valeurs attendues pour la Terre, les autres nombres en étant très éloignés.

Dans ces circonstances, il est légitime de se poser la question du réalisme des modèles numériques de la géodynamo. Ce problème s'approche beaucoup mieux du point de vue des paramètres de sortie de la simulation, dont nous allons parler en détail dans la section 1.3. Pour l'instant nous dirons simplement qu'une étude récente (Christensen et Tilgner, 2004) a très bien éclairé le sujet. Un des paramètres de sortie les plus importants est le nombre de Reynolds magnétique $Rm = U_{rms}D/\lambda$, qui mesure le rapport entre l'induction magnétique sous l'effet d'un écoulement d'amplitude typique U_{rms}, et la dissipation de ce champ magnétique par effet Ohm. L'étude de la variation séculaire des grandes échelles du champ magnétique permet d'estimer sa valeur pour la Terre à $Rm \approx 1200$. Or, l'espace des paramètres explorés par la simulation dynamo est justement tel que Rm ait une valeur relativement proche, depuis environ $Rm = 40$ (le seuil pour l'instabilité dynamo), jusqu'à $Rm = 1000$. En conséquence, les échelles de temps présentes dans le signal magnétique

simulé présentent une bonne similarité avec le signal réel. Plus précisément, il a été montré que pour un nombre de Reynolds magnétique donné, l'échelle de longueur caractéristique de la dissipation magnétique (qui représente la plus petite échelle de champ magnétique, puisque des échelles plus petites sont dissipées avant d'avoir un effet inductif) est telle que $l_B \approx D\sqrt{1/Rm} \approx 70$ km. En d'autres termes, le maillage des simulations numériques actuelles est suffisant pour décrire correctement l'induction magnétique. Le nœud du problème est donc ailleurs, dans la simulation du champ de vitesses, pour lequel l'usage d'une viscosité très forte (nombre d'Ekman pas assez faible) atténue toutes les petites échelles d'espace et de temps. Ceci n'est pas dramatique à première vue, puisque le champ magnétique n'est en principe pas sensible à ces petites échelles en dessous de $l_B \approx 70$ km. Il faut donc voir les simulations dynamo actuelles comme des systèmes qui simulent correctement le champ magnétique, mais utilisent pour l'induction un écoulement de grandes échelles spatiales et de longues périodes temporelles. Ces considérations préliminaires serviront de fil rouge au cours de la description de mes recherches, car le champ d'applications de la modélisation numérique actuelle doit naturellement être restreint en conséquence.

1.2 L'implémentation numérique PARODY-JA

Afin de faire face aux défis de la modélisation, il est apparu que les générations récentes de supercalculateurs mis à notre disposition demandaient un code numérique adapté. A partir de 2005, Emmanuel Dormy et moi-même avons pris le meilleur des codes numériques existants (auxquels j'avais eu accès au cours de mes séjours post-doctoraux) afin de les greffer sur la base écrite par E. Dormy au cours de sa Thèse (1995-1997). Ceci a donné naissance au projet PARODY. Ce code discrétise les équations détaillées précédemment en géométrie sphérique, par une méthode de différences finies dans la direction radiale, et de décomposition en harmoniques sphériques dans la direction latérale. Le schéma en différences finies s'adapte bien à l'architecture en mémoire distribuée des calculateurs récents. En effet, la résolution n'implique alors que des communications entre processeurs aux bords des domaines, ce qui en réduit le coût. Par la suite, j'ai assuré le développement et le maintien de la branche PARODY-JA, dont l'interface, les fonctions et les sorties sont plus particulièrement ciblées vers les problèmes géophysiques. Il est par exemple possible d'imposer un flux de chaleur hétérogène à la frontière noyau-manteau, à la base de l'étude présentée à la section 1.5. De plus, un second niveau de parallélisation a été implémenté, cette fois dans la direction latérale. L'idée est d'exploiter les architectures dites "multicœur", dans lesquelles plusieurs unités de calcul partagent la même mémoire au sein d'un processeur. PARODY-JA est un code "benchmarké", un anglicisme qui veut simplement dire qu'il a été validé sur des cas-tests bien définis, au sein du projet *Dynamo Benchmark* démarré par Uli Christensen en 1998, auquel j'ai participé (Christensen et al., 2001), sur une version préliminaire du code qui allait devenir PARODY-JA plusieurs années plus tard.

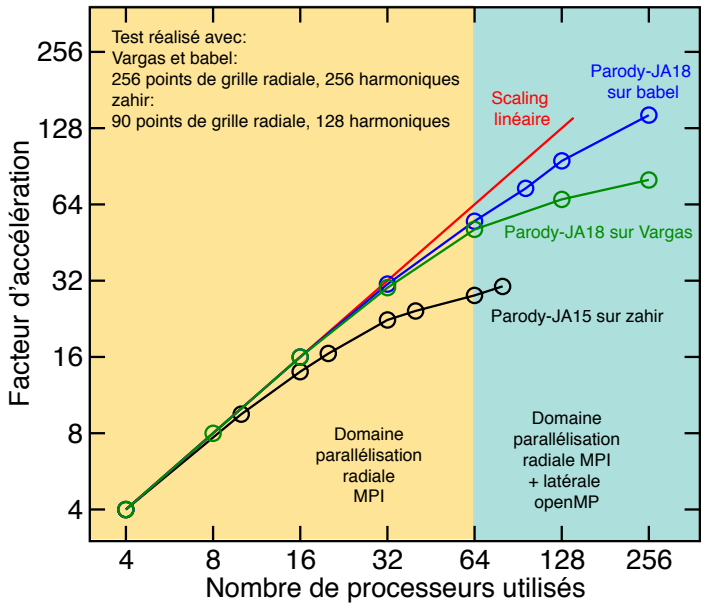

FIG. 1.1 – Facteur d'accélération de PARODY-JA en fonction du nombre de processeurs utilisés. MPI et openMP sont les deux parallélismes utilisés pour ce code. Vargas, zahir et babel sont trois machines de l'IDRIS. Dans la version la plus récente (1.8), l'extensibilité du code est bonne jusqu'à 128 processeurs.

La distribution complète PARODY-JA est documentée, et librement disponible pour la communauté scientifique. A la date de rédaction de ce rapport, les utilisateurs sont : Philippe Cardin et Nathanaël Schaeffer (LGIT Grenoble). Michael Le Bars (IRPHE Marseille), Jonathan Aurnou, Michael Calkins, Jérôme Noir, William Bill Moore (University of California, Los Angeles), Justin Leontini (Monash University, Victoria). Le code dispose d'un module de visualisation avancé (DMFI), qui sera décrit à la section 1.6. Il s'agit de plus d'un code très portable, dont les performances ont été jugées satisfaisantes sur plus d'une dizaine de calculateurs dans le monde (voir figure 1.1).

1.3 Théorie d'échelle pour les dynamos de la Terre et du système solaire

Sur les dix dernières années, le développement des ressources de calcul a permis une exploration systématique de l'espace des paramètres pour les simulations dynamo. Il devenait donc nécessaire d'analyser les quantités diagnostiques moyennes (carré moyen spatial et moyenne temporelle au long terme) des sorties du code, et de formuler une théorie d'échelle, qui devait répondre à trois questions : peut-on établir une continuité de comportement entre les modèles numériques et les objets naturels du système solaire ? Sur quelle base peut-on comparer les dynamos planétaires ?

Est-il possible d'extraire une information géophysique pertinente de l'amplitude des mouvements et du champ magnétique de ces dynamos ? J'ai consacré deux publications récentes à ce travail (Aubert, 2005; Christensen et Aubert, 2006), qui faisaient suite à un travail expérimental de base réalisé au cours de ma Thèse de doctorat (Aubert et al., 2001).

Dans sa version la plus aboutie, l'étude consiste en l'analyse d'une centaine de modèles numériques, couvrant au moins deux ordres de grandeur pour les paramètres E, Pm, Pr, et plus de six ordres de grandeur pour Ra_Q (voir tableau 1.1). Le rapport d'aspect χ est fixé au rapport d'aspect du noyau terrestre actuel, $\chi = 0.35$, et les sources de poussées sont décrites de manière idéalisée par une différence de température entre les frontières du modèle. La section 1.4 décrit une extension récente de la théorie aux cas dans lesquels ces deux dernières conditions deviennent variables. Nous avons mis en évidence (figure 1.2) les lois suivantes pour l'amplitude non-dimensionnelle Lo (nombre de Lorentz) du champ magnétique, celle (Ro, nombre de Rossby) du champ de vitesses, et celle (Ro_z, nombre de Rossby zonal) du mouvement axisymétrique moyen :

$$Ro = \frac{U_{rms}}{\Omega D} \propto Ra_Q^{0.4} \tag{1.10}$$

$$Ro_z = \frac{U_z}{\Omega D} \propto Ra_Q^{0.5} \tag{1.11}$$

$$Lo = \frac{B_{rms}}{(\rho\mu)^{1/2}\Omega D} \propto f_{ohm}^{1/2} Ra_Q^{0.33} \tag{1.12}$$

Ici B_{rms}, U_{rms} et U_z désignent les valeurs dimensionnelles auxquelles correspondent Lo, Ro et Ro_z, et f_{ohm} est un facteur correctif représentant la fraction de l'énergie convective totale qui est dissipée par effet Ohm dans les modèles (pour la Terre, on pense que la très faible viscosité implique une dissipation très majoritairement ohmique, ce qui implique $f_{ohm} \approx 1$). Les justification théorique de ces lois d'échelles sont les suivantes :

- l'exposant 0.4 dans la loi pour Ro reflète un équilibre des forces à trois termes dans l'équation de Navier-Stokes, entre la partie de la force de Coriolis qui n'est pas compensée par le gradient de pression, les forces d'inertie et la poussée d'Archimède (le développement théorique se trouve dans Aubert et al., 2001).
- l'exposant 0.5 dans la loi pour Ro_z reflète un équilibre de vent thermique dans l'équation de Navier-Stokes, entre la force de Coriolis, le gradient de pression et la poussée d'Archimède (le développement théorique se trouve dans Aurnou et al., 2003; Aubert, 2005)
- l'exposant 0.33 dans la loi pour Lo correspond simplement à l'écriture d'une conservation de l'énergie, dans laquelle une partie de la puissance mise à disposition par la convection est dissipée par effet Ohm (le développement théorique se trouve dans Christensen et Aubert, 2006)

La première implication importante de ces lois d'échelle concerne l'absence des diffusivités λ, ν, κ dans l'expression des quantités dimensionalisées U_{rms}, B_{rms}, U_z. Ceci veut dire que les paramètres mal simulés Pm, Pr, E (voir tableau 1.1) ont

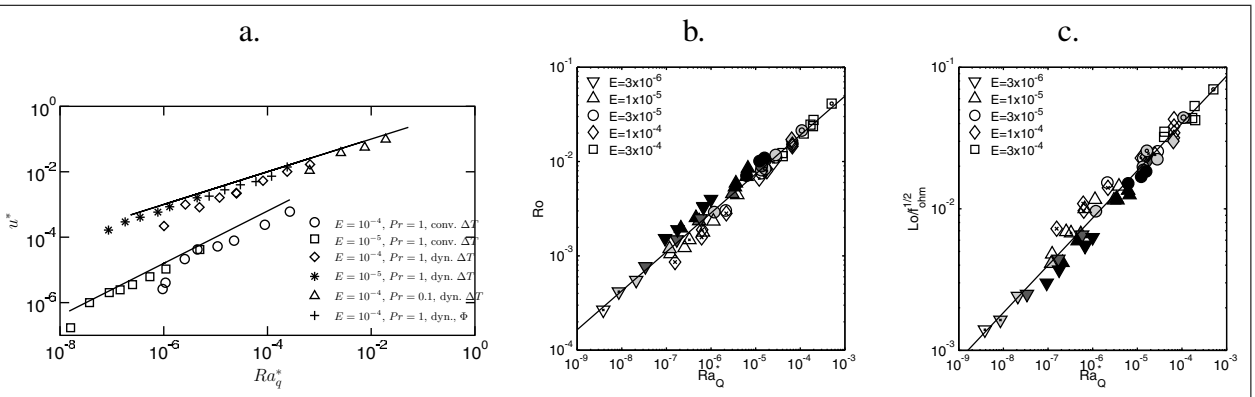

FIG. 1.2 – a. mouvement zonal Ro_z en fonction du flux de co-densité Ra_Q (denoté Ra_Q^* dans cette étude), d'après Aubert (2005) (la courbe du dessus correspond aux dynamos, celle du dessous à la convection non-magnétique). b. et c. : vitesse du fluide Ro et champ magnétique Lo en fonction du flux de co-densité, d'après Christensen et Aubert (2006).

peu ou pas de pertinence dans la description de la saturation du système au long terme. Le paramètre le plus important est la puissance de la convection, exprimée au travers de Ra_Q, qui se trouve être un paramètre correctement simulé. Ceci suggère donc fortement que le régime au long terme dans lequel se trouvent les dynamos numériques peut être directement rapproché du régime des objets naturels, ce qui renforce grandement notre confiance dans ces simulations.

Une estimation des quantités U_{rms}, B_{rms}, U_z permet d'inverser les lois d'échelle pour estimer le flux de co-densité dans la Terre. Les trois lois donnent à peu près le même résultat : $Ra_Q = 10^{-13}$, ou bien $F = 30000$ kg/s. Il est intéressant de noter que les noyaux planétaires sont censés se trouver en général dans la limite $Ra_Q << 1$, car les vitesses convectives qui déterminent F sont en général faibles devant ΩD. Dans ces conditions, on s'attend donc à ce que le mouvement zonal U_z soit en général plus faible ou approximativement égal au mouvement complet U. Pour les dynamos planétaires, ceci montre que le mécanisme dynamo pertinent est du type α^2, correspondant à une double action des mouvements non-zonaux, et non pas du type $\alpha\Omega$, dans lequel le mouvement zonal aurait une importance prépondérante. C'est ce qui distingue par exemple les dynamos planétaires de la dynamo solaire.

Si on considère que pour les noyaux planétaires, $f_{ohm} \approx 1$, la loi d'échelle pour B_{rms} peut se réécrire $B_{rms} = \sqrt{\rho\mu}(FD)^{1/3}$, mettant en lumière une autre implication étonnante : la vitesse de rotation Ω n'intervient pas dans le résultat, contrairement à une loi d'échelle autrefois très populaire (mais infirmée par nos résultats), selon laquelle le nombre d'Elsasser $\Lambda = \sigma B_{rms}^2/\rho\Omega$ vaut environ 1, du fait d'un équilibre entre la force de Coriolis et la force de Lorentz. Une façon simple de comprendre pourquoi la vitesse de rotation n'entre pas dans cette loi d'échelle est de rappeler qu'elle est déterminée par un équilibre énergétique, dans laquelle la force de Coriolis ne peut pas intervenir puisqu'elle ne travaille pas. Cette force définit la géométrie des mouvements convectifs à l'origine de la dynamo, mais ne sature pas l'amplitude

de son champ magnétique.

L'adaptation de ces lois d'échelle aux autres dynamos du système solaire nécessite d'introduire des corrections liés à la géométrie de la région convective, à la nature du fluide conducteur et de son forçage, à la compressibilité. Compte tenu des observations très parcellaires dont on dispose, Uranus, Neptune, Jupiter et Saturne ne semble pas présenter de déviations insurmontables par rapport à ces lois (Aubert et Wicht, 2004; Christensen et Aubert, 2006), mais Mercure pose un problème du fait de la faiblesse du champ mesuré. Il a été montré par la suite (Christensen, 2006) qu'on pouvait tenir compte de cette observation en incluant le fait que le flux de chaleur s'échappant du noyau de Mercure est probablement sous-adiabatique (c'est à dire qu'il s'échappe moins de chaleur du noyau de Mercure que celle qui peut être conduite le long du gradient thermique correspondant au maintien d'un état isentropique bien mélangé), ce qui crée une couche fluide stable filtrant un champ magnétique très variable par un effet de peau.

1.4 Paléo-évolution de la géodynamo

Notre connaissance du magnétisme Terrestre ne se limite pas aux observations géomagnétiques récentes. Le paléomagnétisme nous permet de remonter très loin dans le passé, jusqu'aux plus veilles observations fiables de l'intensité du champ magnétique piégée dans les roches il y a 3.2 milliards d'années (Tarduno et al., 2007). Toutes les observations de paléointensité sont consignées dans la base de données IAGA (Perrin et Schnepp, 2004). De plus, l'analyse de la paléovariation séculaire permet de produire des estimations localisées dans le temps de la dipolarité du champ magnétique (par exemple Smirnov et Tarduno, 2004), et de la fréquence des inversions de polarité (récemment Biggin et al., 2008). Le caractère très parcellaire, et très dispersé des observations a, jusqu'ici, empêché d'arriver à des conclusions fermes concernant l'évolution au long terme de ces quantités (Dunlop et Yu, 2004). Afin d'apporter des éléménts au débat en vigueur, il est naturel de les confronter avec la modélisation numérique dynamo. Dans une étude soumise à la revue Geophysical Journal International, en collaboration avec Stéphane Labrosse (ENS Lyon) et Charles Poitou (IPG Paris), j'ai proposé un cadre théorique d'interprétation global pour la paléo-évolution de la géodynamo.

La géodynamo évolue au cours du temps géologique car la Terre se refroidit, ce qui fait grandir la graine, et fait varier la répartition des sources de poussée d'Archimède. Du point de vue de la dynamo, ces variations sont beaucoup plus lentes que toutes les constantes de temps de la dynamique du noyau. L'idée centrale de l'étude est donc de généraliser les lois d'échelle obtenues pour les moyennes temporelles des sorties du code à des cas pour lesquels on aura prescrit des rapports d'aspect χ différents de 0.35, et une distribution des sources de poussée adéquate. Nous avons donc réalisé des simulations supplémentaires à cette fin.

La prise en compte des sources de poussée introduit deux nouveaux paramètres par rapport à l'étude précédente : le rapport d'aspect χ, et le rapport f_i entre le flux de poussée F_i produit à la frontière interne et le flux de poussée total F. Le paramètre f_i représente donc l'importance de la convection chimique (libération d'éléments légers à la graine). Nous recherchons cependant des lois d'échelles aussi simples que possible, et aussi proches de celles que nous avons déjà déterminées. A ce propos, il apparaît rapidement que le seul paramètre Ra_Q n'était pas à même de décrire toute la variabilité des résultats. Par contre, la puissance P de la convection, pour laquelle nous avons montré dans Christensen et Aubert (2006) qu'elle était proportionnelle à Ra_Q, à un facteur près qui dépend de la géométrie, semble mieux adapté, comme nous allons le voir bientôt. Notre premier travail est donc d'écrire une relation généralisée reliant P à Ra_Q. Pour cela nous écrivons la relation thermodynamique établie par Buffett et al. (1996) entre la dissipation totale de la dynamo Φ et les flux de poussée (valable dans la limite des forts mélanges) :

$$\Phi = F_i(\psi_i - \overline{\psi}) + (F - F_i)(\overline{\psi} - \psi_o) \tag{1.13}$$

Ici ψ_i, ψ_o et $\overline{\psi}$ représentent respectivement les valeurs aux frontières interne et externe, ainsi que la valeur moyenne, du potentiel gravitationnel $\psi = r^2 g_o/2r_o + cst$ correspondant au champ de gravité $\mathbf{g} = -g_o\mathbf{r}/r_o$. Après avoir remarqué qu'en régime permanent, nous avons $P = \Phi$, et en définissant la puissance volumique de la convection par $p = 3P/4\pi(r_o^3 - r_i^3)$, nous obtenons finalement

$$p = \gamma \frac{g_o F}{4\pi D^2} \tag{1.14}$$

avec

$$\gamma = \frac{3(r_o - r_i)^2}{2(r_o^3 - r_i^3)r_o}\left[f_i\left(\frac{3}{5}\frac{r_o^5 - r_i^5}{r_o^3 - r_i^3} - r_i^2\right) + (1 - f_i)\left(r_o^2 - \frac{3}{5}\frac{r_o^5 - r_i^5}{r_o^3 - r_i^3}\right)\right] \tag{1.15}$$

ce qui correspond à la forme non-dimensionnelle suivante :

$$\frac{p}{\rho\Omega^3 D^2} = \gamma Ra_Q \tag{1.16}$$

Nous avons vérifié le très bon accord de cette relation avec les résultats (calcul direct de p et comparaison avec Ra_Q) de nos simulations, dans la limite d'un bon mélange. Nous voyons ici que le facteur γ intègre des dépendances correspondant à la géométrie du système, ainsi qu'à la répartition des sources de poussée. De plus, puisque les lois d'échelles présentées précédemment reposent sur les arguments principalement énergétiques, il est naturel de remplacer Ra_Q par p comme paramètre de mise à l'échelle principal. C'est ce que nous avons fait dans la figure 1.3. Les lois d'échelle obtenues sont exactement les mêmes que dans la section précédente (p remplaçant Ra_Q) :

$$Ro = \frac{U_{rms}}{\Omega D} \propto p^{0.4} \tag{1.17}$$

$$Lo = \frac{B_{rms}}{(\rho\mu)^{1/2}\Omega D} \propto f_{ohm}^{1/2} p^{0.33} \tag{1.18}$$

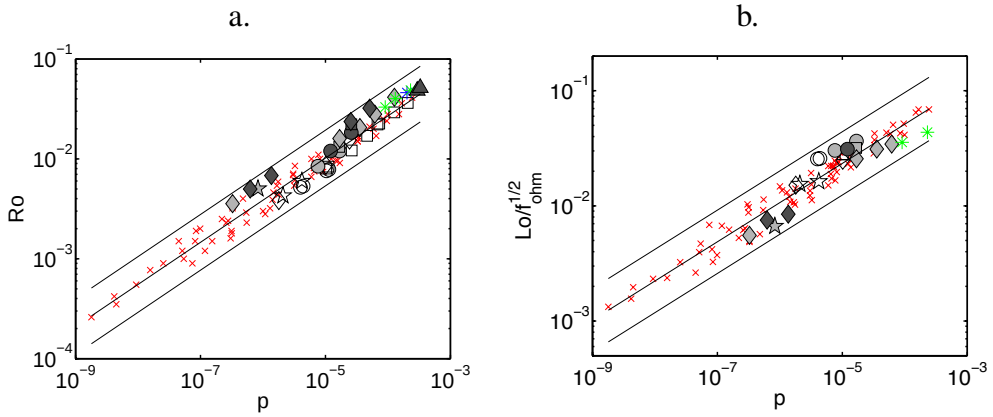

FIG. 1.3 – a,b : Lois d'échelle pour la vitesse (*Ro*), le champ magnétique (*Lo*) en fonction de la puissance volumique de la convection p. Les crois rouges représentent les points déjà étudiés par (Christensen et Aubert, 2006) (section 1.3), les autres symboles représentent les nouvelles simulations pour lesquelles f_i et χ sont variables (voir la publication complète en fin de mémoire pour plus de détails).

Les points déjà obtenus dans Christensen et Aubert (2006) s'alignent avec les nouveaux points obtenus pour f_i et χ variable, confirmant ainsi que l'utilisation de p permet de décrire toutes les dépendances liées à ces deux nouveaux paramètres. En suivant la même démarche, nous avons par la suite quantifié la dipolarité (ou amplitude du dipôle à la frontière noyau-manteau par rapport au champ observable), ainsi que la capacité de ces modèles à produire des inversions de polarité. Les détails de l'étude peuvent être consultés à la fin de ce mémoire.

L'utilisation de p comme paramètre de contrôle principal possède de plus un intérêt géophysique. En effet, la thermodynamique du noyau permet de relier p à l'évolution thermique de la planète, en particulier au flux de chaleur $Q_{cmb}(t)$ traversant la frontière noyau-manteau à une époque donnée (voir par exemple Labrosse et al., 2001; Labrosse, 2003; Lister, 2003) :

$$\frac{4}{3}\pi(r_o^3 - r_i^3)\, p = \Phi = Q_{cmb}(\epsilon_L + \epsilon_B) + (Q_{cmb} - Q_a)\epsilon_S \tag{1.19}$$

Ici Q_a est le flux de chaleur adiabatique s'échappant du noyau, et ϵ_L, ϵ_B, ϵ_S sont les efficacités thermodynamiques respectives des processus de libération de chaleur latente, d'éléments légers (à la frontière de la graine) et de la convection thermique (à la frontière externe). La spécification d'une histoire de refroidissement du noyau $Q_{cmb}(t)$ permet donc, à travers (1.19), de produire une histoire $p(t)$ pour la puissance de la géodynamo, et d'utiliser les lois d'échelle (1.17,1.18) pour prédire les observables de la géodynamo au cours du temps.

L'histoire thermique de la Terre est encore mal contrainte, malgré les progrès sismologiques récents (Hernlund et al., 2005; Lay et al., 2006; van der Hilst et al.,

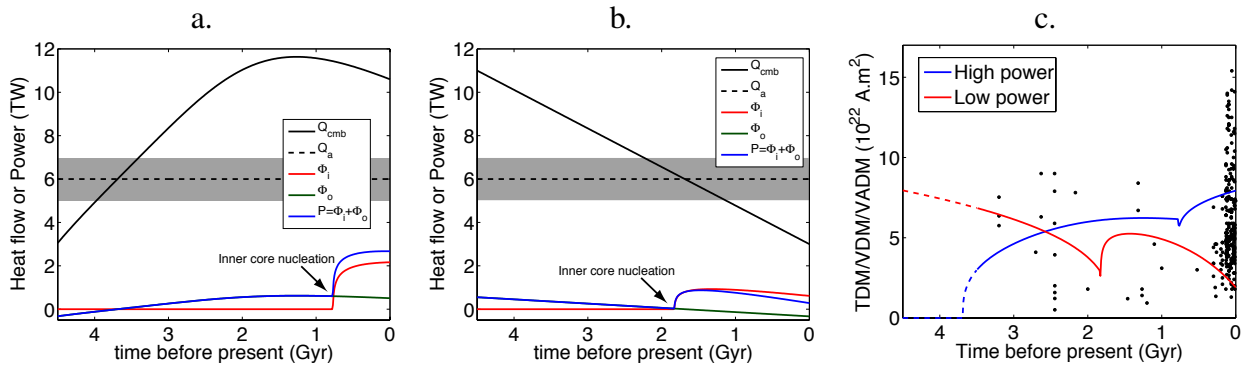

FIG. 1.4 – a,b : Modèles d'évolution thermique de la Terre. Le modèle haute puissance (a) est tiré de Labrosse et al. (2007), le modèle basse puissance (b) est un modèle idéalisé. Le flux de chaleur à la CMB est en noir, la puissance de la dynamo en bleu. La zone grise représente le domaine d'estimation du flux de chaleur adiabatique. c : Modèles d'évolution du moment dipolaire vrai (TDM) en fonction du temps, pour les deux scénarios. Les données de paléointensité sont extraites de la base PINT08 IAGA (Biggin et al., in press, 2008).

2007) qui ont abouti aux premières mesures directes du gradient thermique (et donc à des estimations du flux de chaleur à à la frontière noyau-manteau. C'est la raison pour laquelle nous avons produit nos modèles de paléo-évolution pour deux scénarios de refroidissement (figure 1.4.a,b) représentant des cas extrêmes, afin de fournir des contraintes issues du paléomagnétisme dans ce domaine. Dans le premier, le flux de chaleur actuel à la frontière noyau-manteau vaut $Q_{cmb}(0) = 11$ TW (modèle de dynamo "forte puissance"), et dans le second, le flux de chaleur actuel vaut $Q_{cmb}(0) = 3$ TW (modèle de dynamo "faible puissance"). Le premier scénario correspond à un flux de chaleur qui reste au dessus du flux adiabatique, alors que dans le second, le flux de chaleur passe en dessous de l'adiabat, ce qui veut dire que la dynamo ne peut fonctionner que si la graine est déjà présente, activant de fait le moteur compositionnel pour la convection. la comparaison des modèles pour le moment dipolaire avec les observations paléomagnétiques de moment dipolaire virtuel (figure 1.4.c) ne permet pas de conclure quant à la supériorité de l'un des modèles pour le Précambrien, mais elle favorise assez nettement le modèle haute puissance pour les temps récents. En effet, dans un scénario de basse puissance, le caractère sous-adiabatique du sommet du noyau implique l'existence d'une couche de fluide au repos, qui diminue significativement l'amplitude du dipôle magnétique mesuré à la surface. Nous préférons donc un modèle de type haute puissance, dont le résultat principal est l'augmentation modérée du moment dipolaire au cours des temps géologiques, de 5 10^{22} A.m^2 il y a trois milliards d'années à 8 10^{22} A.m^2 aujourd'hui.

Les autres conclusions robustes (c'est à dire indépendantes du scénario de refroidissement choisi) sont les suivantes. Nous montrons que la dynamo peut être en principe réalisée à partir de 3.8 milliards d'années en arrière, et que les inversions sont présentes depuis 3.5 milliards d'années. Avant l'apparition de la graine (que nos deux modèles prévoit assez jeune, moins de 2 milliards d'années d'âge), une

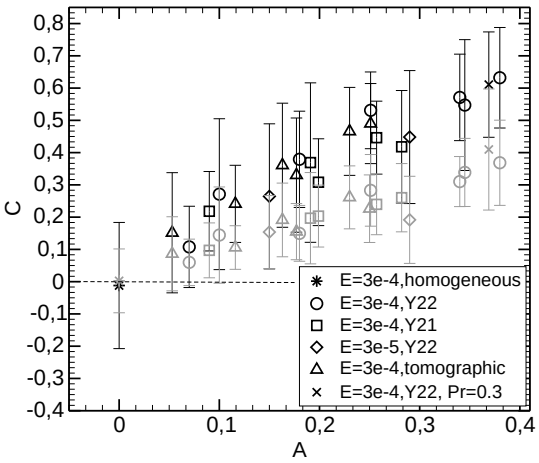

FIG. 1.5 – Mesure C (coefficient de corrélation) de la ressemblance entre un écoulement transitoire sous la frontière noyau-manteau et l'écoulement causé au long term par le manteau pour des moyennes temporelles sur 150 ans (symboles noirs), et des instantanés (symboles gris), en fonction du rapport A entre le forçage homogène et le forçage dû au contrôle thermique hétérogène du manteau. Nous avons évalué $0.1 < A < 1$ pour la Terre, rendant la détection du contrôle mantellique assez probable sur une durée de 150 ans.

dynamo thermique dont l'énergie est fournie par le seul refroidissement séculaire de la planète était tout à fait possible, ce qui réfute une interprétation commune (Dunlop, 2007) selon laquelle l'existence, il y a 3.2 milliards d'années, d'un champ magnétique possiblement aussi fort que le champ présent (Tarduno et al., 2007), est une indication de la présence de la graine. Nous avons aussi trouvé que l'apparition de la graine donne plus de puissance à la dynamo (du fait de l'apparition de la source de poussée compositionnelle), mais le lieu de l'action dynamo migre vers les profondeurs du noyau. Ces deux effets se compensent mutuellement en ce qui concerne leur influence sur le moment dipolaire observé à la surface de la Tere, ce qui nous amène à conclure qu'il est peu probable qu'il existe une signature paléomagnétique de l'apparition de la graine, comme cela a été suggéré par le passé (Hale, 1987). Les dynamos relatives à la Terre au Précambrien sont généralement moins dipolaires, mais aussi moins instables (du point de vue des inversions), ce qui confirme les conclusions obtenues par des études récentes de paléovariation séculaire (Biggin et al., 2008), qui suggèrent que les inversions de polarité magnétiques étaient moins fréquentes il y a 2.4-2.8 milliards d'années.

1.5 Couplage global et hétérogénéité thermo-chimique dans la Terre profonde

Jusqu'ici, nous nous sommes intéressés principalement à l'amplitude du champ magnétique présent ou passé, moyennée sur des temps de l'ordre du million d'an-

nées, sans nous préoccuper de sa géométrie. Les modèles que nous avons du champ paléomagnétique moyen au cours des cinq derniers millions d'années, comme par exemple celui de Kelly et Gubbins (1997) (figure 1.7.a) suggèrent que des lobes de champ magnétique persistent à la frontière noyau-manteau. La modélisation numérique les attribue à l'effet d'un forçage thermique exercé par un manteau profond rendu hétérogène par l'arrivée des plaques froides provenant des zones de subduction (par exemple Olson et Christensen, 2002). Il existe cependant un débat vigoureux concernant la capacité effective des données paléomagnétiques à résoudre ce niveau de détail. L'asymétrie longitudinale se retrouve aussi dans des modèles d'écoulement fluide sous la frontière noyau-manteau pour les 150 dernières années (figure 1.7.c), obtenus par inversion de la variation séculaire du champ géomagnétique historique (Amit et Olson, 2006). La faible longueur de la durée du moyennage temporel dans ce dernier cas pose naturellement la question de l'importance des signaux transitoires (non liés à l'action du manteau) dans ces modèles. Nous avons exploré ce thème dans une étude récente (Aubert et al., 2007), dont le but était d'explorer la possibilité de détecter l'influence du manteau sur des temps aussi courts (figure 1.5). Nous avons conclu que l'effet principal du manteau était de favoriser certains lieux géographiques pour l'émergence des colonnes cycloniques fluides caractéristiques de la convection en rotation, ce qui élève la probabilité d'observer des motifs réminiscents du contrôle mantellique sur des durées courtes, et même sur des instantanés de l'écoulement.

Dans une étude récente publiée dans le magazine *Nature* (Aubert et al., 2008), nous avons rapproché ces deux observations d'une troisième manifestation, beaucoup plus profonde cette fois, de l'hétérogénéité dans la Terre profonde : les signaux sismiques en provenance de la graine révèlent que la surface (premiers 100 km) de l'hémisphère Est est plus rapide, moins anisotrope, et plus atténuante que celle de l'hémisphère ouest (Tanaka et Hamaguchi, 1997; Niu et Wen, 2001; Cao et Romanowicz, 2004). Il a été proposé (Sumita et Olson, 1999; Bergman et al., 2005) que ceci pouvait résulter d'une façonnage de la graine, au moment de sa solidification, par l'écoulement fluide dans le noyau externe. Pour valider ce scénario, il fallait donc montrer que les mêmes écoulements pouvaient expliquer simultanément les trois observations présentées ci-dessus. Notre modèle numérique (figure 1.6), forcé par un manteau hétérogène dont la structure est déduite de la sismologie du manteau profond (Masters et al., 2000), met en évidence, une fois moyenné dans le temps, un grand cyclone fluide sous l'Asie, visible sous la frontière noyau manteau (figure 1.7.d), correspondant aux observations faites dans cette région (figure 1.7.c). Les basses pressions existant au cœur de ce cyclone concentrent le champ magnétique radial au même endroit (figure 1.7.b), ce qui explique la localisation des taches de champ magnétique (figure 1.7.a). Enfin, ce cyclone touche la graine en position equatoriale sous l'Asie centrale (figure 1.7.e), et amène du fluide froid et appauvri en élements légers, causant de ce fait une cristallisation plus rapide de la graine dont les effets peuvent expliquer l'hétérogénéité sismique, au moins du point de vue qualitatif.

L'exploitation que nous avons faite ici du signal magnétique permet finalement

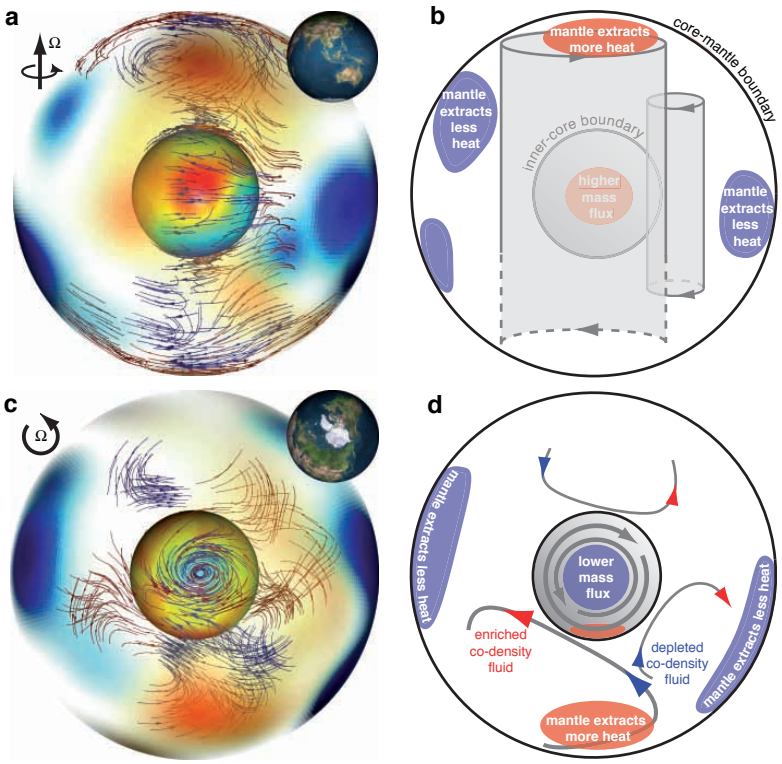

FIG. 1.6 – a,c : visualisation de l'écoulement moyen dans le modèle numérique. les flèches bleues (rouges) représentent l'écoulement descendant (montant). Les taches sur la frontière externe représentent la structure thermique du manteau profond (en rouge, les régions où le manteau extrait plus de chaleur du noyau que la moyenne). b.d : diagrammes explicatifs du mécanisme par lequel la graine croît de manière hétérogène, expliquant de ce fait les différences de propriétés sismiques entre l'hémisphère Est et l'hémisphère Ouest.

de montrer que la Terre est un système d'enveloppes dynamiquement couplées les unes aux autres, et que ce couplage s'exerce depuis la surface (plaque tectoniques) jusqu'au plus profond de la planète (graine).

1.6 Dynamique des lignes de champ magnétique et mécanisme des inversions de polarité

J'ai consacré une seconde étude (Aubert et al., 2008) à l'analyse de la morphologie et des variations (cette fois plus rapides que dans les études précédentes, de l'ordre du miller d'années) du champ magnétique. Le but était de trouver une façon de décrire dynamiquement les structures du champ magnétique profond qui sous-tendent ces observations de surface. S'agissant d'un problème très sous-déterminé, la modélisation numérique s'est révèlée très utile pour isoler des structures magnétiques caractéristiques, correspondant à des entités dynamiques bien identifiées,

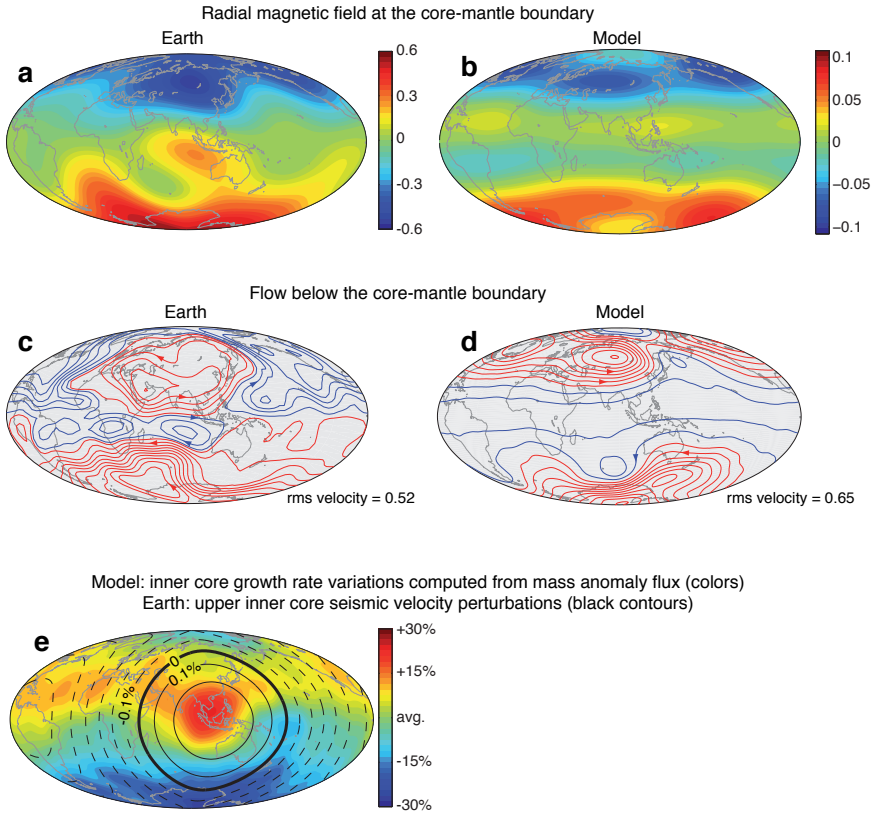

FIG. 1.7 – a : Modèle de champ paléomagnétique radial moyen au cours des 5 derniers millions d'années (Kelly et Gubbins, 1997). c : Modèle d'écoulement moyen sous la frontière noyau-manteau au cours des 150 dernières années (Amit et Olson, 2006). b,d : Modèles numériques correspondant à a,c. e,f : Modèle de l'hétérogénéité en vitesse sismique à la frontière de la graine (contours noirs, d'après Tanaka et Hamaguchi, 1997), et modèle numérique du de la vitesse de cristallisation de la graine du fait de l'écoulement dans le noyau externe.

mais c'est surtout l'exploration du concept de ligne de champ magnétique (qui, par le passé, a fondé la réflexion théorique sur les mécanismes dynamo) qui nous a donné un outil à même de progresser dans ce domaine.

La formulation du théorème du flux gelé (Alfvén, 1943) a profondément influencé notre compréhension du mécanisme dynamo : dans un milieu de conductivité infinie, les lignes de force du champ magnétique (lignes parallèles en tout point au vecteur champ magnétique, que nous appellerons "lignes de champ" par la suite) se déplacent avec le milieu, comme s'il s'agissait de lignes matérielles gelées dans l'écoulement. Avant le développement massif des modèles numériques, ce théorème a suscité de nombreux modèles conceptuels (tels que les modèles d'Alfvén et Zeldovitch) expliquant comment un mouvement fluide peut régénérer un champ magnétique pré-existant, par l'étirement, la torsion et le repliement des lignes de champ. Dans le noyau de la Terre, ainsi que dans les modèles numériques, la conductivité n'est pas infinie, ce qui limite la validité du théorème aux grandes échelles d'espace et aux temps plus courts que le siècle.

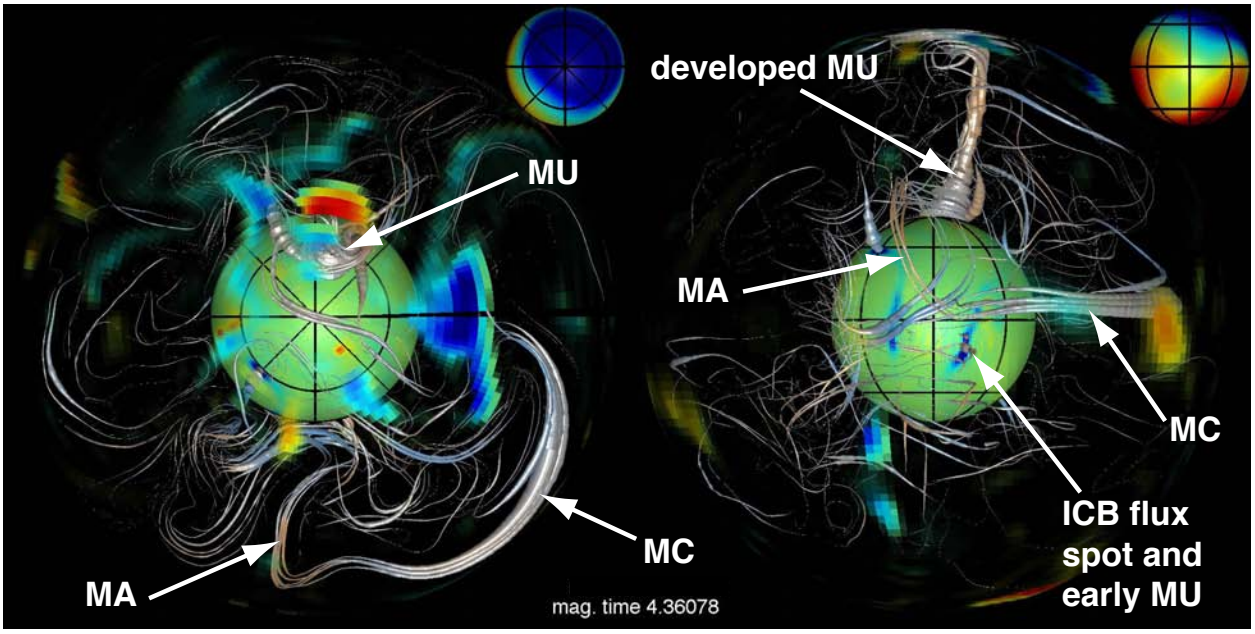

FIG. 1.8 – Visualisation DMFI d'un modèle numérique dynamo. Gauche : vue du pôle Nord. Droite : vue equatoriale. La frontière noyau-manteau est partiellement transparente, ne laissant voir que les taches de champ magnétique radial de surface. Sur la graine, la cartographie du champ magnétique radial est aussi représentée. Les lignes de champ magnétique (en gris) ont une épaisseur qui reflète l'énergie magnétique locale. Les petites sphères représentent le champ magnétique radial à la surface de la Terre.

Le but de cette étude était d'utiliser les bases solides de raisonnement posées par le théorème du flux gelé dans ce contexte dissipatif, ce qui a suscité plusieurs difficultés. Tout d'abord, les lignes de champ magnétique ne bougent pas seulement avec le fluide, mais apparaissent et disparaissent. Ensuite, la visualisation informatique de ces lignes nécessite la sélection adéquate de points d'ancrage, et leur suivi au cours du temps. L'algorithme DMFI (pour Dynamical Magnetic Fieldline Imaging) est la combinaison d'une représentation statique des lignes de champ tenant compte de l'énergie qu'elles contiennent (cette énergie déterminant leur épaisseur), et d'un algorithme de suivi des points d'ancrage, dont le principe est le suivant : à chaque itération, le point d'ancrage servant pour l'itération future est le point de plus haute énergie magnétique de la ligne. Des animations utilisant cette méthode sont disponibles à l'URL `http ://www.ipgp.jussieu.fr/~aubert/DMFI.html`.

Nous avons d'abord vérifié que DMFI produit des visualisations adéquates de mécanismes dynamo déjà identifiés, tels que ceux présentés dans Olson et al. (1999). La méthode met en évidence deux types de structures magnétiques, correspondant aux structures de plus grande échelle de l'écoulement : les cyclones et anticicyclones magnétiques (respectivement notés MC and MA sur la figure 1.8). Les anticyclones magnétiques constituent le cœur du mécanisme dynamo de type "alpha carré", et régénèrent le dipôle magnétique par étirement des lignes de champ. Les cyclones magnétiques participent à la dissipation du champ magnétique par concentration

des lignes de champ.

Nous avons isolé ensuite un nouveau type de structure magnétique : les panaches magnétiques (“magnetic upwellings” en anglais, notés MU sur la figure 1.8). Ces structures magnetiques se développent dans les panaches hydrodynamiques ascendants, par étirement du champ magnétique, et prennent la forme de grands filaments, en position axiale ou équatoriale. Ces structures amplifient et apportent vers la surface une trace du champ magnétique présent à la frontière de la graine. Or, le champ magnétique à la graine est très multipolaire, et n’est pas organisé avec une composante dipolaire forte comme il l’est à la frontière noyau-manteau. En montrant que ces panaches magnétiques amènent les perturbations du dipôle magnétique qui sont à l’origine des excursions et inversions de polarité, nous avons décrit en termes de lignes de champ, pour la première fois, les mécanismes qui sous-tendent ces évènements. De plus, chaque structure magnétique possède une signature caractéristique à la frontière noyau-manteau. La méthode DMFI ouvre donc la voie à de nouvelles recherches visant à cartographier la structure magnétique de l’intérieur de la Terre à l’aide des observations de surface et de la modélisation numérique.

Bibliographie

Alfvén, H., On the existence of electromagnetic-hydrodynamic waves, *Ark. Mat. Astron. Fys.*, *29*, 1–7, 1943.

Amit, H. et Olson, P., Time average and time dependent parts of core flow, *Phys. Earth Planet. Int.*, *155*, 120–139, doi : 10.1016/J.pepi.2005.10.006, 2006.

Aubert, J., Steady zonal flows in spherical shell dynamos, *J. Fluid. Mech.*, *542*, 53–67, 2005.

Aubert, J. et Wicht, J., Axial versus equatorial dipolar dynamo models with implications for planetary magnetic fields, *Earth. Plan. Sci. Let.*, *221*, 409–419, doi :10.1016/S0012-821X(04)00102-5, 2004.

Aubert, J., Brito, D., Nataf, H.-C., Cardin, P., et Masson, J. P., A systematic experimental study of spherical shell convection in water and liquid gallium, *Phys. Earth Planet. Int.*, *128*, 51–74, 2001.

Aubert, J., Amit, H., et Hulot, G., Detecting thermal boundary control in surface flows from numerical dynamos, *Phys. Earth Planet. Int.*, *160*, 143–156, 2007.

Aubert, J., Aurnou, J., et Wicht, J., The magnetic structure of convection-driven numerical dynamos, *Geophys. J. Int.*, *172*, 945–956, 2008.

Aubert, J., Amit, H., Hulot, G., et Olson, P., Thermochemical flows couple the Earth's inner core growth to mantle heterogeneity, *Nature*, *454*, 758–U80, 2008.

Aurnou, J., Andreadis, S., Zhu, L., et Olson, P., Experiments on convection in Earth's core tangent cylinder, *Earth Plan. Sci. Let.*, *212*, 119–134, 2003.

Bergman, M. I., Macleod-Silberstein, M., Haskel, M., Chandler, B., et Akpan, N., A laboratory model for solidification of Earth's core, *Phys. Earth Planet. Int.*, *153*, 150–164, 2005.

Biggin, A. J., Strik, G. H. M. A., et Langereis, C. G., The intensity of the geomagnetic field in the late-archaean : new measurements and an analysis of the updated iaga palaeointensity database, *Earth Planets Space*, in press, 2008.

Biggin, A. J., Strik, G. H. M. A., et Langereis, C. G., Evidence for a very-long-term trend in geomagnetic secular variation, *Nature Geosci.*, *1*, 395–398, 2008.

Braginsky, S. I. et Roberts, P. H., Equations governing convection in Earths core and the geodynamo, *Geophys. Astrophys. Fluid Dyn.*, *79*, 1–97, 1995.

Buffett, B., Huppert, H., Lister, J., et Woods, A., On the thermal evolution of the Earth's core, *J. Geophys. Res.*, *101*, 7989–8006, 1996.

Cao, A. et Romanowicz, B., Hemispherical transition of seismic attenuation at the top of the Earth's inner core, *Earth Plan. Sci. Let.*, *228*, 243–253, 2004.

Christensen, U. et Aubert, J., Scaling properties of convection-driven dynamos in rotating spherical shells and application to planetary magnetic fields, *Geophys. J. Int.*, *117*, 97–114, 2006.

Christensen, U. et Tilgner, A., Power requirement of the geodynamo from ohmic losses in numerical and laboratory dynamos, *Nature*, *429*, 169–171, doi : 10.1038/nature02508., 2004.

Christensen, U. R., A deep dynamo generating Mercury's magnetic field, *Nature*, *444*, 1056–1058, 2006.

Christensen, U. R., Aubert, J., Busse, F. H., Cardin, P., Dormy, E., Gibbons, S., Glatzmaier, G. A., Honkura, Y., Jones, C. A., Kono, M., Matsushima, M., Sakuraba, A., Takahashi, F., Tilgner, A., Wicht, J., et Zhang, K., A numerical dynamo benchmark, *Phys. Earth Planet. Int.*, *128*, 25–34, 2001.

Dunlop, D. et Yu, Y., Intensity and polarity of the geomagnetic field during Precambrian time, in *Timescales of the paleomagnetic field*, edité par Channell, JET and Kent, DV and Lowrie, W and Meert, JG, vol. 145, pp. 85–100, AGU Monograph, 2004.

Dunlop, D. J., Palaeomagnetism - A more ancient shield, *Nature*, *446*, 623+, 2007.

Dziewonski, A. et Anderson, D., Preliminary reference Earth model PREM, *Phys. Earth Planet. Int.*, *25*, 297–356, 1981.

Hale, C. J., Paleomagnetic data suggest link between the Archean-Proterozoic boundary and inner-core nucleation, *Nature*, *329*, 233–237, 1987.

Hernlund, J. W., Thomas, C., et Tackley, P. J., Phase boundary double crossing and the structure of Earth's deep mantle, *Nature*, *434*, 882–886, doi :10.1038/nature03472, 2005.

Kelly, P. et Gubbins, D., The geomagnetic field over the past 5 million years, *Geophys. J. Int.*, *128*, 315–330, 1997.

Labrosse, S., Thermal and magnetic evolution of the Earth's core, *Phys. Earth Planet. Int.*, *140*, 127–143, 2003.

Labrosse, S., Poirier, J. P., et Le Mouel, J. L., The age of the inner core, *Earth Planet. Sci. Let.*, *190*, 111–123, 2001.

Labrosse, S., Hernlund, J. W., et Coltice, N., A crystallizing dense magma ocean at the base of the earth's mantle, *Nature*, *450*, 866–869, 2007.

Lay, T., Hernlund, J., Garnero, E. J., et Thorne, M. S., A post-perovskite lens and D" heat flux beneath the central pacific, *Science*, *314*, 1272–1276, 2006.

Lister, J. R., Expressions for the dissipation driven by convection in the Earth's core, *Phys. Earth Planet. Int.*, *140*, 145–158, 2003.

Lister, J. R. et Buffett, B. A., The strength and efficiency of thermal and compositional convection in the geodynamo, *Phys. Earth Planet. Int.*, *91*, 17–30, 1995.

Masters, G., Laske, G., Bolton, H., et Dziewonski, A., The relative behavior of shear velocity, bulk sound speed, and compressional velocity in the mantle : Implications for chemical and thermal structure, in *Earth's Deep Interior*, edité par S. Karato, A. Forte, R. C. Liebermann, M. G., et L. Stixrude, vol. 117, AGU Monograph, Washington D.C., 2000.

Niu, F. L. et Wen, L. X., Hemispherical variations in seismic velocity at the top of the Earth's inner core, *Nature*, *410*, 1081–1084, 2001.

Olson, P. et Christensen, U., The time averaged magnetic field in numerical dynamos with non-uniform boundary heat flow, *Geophys. J. Int.*, *151*, 809–823, 2002.

Olson, P., Christensen, U., et Glatzmaier, G. A., Numerical modelling of the geodynamo : mechanisms of field generation and equilibration, *J. Geophys. Res.*, *104*, 10 383–10 404, 1999.

Perrin, M. et Schnepp, E., IAGA paleointensity database : distribution and quality of the data set, *Phys. Earth Planet. Int.*, *147*, 255–267, Joint Meeting of the European-Geophysical-Society/American-Geophysical-Union and European-Union-of-Geoscience, Nice, FRANCE, APR 06-11, 2003, 2004.

Smirnov, A. et Tarduno, J., Secular variation of the Late Archean Early Proterozoic geodynamo, *Geophys. Res. Let.*, *31*, 2004.

Sumita, I. et Olson, P., A laboratory model for convection in earth's core driven by a thermally heterogeneous mantle, *Science*, *286*, 1547–1549, 1999.

Tanaka, S. et Hamaguchi, H., Degree one heterogeneity and hemispherical variation of anisotropy in the inner core from PKP(BC)-PKP(DF) times, *J. Geophys. Res.*, *102*, 2925–2938, 1997.

Tarduno, J. A., Cottrell, R. D., Watkeys, M. K., et Bauch, D., Geomagnetic field strength 3.2 billion years ago recorded by single silicate crystals, *Nature*, *446*, 657–660, 2007.

van der Hilst, R., De Hoop, M. V., Wang, P., Shim, S.-H., Ma, P., et Tenorio, L., Seismostratigraphy and thermal structure of Earth's core-mantle boundary region, *Science*, *315*, 1813–1817, 2007.

Wicht, J., Inner-core conductivity in numerical dynamo simulations, *Phys. Earth Planet. Int.*, *132*, 281–302, 2002.

Chapitre 2

Perspectives scientifiques

2.1 Résumé et potentiel de l'approche

J'ai montré dans le chapitre précédent comment on peut extraire des contraintes géophysiques importantes des données magnétiques, en les interprétant à l'aide de la modélisation numérique de la dynamique des noyaux de la Terre et des planètes du système solaire. J'ai aussi montré que si l'on s'intéresse à l'état statistiquement stationnaire du système (ou du moins au longues échelles de temps), l'écart entre les modèles et la réalité n'est pas si important qu'on a pu le penser auparavant, puisque les paramètres mal simulés semblent avoir une importance secondaire dans la détermination de cet état. C'est pourquoi l'utilisation des lois d'échelle est un outil essentiel pour réaliser l'adaptation des modèles numériques à la réalité.

Dans ce chapitre, je détaille les perspective de ma recherche, qui découlent d'une part des améliorations attendues dans mon domaine, et d'autre part dans celles attendues dans les domaines connexes : progrès en modélisation géodynamique globale, en sismologie, géochimie, géomagnétisme et paléomagnétisme, dans les modèles thermodynamiques, et utilisation de données nouvelles (pour mon approche) telles que les séries temporelles de la longueur du jour.

2.2 Perspectives en modélisation numérique directe

2.2.1 Lois d'échelle complémentaires

Malgré nos progrès récents dans la compréhension des lois d'échelle régissant les dynamos numériques, il subsiste encore un domaine dans lequel nous n'avons

pas pu conclure : la description des échelles de longueur du champ de vitesse et du champ magnétique. Il s'agit d'un domaine dans lequel la modélisation a une contribution décisive à apporter, car l'observation du champ magnétique d'origine interne est limitée par le champ magnétique crustal, ce qui, en pratique, nous empêche de savoir quel en est le contenu haute fréquence (degré d'harmonique sphérique supérieur à 14). Il est possible cependant de décrire la variation séculaire du champ magnétique avec une finesse supérieure, puisqu'on peut alors soustraire le champ crustal (Hulot et al., 2002). Cette procédure fonde d'ailleurs la mission satellitaire SWARM, dont le lancement est prévu pour le début de la prochaine décennie.

La principale difficulté liée à ce projet est la faible gamme de variation de ces échelles. Les lois que nous avons dégagées jusqu'ici font intervenir des puissances du forçage convectif de l'ordre de 0.4-0.6, ce qui permet une bonne résolution de l'exposant si on dispose d'une dynamique de 9 décades en forçage. La situation est différente pour les échelles de longueur, pour lesquelles l'exposant est plutôt de l'ordre de 0.1-0.2. Il importe donc d'élargir l'espace des paramètres disponible. Une autre difficulté vient du fait que les échelles de longueur sont fortement anisotropes, du fait de la contrainte imposée par la rotation rapide du système. Nous devons donc séparer les différentes directions d'espace.

Cette étude permettra de fermer notre théorie d'échelle pour les dynamos numériques, et elle fournira des contraintes importantes pour l'estimation de la structure à petite échelle de la géodynamo.

2.2.2 Etat thermodynamique passé et présent du noyau de la Terre

Dans l'étude sur la paléo-évolution de la géodynamo, nous avons jeté les bases de l'interaction entre modèles dynamo et thermodynamique du noyau. Ceci rend les observations magnétiques susceptibles de contraindre l'état thermodynamique présent et passé du noyau. Nous attendons que les progrès du paléomagnétisme au précambrien permettent, à terme, de discriminer les scénarios de refroidissement du noyau que proposent les études thermodynamiques. Puisque les meilleures données proviennent des époques récentes, il importe d'en faire une étude plus poussée, en particulier en comparant de manière plus systématique les différences de comportement entre dynamos sous- et super- adiabatiques. En particulier, une quantité importante d'informations semble résider dans les fluctuations des champs géomagnétique et paléomagnétique. Une étude correspondante des fluctuations dans les dynamos numériques doit permettre d'utiliser l'information contenue dans ces fluctuations, en particulier en contraignant l'amplitude maximale de ces fluctuations qui est compatible avec le maintien d'une dynamo. Les progrès concernant l'état thermodynamique du noyau seront probablement fortement influencés par l'effort que consacre actuellement la communauté sismologique à l'imagerie de la frontière noyau-manteau, en vue de l'estimation du flux de chaleur qui la traverse. Il faut

effectivement garder à l'esprit que les études existantes se basant sur la transition vers la post-perovskite (Lay et al., 2006; van der Hilst et al., 2007) possèdent actuellement deux limitations : ce sont des études localisées, et elles ne fournissent qu'une borne supérieure du flux de chaleur, puisqu'elles approximent un gradient de température de pente variable par une sécante.

2.2.3 Couplages graine-noyau-manteau, rotation différentielle de la graine, longueur du jour

Notre étude du couplage entre le manteau et la graine a suscité un questionnement nouveau : si le manteau est capable d'imprimer sa signature sur la graine pendant des temps de l'odre de la centaine de millions d'années, il est évident que la graine ne peut pas beaucoup tourner, sinon cette signature serait présente à toutes les longitudes et deviendrait par là même invisible. La rotation de la graine est un sujet de recherches assez actif en sismologie (Souriau, 2007), et il subsiste encore de grandes incertitudes concernant l'amplitude et la stabilité de cette rotation. Il s'agit là de questions auxquelles doit répondre la modélisation numérique de la dynamo. Pour celà, l'équilibre des couples visqueux, magnétique, gravitationnel doit être pris en compte (Dumberry, 2007) aux deux frontières du noyau (manteau et graine), et la conservation du moment angulaire global doit être implémentée dans PARODY-JA.

Plus généralement, nous attendons de cette nouvelle génération de modèles numériques une capacité accrue à interagir avec les séries temporelles de la longueur du jour, puisque ces séries mesurent la vitesse de rotation du manteau. Du point de vue de la pertinence des modèles numériques actuels, la partie la plus intéressante du signal concerne les données sur le millénaire (voir par exemple Dumberry et Bloxham, 2006). Ici la modélisation numérique s'efforcera d'expliquer les variations observées de longueur du jour en termes de variations de mouvements zonaux profonds. Plus généralement, nos modèles pourront permettre de contraindre la viscosité de la graine, qui intervient dans le couple gravitationnel senti par le noyau, et de comparer nos résultats avec les études fines des variations décennales de la longueur du jour, qui font apparaître un signal lié à la relaxation de ce couple (Mound et Buffett, 2006). Un dernier aspect important lié à la conservation du moment angulaire dans le noyau concerne les ondes de courtes période. Récemment, un formalisme basé sur les fonctions de Green a été développé afin de retrouver le lieu d'excitation de ces ondes dans le noyau à partir des données de longueur du jour (Buffett et Mound, 2005). Nous pourrons tester ce formalisme à l'aide de données synthétiques produites par les modèles numériques, afin d'en évaluer la résolution et de mieux comprendre la signature des ondes de torsion, qui dominent le signal décennal.

2.2.4 Dynamos naturelles dans le système solaire

L'action dynamo ne se limite pas à la Terre, et le champ des dynamos planétaires connaît des évolutions intéressantes depuis quelques années. En particulier, l'arrivée imminente de la mission Messenger en orbite de Mercure permettra de décrire le champ magnétique de la planète avec une précision bien meilleure que celle disponible actuellement. Nous savons déjà que le champ magnétique de Mercure possède une amplitude beaucoup plus faible que celle que prédisent nos lois d'échelle (Christensen, 2006). La structure interne de Mercure constitue par ailleurs un sujet actif en géochimie. En particulier, la pression relativement faible de la partie supérieure du noyau de Mercure pourrait avoir des conséquences importantes sur la miscibilité du soufre et du silicium, ainsi que sur la ségrégation des éléments radioactifs (Michael J. Toplis, communication personnelle). La modélisation dynamo peut s'adapter à ces contraintes par la modification de la géométrie et du type de forçage de la région dynamo.

La dynamique des fluides en rotation peut trouver un champ d'applications intéressant dans le domaine du système solaire primitif (premières centaines de millions d'années) : le problème de la durée de la cristallisation d'un océan de magma dans les planètes primitives relève en effet de la dynamique des fluides en rotation. De plus, un nouveau champ d'applications se développe en marge de l'étude des dynamos planétaires : la possibilité de dynamos dans des petits corps (rayon inférieur à 1000 km). On commence en effet à avoir des contraintes géochimiques sur le chauffage initial et la différentiation de noyaux métalliques dans les petits corps présents au cours des premiers 100 millions d'années du système solaire (Markowski et al., 2007). La faisabilité de dynamos dans les petits corps doit donc être étudiée.

2.3 Vers une modélisation inverse et l'assimilation de données

En marge de l'effort actuel que dévoue à la communauté scientifique à l'assimilation des données géomagnétiques, nous désirons étudier plusieurs questions qui relèvent de la faisabilité de l'assimilation des les modèles numériques tridimensionnels actuels. La première d'entre elle concerne l'évaluation de notre capacité de prédiction des variations géomagnétiques : compte tenu de notre connaissance imparfaite de l'état du noyau, combien de temps à l'avance pouvons nous espérer prévoir l'évolution du champ magnétique ? Cette question se trouve au centre de la Thèse que Florian Lhuillier a débuté, sous la direction de Gauthier Hulot et moi-même, à l'Institut de Physique du Globe de Paris. Nous désirons adapter au noyau l'approche en perturbations utilisée par les premiers météorologues, qui a permis d'aboutir à la conclusion que la météo ne pouvait être donnée plus de quelques jours à l'avance. Une question connexe concerne la résolution sous-maille des modèles

dynamo : selon la précision avec laquelle on résoud les plus petites échelles d'espace et de temps, un modèle mieux ou moins bien résolu peut présenter un comportement qui diverge rapidement de celui d'un modèle de référence. Il importe donc d'établir une résolution sous-maille permettant de s'affranchir de ce problème sur les échelles de temps pertinentes pour l'assimilation. Une dernière question à laquelle je m'intéresse, en collaboration avec Alexandre Fournier (IPGP), est la description de l'évolution des modèles dynamo sur des bases orthogonales empiriques réduites qui expliquent l'essentiel de la variance du signal. Une telle approche pourrait permettre de réduire la sous-détermination dans la description de l'état dynamique et magnétique du noyau profond en fonction des observations de surface, et doit donc complémenter les progrès qui ont déjà été fournis dans ce domaine par la technique DMFI.

Bibliographie

Buffett, B. et Mound, J., A Green's function for the excitation of torsional oscillations in the Earth's core, *J. Geophys. Res.*, *110*, 2005.

Christensen, U. R., A deep dynamo generating Mercury's magnetic field, *Nature*, *444*, 1056–1058, 2006.

Dumberry, M., Geodynamic constraints on the steady and time-dependent inner core axial rotation, *Geophys. J. Int.*, *170*, 886–895, 2007.

Dumberry, M. et Bloxham, J., Azimuthal flows in the earth's core and changes in length of day at millennial time scales, *Geophys. J. Int.*, *165*, 32–46, 2006.

Hulot, G., Eymin, C., Langlais, B., Mandea, M., et Olsen, N., Small-scale structure of the geodynamo inferred from Oersted and Magsat satellite data, *Nature*, *416*, 620–623, 2002.

Lay, T., Hernlund, J., Garnero, E. J., et Thorne, M. S., A post-perovskite lens and D" heat flux beneath the central pacific, *Science*, *314*, 1272–1276, 2006.

Markowski, A., Quitte, G., Kleine, T., Halliday, A. N., Bizzarro, M., et Irving, A. J., Hafnium-tungsten chronometry of angrites and the earliest evolution of planetary objects, *EARTH AND PLANETARY SCIENCE LETTERS*, *262*, 214–229, 2007.

Mound, J. E. et Buffett, B. A., Detection of a gravitational oscillation in length-of-day, *Earth Planet. Sci. Lett.*, *243*, 383–389, 2006.

Souriau, A., The Earth's cores, in *Treatise on Geophysics. 1- Seismology and Structure of the Earth*, edité par A. Dziewonski et B. Romanowicz, vol. 11, pp. 655–693, Elsevier, 2007.

van der Hilst, R., De Hoop, M. V., Wang, P., Shim, S.-H., Ma, P., et Tenorio, L., Seismostratigraphy and thermal structure of Earth's core-mantle boundary region, *Science*, *315*, 1813–1817, 2007.

C.V., liste des activités d'encadrement et liste complète des publications

1 C.V.

Identité

Julien Aubert
36 ans
Chargé de recherches 1ère classe au CNRS
Laboratoire de Dynamique des Fluides Géologiques
Institut de Physique du Globe de Paris, UMR7154

Diplômes

Doctorat de 3ème cycle en Géophysique Interne, mention très honorable. Université Joseph Fourier, Grenoble, 2001.
Agrégation de Sciences Physiques, option Physique. Reçu 45ème (1996).

Postes occupés

Thèse (1998 – 2001)

Laboratoire de Géophysique Interne et Tectonophysique, Université Joseph Fourier, Grenoble.
Modèles expérimentaux et numériques de la convection dans le noyau de la Terre. Direction Henri-Claude Nataf.

Post-doctorat I (2001-2002)

Lauréat de la bourse Lavoisier du Ministère des Affaires Étrangères. Center for Nonlinear Dynamics, the University of Texas at Austin, États-Unis.

Turbulence quasigéostrophique. Expériences et modèles numériques. En collaboration avec Harry Swinney.

Post-doctorat II (2002-2003)

Lauréat de la bourse Marie Curie de la Communeauté Européenne. Institüt für Geophysik, Université de Göttingen, Allemagne.
Modèles numériques de la géodynamo. En collaboration avec Ulrich Christensen et Johannes Wicht.

Post doctorat III (2003-2004)

Max-Planck Institut for Planetary Research, Katlenburg-Lindau, Allemagne.
Magnétisme des planètes du système solaire. En collaboration avec Ulrich Christensen et Johannes Wicht.

CNRS (2004 – 2008)

Chargé de recherches au laboratoire de Dynamique des Systèmes Géologiques, Institut de Physique du Globe de Paris.
Modèles numériques de la géodynamo - interaction avec les observations, les modèles d'histoire thermique de la Terre.

2 Distinctions scientifiques

En 2006, j'ai reçu le *prix Doornbos* de l'organisation SEDI (Study of the Earth's Deep Interior) à l'occasion de son congrès international de Prague.

3 Liste des activités d'encadrement

J'ai assuré, entre 2004 et 2008, les travaux dirigés du module de Dynamique des Fluides Géophysiques en Master 2 Physique des liquides, université Paris 7. Il s'agissait d'un module de 20 heures annuelles.
J'ai enseigné en 2006 le module "Dynamos planétaires" de l'école doctorale de l'institut de Physique du Globe de Paris, pour un volume horaire de 8 heures.
J'ai enseigné en 2007 le module "Quasigeostrophic Dynamics" de l'école d'été internationale "Dynamos", les Houches, pour un volume horaire d'une heure.
J'ai encadré les stages de M1, M2, et je co-encadre actuellement la Thèse de Florian Lhuillier, à l'IPGP.
Je suis membre depuis début 2007 du conseil scientifique de l'Institut de Physique du Globe de Paris.
J'ai assuré pour 2007-2008 l'organisation des séminaires généraux de l'Institut de Physique du Globe de Paris.

4 Collaborations et séjours

Je collabore régulièrement avec Johannes Wicht et Ulrich Christensen, au Max-Planck-Institute for Solar System Research, Lindau, Allemagne. J'y ai effectué trois séjours de travail d'une semaine en Février 2005, Mai 2006 et Mai 2007.
Mes autres collaborateurs depuis 2004 ont été : Jonathan Aurnou (Earth and Space Sciences, University of California, USA), Peter Olson (Johns Hopkins University, USA), Gauthier Hulot (Géomagnétisme, IPGP), Hagay Amit (Géomagnétisme, IPGP), Stéphane Labrosse (ENS Lyon), Emmanuel Dormy (ENS Paris), Michael le Bars (IRPHE, Marseille).

5 Transfert technologique et valorisation

Je distribue actuellement deux logiciels liés à mon activité : PARODY-JA et DMFI. Ces deux logiciels sont librement disponibles pour la communauté internationale.

6 Liste complète des publications

Toutes les publications écrites se trouvent sur la page
`http ://www.ipgp.jussieu.fr/~aubert` .

Publications dans des revues de rang A à comité de lecture

A la date du 8 décembre 2008, les 14 publications ci-dessous totalisent 237 citations sur *ISI Web Of Science*, pour un facteur h (ou nombre h de publications citées au moins h fois) valant $h = 9$.

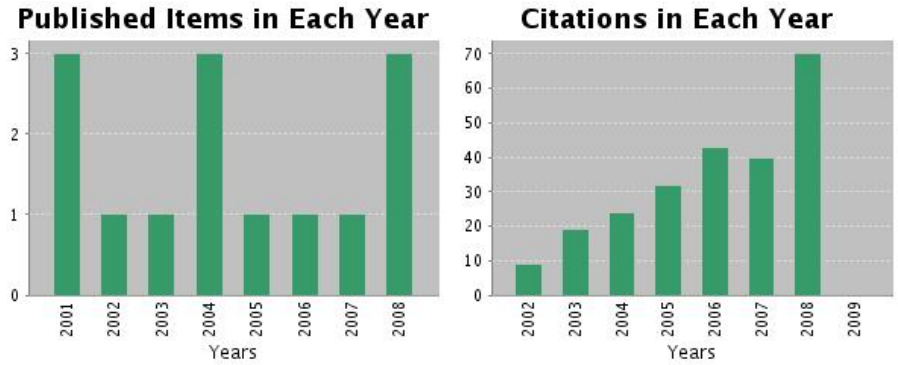

1- Aubert, J., Amit H., Hulot G., Olson P. : Thermochemical flows couple the Earth's inner core growth to mantle heterogeneity, Nature 454, 758-761, 2008, doi :10.1038/nature07109
2- Aubert, J., Aurnou J., Wicht, J. : The magnetic structure of convection-driven numerical dynamos, Geophys. J. Int. 172, 945-956, 2008, doi : 10.1111/j.1365-246X.2007.03693.x

3-Aubert, J., Amit, H., and Hulot, G. : Detecting thermal boundary control in surface flows from numerical dynamos, Phys. Earth. Plan. Int. 160, 143-156, 2007, doi : 10.1016/j.pepi.2006.11.003
4- Aubert, J. : Steady zonal flows in spherical shell fluid dynamos, J. Fluid. Mech. 542, 53-67, 2005.
5- Aubert, J., Wicht, J. : Axial versus equatorial dipolar dynamo models with implications for planetary magnetic fields, Earth. Plan. Sci. Lett. 221, 409-419, 2004. doi :10.1016/S0012-821X(04)00102-5
6- Aubert, J., Cardin, P., Gillet, N. : Quasigeostrophic models of convection in rotating spherical shells, Geochem. Geophys. Geosyst., 4(7), 1052,
doi :10.1029/2002GC000456, 2003.
7- Aubert, J., Jung, S., Swinney, H. : Observations of zonal flow created by potential vorticity mixing in a rotating fluid, Geophys. Res. Lett., 29(18), 1876, doi :10.1029/2002GL015422, 2002.
8- Aubert, J., Brito, D., Nataf, H.-C., Cardin, P., Masson, J.-P. : A systematic experimental study of rapidly rotating spherical convection in water and liquid gallium, Phys. Earth Plan. Int. 128, pp 51-74, 2001.
9- Amit H., Aubert J., Hulot G., Olson P. : A simple model for mantle-driven flow at the top of Earth's core, Earth, Planets, Space 60, pp 845-854, 2008.
10- Christensen, U. and Aubert, J. : Scaling properties of convection-driven dynamos in rotating spherical shells and application to planetary magnetic fields, Geophys. J. Int. 166, pp. 97-114, 2006, doi : 10.1111/j.1365-246X.2006.03009.x
11- Jung, S., Storey, B., Aubert, J., Swinney, H. : Nonextensive statistical mechanics for a forced quasi-two-dimensional flow, Physica D. 193, pp. 252-264, 2004.
12- Jung, S., Storey, B., Aubert, J., Swinney, H. : Nonextensive model for turbulent flow in a rapidly rotating annulus, in Reynolds Number Scaling in Turbulent Flow, edited by A.J. Smits (Kluwer Academic Publishers, Dordrecht), pp. 137-140, 2003.
13- Christensen et al. : A numerical dynamo benchmark, Phys. Earth. Plan. Int. 128, pp 51-74, 2001.
14- Brito, D., Nataf, H.-C., Cardin, P., Masson, J.-P., Aubert, J. : Ultrasonic Doppler velocimetry in liquid gallium, Exp. Fluids. 31, pp 653-663, 2001.

Conférences invitées dans des congrès internationaux

1- Aubert, J., Amit H., Hulot G., Olson P. : Thermo-chemical coupling between the mantle, core and inner core, SEDI 2008, Kunming, Chine.
2- Aubert, J. : Quasigeostrophic Dynamics, Dynamos Summer School, les Houches, 2007.
3- Aubert, J., Aurnou, J., Wicht, J. : The magnetic structure of numerical dynamos. IUGG 2007, Perugia, Italie.
4- Aubert, J., Amit, H., Hulot, G., Olson, P. : A possible mechanism for coupling the Earth's inner core to thermal mantle structures, IUGG 2007, Perugia, Italie
5- Christensen, U., Aubert, J : Scaling laws for dynamos in rotating spherical shells, IAGA 2005 Scientific Assembly, Toulouse, France.
6- Aubert, J. and Wicht, J. : Axial and Equatorial Dipoles in Dynamo Simulations and Implications for Planetary Magnetic Fields, AGU 2004, Montréal, Canada.

Publications dans des revues sans comité de lecture

Davaille, A., Aubert, J. : La physique des systèmes naturels : du grain à la planète, de la seconde au milliard d'années, Bulletin de la Société Française de Physique, numéro spécial pour l'Année Internationale de la Physique, 2005

Communications non invitées dans des congrès internationaux

1- Tackley P., Aurnou J., Aubert J. : Influence of Mercury's laterally varying surface temperature on its mantle convection, geoid, lithospheric stress distribution and dynamo action, EPSC 2008, Münster.
2- Aubert, J., Labrosse, S., Poitou, C. : Was the early Earth dynamo reversing its polarity ? EGU 2008, Vienne.
3- Aubert J., Amit H., Hulot G., Olson P. : Thermochemical wind flows couple the Earth's inner core growth to mantle heterogeneity, AGU 2007, San Francisco
4- Aubert, J., Amit, H., Hulot, G. : Can Thermal Mantle Control be Identified in Earth's Core Surface Flows ? AGU 2006, San Francisco
5- Amit H., Aubert J., Hulot G., Olson P. : Thermal Wind at the top of the Core, AGU 2006, San Francisco
6- Aubert, J., Amit, H., Hulot, G. : Core flows in numerical dynamos with non-uniform boundary heat flow, SEDI 2006, Prague
7- Amit H., Aubert J., Hulot G., Olson P. : Mantle-driven thermal wind at the top of the core, SEDI 2006, Prague
8- Labrosse S., Hernlund J. , Aubert J., Tackley P. : Fluctuations in core-mantle thermal coupling, SEDI 2006, Prague
9- Aubert J. : Inside a geomagnetic polarity reversal with DMFI, SEDI 2006, Prague
10- Aubert J., Christensen U. : Scaling properties of planetary dynamos, AGU 2005, San Francisco
11- Aurnou J., Aubert J., Amit H., Andreadis S., Olson P. : Thermal Winds in the Tangent Cylinder, AGU 2005, San Francisco
12- Aubert J., Christensen U. : Scaling properties of numerical dynamos, EGU 2005, Vienne
13- Labrosse, S., Aubert, J. : The Thermal and Magnetic Evolution of the Core. Gordon Conference on the interior of the Earth 2005, Mount Holyoke, États-Unis.
13 autres communications données aux congrès SEDI 2004, IUGG 2003, American Physical Society DFD 2002, American Geophysical Union 2002 & 2001, European Geophysical Society 2003, 2001 & 2000, IAGA-IASPEI 2001, Study of the Earth's Deep Interiors 2000.

Séminaires invités récents

LGIT Grenoble, février 2009
Oxford University, février 2009
Observatoire Midi-Pyrénées, novembre 2008
ETH Zürich, avril 2007
ENS Lyon, avril 2007

IRPHE Marseille, novembre 2006

Thèse

Aubert, J. : Modèles expérimentaux et numériques de la convection dans le noyau de la Terre, Université Joseph Fourier, 2001.

Apparitions dans la presse écrite et audiovisuelle

L'article que j'ai publié dans la revue *Nature* le 7 août 2008 a fait l'objet de communiqués de presse émis par le journal *Nature*, le CNRS et l'INSU : "Au centre de la Terre, un nouveau modèle pour l'évolution du noyau solide", 7 et 8 août 2008.
Ces recherches ont également fait l'objet du flash info sur le site cordis.europa.eu de la recherche européenne : "Getting to the heart of the Earth's core", 8 août 2008.
La revue *New Scientist* a aussi consacré l'article "Did iron cyclones give Earth a wonky core ?" à ce travail dans son édition écrite du 11 août 2008. J'ai par ailleurs été interviewé dans l'émission de radio *Nature Podcast* le 6 août 2008. Un "Editor summary" et un "news and views" ont été publiés concernant cet article dans la revue *Nature* du 7 août 2008 : "How the other hemisphere lives", et "Structuring the inner core". Finalement, le journal du CNRS en version anglaise consacre un article à ces recherches dans son numéro du 15 décembre 2008.
Le magazine Physics Today a consacré sa rubrique "Back Scatter" a mes recherches et visualisations en septembre 2008.
Mes infographies sur les simulations dynamos ont été utilisées dans
- la photothèque du CNRS
- le livre "Terre, planète mystérieuse", CNRS/INSU et Le Cherche Midi, septembre 2008.
- l'image de la semaine du 10 mars 2008 (site web de l'INSU)
- le journal du CNRS numéro 216-217, janvier 2008
- le magazine research.eu de la communauté européenne, 2008
- le magazine les dossiers de la recherche, numéro 25 (2007)

Un article de A. Khalatbari décrivant mes recherches est paru dans "Sciences et Avenir" : Découvertes au cœur de la Terre, numéro 718, 2006.
J'ai réalisé des infographies pour l'émission Rayon X, France 2, 2005.

Recueil des articles et travaux significatifs

Geophys. J. Int. (2006) doi: 10.1111/j.1365-246X.2006.03009.x

Scaling properties of convection-driven dynamos in rotating spherical shells and application to planetary magnetic fields

U. R. Christensen[1] and J. Aubert[2]

[1]*Max-Planck-Institut für Sonnensystemforschung, Katlenburg-Lindau, Germany. E-mail: christensen@mps.mpg.de*
[2]*Institut de Physique du Globe de Paris, Paris, France*

Accepted 2006 March 17. Received 2006 March 17; in original form 2005 September 28

SUMMARY

We study numerically an extensive set of dynamo models in rotating spherical shells, varying all relevant control parameters by at least two orders of magnitude. Convection is driven by a fixed temperature contrast between rigid boundaries. There are two distinct classes of solutions with strong and weak dipole contributions to the magnetic field, respectively. Non-dipolar dynamos are found when inertia plays a significant role in the force balance. In the dipolar regime the critical magnetic Reynolds number for self-sustained dynamos is of order 50, independent of the magnetic Prandtl number Pm. However, dynamos at low Pm exist only at sufficiently low Ekman number E. For dynamos in the dipolar regime we attempt to establish scaling laws that fit our numerical results. Assuming that diffusive effects do not play a primary role, we introduce non-dimensional parameters that are independent of any diffusivity. These are a modified Rayleigh number based on heat (or buoyancy) flux Ra_Q^*, the Rossby number Ro measuring the flow velocity, the Lorentz number Lo measuring magnetic field strength, and a modified Nusselt number Nu^* for the advected heat flow. To first approximation, all our dynamo results can be collapsed into simple power-law dependencies on the modified Rayleigh number, with approximate exponents of $2/5$, $1/2$ and $1/3$ for the Rossby number, modified Nusselt number and Lorentz number, respectively. Residual dependencies on the parameters related to diffusion (E, Pm, Prandtl number Pr) are weak. Our scaling laws are in agreement with the assumption that the magnetic field strength is controlled by the available power and not necessarily by a force balance. The Elsasser number Λ, which is the conventional measure for the ratio of Lorentz force to Coriolis force, is found to vary widely. We try to assess the relative importance of the various forces by studying sources and sinks of enstrophy (squared vorticity). In general Coriolis and buoyancy forces are of the same order, inertia and viscous forces make smaller and variable contributions, and the Lorentz force is highly variable. Ignoring a possible weak dependence on the Prandtl numbers or the Ekman number, a surprising prediction is that the magnetic field strength is independent both of conductivity and of rotation rate and is basically controlled by the buoyancy flux. Estimating the buoyancy flux in the Earth's core using our Rossby number scaling and a typical velocity inferred from geomagnetic secular variations, we predict a small growth rate and old age of the inner core and obtain a reasonable magnetic field strength of order 1 mT inside the core. From the observed heat flow in Jupiter, we predict an internal field of 8 mT, in agreement with Jupiter's external field being 10 times stronger than that of the Earth.

Key words: convection, core flow, dynamo theory, geomagnetic field, inner core, planetology.

1 INTRODUCTION

In the past 10 yr numerical models of convection-driven dynamos in rotating spherical shells have been successful in reproducing the main properties of the geomagnetic field, including the dipole dominance and approximate dipole strength, details of the field morphology at the outer boundary of the dynamo region, secular variation of the magnetic field and stochastic dipole reversals resembling those seen in the paleomagnetic record (Kageyama *et al.* 1995; Glatzmaier & Roberts 1995a,b; Kuang & Bloxham 1997; Christensen *et al.* 1998; Busse *et al.* 1998; Christensen *et al.* 1999; Kuang & Bloxham 1999; Takahashi *et al.* 2005). Dynamo models have been used to investigate the possible field generation mechanism in the Earth's core

(Olson *et al.* 1999; Ishihara & Kida 2002), the influence of lower mantle heterogeneity on magnetic field properties (Glatzmaier *et al.* 1999; Bloxham 2000a,b; Olson & Christensen 2002; Bloxham 2002; Christensen & Olson 2003; Kutzner & Christensen 2004) and the generation of planetary magnetic fields that differ in geometry (Uranus, Neptune) or strength (Mercury) from the Earth's field (Stanley & Bloxham 2004; Stanley *et al.* 2005).

However, for practical reasons the values of some of the control parameters in the dynamo models differ strongly from planetary values. In particular, the Ekman number that measures the relative importance of viscous forces to Coriolis forces is typically five to ten orders of magnitude too large, depending on whether molecular or 'turbulent' viscosities are assumed, and the magnetic Prandtl number, the ratio of viscosity to magnetic diffusivity, is six orders of magnitude larger than the appropriate value for liquid iron. Therefore, it remains doubtful if the flow regime in the numerical models is basically the same as in planetary cores or if the agreement with the Earth's magnetic field is rather fortuitous.

One way to assess the relevance of the dynamo models is to determine how their characteristic properties depend on the control parameters. Systematic parameter studies have been started by Christensen *et al.* (1999), Grote *et al.* (2000) and Simitev & Busse (2005). The main aim of these studies has been to determine in which parts of the parameter space dynamo solutions exist and what their fundamental magnetic field geometry is. The results show an influence of the mechanical boundary conditions and the mode of driving convection. For rigid boundaries and a strong source of buoyancy at the inner core boundary, the magnetic field outside the fluid shell is dominated by the axial dipole component at moderately supercritical values of the Rayleigh number, but is small scaled with a weak dipole component at strongly supercritical values (Kutzner & Christensen 2002). With stress-free boundaries and/or a strong component of driving by volumetric heat sources, dipole-dominated solutions give way to a non-dipolar magnetic fields (quadrupolar, small scaled or magnetic fields restricted to one hemisphere), in particular at lower values of the magnetic Prandtl number (Grote *et al.* 1999, 2000; Kutzner & Christensen 2000; Simitev & Busse 2005). Christensen *et al.* (1999) found that the minimum value of the magnetic Prandtl number at which dynamo solutions exist depends on the Ekman number. Dynamos at low, that is, more realistic, values of the magnetic Prandtl number are found only at low enough Ekman number, which makes their study computationally very demanding.

The next step toward understanding the dynamo process and to ascertain if the numerical models can be applied to planetary conditions is to derive scaling laws that relate characteristic properties of the dynamo solutions to the control parameters. Before, such scaling laws have been suggested on the basis of physical reasoning with little or no reference to actual dynamo solutions (e.g. Stevenson 1979; Starchenko & Jones 2002). Finding scaling laws for the magnetohydrodynamic dynamo problem is a particularly difficult task, because it is governed by at least four relevant control parameters and because the relative importance of the various forces on the flow (inertia, Coriolis force, Lorentz force, viscosity, buoyancy) may change over the accessible parameter range, which could prevent a unique scaling relation. For flow in planetary cores it is usually assumed that inertia and in particular viscosity play a negligible role and that the primary forces balance is between Coriolis force, Lorentz force, buoyancy and pressure gradient forces (magnetostrophic or MAC balance). A systematic numerical study of non-magnetic convection in a rotating shell with stress-free boundaries (Christensen 2002) has suggested that a regime in which viscous forces become unimportant can actually be approached with the present-day computational means and asymptotic scaling laws have been derived for the limit of small Ekman number. With the Lorentz force lacking, inertia retains an important role to balance the Coriolis forces in this case (Aubert *et al.* 2001). A first step in finding scaling laws from numerical dynamo solutions has been made by Christensen & Tilgner (2004), who derived a relation between the magnetic dissipation time, describing the rate at which magnetic energy is destroyed by Ohmic dissipation, and the magnetic Reynolds number, a measure for the flow velocity in terms of shell thickness and magnetic diffusion time. Based on the numerical results alone Christensen & Tilgner (2004) could not exclude a weak additional dependence on the magnetic Prandtl number, but by using results from the Karlsruhe laboratory dynamo experiment (Stieglitz & Müller 2001; Müller *et al.* 2004) they concluded that this dependency is absent or vanishes at small values of the magnetic Prandtl number. Aubert (2005) studied the zonal flow velocity in non-magnetic convection and in dynamos and found distinct scaling laws that indicate a different balance of forces in the two cases. In the dynamo case both viscosity and inertia were found to be unimportant, suggesting that at least the zonal flow is in a magnetostrophic balance.

In this paper we use an extensive set of numerical dynamo results in order to derive scalings for the mean flow velocity, the heat transport and the magnetic field strength. We restrict the analysis to dynamos that generate a dipole-dominated magnetic field.

2 GOVERNING EQUATIONS AND NON-DIMENSIONAL PARAMETERS

For numerical modelling the equations of convection-driven magnetohydrodynamic flow and electromagnetic induction in an electrically conducting, rotating spherical shell are usually cast into non-dimensional form. However, different schemes for non-dimensionalization are possible. Conventionally, time is scaled by some diffusion time, where the choice is between viscous, thermal or magnetic diffusivity. Based on the hypothesis that diffusive processes do not play a primary role, in contrast to the effects of rotation, we follow the path introduced by Christensen (2002) and Aubert (2005) and select the inverse rotation frequency Ω^{-1} of the shell as the basic timescale. Length scale is the shell thickness D, the non-hydrostatic pressure Π is scaled by $\rho\Omega^2 D^2$, where ρ is the density, and the scale for temperature is ΔT, the imposed temperature difference between the isothermal inner boundary at radius r_i and outer boundary at r_o. Here, we fix the ratio $\eta = r_i/r_o$ to 0.35. For dynamo problems in rotating systems the magnetic induction B is frequently scaled by $(\rho\mu\lambda\Omega)^{1/2}$ with μ the magnetic permeablity and λ the magnetic diffusivity. This choice makes the square of the mean non-dimensional magnetic field strength equal to the Elsasser number

$$\Lambda = B_{\rm rms}^2 \big/ \rho\mu\lambda\Omega, \tag{1}$$

which is considered to represent the ratio of Lorentz forces to Coriolis forces acting on the flow. Here we follow again a different path and select $(\rho\mu)^{1/2}\ \Omega D$ for scaling B. With this choice none of the diffusivites appears in any of the scales and the governing equations in the Boussinesq approximation can be written in a rather simple and symmetric form:

$$\frac{\partial \mathbf{u}}{\partial t} + \mathbf{u}\cdot\nabla\mathbf{u} + 2\hat{\mathbf{z}}\times\mathbf{u} + \nabla\Pi = E\nabla^2\mathbf{u} + Ra^*\frac{\mathbf{r}}{r_o}T + (\nabla\times\mathbf{B})\times\mathbf{B}, \tag{2}$$

$$\frac{\partial \mathbf{B}}{\partial t} - \nabla \times (\mathbf{u} \times \mathbf{B}) = E_\lambda \nabla^2 \mathbf{B}, \tag{3}$$

$$\frac{\partial T}{\partial t} + \mathbf{u} \cdot \nabla T = E_\kappa \nabla^2 T, \tag{4}$$

$$\nabla \cdot \mathbf{u} = 0, \quad \nabla \cdot \mathbf{B} = 0. \tag{5}$$

Here the unit vector $\hat{\mathbf{z}}$ indicates the direction of the rotation axis and gravity varies linearly with the radius $\mathbf{r}$. The four non-dimensional control parameters are the (viscous) Ekman number

$$E = \frac{\nu}{\Omega D^2}, \tag{6}$$

the magnetic Ekman number

$$E_\lambda = \frac{\lambda}{\Omega D^2} = \frac{E}{Pm}, \tag{7}$$

the thermal Ekman number

$$E_\kappa = \frac{\kappa}{\Omega D^2} = \frac{E}{Pr}, \tag{8}$$

and the modified Rayleigh number

$$Ra^* = \frac{\alpha g_o \Delta T}{\Omega^2 D}, \tag{9}$$

where ν is viscosity, κ thermal diffusivity, α thermal expansivity and g_o gravity at the outer radius r_o. In our scaling, the diffusive terms in eqs (2)–(4) multiply with the respective Ekman numbers, the buoyancy term is multiplied with a modified Rayleigh number that is independent of any diffusivity, and all other terms are parameter free. In place of the magnetic and thermal Ekman numbers we will later use the more conventional hydrodynamic Prandtl number $Pr = \nu/\kappa$ and magnetic Prandtl number $Pm = \nu/\lambda$.

We are interested in how characteristic values of the non-dimensional velocity and of the non-dimensional magnetic field strength depend on the control parameters. The kinetic energy and the magnetic energy, scaled by $\rho\Omega^2 D^5$, are given by

$$E_{\rm kin} = \frac{1}{2} \int \mathbf{u} \cdot \mathbf{u} \, dV, \tag{10}$$

and

$$E_{\rm mag} = \frac{1}{2} \int \mathbf{B} \cdot \mathbf{B} \, dV, \tag{11}$$

respectively, where the integral is taken over the fluid shell in case of eq. (10) and over all space in case of eq. (11). The characteristic mean velocity is the Rossby number,

$$Ro = \left(\frac{2E_{\rm kin}}{V_s} \right)^{1/2}, \tag{12}$$

and we call the characteristic non-dimensional magnetic field strength the Lorentz number

$$Lo = \left(\frac{2E_{\rm mag}}{V_s} \right)^{1/2}, \tag{13}$$

where V_s is the volume of the spherical shell. The relation between the Elsasser number and the Lorentz number is given by

$$\Lambda = Lo^2 Pm E^{-1}. \tag{14}$$

In a regime where diffusive processes do not play a major role, the Rossby number and the Lorentz number are expected to depend on the modified Rayleigh number rather than on the conventional Rayleigh number

$$Ra = \frac{Ra^*}{E_\kappa E}. \tag{15}$$

To obtain a non-dimensional measure for convective heat transport that is independent of the thermal diffusivity we use a modified Nusselt number

$$Nu^* = \frac{1}{4\pi r_o r_i} \frac{Q_{\rm adv}}{\rho c \Delta T \Omega D}, \tag{16}$$

where the advected heat flow $Q_{\rm adv}$ is the time-average total heat flow Q minus the conductive heat flow $Q_{\rm cond} = 4\pi r_o r_i \rho c \, \kappa \Delta T / D$ and c is the heat capacity. The relation to the conventional Nusselt number

$$Nu = \frac{1}{4\pi r_o r_i} \frac{Q D}{\rho c \kappa \Delta T}, \tag{17}$$

is given by

$$Nu^* = (Nu - 1) E_\kappa. \tag{18}$$

Note that the modified Nusselt number used here is based on the advective heat flux alone, in contrast to the definition employed by Christensen (2002) and Aubert (2005).

Finally, although the solutions have been calculated for a fixed temperature contrast, we analyse our results in terms of a modified Rayleigh number Ra^*_Q based on the advected heat flux rather than on ΔT

$$Ra^*_Q = \frac{1}{4\pi r_o r_i} \frac{\alpha g_o Q_{\rm adv}}{\rho c \Omega^3 D^2}. \tag{19}$$

The relation between the various Rayleigh numbers is $Ra^*_Q = Ra^* Nu^* = Ra(Nu - 1) E_\kappa^2 \, E$.

Considering more general sources of buoyancy, we can replace the heat flux by the buoyancy flux, or mass anomaly flux, Q_B, which in case of thermal buoyancy is given by $Q_B = \alpha Q_{\rm adv}/c$. The Rayleigh number

$$Ra^*_B = \frac{1}{4\pi r_o r_i} \frac{g_o Q_B}{\rho \Omega^3 D^2}, \tag{20}$$

is a non-dimensional expression for the buoyancy flux. In case of thermal convection it is identical to Ra^*_Q.

For planetary applications the flux-based Rayleigh numbers are more convenient, since estimates for the heat flux or buoyancy flux exist, whereas the (superadiabatic) temperature contrast is not known. Moreover, Ra^*_Q is very closely connected to the power P generated by buoyancy forces (scaled by $\rho\Omega^3 D^5$)

$$P = Ra^* \int \frac{r}{r_o} u_r T \, dV. \tag{21}$$

In the appendix we show that to a very good approximation

$$P = 2\pi\eta \frac{1+\eta}{(1-\eta)^2} Ra^*_Q \quad \approx \quad 7.01 Ra^*_Q. \tag{22}$$

The rate of Ohmic dissipation is given by

$$D_\lambda = E_\lambda \int (\nabla \times \mathbf{B})^2 \, \mathbf{dV}. \tag{23}$$

For our models we calculate the time-average fraction of Ohmic dissipation

$$f_{\rm ohm} = D_\lambda / P. \tag{24}$$

We employ rigid mechanical boundary conditions and assume no heat sources inside the fluid shell, which is more favourable to obtain dipole-dominated dynamo solutions. The magnetic field is matched to a potential field outside the fluid shell and in most cases also to a potential field inside the (insulating) inner core. In some cases we assumed a conducting inner core, with a ratio $r_\lambda = 1$ of outer core diffusivity to inner core diffusivity. This requires the solution

of eq. (3) for $\mathbf{u} = 0$ in this region. Wicht (2002) found only small differences between the two options and we confirmed this in a few cases that have been run with both kinds of conditions.

The equations are solved by a spectral transform method described in Glatzmaier (1984), Christensen *et al.* (1999) or Tilgner (1999). The resolution in terms of the maximum harmonic degree and order $\ell_{\max}$ and number of radial grid levels N_r was selected so that a drop by a factor of 50 or more is found in the kinetic and magnetic energy spectra from the maximum to the energy at the cut-off wavelength. This resolution has been found to be sufficient for the robust determination of characteristic mean properties of the solution (Christensen *et al.* 1999; Kutzner & Christensen 2002). At larger values of the Ekman number, solutions are calculated for a full sphere (symmetry parameter $m_s = 1$), at lower values two-fold symmetry in longitude ($m_s = 2$) and at the lowest Ekman numbers four-fold symmetry ($m_s = 4$) is used to save computer time. Comparing results for different symmetries in a few cases showed no significant influence on the average properties of the dynamos.

Usually a solution obtained at different parameters served as initial condition. The run time $t_{\rm run}$ of each case covers at least 50 advection times, where one advection time unit is the shell thickness divided by the rms velocity. An exception is a case at the lowest Ekman number that we reached, which was run for only 28 advection times, but seems to have equilibrated. The transient adjustment to the new condition occurs in about 5 to 20 advection time units after which a statistically equilibrated solution is established. We reject the first part of the time-series, typically about 20 advection times, and for the remainder we average in time several properties of interest to obtain characteristic values. In particular, we calculate time-average values of the Rossby number Ro, the Lorentz number Lo, the modified Nusselt number Nu^*, the power P, and the fraction of Ohmic dissipation $f_{\rm ohm}$. In addition, we determine the relative dipole field strength $f_{\rm dip}$, defined as the time-average ratio on the outer shell boundary of the mean dipole field strength to the field strength in harmonic degrees $\ell = 1$–12, and the ratio $b_{\rm dip}$ of the mean field strength inside the shell to the dipole strength on the outer boundary.

3 RESULTS

The data base for this study has been built over several years. Some of the results have been published in Christensen *et al.* (1999), Kutzner & Christensen (2000), Kutzner & Christensen (2002), Christensen & Tilgner (2004) and Aubert (2005), although previous cases have been rerun to obtain additional data that had not been recorded before or to get a more representative time average. Additional, not previously reported, cases have been calculated in particular to extend the data base to smaller Ekman numbers and magnetic Prandtl numbers and to hydrodynamic Prandtl numbers different from one. For a detailed analysis we selected from this data base cases that satisfy the following criteria:

(1) The dynamo generates a non-decaying and dipole-dominated magnetic field. The latter condition is met when the relative dipole strength $f_{\rm dip}$ exceeds 0.35.

(2) The Ekman number is 3×10^{-4} or smaller. The lowest value of the Ekman number is 10^{-6}. We note that our definition of the Ekman number is conservative; with the definition of Kono & Roberts (2002), $E' = \nu/(2\Omega r_o^2)$, the range is roughly from 2×10^{-7} to 6×10^{-5}.

(3) Convection must be sufficiently vigorous and fill the entire volume. For this we require $Nu > 2$, which normally implies that the Rayleigh number exceeds the critical value by a factor of five or more. We list critical values of the Rayleigh number $Ra_{\rm crit}$ and the critical azimuthal wavenumber $m_{\rm crit}$ in Table 1.

Table 1. Critical Rayleigh number.

E	Pr	$Ra_{\rm crit}$	$Ra^*_{\rm crit}$	$m_{\rm crit}$
3×10^{-4}	3.0	2.391×10^5	7.173×10^{-3}	5
3×10^{-4}	1.0	2.026×10^5	1.823×10^{-2}	5
3×10^{-4}	0.3	1.373×10^5	4.119×10^{-2}	5
10^{-4}	10	9.410×10^5	9.410×10^{-4}	7
10^{-4}	3	8.627×10^5	2.876×10^{-3}	8
10^{-4}	1.0	6.965×10^5	6.965×10^{-3}	8
10^{-4}	0.3	4.407×10^5	1.469×10^{-2}	7
10^{-4}	0.1	2.865×10^5	2.865×10^{-2}	6
3×10^{-5}	3.0	3.674×10^6	1.102×10^{-3}	12
3×10^{-5}	1.0	2.833×10^6	2.550×10^{-3}	11
3×10^{-5}	0.3	1.684×10^6	5.052×10^{-3}	10
3×10^{-5}	0.1	1.047×10^6	9.423×10^{-3}	8
10^{-5}	3.0	1.426×10^7	4.753×10^{-4}	16
10^{-5}	1.0	1.057×10^7	1.057×10^{-3}	15
3×10^{-6}	3.0	6.475×10^7	1.943×10^{-4}	22
3×10^{-6}	1.0	4.591×10^7	4.132×10^{-4}	22
10^{-6}	1.0	1.791×10^8	1.791×10^{-4}	31

We have 66 different dynamos that satisfy the three criteria, covering at least two orders of magnitude in all control parameters. The modified Rayleigh number Ra^* is in the range of 0.001–0.4, or between 5 and 50 times supercritical. The magnetic Prandtl number ranges between 0.06 and 10 and the hydrodynamic Prandtl number falls between 0.1 and 10. In terms of mean-field dynamo theory, our dipolar solutions can be classified as α^2-dynamos (Olson *et al.* 1999). Differential rotation is weak, the toroidal magnetic field is of similar strength as the poloidal field and the axisymmetric toroidal field is usually weaker than the axisymmetric poloidal field, except inside the inner core tangent cylinder. The results for the selected cases are summarized in Table 2.

3.1 Dynamo regimes

Before we turn to the scaling laws for dipole-dominated dynamos, we first revisit the question of the existence of dynamo solutions and the class of magnetic field that they produce, following up earlier studies with a more extensive data basis. In Fig. 1 we show for a fixed Prandtl number of one and various values of the Ekman number the type of solution obtained in dependence of the Rayleigh number and the magnetic Prandtl number. Here we note that close to the regime boundaries the transient adjustment of the magnetic field may take longer than 50 advective time units and is more typically on the magnetic diffusion timescale. When in doubt we, therefore, run a case twice, starting from different initial magnetic field structures.

First we confirm the earlier result (Christensen *et al.* 1999) that the minimum magnetic Prandtl number at which dynamos exist, at least those generating a dipole-dominated magnetic field, increases with the Ekman number. In Fig. 2(a) we plot for $Pr = 1$ the lowest magnetic Prandtl number at which we found a dipolar dynamo as a function of Ekman number. The solid line for the minimum magnetic Prandtl number is given by the relation suggested in Christensen *et al.* (1999) on the basis of results restricted to Ekman numbers $E \geq 10^{-4}$:

$$Pm_{\min} = 450 E^{0.75}. \tag{25}$$

Table 2. Results.

Ra^*	Pr	Pm	r_λ	$\ell_{\max}$	N_r	m_s	$t_{\rm run}$	Ro	$\bar{\ell}_u$	Nu	Lo	$f_{\rm dip}$	$b_{\rm dip}$	$f_{\rm ohm}$
							$E = 1 \times 10^{-6}$							
0.0011	1.0	1.000	0	201	81	4	162 000	1.72×10^{-4}	42	2.18	7.78×10^{-4}	0.87	4.9	0.80
							$E = 3 \times 10^{-6}$							
0.0198	1.0	0.060	0	224	97	4	13 000	3.98×10^{-3}	55	17.80	4.02×10^{-3}	0.98	3.0	0.41
0.0162	1.0	0.075	0	224	97	4	15 000	3.34×10^{-3}	56	14.90	3.51×10^{-3}	0.96	3.2	0.40
0.0072	1.0	0.100	0	201	81	4	42 000	1.53×10^{-3}	56	5.33	1.50×10^{-3}	0.99	3.0	0.25
0.0090	1.0	0.100	0	201	81	4	28 000	1.90×10^{-3}	59	7.57	2.16×10^{-3}	0.95	3.2	0.34
0.0162	1.0	0.100	0	224	97	4	29 000	3.27×10^{-3}	58	14.90	3.61×10^{-3}	0.92	3.4	0.44
0.0045	1.0	0.500	0	168	81	4	85 000	7.71×10^{-4}	46	3.50	1.96×10^{-3}	0.82	5.3	0.62
0.0090	1.0	0.500	0	201	81	4	34 000	1.48×10^{-3}	49	7.33	3.61×10^{-3}	0.87	5.1	0.67
0.0162	1.0	0.500	0	224	97	4	22 000	2.36×10^{-3}	45	12.70	5.72×10^{-3}	0.92	4.9	0.74
0.0021	3.0	1.000	0	168	81	4	119 000	4.18×10^{-4}	56	5.09	1.12×10^{-3}	0.68	6.5	0.47
0.0036	1.0	1.000	0	168	81	4	92 000	5.52×10^{-4}	35	2.95	2.11×10^{-3}	0.89	5.5	0.76
0.0015	3.0	1.500	0	168	81	4	188 000	2.68×10^{-4}	47	3.57	1.08×10^{-3}	0.81	5.3	0.60
							$E = 1 \times 10^{-5}$							
0.0500	1.0	0.100	0	168	81	2	6100	8.49×10^{-3}	36	14.40	7.83×10^{-3}	0.96	2.8	0.39
0.0350	1.0	0.150	0	168	81	2	12 000	5.93×10^{-3}	39	11.30	7.73×10^{-3}	0.96	3.0	0.45
0.0110	1.0	0.200	0	134	65	2	26 000	1.97×10^{-3}	37	2.92	1.91×10^{-3}	0.98	3.1	0.21
0.0150	1.0	0.200	0	134	65	2	20 000	2.54×10^{-3}	40	4.06	3.41×10^{-3}	0.95	3.3	0.33
0.0350	1.0	0.250	0	168	81	2	12 000	5.37×10^{-3}	38	10.80	8.86×10^{-3}	0.95	3.1	0.56
0.0500	1.0	0.250	0	168	81	2	12 000	6.93×10^{-3}	38	13.50	1.03×10^{-2}	0.96	3.2	0.58
0.0150	1.0	0.500	0	133	65	2	35 000	2.35×10^{-3}	36	4.61	5.03×10^{-3}	0.89	4.3	0.57
0.0350	1.0	0.500	0	168	81	2	18 000	4.56×10^{-3}	36	9.58	9.35×10^{-3}	0.94	3.7	0.66
0.0080	1.0	1.000	0	133	65	2	91 000	1.19×10^{-3}	25	2.47	3.31×10^{-3}	0.86	5.5	0.65
0.0117	3.0	1.500	0	168	81	2	34 000	1.48×10^{-3}	35	9.12	5.44×10^{-3}	0.94	4.1	0.67
0.0075	1.0	2.000	1	128	65	4	120 000	1.05×10^{-3}	23	2.65	4.14×10^{-3}	0.88	6.1	0.75
0.0100	1.0	2.000	1	128	65	4	120 000	1.22×10^{-3}	23	3.55	6.20×10^{-3}	0.89	4.8	0.81
0.0150	1.0	2.000	1	170	65	4	40 000	1.79×10^{-3}	26	5.41	8.95×10^{-3}	0.89	4.6	0.80
0.0200	1.0	2.000	1	170	81	4	45 000	2.34×10^{-3}	28	6.65	1.03×10^{-2}	0.87	5.1	0.79
0.0400	1.0	2.000	1	212	81	4	10 000	4.44×10^{-3}	32	10.70	1.21×10^{-2}	0.83	6.0	0.70
							$E = 3 \times 10^{-5}$							
0.0630	1.0	0.200	0	106	49	1	5200	1.01×10^{-2}	27	7.48	9.38×10^{-3}	0.96	2.8	0.31
0.0450	1.0	0.250	0	106	49	1	13 000	7.09×10^{-3}	28	5.63	9.07×10^{-3}	0.97	2.9	0.36
0.0720	1.0	0.250	0	133	65	1	13 000	1.09×10^{-2}	26	8.30	1.13×10^{-2}	0.94	2.9	0.38
0.0720	1.0	0.500	0	106	49	1	7000	8.95×10^{-3}	26	7.32	1.38×10^{-2}	0.95	3.5	0.54
0.0225	1.0	1.000	0	106	49	1	44 000	2.91×10^{-3}	20	2.75	7.51×10^{-3}	0.90	4.4	0.61
0.0750	0.3	1.000	0	106	49	2	13 000	8.36×10^{-3}	17	3.18	2.24×10^{-2}	0.85	4.7	0.76
0.1800	0.1	1.000	0	106	49	2	5000	2.13×10^{-2}	18	3.01	3.67×10^{-2}	0.73	6.6	0.69
0.0720	1.0	1.000	0	106	49	1	15 000	8.09×10^{-3}	24	7.18	1.56×10^{-2}	0.90	4.2	0.62
0.1080	1.0	1.000	0	133	65	1	17 000	1.17×10^{-2}	25	9.67	1.69×10^{-2}	0.87	4.7	0.57
0.0270	1.0	2.500	0	85	41	1	47 000	3.03×10^{-3}	17	3.64	1.34×10^{-2}	0.83	4.7	0.76
0.0720	1.0	2.500	0	106	49	1	20 000	7.53×10^{-3}	24	7.32	1.81×10^{-2}	0.78	5.6	0.63
0.1080	1.0	2.500	0	133	65	1	8300	1.11×10^{-2}	26	9.85	1.91×10^{-2}	0.74	6.6	0.56
0.0054	3.0	3.000	0	85	41	1	69 000	8.61×10^{-4}	20	2.13	2.03×10^{-3}	0.81	5.8	0.37
							$E = 1 \times 10^{-4}$							
0.0750	1.0	0.500	0	64	41	1	14 000	1.00×10^{-2}	18	3.25	1.22×10^{-2}	0.97	2.9	0.32
0.0750	1.0	1.000	0	64	41	1	9700	8.43×10^{-3}	16	3.06	1.68×10^{-2}	0.95	3.4	0.52
0.1500	1.0	1.000	0	85	41	1	6800	1.71×10^{-2}	18	5.28	1.95×10^{-2}	0.87	4.0	0.42
0.0750	1.0	2.000	0	106	49	1	23 000	8.27×10^{-3}	15	3.26	1.89×10^{-2}	0.86	4.3	0.59
0.1500	1.0	2.000	0	85	41	1	7700	1.65×10^{-2}	18	5.40	2.13×10^{-2}	0.75	5.3	0.45
0.3200	0.1	1.500	0	64	41	1	6700	3.61×10^{-2}	12	2.14	5.30×10^{-2}	0.66	7.1	0.58
0.1033	3.0	3.000	0	106	49	1	5300	0.98×10^{-2}	19	8.26	1.56×10^{-2}	0.80	4.8	0.42
0.1500	1.0	3.000	0	106	49	1	4800	1.57×10^{-2}	18	5.46	2.41×10^{-2}	0.70	6.1	0.49
0.0750	1.0	3.330	0	85	41	1	8100	8.29×10^{-3}	15	3.47	2.11×10^{-2}	0.74	5.2	0.59
0.0150	10.0	3.330	0	85	41	1	30 000	1.89×10^{-3}	20	5.22	5.13×10^{-3}	0.96	3.2	0.28
0.1500	1.0	5.000	0	106	49	1	3300	1.51×10^{-2}	17	5.43	2.64×10^{-2}	0.63	7.6	0.48
0.0667	3.0	6.000	0	106	49	1	12 000	6.56×10^{-3}	18	6.42	1.61×10^{-2}	0.74	5.5	0.50
0.0833	3.0	6.000	0	106	49	1	8500	7.95×10^{-3}	18	7.41	1.67×10^{-2}	0.70	6.1	0.46
0.1500	1.0	10.000	0	133	65	1	3500	1.45×10^{-2}	18	5.44	2.91×10^{-2}	0.55	10.1	0.46
0.0075	10.0	10.000	0	64	41	1	171 000	8.53×10^{-4}	15	3.10	5.38×10^{-3}	0.93	3.7	0.54
0.0150	10.0	10.000	0	85	41	1	37 000	1.57×10^{-3}	17	5.11	7.61×10^{-3}	0.88	4.1	0.49
0.0310	10.0	10.000	0	106	49	1	54 000	2.82×10^{-3}	18	8.10	9.54×10^{-3}	0.82	4.9	0.46

Table 2. (*Continued.*)

Ra^*	Pr	Pm	r_λ	$\ell_{\max}$	N_r	m_s	$t_{\rm run}$	Ro	$\bar{\ell}_u$	Nu	Lo	$f_{\rm dip}$	$b_{\rm dip}$	$f_{\rm ohm}$
							$E = 3 \times 10^{-4}$							
0.1125	1.0	1.500	0	42	33	1	10 000	1.23×10^{-2}	11	2.18	2.09×10^{-2}	0.92	3.5	0.42
0.1125	1.0	3.000	0	42	33	1	5500	1.15×10^{-2}	10	2.20	2.48×10^{-2}	0.80	4.5	0.50
0.3750	0.3	3.000	0	64	41	1	2400	4.11×10^{-2}	10	2.35	4.58×10^{-2}	0.53	8.6	0.43
0.1890	1.0	3.000	0	64	41	1	115 000	1.99×10^{-2}	12	3.11	2.71×10^{-2}	0.67	5.3	0.39
0.2250	1.0	3.000	0	64	41	1	13 000	2.45×10^{-2}	13	3.51	2.40×10^{-2}	0.63	6.1	0.30
0.2430	1.0	3.000	0	64	41	1	27 000	2.77×10^{-2}	13	3.72	1.98×10^{-2}	0.59	7.3	0.22
0.0990	3.0	3.000	0	64	41	1	13 000	9.70×10^{-3}	13	3.92	1.79×10^{-2}	0.86	3.8	0.35
0.0990	3.0	9.000	0	64	41	1	11 000	9.65×10^{-3}	13	4.14	2.03×10^{-2}	0.62	6.2	0.38
0.2430	1.0	5.000	0	64	41	1	4500	2.38×10^{-2}	12	3.64	3.28×10^{-2}	0.57	7.6	0.38

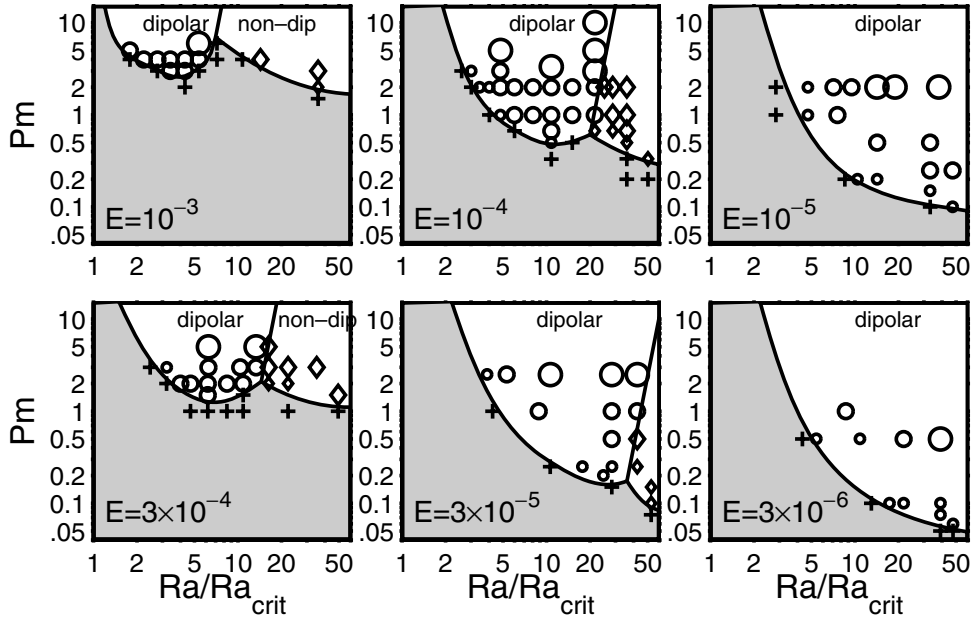

Figure 1. Regime diagram for dynamos at $Pr = 1$ with rigid boundaries driven by an imposed temperature contrast at different values of the Ekman number. Circles show dipolar dynamos, diamonds non-dipolar dynamos and crosses failed dynamos. The size of the symbol has been chosen according to the value of the Elsasser number. In parameter ranges not well covered by case studies the regime boundaries are tentative.

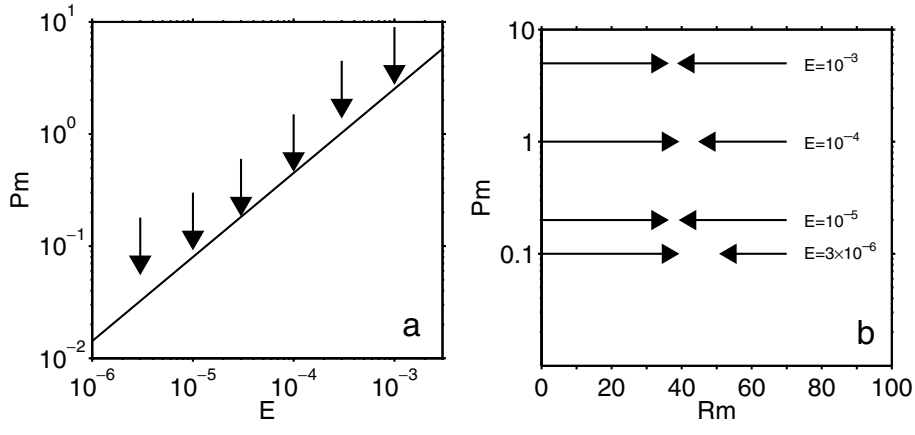

Figure 2. (a) The tip of the arrow indicates the lowest magnetic Prandtl number at which a non-decaying dipolar dynamo was found. Solid line according to eq. (25). (b) Tip of right arrow indicates lowest magnetic Reynolds number for self-sustained dipolar dynamos, left arrow highest magnetic Reynolds number for cases with decaying field. Intermediate cases have not been tested.

This relation is confirmed by the new results at lower Ekman number. At $E = 3 \times 10^{-6}$ the lowest magnetic Prandtl number at which we found a dynamo, $Pm = 0.06$, lies somewhat above the fitting line. However, from the systematic shift of the minimum Pm for dipolar dynamos towards higher supercritical Rayleigh number (Fig. 1), it seems likely that we have not reached the minimum, which may require a Rayleigh number more than 60 times supercritical at $E = 3 \times 10^{-6}$.

Since the hydrodynamic Prandtl number is one for all the cases considered here, eq. (25) holds also when the magnetic Prandtl number is replaced by the Roberts number $q = \kappa/\lambda = Pm/Pr$. Simitev & Busse (2005) noted that q may be a more relevant parameter than the magnetic Prandtl number. They found dynamos with a low Pm only in cases when Pr is also low and speculated that for $Pr \leq O(1)$ dynamo action occurs only at values of the Roberts number of order unity or larger, which is contradicted by our results.

Another question is whether the minimum value for self-sustained dynamo action of the magnetic Reynolds number

$$Rm = \frac{Ro}{E_\lambda} = \frac{u_{\rm rms}}{\lambda D}, \tag{26}$$

depends on Pm. For dynamos in non-rotating systems that generate a magnetic field from small-scale turbulence it had been found that the critical Reynolds number increases strongly when Pm is lowered below one and it has been debated if such dynamos exist at all for $Pm < 0.1$ (Schekochihin *et al.* 2004,2005). When a large-scale flow component is also present, low-Pm dynamos have been found (Ponty *et al.* 2005), but require a magnetic Reynolds number of the order 200, substantially higher than for dynamos at $Pm \approx 1$. In Fig. 2(b) we bracket the critical magnetic Reynolds number as function of the magnetic Prandtl number at appropriate values of the Ekman number. For the class of dynamos studied here, there is no strong dependence of the critical magnetic Reynolds number on Pm, provided the Ekman number is low enough. Our results are compatible with a nearly constant critical Rm of about 40–45.

Kutzner & Christensen (2002) found that the dipolar dynamo regime gives way to a class of dynamos that generate small-scale magnetic fields when the Rayleigh number is sufficiently increased with all other parameters held constant. The two regimes are clearly distinguished in the magnetic spectra at the outer boundary: the power is usually rather evenly distributed among the low-order harmonics, except for the dipole term, which is clearly stronger or clearly weaker, respectively, than the rest. When convection is driven by an imposed temperature contrast between the shell boundaries, as in the cases considered here, the transition is sharp, whereas for other modes of driving convection it can be more gradual. The degree of supercriticality of the Rayleigh number at which the transition occurs was found to increase when the Ekman number was lowered from 10^{-3} to 10^{-4} (Kutzner & Christensen 2002), thus making the parameter space domain of dipolar dynamos comparatively larger at low Ekman numbers. Here this trend is confirmed to continue for $E < 10^{-4}$ (Fig. 1). For the non-dipolar dynamos the critical magnetic Reynolds number is larger than 100. The dynamo mechanism in the non-dipolar regime seems, therefore, less efficient than in the dipolar regime.

Combining all results for different values of the Ekman number and the Prandtl numbers, we find non-dipolar dynamos at high values of the Rossby number and dipolar ones at low values, with some overlap of the two classes in the range $Ro \approx 1.5$–4×10^{-2}. The Rossby number can be considered as measuring the importance of inertial forces relative to the Coriolis force. Therefore, we hypothesize that the dipolar dynamo regime breaks down when inertia starts to play an essential role in the force balance. Sreenivasan & Jones (2006) observed a similar change of dynamo regime when they varied the two Prandtl numbers together at fixed values of the Ekman number and the Rayleigh number and attributed the change to the non-dipolar regime to the growing influence of inertial forces. They estimated that inertial effects become small when $Ro < 0.1$.

Because the inertial term in eq. (2) involves a length scale whereas the Coriolis term does not, a modified Rossby number that depends on the characteristic length scale of the flow rather than on the shell thickness is potentially a better measure for the balance between inertia and Coriolis force. Assuming that the radial and horizontal length scales are roughly similar, we estimate a characteristic value from the spectra of kinetic energy as function of spherical harmonic degree ℓ. The mean value $\bar{\ell}_u$ is obtained from the time-averaged kinetic energy spectrum

$$\bar{\ell}_u = \frac{\sum \ell \langle \mathbf{u}_\ell \cdot \mathbf{u}_\ell \rangle}{2E_{\rm kin}}, \tag{27}$$

where u_ℓ is the flow component at degree ℓ. As the mean radius to a point inside the shell is of order one, we set the characteristic half-wavelength of the flow to $\pi/\bar{\ell}_u$ and the modified Rossby number is

$$Ro_\ell = Ro\frac{\bar{\ell}_u}{\pi}. \tag{28}$$

In Fig. 3 we plot the relative dipole strength $f_{\rm dip}$ versus the modified Rossby number. We have included all cases, independent of the dipole strength, that satisfy the conditions (2) and (3) mentioned at the beginning of the section. There is a rather clear transition from the dipolar regime ($f_{\rm dip} > 0.5$) to the non-dipolar one ($f_{\rm dip} < 0.3$) at $Ro_\ell \approx 0.12$, irrespective of the values of the Ekman number, Prandtl number and magnetic Prandtl number. The only outlier is a non-dipolar case at $Ro_\ell \approx 0.09$. However, in this case the type of dynamo solution was sensitive to the starting condition. Depending on the initial magnetic field either a dipolar or a non-dipolar state persisted, the latter for 1.2 magnetic diffusion times (the two solutions are joined by a broken line in Fig. 3). In another case it took

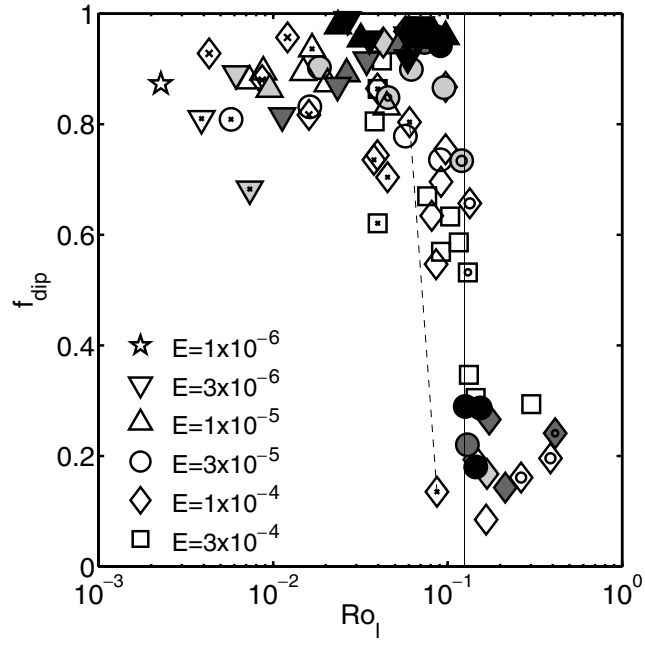

Figure 3. Relative dipole strength versus modified Rossby number. The Ekman number is indicated by the shape of the symbol and the magnetic Prandtl number by the shading ($Pm < 0.3$ black, $0.3 < Pm < 1$ dark grey, $Pm = 1$ light grey, $Pm > 1$ white). Hydrodynamical Prandtl numbers other than one are indicated by an additional small cross ($Pr = 3$), larger cross ($Pr = 10$), small circle ($Pr = 0.3$) or larger circle ($Pr = 0.1$) inside the main symbol. The two symbols joined by a broken line indicate a case where the dynamo regime depends on the starting condition.

approximately three magnetic diffusion times for the transition from a non-dipolar to a dipolar state to occur. Therefore, it is not clear if both branches of the solution are stable in the long term. In general the clear dependence of the regime on the modified Rossby number supports the assumption that inertial forces play the key role in the breakdown of dipolar dynamo solutions.

3.2 Heat transport

In Fig. 4(a) we plot in the conventional way the Nusselt number versus the Rayleigh number normalized by its critical value for all cases satisfying criteria (1)–(3). Of course the Nusselt number and Rayleigh number correlate, however, there is substantial scatter and the results do not fall on a single line. This changes remarkably when we plot the modified Nusselt number versus the flux-based modified Rayleigh number (Fig. 4b). We note that since both Nu^* and Ra^*_Q are defined in terms of the advected heat flux $Q_{\rm adv}$, the driving temperature contrast ΔT in eq. (16) assumes the role of the physical property that is determined by the functional dependence $Nu^*(Ra^*_Q)$. By the introduction of the modified 'diffusionless' parameters it is possible to collapse the data for all dynamos, regardless of the values of E, Pm and Pr, on a single regression line with a mean relative misfit of 5 per cent. We obtain the following power-law dependence

$$Nu^* = 0.076 Ra_Q^{*0.53}. \tag{29}$$

This is not much different from the scaling law obtained for non-magnetic rotating convection between stress-free boundaries, for which an exponent of 5/9 has been suggested (Christensen 2002). The exponent for the dependence of Nu^* on the Rayleigh number Ra^* based on ΔT is approximately 1.1. This very strong dependence compared to an exponent of order 1/3 that is typical for Benard-type convection seems to be a particular property of rotating convection. A requirement is that convection fills the entire fluid volume, that is, the Rayleigh number must be sufficiently supercritical (Tilgner & Busse 1997).

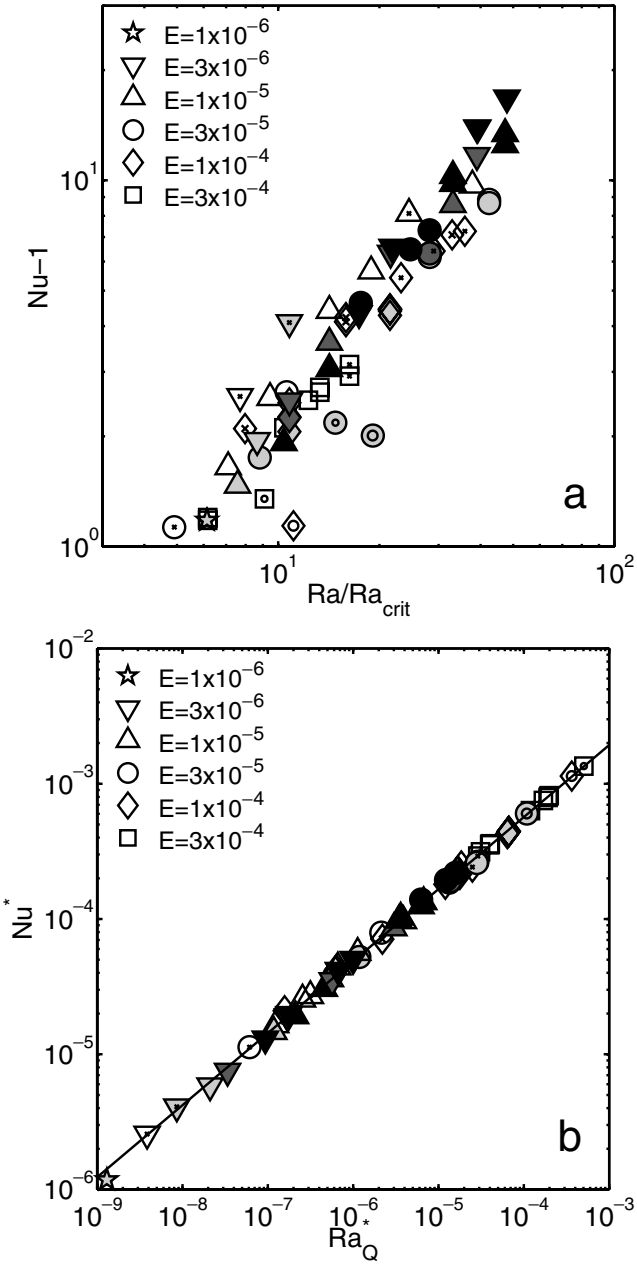

Figure 4. (a) Conventional Nusselt number versus Rayleigh number normalized by its critical value. (b) Modified Nusselt number versus modified flux-based Rayleigh number. Symbols as in Fig. 3.

3.3 Flow velocity

In Fig. 5 we plot the Rossby number, that is, the non-dimensional rms velocity, against the modified Rayleigh number. The best-fitting power law has the form

$$Ro = 0.85 Ra_Q^{*0.41}. \tag{30}$$

With a mean relative deviation of 18 per cent the fit is decent given that the cases cover a broad range of the control parameters E, Pm and Pr, and almost six decades in Ra^*_Q, but is not as good as in case of the Nusselt number.

We attempted to reduce the residual scatter by assuming an additional dependence on one more parameter. The best result is obtained

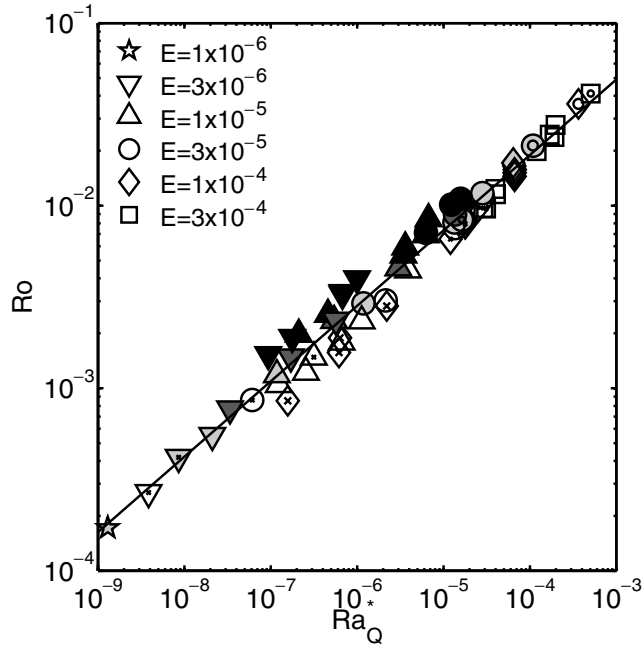

Figure 5. Rossby number versus modified Rayleigh number. Symbols as in Fig. 3.

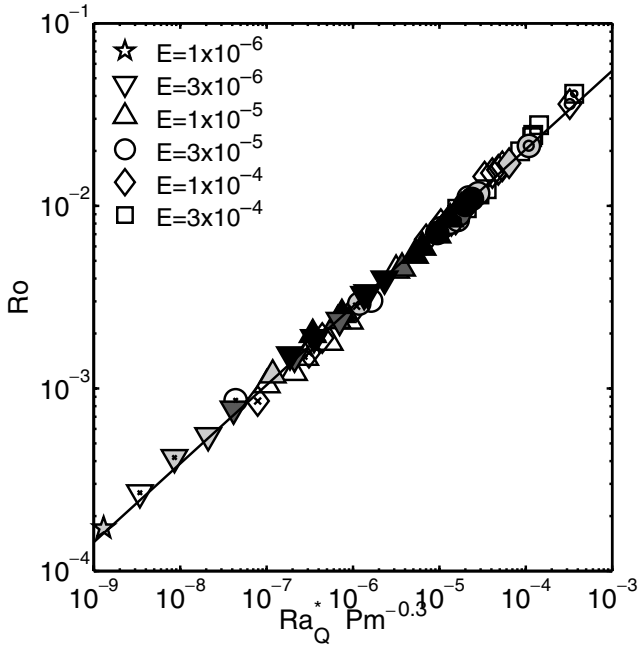

Figure 6. Rossby number versus a combination of modified Rayleigh number and magnetic Prandtl number. Symbols as in Fig. 3.

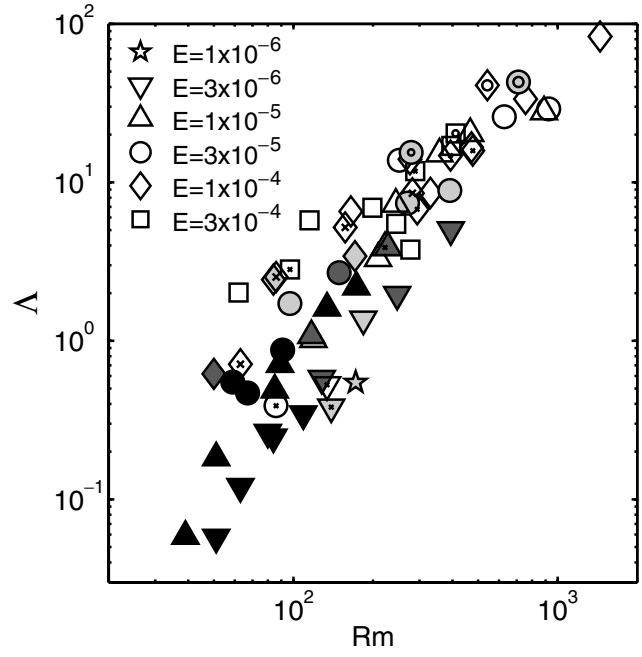

Figure 7. Elsasser number versus magnetic Reynolds number. Symbols as in Fig. 3.

with a two-parameter fit that involves the magnetic Prandtl number (Fig. 6), for which the optimal exponent is −0.13.

$$Ro = 1.07 Ra_Q^{*0.43} Pm^{-0.13}. \tag{31}$$

This reduces the mean deviation of the dynamo results from the fitting law to 8 per cent. The improvement is substantial, but not so large that a dependence on *Pm* can be firmly assumed. A similar improvement on including a dependence on *Pm* had been found by Christensen & Tilgner (2004) when scaling the magnetic diffusion time as function of the magnetic Reynolds number. However, based on results of a laboratory dynamo with a much lower *Pm* they rejected the additional dependence on the magnetic Prandtl number at least for $Pm \ll 1$.

3.4 Magnetic field strength

It is often assumed that in a magnetostrophic force balance the Elsasser number Λ should be of order one. For our dipole-dominated dynamos we find a broad range of values for the Elsasser number, between 0.06 and 100. There is some correlation with the magnetic Reynolds number *Rm* (Fig. 7), but clearly Λ does not simply depend on *Rm* alone. For a fixed value of *Rm*, the Elsasser number tends to decrease with decreasing Ekman number. The large range of values for Λ suggests that the dynamos are either not in a magnetostrophic balance or that the conventional Elsasser number is not a good measure for the degree of magnetostrophy.

A somewhat better fit is obtained when we relate the Lorentz number, that is, the non-dimensional mean magnetic field strength in our scaling, to the modified Rayleigh number (not shown). We do not discuss this results in detail, because a consideration based on the energetics of the dynamo suggests a correction term that significantly improves the fit to the numerical data. The fundamental idea is that the magnetic field strength is not determined by a force balance, but by the power available to balance Ohmic dissipation. Dissipation and magnetic field strength are linked through the length scale of the field, or a dissipation timescale, which we take as being a function of the flow properties. Christensen & Tilgner (2004) found an inverse relation between the magnetic dissipation time τ', that is, the ratio of magnetic energy $E_{\rm mag}$ to Ohmic dissipation D_λ, and the magnetic Reynolds number *Rm*. τ' is scaled with the magnetic diffusion time and by τ we denote the dissipation timescaled with the rotational timescale used here. From the relations $\tau = E_\lambda^{-1}\tau'$ and $Ro = E_\lambda Rm$ we find that $\tau \sim Ro^{-1}$. Furthermore, from eqs (13), (22) and (24) we obtain with $D_\lambda = f_{\rm ohm} P \sim f_{\rm ohm} Ra_Q^*$ and $Lo^2 = 2E_{\rm mag} = 2D_\lambda \tau$ the relation

$$\frac{Lo}{f_{\rm ohm}^{1/2}} \sim \left(\frac{Ra_Q^*}{Ro}\right)^{1/2}. \tag{32}$$

Using eq. (30) for the relation between Rossby number and Rayleigh number, a dependence of the Lorentz number, corrected for the fraction of Ohmic dissipation, on the modified Rayleigh number with an exponent of order 0.3 is predicted.

In Fig. 8 we plot the corrected Lorentz number against the modified Rayleigh number. For our selected dynamos the best-fitting power law is

$$\frac{Lo}{f_{\rm ohm}^{1/2}} = 0.92 Ra_Q^{*0.34}, \tag{33}$$

with a mean relative misfit of 17 per cent.

Again, as in the case of the Rossby number, the fit can be improved by assuming a weak additional dependence on the magnetic Prandtl number. A two-parameter best fit (Fig. 9) results in

$$\frac{Lo}{f_{\rm ohm}^{1/2}} = 0.76 Ra_Q^{*0.32} Pm^{0.11}. \tag{34}$$

The reduction of the misfit, to 10 per cent, is not as strong as in the case of the Rossby number.

3.5 Robustness of the scaling laws

We have found that the Rossby number and the Lorentz depend on the modified Rayleigh number through a power law. They may

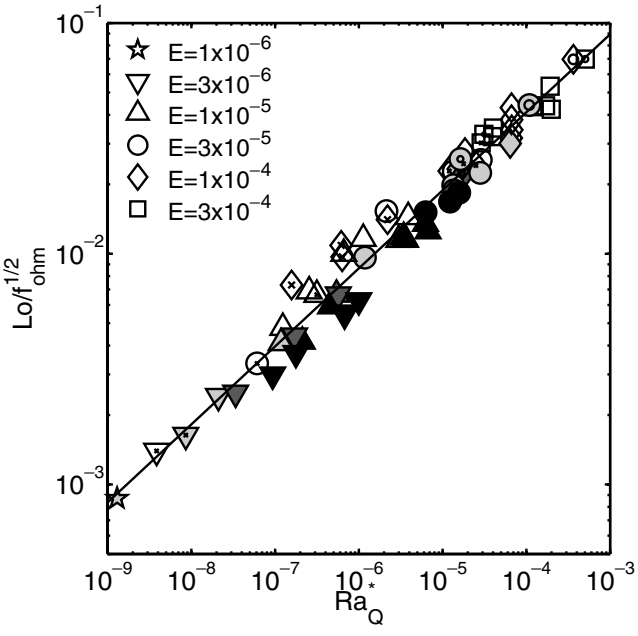

Figure 8. Lorentz number corrected for the relative fraction of Ohmic dissipation versus modified Rayleigh number. Symbols as in Fig. 3.

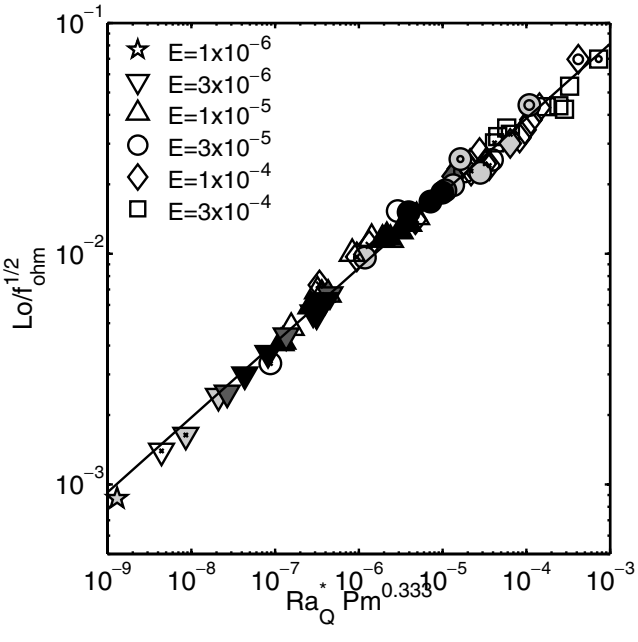

Figure 9. Lorentz number corrected for the relative fraction of Ohmic dissipation versus a combination of modified Rayleigh number and magnetic Prandtl number. Symbols as in Fig. 3.

also depend weakly on the magnetic Prandtl number. Because of the large range of extrapolation required for a planetary application, it is important to verify that the power-law exponents are not biased by dynamo cases that lie far away from an asymptotic regime. For example, an exponent of 0.4 for the relation between Rossby number and modified Rayleigh number has been found for non-magnetic rotating convection, where the main force balance is between inertia, Coriolis force and buoyancy force (Aubert *et al.* 2001). Inertia is assumed to play a small role in planetary dynamos, however, it may still be important in some of our dynamo cases. This might bias the power-law exponent towards a value appropriate for the inertial regime. We test this by fitting only subsets of our dynamo data to a power law.

Table 3. Best-fitting parameters.

	A	α	β	γ	δ
Nu^*	0.0861	0.527	−0.010	0.018	−0.007
Ro	1.159	0.419	−0.131	0.020	−0.028
$Lo/\sqrt{f_{\rm ohm}}$	0.837	0.312	−0.105	0.023	−0.026

Cases with a large value of the scale-sensitive Rossby number Ro_ℓ are more affected by inertial forces than those at low Ro_ℓ. We set a threshold for the modified Rossby number of 0.05, that is, a factor 2.5 below the critical value at which the dipolar dynamo regime breaks down. When we reject all cases above this threshold, retaining 36 models, the exponent to Ra_Q^* for the Rossby number is 0.39 and that for the corrected Lorentz number is 0.36. This is not very different from the exponents obtained when all data are included. When we reject all dynamos with an Ekman number of 10^{-4} or larger, which are presumably more affected by viscous forces than those at lower values of the Ekman number, the power-law exponents relating Ro and $Lo/f_{\rm ohm}^{1/2}$ to the modified Rayleigh number remain unchanged within one percent.

In order to verify that the parameters not included in the fit, the Ekman number and the hydrodynamic Prandtl number, do not affect the dynamo properties significantly we calculate a general least-squares fit of the form

$$Y = A Ra_Q^{*\alpha} Pm^{\beta} E^{\gamma} Pr^{\delta}, \tag{35}$$

where Y stands for any of Nu^*, Ro, or $Lo/f_{\rm ohm}^{1/2}$. The best-fitting exponents are listed in Table 3. Those describing a dependence on the Ekman number or on the Prandtl number differ only very marginally from zero.

These tests suggest that power laws relating the Rossby number and the Lorentz number to the flux-based modified Rayleigh number, with exponents of the order 2/5 and 1/3, respectively, are robust within our range of model parameters and can probably be extrapolated beyond this range.

4 FORCE BALANCE

The scaling laws presented in the previous sections are mainly empirical, that is, they are derived by fitting numerical data. Usually such laws can be understood in terms of a balance of dominant forces or physical effects. We have presented a rationale for the scaling of the magnetic field strength based on the available power that lead to eq. (32). However, to arrive at our final expression (33) we had to resort to the empirical relation between Rossby number and Rayleigh number, for which an explanation is missing so far.

In the so-called mixing length theory for non-magnetic rotating convection a triple balance between buoyancy, Coriolis force and inertia is supposed. A critical point is the value of the characteristic length scale δ. With the simple assumption $\delta \sim D$ the flow velocity is predicted to depend on the 1/3 power of the heat flux (Starchenko & Jones 2002; Stevenson 2003). Aubert *et al.* (2001) invoked different length scales parallel to the rotation axis, $\delta_z \sim D$, and perpendicular to it, $\delta_\phi \ll D$, and obtained with the triple force balance a 2/5 power law for the dependence of the Rossby number on the modified flux-based Rayleigh number. In the dynamo case the presence of the Lorentz force adds complexity to any such analysis. In the magnetostrophic assumption, usually made for dynamos

in an earth-like regime, inertia is replaced by the Lorentz force in the triple balance. Starchenko & Jones (2002) derived a dependence of the magnetic field strength $\sim (Q_B\ \Omega)^{1/4}$ and found an order-of-magnitude agreement with the estimated field inside the Earth and Jupiter. In their analysis they supposed that the characteristic length scale of the magnetic field is independent of the magnetic Reynolds number and fixed the value to $\delta_B \approx r_o/50$ from numerical simulations at $Rm = 200$. However, the inverse dependence of the magnetic dissipation time on the magnetic Reynolds number found by Christensen & Tilgner (2004) in the range of 50–1000 for Rm implies that $\delta_B \sim Rm^{-1/2}$.

Analysing the zonal part of the flow in numerical models, Aubert (2005) found that the zonal velocity scales differently for dynamos and for non-magnetic convection, which can be explained by Lorentz forces playing a significant role in the former case and inertia in the latter. The importance of the Lorentz force seems less clear in our case, where the total velocity and magnetic field are considered. The large variability of the Elsasser number casts some doubt on a basically magnetostrophic balance. However, the conventional Elsasser number (eq. 1) does not take into account that the Lorentz force depends on the length scale of the magnetic field, whereas the Coriolis force does not depend on any length scale, hence Λ may not be a good measure for the relative importance of these two forces. By a simple scaling argument we get the length scale δ_B from Ohmic dissipation: $D_\lambda \sim E_\lambda\, Lo^2/\delta_B^2 \sim f_{\rm ohm}\, P \sim f_{\rm ohm}\, Ra_Q^*$. Using eq. (33), we obtain $\delta_B \sim E_\lambda^{1/2} Ra_Q^{*-1/6}$. The ratio of the Lorentz force term to the Coriolis term in eq. (2) scales as $Lo^2/(\delta_B\, Ro) \sim f_{\rm ohm} E_\lambda^{-1/2} Ra_Q^{*0.42}$. Therefore, our scaling laws suggest a rather variable influence of the Lorentz forces depending on the control parameters. Obviously the Lorentz force must have a significant effect on the flow in every dynamo, because this is the only way how the magnetic field strength can saturate. However, it does not necessarily mean that a global balance with the Coriolis force holds, which is implied in our formula. The spatial distribution of the Lorentz force can be very intermittent (see for example Figure 14 in Rotvig & Jones (2002)), and the balance may be local rather than global. Furthermore, major parts of the Coriolis force and/or the Lorentz force can be balanced by pressure gradients, and only the unbalanced residuals are meaningful in a MAC balance.

4.1 Enstrophy budget

We calculate for several of our models sources and sinks of enstrophy $\boldsymbol{\omega}^2$, which is the 'energy of vorticity' $\boldsymbol{\omega} = \nabla \times \mathbf{u}$. In fluid systems where the Coriolis force plays a significant role, the geostrophic equilibrium usually holds between the Coriolis force and the pressure gradient. However, the dynamics of the system is not controlled by this equilibrium, but by departures from it, where the contributions of other forces play an decisive role. It is, therefore, useful to remove the geostrophic balance from the Navier–Stokes equation by considering the vorticity equation, obtained by taking the curl of eq. (2):

$$\frac{\partial \boldsymbol{\omega}}{\partial t} + \nabla \times (\boldsymbol{\omega} \times \mathbf{u}) - 2\frac{\partial \mathbf{u}}{\partial z} = \frac{Ra^*}{r_o}\nabla \times (T\mathbf{r}) + \nabla \times [(\nabla \times \mathbf{B}) \times \mathbf{B}] + E\nabla^2 \boldsymbol{\omega} \tag{36}$$

The pressure gradient disappears in eq. (36) and the Coriolis term is reduced to the contribution of the departure from geostrophy $\partial \mathbf{u}/\partial z$. Taking the dot-product of eq. (36) with $\boldsymbol{\omega}$ we obtain the enstrophy equation:

$$\frac{1}{2}\frac{\partial \boldsymbol{\omega}^2}{\partial t} = \underbrace{-[\nabla \times (\boldsymbol{\omega} \times \mathbf{u})] \cdot \boldsymbol{\omega}}_{N_I} \underbrace{-2\frac{\partial \mathbf{u}}{\partial z} \cdot \boldsymbol{\omega}}_{N_C} + \underbrace{\frac{Ra^*}{r_o}[\nabla \times (T\mathbf{r})] \cdot \boldsymbol{\omega}}_{N_B} + \underbrace{(\nabla \times [(\nabla \times \mathbf{B}) \times \mathbf{B}]) \cdot \boldsymbol{\omega}}_{N_L} + \underbrace{E(\nabla^2 \boldsymbol{\omega}) \cdot \boldsymbol{\omega}}_{N_V} \tag{37}$$

Each of the quantities $N_{I,C,B,L,V}$ gives insight into how the respective forces affect the dynamics of vorticity in the convective dynamo. To get an estimate of the importance of these quantities, unsigned, time-averaged and normalized shell integrals $I_{I,C,L,V}$ are defined as

$$I_{I,C,B,L,V} = \left\langle \frac{\int_{V'} |N_{I,C,B,L,V}|\, dV}{\int_{V'} |N_B|\, dV} \right\rangle. \tag{38}$$

The angular brackets denote the time-averaging operator, and V' is the spherical shell volume minus the inner and outer viscous boundary layers. These layers are excluded because rigid walls are sources and sinks of enstrophy. $I_{I,C,L,V}$ represents the respective contribution of inertia, Coriolis force, Lorentz force and viscous force in the enstrophy budget, normalized by the driving contribution of buoyancy ($I_B = 1$).

The different contributions to the enstrophy budget are illustrated in Fig. 10 for a reference case. N_B is positive almost everywhere, which correlates with the location of the axial vortices: buoyancy is the main creator of enstrophy. The negative contribution of N_V shows that viscosity is destroying enstrophy mainly near the boundaries and at the edges of axial vortices. The Lorentz force makes a mainly negative contribution N_L. The Coriolis force withdraws enstrophy from the interior of the fluid and creates enstrophy close to the boundaries. This redistribution of enstrophy can be seen as an effect of the Proudman–Taylor constraint. In the interior the fluid the enstrophy associated with gradients of the velocity along $\hat{\mathbf{z}}$ tends to be eliminated and recreated close to the boundary. N_I is sizeable near the inner boundary.

To explore the dependence of the various contributions to the enstrophy budget on the control parameters we have calculated $I_{I,C,L,V}$ for several other dynamo models. The results are shown in Fig. 11, where each of the control parameters is varied separately. The contribution of the Coriolis force I_C is found to be consistently in balance with the contribution of buoyancy $I_B = 1$. Since the integrals are normalized with I_B, they can also be seen as normalized by I_C, and as a logical result, the variations of $I_{I,L,V}$ basically reflect the respective variations of the Rossby, Elsasser and Ekman numbers. The contribution I_L of the Lorentz force is quite variable, suggesting again that the saturation of the magnetic field does not originate in a force balance, but rather in an energy balance. In the case of a non-dipolar dynamo included in Fig. 11(a), inertia is dominating the enstrophy balance, in agreement with our previous assumption that the dipolar dynamo regime breaks down when inertia becomes important.

While the inertial and viscous contributions to the enstrophy budget are usually smaller than those of the Coriolis and buoyancy force, there is not an order-of-magnitude difference. However, we note that by considering a vorticity equation rather than the original Navier–Stokes equation smaller scales are more strongly emphasized. Both the inertial term and the viscous term in the Navier–Stokes equation involve a length scale, whereas the Coriolis term does not. Hence we expect that inertia and viscosity contribute less to a force balance of the flow at large scales.

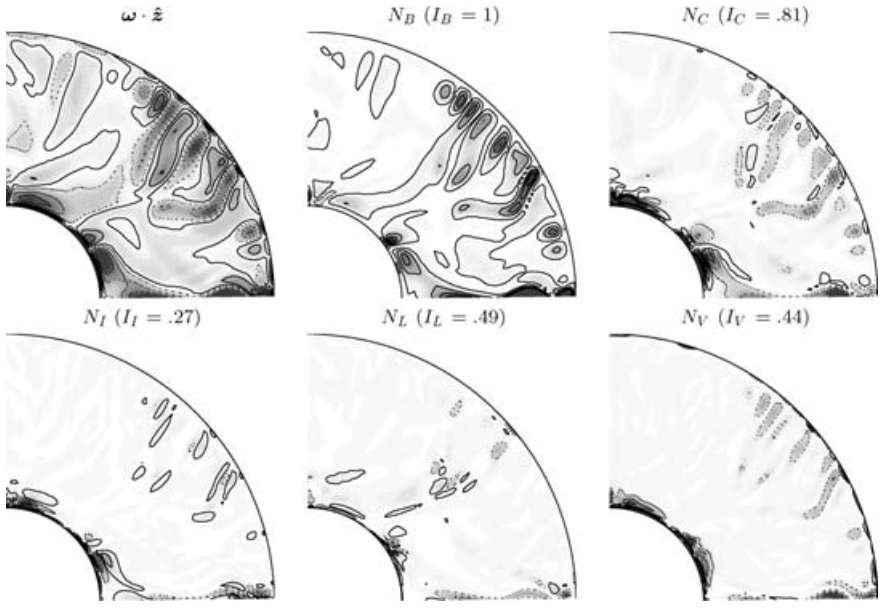

Figure 10. Equatorial cuts of the axial vorticity $\omega \cdot \hat{z}$ (dotted contours: negative values, plain contours: positive values, contour increment: 0.15), and the various contributions to the enstrophy budget (same convention, contour increment: 0.018). $E = 10^{-4}$, $Pm = Pr = 1$, $Ra^* = 0.075$.

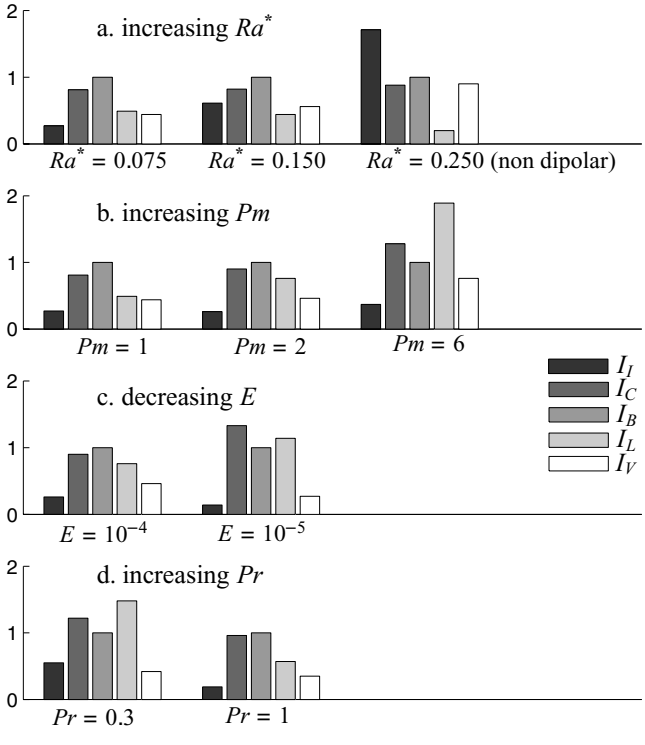

Figure 11. Contributions to the enstrophy budget for various cases. (a) Ra^* is variable ($Pm = 1$, $Pr = 1$, $E = 10^{-4}$). (b) Pm is variable ($Ra^* = 0.075$, $Pr = 1$, $E = 10^{-4}$). (c) E is variable (Ra^* is 10 times supercritical, $Pr = 1$, $Pm = 2$). (d) Pr is variable ($E = 3 \times 10^{-5}$, Ra^* is 10 times supercritical, $Pm = 1$).

4.2 Scaling of the Rossby number

We now attempt to explore the theoretical background for the scaling of the typical value Ro of the velocity. We assume that the thermal fluctuations of typical amplitude δT have an azimuthal size of order δ_φ, different from the characteristic length scale of the flow δ_z in the direction of the rotation axis. In the previous section we have seen that a balance between the curled Coriolis force and the curled buoyancy force generally holds in the enstrophy budget (eq. 37):

$$2\frac{\partial \mathbf{u}}{\partial z} \sim \frac{Ra^*}{r_o}\nabla \times (\delta T \mathbf{r}). \tag{39}$$

An order-of-magnitude analysis yields

$$\frac{Ro}{\delta_z} \sim Ra^* \frac{\delta T}{\delta_\varphi}. \tag{40}$$

Temperature fluctuations and velocity can also be related through an estimate of the convective Nusselt number:

$$Ro\ \delta T \sim Nu^*, \tag{41}$$

hence

$$Ro \sim (Ra_Q^*)^{1/2} \sqrt{\frac{\delta_z}{\delta_\varphi}}. \tag{42}$$

The variation of $\sqrt{\delta_z/\delta_\varphi}$ with the Rayleigh number must account for the difference between the observed scaling exponent of 0.41 and the reference value of 1/2 in eq. (42). Either δ_φ must increase with Ra_Q^*, or δ_z decrease, or both may vary. For non-magnetic convection, Aubert *et al.* (2001) proposed that δ_z/D remains of order one due to the geostrophy of the convective flow, and that δ_φ is determined by a balance between inertia and Coriolis force and increases with the vigour of convection. This theory yields $Ro \sim (Ra_Q^*)^{0.4}$, in close agreement with our empirical results. Because of the strongly variable and often rather small contribution of inertia to the enstrophy budget (Fig. 11), it seems unlikely that the balance between inertia and the Coriolis force can generally be invoked in our dynamo models. Furthermore, we calculated the mean harmonic order $\bar{m}$ in the kinetic energy spectrum, which should be inversely proportional to δ_φ. In models of non-magnetic convection (not reported here), we found indeed a systematic decrease of $\bar{m}$ with the Rayleigh number, consistent with the increase of δ_φ observed experimentally by Aubert *et al.* (2001). In the dynamo cases however, the variation of $\bar{m}$ with the Rayleigh number is smaller and incoherent. This suggests

that the force balance differs between non-magnetic and magnetic cases. We must, therefore, assume that in the dynamos δ_z is reduced when the flow becomes more vigorous, which might be affected by Lorentz forces. However, we did not record the characteristic length scale in z-direction in our models and a more definitive analysis remains a task for the future.

5 APPLICATION TO THE EARTH AND PLANETS

In this section we discuss the scaling laws for the heat flow, flow velocity and magnetic field in physical units and make applications to the geodynamo and other planetary dynamos, assuming that the scaling laws remain valid under planetary conditions.

5.1 Core heat flow

The exponent in the scaling law for the modified Nusselt number (eq. 29) is close to 0.5, and in order to simplify the following discussion, we assume it to be exactly 0.5. With the exponent fixed in this way, the constant in eq. (29) should be adjusted:

$$Nu^* \approx 0.05 Ra_Q^{*1/2}. \tag{43}$$

Casting the scaling law into dimensional form we then obtain

$$Q_{\rm adv} \approx 0.01 \frac{\pi r_o r_i \alpha g_o \rho c \Delta T^2}{\Omega}. \tag{44}$$

A remarkable point about eq. (44) is that the (advected) heat flow is independent of thermal conductivity. Of course, this is a consequence of the existence of a relation between non-dimensional parameters Nu^* and Ra_Q^* that are both independent of thermal conductivity. However, it is surprising that conductivity plays no role because the heat must be conducted through boundary layers at the inner and outer shell boundaries. Obviously eq. (44) cannot hold in the limit of vanishingly small conductivity where the thermal boundary layer thickness must go to zero. The validity of eq. (44) probably requires that the thermal boundary layer extends beyond the Ekman layer. With an Ekman layer thickness of $DE^{1/2}$ and a thermal boundary layer thickness of D/Nu, using eqs (18) and (43) and neglecting the difference between Nu and $Nu - 1$, we arrive at the condition

$$Ra_Q^* < 400 E Pr^{-2}. \tag{45}$$

This condition is satisfied in all numerical models. With the estimates for Ra_Q^* given below it also satisfied in the Earth's core.

Let us assume that convection in the Earth's core is mainly thermally driven. Estimates for the core heat flow vary widely (e.g. Buffett 2002). Taking a value of 2 TW for the advected heat flow and appropriate values for the other parameters ($\alpha = 10^{-5}$, $g_o = 10$, $\rho = 10^4$, $c = 700$, $r_o = 3.48 \times 10^6$, $r_i = 1.22 \times 10^6$, $\Omega = 7.3 \times 10^{-5}$, in SI-units), we can use eq. (44) to estimate a driving (superadiabatic) temperature contrast of $\Delta T \approx 1$ mK. The corresponding density anomaly providing the buoyancy is 10^{-4} kg m^{-3}. The same value has been estimated by Aurnou *et al.* (2003) from a study of vortex-flow driven by a thermal wind inside the core's tangent cylinders.

5.2 Buoyancy flux and inner core growth

Since the buoyancy flux in the Earth's core is poorly constrained, the value of the Rayleigh number Ra_Q^* cannot be calculated directly. However, decent estimates for the characteristic flow velocity in the core have been derived from geomagnetic secular variation. Therefore, we use the relation between Rossby number and Rayleigh number to estimate a value for the latter. A typical velocity of flow near the core's surface obtained by inverting secular variation data is 0.4–0.5 mm s^{-1} (Voorhies 1986; Bloxham *et al.* 1989). Only the large-scale part of the flow is retrieved in these inversions and it is an open question how much energy is present at smaller scales and contributes to the rms velocity. In our models we find that the velocity of the large-scale flow below the Ekman layer near the outer surface, for harmonic degrees ℓ up to 12, is typically of the order of 1/4 to 1/2 of the total rms velocity in the entire shell. Taking this ratio as a rough guide, a better estimate for the true rms velocity in the core may be 1 mm s^{-1}, which gives a Rossby number of 6×10^{-6}. From eq. (30) the flux-based modified Rayleigh number in the core is then obtained as $Ra_Q^* = 3 \times 10^{-13}$.

A somewhat independent estimate of Ra_Q^* is obtained from the scaling relation for the Rossby number related to the zonal part of the flow that has been obtained by Aubert (2005): $Ro_{\rm zonal} \approx 0.9\, Ra_Q^{*1/2}$. The zonal flow contributes significantly inside the Earth's inner core tangential cylinder, but is substantially weaker outside. A characteristic value is 0.1 mm s^{-1} (Olson & Aurnou 1999; Hulot *et al.* 2002). The zonal flow Rossby number of 6×10^{-7} leads to an estimate for the Rayleigh number of $Ra_Q^* = 4 \times 10^{-13}$, very similar to the value derived using the global velocity.

Assuming a core viscosity of $\nu = 2 \times 10^{-6}$ m^2 s^1 and thermal diffusivity of 8×10^{-6} m^2 s^{-1}, which gives $E = 5 \times 10^{-15}$ and $Pr = 0.25$, other parameters of interest have the following values: $Nu^* \approx 10^{-8}$, $Nu \approx 10^6$, $Ra^* \approx 10^{-5}$ and $Ra \approx 10^{23}$. The critical Rayleigh number for non-magnetic convection at this Prandtl number is $Ra_{\rm crit} \sim 2\, E^{-4/3} \approx 2 \times 10^{19}$ (Jones *et al.* 2000), hence convection in the core would be 5000 times supercritical even in the absence of a magnetic field. Our estimate for the degree of supercriticality is fairly similar to that obtained by Gubbins (2001) along different lines of reasoning for 'turbulent' parameters, where his ratio between turbulent and molecular thermal diffusivity is equivalent to our Nusselt number.

If core convection were completely thermally driven, these values of the the Rayleigh number would correspond to a superadiabatic heat flow of 2–3 TW. However, it is believed that most of the driving buoyancy arises from the rejection of the light alloying element from the growing inner core (Loper 1978; Buffett *et al.* 1996). Kutzner & Christensen (2002) found that the properties of chemically driven dynamos, in which the buoyancy flux originates at the inner shell boundary and is zero on the outer boundary, are fairly similar to those of dynamos driven by a fixed temperature contrast. We assume that the same scaling laws hold, with Ra_Q^* replaced by the Rayleigh number based on the buoyancy flux Ra_B^* (eq. 20). Our estimated value for the flux-based modified Rayleigh number of 3–4 $\times 10^{-13}$ translates into a buoyancy flux of $3 - 4 \times 10^4$ kg s^{-1}. The rate of growth of the inner core radius r_i is obtained as

$$\frac{dr_i}{dt} = \frac{Q_B}{4\pi r_i^2 \Delta\rho_{ic}}. \tag{46}$$

$\Delta\rho_{ic}$ is the compositional contribution to the density contrast at the inner core boundary, which is estimated to be in the range 350–700 kg m^{-3} (Gubbins *et al.* 2004). The predicted rate of inner core growth is approximately 0.1 mm yr^{-1}. Assuming for simplicity a constant buoyancy flux, which concurs with a magnetic field strength that did not change substantially over geological time, the age of the inner core $t_{ic} = 4\pi r_i^3 \Delta\rho_{ic}/(3Q_B)$ is obtained as 3.5 ± 1.5 Gyr. The calculated rate of inner core growth is smaller and the suggested inner

core age substantially larger than other recent estimates (Labrosse *et al.* 2001; Nimmo *et al.* 2004), which assumed that a higher heat flux from the core (or higher buoyancy flux) was necessary to drive to geodynamo. With typical values for the relevant thermodynamic parameters, a slightly subadiabatic value of the CMB heat flux is sufficient to let the inner core grow at 0.1 mm yr^{-1} and generate a buoyancy flux at the inner core boundary of the order required by our analysis. The buoyancy flux at the CMB is weakly negative in such a scenario, which should be taken into account for a more quantitative analysis.

We close this section by giving for later purposes the relation between the dimensional characteristic velocity U and the flux, where we set for simplicity the exponent in eq. (30) equal to 0.4 and adjust the constant:

$$U \approx 0.7 \left(\frac{D}{\Omega}\right)^{1/5} \left(\frac{\alpha g_o Q_{\rm adv}}{4\pi r_o r_i \rho c}\right)^{2/5}. \qquad (47)$$

5.3 Core magnetic field

Next we derive a law for the dimensional magnetic field strength by using the dependence of the Lorentz number on the Rayleigh number with a power-law exponent of $1/3$ and no influence of the magnetic Prandtl number (eq. 33). The fraction of Ohmic dissipation in most of our models is in the range of 0.3–0.8. For the Earth's core $f_{\rm ohm} \approx 1$ is usually assumed, based on a ratio of magnetic energy to kinetic energy much larger than one and the high magnetic diffusivity. However, if the kinetic energy is allowed to cascade to much smaller length scales than the magnetic energy, viscous dissipation may still be significant. From our model results we did not find a simple rule of how $f_{\rm ohm}$ varies with the control parameters, but for simplicity we will make the usual assumption that viscous dissipation becomes negligible under core conditions. Replacing again the heat flux by the buoyancy flux, we then obtain for the characteristic value of magnetic induction inside the dynamo region

$$B \approx 0.9\, \mu^{1/2} \rho^{1/6} \left(\frac{g_o Q_B D}{4\pi r_o r_i}\right)^{1/3}. \qquad (48)$$

This scaling law is remarkable, because it predicts that the magnetic field strength is not only independent of the electrical conductivity (or magnetic diffusivity) but also of the rotation rate. It does not imply that these two properties are irrelevant; obviously the diffusivity must be low enough for the magnetic Reynolds number to be supercritical and, as was shown above, the rotational effects must be strong in comparison to the inertial force in order to get a dipole-dominated dynamo at all. However, eq. (48) implies that once these two conditions are satisfied, the precise values of the conductivity and of the rotation rate become unimportant and the magnetic field strength is basically determined by the buoyancy flux and the size of the dynamo.

For the estimated buoyancy flux of $3-4 \times 10^4$ kg s^{-1} an average magnetic field strength in the core of about 1.2 mT is obtained from eq. (48). The corresponding Lorentz number is 6×10^{-5}. Our prediction is somewhat lower than usually quoted values for the core field in the range of 2–4 mT, but the magnetic field strength inside the core is poorly known. It can be estimated via an assumption on how the mean field in the interior relates to the large-scale magnetic field on the core–mantle boundary (CMB). The observed mean dipole field on the CMB is 0.26 mT and the mean field strength in harmonic degrees 1–12 is 0.39 mT (Bloxham & Jackson 1992). In our dynamo models, the magnetic field inside the fluid shell is 3–10 times stronger than the dipole field on the outer boundary (factor $b_{\rm dip}$ in table 2). If such factor applies also to the geodynamo, the core field should be in the range 0.8–2.6 mT. Many of our dynamo models overestimate the contribution of the dipole to the external field, that is, have factors $f_{\rm dip} > 0.8$ as compared to $f_{\rm dip} \approx 0.68$ for the geomagnetic field. $b_{\rm dip}$ is anticorrelated with $f_{\rm dip}$ and for models with earth-like values of $f_{\rm dip}$ the factor $b_{\rm dip}$ is typically 6–7, suggesting a core field strength of 1.7 mT. In a different approach, Zatman & Bloxham (1997) analysed secular geomagnetic variations in terms of torsional oscillations in the core and obtained an rms strength of the magnetic field component B_s pointing away from the rotation axis of ≈0.4 mT. While in some conceptual dynamo models the B_s component is comparatively small (Braginsky 1975), we find that in our models B_s is not significantly weaker than the other components. In this case the inferred $B_s \approx 0.4$ mT corresponds to an overall field strength of about 1 mT. We conclude that our prediction from the scaling laws is in reasonable agreement with independent estimates for the core field strength.

When we use the scaling laws involving a dependence on the magnetic Prandtl number, first eq. (34) to estimate the Rayleigh number in the Earth's core, and in the next step eq. (31) to obtain the magnetic field strength, the results differ substantially. For a value $Pm \approx 2 \times 10^{-6}$ a Rayleigh number $Ra_Q^* \approx 10^{-14}$ is obtained, with a corresponding buoyancy flux of about 1000 kg s^{-1}, a factor of 30 lower than the above estimate. Such a low value seems unlikely. The predicted Lorentz number is 7×10^{-6}, corresponding to a magnetic field strength of 0.13 mT. This is only one-third of the strength of the poloidal field at the core-mantle boundary and can, therefore, be ruled out as a characteristic value for the magnetic field inside the core.

5.4 Jupiter's dynamo

Jupiter's magnetic field is similar to the Earth's field in terms of the ratio of dipole to higher multipole moments and the dipole tilt relative to the rotation axis, but is about 10 times stronger at the surface than Earth's field (Connerney 1981). The internal heat flow is well known, so that we can compare the prediction for the magnetic field strength from our scaling laws with the observed field strength. One complication is that the dynamos in the metallic hydrogen core of these planets are powered by secular cooling, that is, the sources of buoyancy are volumetrically distributed whereas in our numerical model they are located at the inner boundary. To account for this, we replace the inner radius r_i in eq. (48), which refers actually to the radius at which the heat enters, by an effective value of $r_o/2$ and set $D = r_o/2$, thus replacing the term in parenthesis by $g_o Q_B/(4\pi r_o)$. The outer limit of the dynamo region is in the pressure range $P \approx$ 130–160 GPa (Guillot *et al.* 2005), which corresponds to approximately 0.83 of the planetary radius. Probably most of the observed internal heat flow of 5.4 Wm^{-2} (Guillot *et al.* 2005) originates in the deep interior. The factor for conversion of heat flux into buoyancy flux, $\alpha/c_p = \rho/P\,(\partial logT/\partial logP)_S$ is approximately 10^{-9} kg J^{-1} in the dynamo region (Guillot 1999), which leads to a buoyancy flux of 3×10^8 kg s^{-1}. From this and $r_o = 58\,000$ km, $g_o = 30$ m s^{-2} and $\rho = 1400$ kg m^{-3} we obtain a magnetic field strength of 8 mT. The mean dipole field strength of Jupiter, downward continued to r_o, is 1.1 mT. Applying a factor of 6–7 between the field strength inside the dynamo region and that of the dipole on its the outer boundary, as discussed above, leads to an estimate for the internal field in good agreement with the prediction from the scaling law.

A characteristic velocity in Jupiter's dynamo region of approximately 2 cm s^{-1} is predicted from eq. (47), that is, 20 times faster than in the Earth's core. Details of the secular variation of Jupiter's

magnetic field are not known, but Russell *et al.* (2001) determined a change of the dipole tilt by 0.5° between 1975 and 2000. The change of tilt of the Earth's dipole in 25 yr intervals during the time period 1690–2005 according to the ufm1 (Bloxham & Jackson 1992) and IGRF (http://swdcwww.kugi.kyoto-u.ac.jp/igrf) models was highly variable, between zero and 1.3°. The average value of 0.4° change in 25 yr is comparable to the rate of change of Jupiter's dipole. Assuming that the changing tilt represents predominantly magnetic field advection in both cases, the magnitude of the large-scale flow component that advects the dipole field must differ in proportion of the radii of the dynamo regions in Jupiter and Earth, that is, be larger in Jupiter by a factor of about 17, in good agreement with the predicted difference of the rms velocity.

5.5 Magnetic fields of other planets

A similar calculation for Saturn, whose dynamo region is bounded to approximately 60 per cent of the planetary radius, predicts an internal magnetic field strength of about 4 mT, when we assume that roughly one-half of the observed internal heat flow originates in the metallic and deeper layers. In comparison, the observed dipole field projected to the outer boundary of the dynamo region has a mean strength of only 0.15 mT. Either our scaling law fails in the case of Saturn, or the ratio of the internal field strength to the external dipole strength is much larger than in the case of Jupiter and Earth. The very high degree of axisymmetry of Saturn's field (Acuña *et al.* 1981) suggest that the dynamo could be of a different type compared to that in the other two planets. It has been suggested that ongoing fractionation and downward segregation of helium in the outer parts of the metallic region provides energy to drive the dynamo but also leads to a stably stratified conducting region, which may have a strong influence on the magnetic field escaping through this layer (Stevenson 1982a,b). Wicht (personal communication, 2005) found that a dynamo model driven by differential rotation between the inner and outer boundaries of a spherical fluid shell can have a highly axisymmetric external magnetic field. In his models, the ratio $b_{\rm dip}$ is approximately 15.

The magnetic fields of Uranus and Neptune have a strongly tilted dipole that does not dominate compared to higher multipole components, so that our scaling laws do not apply. The relatively low conductivity in the dynamo regions of these planets implies a low Elsasser number Λ. Simple models of dynamos with non-axial dipoles (Aubert & Wicht 2004) suggest that in this case the magnetic field saturates at low values of Λ. Stanley & Bloxham (2004) present a dynamo model where convection is restricted to a relatively thin region overlying a stable fluid layer and which reproduces the observed spectral characteristic of the magnetic field of Uranus and Neptune.

Mercury's field is probably dipolar, but very weak compared to that of the other planets. Could this be due to a low buoyancy flux driving Mercury's dynamo? Because neither the heat flux nor a characteristic velocity in the core are known, we use the magnetic field strength to estimate the buoyancy flux. The size of the inner core is unknown. The scaling laws for thin-shell dynamos or for dynamos with a very small inner core probably differ from those derived here, therefore, we assume a fluid shell of moderate thickness $D = 1000$ km. Arguing along the same lines that we applied to other planets, we estimate from the magnetic field strength of 0.3 μT at the planetary surface a characteristic field strength in the core of 5 μT, which corresponds to a Lorentz number $Lo \approx 4 \times 10^{-5}$. The Rayleigh number obtained from eq. (33) is $Ra_Q^* \approx 10^{-13}$. While this value is similar to our estimate for the Earth, the smaller size and the much slower rotation ($\Omega \approx 1.3 \times 10^{-6}$) make the absolute value of the buoyancy flux inconceivably small, of the order 0.01 kg s^{-1}. The magnetic Reynolds number obtained with eqs (36) and (30) would be around 4, insufficient for sustaining a dynamo. Clearly, weak driving of the dynamo (alone) cannot explain the weakness of Mercury's magnetic field and the explanation may lie in some intrinsic difference between dynamos with a moderate size of the inner core, as in case of the Earth, and dynamos with a very large inner core (Stanley *et al.* 2005) or a very small one (Heimpel *et al.* 2005).

6 DISCUSSION AND CONCLUSIONS

Our analysis shows that dynamos which generate a dipole-dominated magnetic field are preferred when rotational effects on the flow are strong. A strong influence of inertia favours dynamos characterized by weaker magnetic fields dominated by higher multipole components (see also Sreenivasan & Jones 2006). They are less efficient in the sense that they require a higher magnetic Reynolds number. This explains the earlier finding that dipolar dynamos at realistic values of the magnetic Prandtl number $Pm \ll 1$ require also very low values of the Ekman number. Pm can be considered as the ratio of the magnetic Reynolds number to the hydrodynamic Reynolds number. In order to exceed the critical value of Rm, which we find consistently to be approximately 50 for dipolar dynamos, the hydrodynamic Reynolds number has to be very large at low Pm. To 'fight' the associated inertial effects, the rotational constraints must be made very strong, that is, the Ekman number low. If the scaling law for the minimum magnetic Prandtl number at which a dipolar dynamo is possible (eq. 25) remains valid to earth-like values of the Ekman number, the minimum magnetic Prandtl number would be of order 10^{-8}, well below the estimated core values of $Pm \approx 10^{-6}$. Without rotational effects, dynamos are more difficult to obtain at $Pm \ll 1$ (Schekochihin *et al.* 2004; Ponty *et al.* 2005).

In all available numerical geodynamo models several control parameters are far from earth values, mainly because it is not possible to run simulations at the appropriate low values of the viscosity and thermal diffusivity. Whether or not the difference is important depends on the role that diffusive processes play in these models. In the present study we have varied each of the key parameters (E, Pm, Pr, Ra^*) over at least two orders of magnitude and found that within our parameter range the characteristic dynamo properties are at most weakly dependent on the diffusivities. Defining the non-dimensional properties (Rossby number, Lorentz number, modified Nusselt number) and the key control parameter (modified Rayleigh number) in a way that makes them independent of any diffusivity has been very helpful to demonstrate this point. It allows to collapse the data from a substantial range of the 4-D parameter space into a simple dependence on the modified Rayleigh number, at least as a first approximation.

While a simple power law relating the modified Nusselt number to the modified Rayleigh number gives an excellent fit to our results, in the cases of the characteristic flow velocity (Rossby number) and magnetic field strength (Lorentz number) we cannot rule out an additional dependence on other parameters, in particular the magnetic Prandtl number. Although the suggested dependence is weak, it poses a serious problem. Given the large range of extrapolation over five orders of magnitude from our models to planetary values of Pm, the results obtained from the scaling laws with or without a dependence on Pm differ substantially. It is difficult to verify or reject such a dependence based on the numerical results alone;

furthermore, it may change outside the parameter range covered by the model calculations. In the case of scaling the magnetic dissipation time Christensen & Tilgner (2004) tried to resolve the ambiguity by invoking results from the Karlsruhe dynamo experiment (Müller *et al.* 2004), which do not support an additional dependence on the magnetic Prandtl number. Because the flow is strongly constrained in this experiment it cannot be used to test our scaling for the Rossby number and would be of limited help to test the Lorentz number scaling, which through eq. (32) is related to that of the Rossby number. Future dynamo experiments with unconstrained flow in rotating spherical containers (Lathrop *et al.* 2001; Cardin *et al.* 2002) will be better suited to investigate a possible dependence of the magnetic field strength on the diffusion constants or rotation rate.

The rationale for our scaling of the magnetic field strength is not based on the MAC balance, as most previously suggested heuristic scaling laws are (Stevenson 1979,2003; Starchenko & Jones 2002), but on the energetics of the dynamo. These two approaches are not exclusive. Energy is necessarily conserved, but the MAC balance could be satisfied as well. The large variability of the Elsasser number suggests that this is not generally the case, but the Elsasser number may not be adequate to describe the force balance. Therefore, we have calculated the enstrophy budget of several of our models, which eliminates from consideration those parts of the Coriolis or Lorentz forces that are balanced by pressure gradients. The results suggest that the Coriolis and buoyancy forces are globally in balance, however, the total contribution of the Lorentz force is again quite variable. A drawback of studying enstrophy is that it emphasizes the balance for small scales in the flow more strongly than that on large scales. We conclude that the force balance in our models is rather complex. It cannot be understood in terms of a simple MAC balance, in the sense of a close agreement of the mean values of the forces in questions or of their contribution to the enstrophy budget. Whether a MAC balance holds in planetary cores, or in what sense it holds, must be considered an open question. Inertial and viscous forces can play a role provided the flow contains energy at sufficiently short length scales. These scales may be too small for being relevant to the magnetic induction process, however, by inverse cascading of energy (by Reynolds stresses) they can strongly influence the larger-scale flow.

There are some remarkable differences between previously suggested scaling laws and ours. Our scaling of the velocity (eq. 47) is only weakly dependent on the rotation frequency, $U \sim \Omega^{-1/5}$ compared to $U \sim \Omega^{-1/2}$ in case of a MAC balance (Starchenko & Jones 2002; Stevenson 2003). We note that this result depends crucially on the exact value of the exponent in the power law relating the Rossby number to the modified Rayleigh number (eq. 30). A value of 0.5 instead of our preferred 0.4 leads to the MAC balance result. The scaling law for the magnetic field (eq. 48) is completely independent of the rotation rate and the electrical conductivity σ. Under the magnetostrophic assumption it is usually suggested that B is independent of the buoyancy flux Q_B and varies as $B \sim \Omega^{1/2}\sigma^{-1/2}$, based on a balance of Lorentz and Coriolis force expressed by an Elsasser number of order one (e.g. Stevenson 2003). With the different approach of balancing Lorentz force and buoyancy and assuming a fixed length scale δ_B of the magnetic field, Starchenko & Jones (2002) suggested a dependence $B \sim \Omega^{1/4} Q_B^{1/4}$. We would obtain the same result following the reasoning given in Section 3.4 when we assume an exponent of 1/2 instead of 2/5 in the power law for the Rossby number.

Estimates for the buoyancy flux in the Earth's core, which presumably is mostly the compositional flux related to inner core growth, are important because they put constraints on the age of the Earth's inner core, the necessity for heat-producing elements such as ^{40}K in the core, and the degree to which convection in the Earth's mantle is driven by heating from the core (Labrosse 2002; Buffett 2003). Our estimate of 3×10^4 kg s^{-1} based on the scaling of the characteristic flow velocity is in good agreement with results from scaling laws for the zonal flow component alone (Aurnou *et al.* 2003; Aubert 2005). Furthermore, the estimate for the power consumption of the geodynamo of 0.2–0.5 TW obtained from a scaling law of the Ohmic dissipation time (Christensen & Tilgner 2004) can be translated using eqs (20) and (21) into a buoyancy flux of $1.3-3.3 \times 10^4$ kg s^{-1}, in agreement with the other estimates. The rather low values imply that the inner core grows slowly and started to nucleate early in the Earth's history.

Our predictions for the magnetic field strength in the Earth's and Jupiter's core agree well with estimates based on the observed field and reasonable assumptions on the ratio between internal and external field. This is also true for other suggested scaling laws based on simple force-balance arguments. The magnetic fields of Mercury and to lesser degree of Saturn pose a problem for our scaling laws, but also for the other approaches. Mercury and Saturn probably represent different classes of dynamos, whereas Earth and Jupiter basically fall into the same category. The advantage of our scaling laws is that they are based on a fair number of actual dynamo simulations, even if these have been performed at parameters values different from the planetary ones. A drawback is that we can only give a partial theoretical basis for our scaling laws and cannot exclude slightly more complex dependencies that would lead to quite different results when applied to the Earth. However, the fact that Earth and Jupiter fit well with our simple scaling laws supports the view that the present numerical dynamo models operate indeed in the same regime as these two planetary dynamos do. This enhances our confidence that dynamo models are a useful tool to understand not only the bulk properties of planetary magnetic fields but also details of its spatial and temporal behaviour.

NOTE ADDED IN PROOF

Continuing the simulation at the lowest Ekman number of 10^{-6} for another 14 advection times suggested that it has not reached its final equilibrium. Its data should not be used. Omitting this case does not affect any of the scaling laws.

ACKNOWLEDGMENTS

This project is part of the Priority Program *Geomagnetic Variations* of the Deutsche Forschungsgemeinschaft. We are grateful for support through grant Ch77/11.

REFERENCES

Acuña, M.H., Connerney, J.E.P. & Ness, N.F., 1981. Topology of Saturns main magnetic field, *Nature,* **292,** 721–726.

Aubert, J., 2005. Steady zonal flows in spherical shell fluid dynamos, *J. Fluid Mech.,* **542,** 53–67.

Aubert, J., Brito, D., Nataf, H.-C., Cardin, P. & Masson, J.-P., 2001. A systematic experimental study of rapidly rotating spherical convection in water and liquid gallium, *Phys. Earth planet. Int.,* **128,** 51–74.

Aubert, J. & Wicht, J., 2004. Axial versus equatorial dipolar dynamo models with implications for planetary magnetic fields, *Earth planet. Sci. Lett.,* **221,** 409–419.

Aurnou, J., Andreadis, S., Zhu, L.X. & Olson, P., 2003. Experiments on convection in Earth's core tangent cylinder, *Phys. Earth planet. Int.,* **212,** 119–134.

Bloxham, J., 2000a. The effect of thermal core-mantle interactions on the paleomagnetic secular variation, *Phil. Trans R. Soc. Lond.,* A, **358,** 1171–1179.

Bloxham, J., 2000b. Sensitivity of the geomagnetic axial dipole to thermal core-mantle interactions, *Nature,* **405,** 63–65.

Bloxham, J., 2002. Time-independent and time-dependent behaviour of high-latitude flux bundles at the core-mantle boundary, *Geophys. Res. Lett.,* **29,** 1854, doi: 10.1029/2001GL014543.

Bloxham, J., Gubbins, D., Jackson, A., 1989. Geomagnetic secular variation, *Phil. Trans R. Soc. Lond.,* A, **329,** 415–502.

Bloxham, J. & Jackson, A., 1992. Time-dependent mapping of the magnetic field at the core-mantle boundary, *J. geophys. Res.,* **97,** 19 537–19 563.

Braginsky, S.I., 1975. Nearly axisymmetric model of the hydromagnetic dynamo of the Earth I., *Geomag. Aeron.,* **15,** 122–128.

Buffett, B.A., 2002. Estimates of heat flow in the deep mantle based on the power requirements for the geodynamo, *Geophys. Res. Lett.,* **29,** doi:10.1029/2001GL014649.

Buffett, B.A., 2003. The thermal state of the Earth's core, *Science,* **299,** 1675–1677.

Buffett, B.A., Huppert, H.E., Lister, J.R. & Woods, A.W., 1996. On the thermal evolution of the Earth's core, *J. geophys. Res.,* **101,** 7989–8006.

Busse, F.H., Grote, E. & Tilgner, A., 1998. On convection driven dynamos in rotating spherical shells, *Studia Geoph. et Geod.,* **42,** 1–6.

Cardin, P., Brito, D., Jault, D., Nataf, H.-C. & Masson, J.-P., 2002. Towards a rapidly rotating liquid sodium dynamo experiment, *Magnetohydrodynamics,* **38,** 177–189.

Christensen, U.R., 2002. Zonal flow driven by strongly supercritical convection in rotating spherical shells, *J. Fluid Mech.,* **470,** 115–133.

Christensen, U., Olson, P. & Glatzmaier, G.A., 1998. A dynamo model interpretation of geomagnetic field structures, *Geophys. Res. Lett.,* **25,** 1565–1568.

Christensen, U., Olson, P. & Glatzmaier, G.A., 1999. Numerical modelling of the geodynamo: a systematic parameter study, *Geophys. J. Int.,* **138,** 393–409.

Christensen, U.R. & Olson, P., 2003. Secular variation in numerical geodynamo models with lateral variations of boundary heat flow, *Phys. Earth planet. Int.,* **138,** 39–54.

Christensen, U.R. & Tilgner, A., 2004. Power requirement of the geodynamo from ohmic losses in numerical and laboratory dynamos, *Nature,* **439,** 169–171.

Connerney, J.E.P., 1981. The magnetic field of Jupiter: a generalized inverse approach, *J. geophys. Res.,* **86,** 7679–7693.

Glatzmaier, G.A., 1984. Numerical simulations of stellar convective dynamos. I. the model and method, *J. Comput. Phys.,* **55,** 461–484.

Glatzmaier, G.A. & Roberts, P.H., 1995. A three-dimensional convective dynamo solution with rotating and finitely conducting inner core and mantle. *Phys. Earth planet. Inter.,* **91,** 63–75.

Glatzmaier, G.A. & Roberts, P.H., 1995b. A three-dimensional self-consistent computer simulation of a geomagnetic field reversal, *Nature,* **377,** 203–209.

Glatzmaier, G.A., Coe, R.S., Hongre, L., & Roberts, P.H., 1999. The role of the Earth's mantle in controlling the frequency of geomagnetic reversals, *Nature,* **401,** 885–890.

Grote, E., Busse, F.H., Tilgner, A., 1999. Convection-driven quadrupolar dynamos in rotating spherical shells, *Phys. Rev. E,* **60,** 5025–5028.

Grote, E., Busse, F.H. & Tilgner, A., 2000. Regular and chaotic spherical shell dynamos. *Phys. Earth planet. Int.,* **117,** 259–272.

Gubbins, D., 2001. The Rayleigh number for convection in the Earth's core, *Phys. Earth planet. Int.,* **128,** 3–12.

Gubbins, D., Alfè, D., Masters, G., Price, G.D. & Gillan, M.J., 2004. Gross thermodynamics of 2-component core convection, *Geophys. J. Int.,* **157,** 1407–1414.

Guillot, T., 1999. A comparison of the interiors of Jupiter and Saturn, *Planet Space Sci.,* **47,** 1183–1200.

Guillot, T., Stevenson, D.J., Hubbard, W.B. & Saumon, D., 2005. The interior of Jupiter, in: *Jupiter*, pp. 35–37, eds Bagenal, F., Towling, T.E. & McKinnon, W.B., Cambridge Univ. Press, Cambridge.

Heimpel, M.H., Aurnou, J.M., Al-Shamali, F.M. & Gomez Perez, N., 2004. A numerical study of dynamo action as a function of spherical shell geometry, *Earth planet. Sci. Lett.,* **236,** 542–557.

Hulot, G., Eymin, C., Langlais, B., Mandea, M. & Olsen, N., 2002. Small-scale structure of the geodynamo inferred from Oersted and Magsat satellite data, *Nature,* **416,** 620–623.

Ishihara, N. & Kida, S., 2002. Dynamo mechanism in a rotating spherical shell: competition between magnetic field and convection vortices, *J. Fluid Dyn.,* **465,** 1–32.

Jones, C.A., Soward, A.M. & Mussa, A.I., 2000. The onset of thermal convection in a rapidly rotating sphere, *J. Fluid Mech.,* **405,** 157–179.

Kageyama, A., Sato, T. & the Complexity Simulation Group, 1995. Computer simulation of a magnetohydrodynamic dynamo. *Phys. Plasma,* **2,** 1421–1431.

Kono, M. & Roberts, P.H., 2002. Recent geodynamo simulations and observations of the geomagnetic field, *Rev. Geophys.,* **40,** 1013, doi:10.1029/2000RG000102.

Kuang, W. & Bloxham, J., 1997. An Earth-like numerical dynamo model. *Nature,* **389,** 371–374.

Kuang, W. & Bloxham, J., 1999. Numerical modeling of magnetohydrodynamic convection in a rapidly rotating spherical shell: weak and strong field dynamo action, *J. Comput. Phys.,* **153,** 51–81.

Kutzner, C. & Christensen, U.R., 2000. Effects of driving mechanisms in geodynamo models, *Geophys. Res. Lett.,* **27,** 29–32.

Kutzner, C. & Christensen, U.R., 2002. From stable dipolar towards reversing numerical dynamos, *Phys. Earth planet. Int.,* **131,** 29–45.

Kutzner, C. & Christensen, U.R., 2004. Simulated geomagnetic reversals and preferred virtual geomagnetic pole paths, *Geophys. J. Int.,* **157,** 1105–1118.

Labrosse, S., 2002. Hotspots, mantle plumes and core heat loss, *Earth planet Sci. Lett.,* **199,** 147–156.

Labrosse, S., Poirier, J.P. & LeMouël, J.L., 2001. The age of the inner core, *Earth planet. Sci. Lett.,* **190,** 111–123.

Lathrop, D.P., Shew, W.L. & Sisan, D.R., 2001. Laboratory experiments on the transition to MHD turbulence, *Plasma Phys. Control. Fusion,* **43,** A151–A160.

Loper, D.E., 1978. Some thermal consequences of the gravitationally powered dynamo, *J. geophys. Res.,* **83,** 5961–5970.

Müller, U., Stieglitz, R. & Horanyi, S., 2004. A two-scale hydromagnetic dynamo experiment, *J. Fluid. Mech.,* **498,** 31–71.

Nimmo, F., Price, G.D., Brodholt, J. & Gubbins, D., 2004. The influence of potassium on core and geodynamo evolution, *Geophys. J. Int.,* **156,** 363–376.

Olson, P. & Aurnou, J., 1999. A polar vortex in the Earth's core, *Nature,* **404,** 170–173.

Olson, P., Christensen, U.R. & Glatzmaier, G.A., 1999. Numerical modeling of the geodynamo: Mechanisms of field generation and equilibration, *J. geophys. Res.,* **104,** 10 383–10 404.

Olson, P. & Christensen, U.R., 2002. The time-averaged magnetic field in numerical dynamos with non-uniform boundary heat flow, *Geophys. J. Int.,* **151,** 809–823.

Ponty, Y., Mininni, P.D., Montgomery, D.C., Pinton, J.F., Politano, H. & Pouquet, A., 2005. Numerical study of dynamo action at low magnetic Prandtl numbers, *Phys. Rev. Lett.,* **94,** 164502.

Rotvig, J. & Jones, C.A., 2002. Rotating convection-driven dynamos at low Ekman number, *Phys. Rev. E,* **66,** 056308.

Russell, C.T., Yu, Z.J., Khurana, K.K. & Kivelson, M.G., 2001. Magnetic field changes in the inner magnetosphere of Jupiter, *Adv. Space Res.,* **28,** 897–902.

Schekochihin, A.A., Cowley, S.C., Maron, J.L. & McWilliams, J.C., 2004. Critical magnetic Prandtl number for small-scale dynamo, *Phys. Rev. Lett.,* **92,** 054502.

Schekochihin, A.A., Haugen, N.E.L., Brandenburg, A., Cowley, S.C., Maron, J.L. & McWilliams, J.C., 2005. The onset of a small-scale

turbulent dynamo at low magnetic Prandtl numbers, *Astrophys. J. Lett.,* **625,** 115–118.
Simitev, R. & Busse, F.H., 2005. Prandtl-number dependence of convection-driven dynamos in rotating spherical fluid shells, *J. Fluid Mech.,* **532,** 365–388.
Starchenko, S.V. & Jones, C.A., 2002. Typical velocities and magnetic field strengths in planetary interiors, *Icarus,* **157,** 426–435.
Stanley, S. & Bloxham, J., 2004. Convective-region geometry as the cause of Uranus' and Neptune's unusual magnetic fields, *Nature,* **428,** 151–153.
Stanley, S., Bloxham, J., Hutchison, W.E. & Zuber, M., 2005. Thin shell dynamo models consistent with Mercury's weak observed magnetic field, *Earth planet. Sci. Lett.,* **234,** 341–353.
Sreenivasan, B. & Jones, C., 2006. The role of inertia in the evolution of spherical dynamos, *Geophys. J. Int.,* **164,** 467–476.
Stevenson, D.J., 1979. Turbulent thermal convection in the presence of rotation and a magnetic field: a heuristic theory, *Geophys. Astrophys. Fluid Dyn.,* **12,** 139–169.
Stevenson, D.J., 1982a. Interiors of the giant planets, *Annu. Rev. Earth Planet. Sci.,* **10,** 257–295.
Stevenson, D.J., 1982b. Reducing the non-axisymmetry of a planetary dynamo and an application to Saturn, *Geophys. Astrophys. Fluid Dyn.,* **21,** 113–127.
Stevenson, D.J., 2003. Planetary magnetic fields, *Earth planet. Sci. Lett.,* **208,** 1–11.
Stieglitz R. & Müller, U., 2001. Experimental demonstration of the homogeneous two-scale dynamo. *Phys. Fluids,* **13,** 561–564.
Takahashi, F., Matsushima, A. & Honkura, Y., 2005. Simulation of a quasi-Taylor state geomagnetic field including polarity reversals on the Earth simulator, *Science,* **309,** 459–461.
Tilgner, A. & Busse, F.H., 1997. Final amplitude convection in rotating spherical fluid shells. *J. Fluid Mech.,* **332,** 359–376.
Tilgner, A., 1999. Spectral methods for the simulation of incompressible flow in spherical shells. *Int. J. Numer. Meth. Fluids,* **30,** 713–724.
Voorhies, C.V., 1986. Steady flows at the top of the Earth's core derived from geomagnetic field models, *J. geophys. Res.,* **91,** 12 444–12 466.
Wicht, J., 2002. Inner-core conductivity in numerical dynamo simulations, *Phys. Earth planet. Int.,* **132,** 281–302.
Zatman, S. & Bloxham, J., 1997. Torsional oscillations and the magnetic field inside the Earth's core, *Nature,* **388,** 760–763.

APPENDIX A: POWER GENERATION

Here we show that the flux-based modified Rayleigh number is a measure for the power P generated by the buoyancy forces. Denoting the time average by angular brackets and using non-dimensional quantities throughout, we write the averaged eq. (21) as

$$P = Ra^* \int_{r_i}^{r_o} \frac{r}{r_o} \left(\int_S \langle u_r T \rangle \, dS \right) dr, \tag{A1}$$

The surface integral in (A1) is equivalent to the non-dimensional advected heat flux $Q_a(r)$ through a spherical surface at radius r. In general Q_a will vary with r. The conservation of the total (advective and diffusive) heat flux Q can be written by taking the surface integral form of (4) and averaging in time:

$$\frac{dQ}{dr} = \frac{d}{dr} \left(Q_a - E_\kappa \int_S \left\langle \frac{\partial T}{\partial r} \right\rangle dS \right) = 0. \tag{A2}$$

Q, Q_a and P refer here to the time-average values. The total heat flow is constant with radius and by definition equal to the heat flow in a conductive state times the Nusselt number. Using square brackets for the mean on a spherical surface, we can write:

$$Q_a = 4\pi r_i r_o Nu E_\kappa + E_\kappa 4\pi r^2 \frac{d \langle [T] \rangle}{dr}, \tag{A3}$$

Combining (A1) and (A3) we obtain:

$$P = 4\pi Ra^* E_\kappa \left(Nu \int_{r_i}^{r_o} r_i r \, dr + \int_{r_i}^{r_o} \frac{r^3}{r_o} \frac{\langle [T] \rangle}{dr} \, dr \right). \tag{A4}$$

The second integral is negative. It is of order one and, therefore, small compared to the first term in parenthesis when $Nu \gg 1$. The precise result at moderate values of the Nusselt number depends on the radial distribution of the temperature gradient, or in other words, on the partitioning of conductive and advective heat transport with radius. To obtain an approximate expression we evaluate the second integral for a purely conductive temperature gradient $dT/dr = -r_i r_o / r^2$, which assumes that the ratio of advective to conductive heat flow does not change with r:

$$P \approx 2\pi Ra^* E_\kappa \, (Nu - 1) r_i \left(r_o^2 - r_i^2 \right). \tag{A5}$$

Writing the result in terms of the ratio $\eta = r_i / r_o$ and the heat-flux-based modified Rayleigh number we obtain:

$$P \approx 2\pi \eta \frac{1+\eta}{(1-\eta)^2} Ra_Q^* \approx 7.01 Ra_Q^*. \tag{A6}$$

We have recorded the power in our selected dynamo models by evaluating and time averaging the integral (21) and plot it in Fig. A1 against the Rayleigh number Ra_Q^*. The points fall almost perfectly on the line given by eq. (A6). Although the radial temperature distribution certainly deviates from the conductive one, this appears to be of little consequence. However, the good agreement holds only for fully developed convection with $Nu > 2$. In cases with smaller values of the Nusselt number we find that the power is below the value given by eq. (A6).

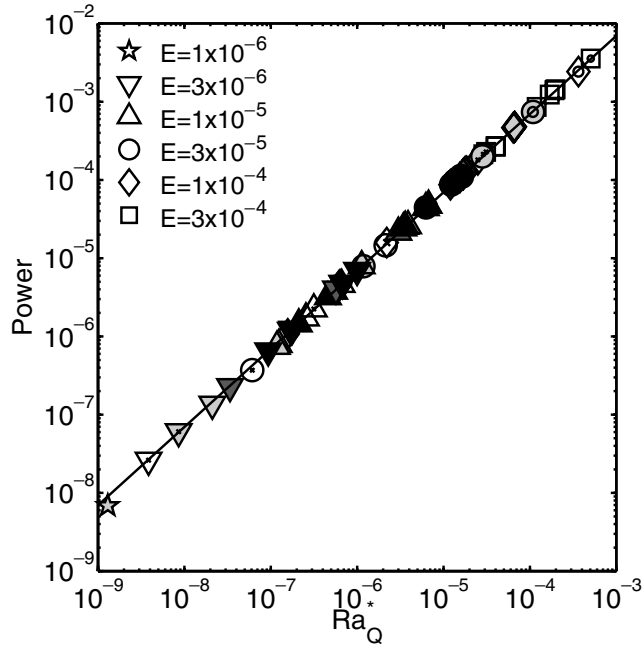

Figure A1. Power versus modified flux-based Rayleigh number. Symbols as in Fig. 3. The slope of the fitting line has been set to one, the constant obtained from a best fit is 6.97.

Available online at www.sciencedirect.com
ScienceDirect
Physics of the Earth and Planetary Interiors 160 (2007) 143–156
PHYSICS OF THE EARTH AND PLANETARY INTERIORS
www.elsevier.com/locate/pepi

Detecting thermal boundary control in surface flows from numerical dynamos

Julien Aubert [a,*], Hagay Amit [b], Gauthier Hulot [b]

[a] *Dynamique des Systèmes Géologiques, Institut de Physique du Globe de Paris, 4 place Jussieu, 75231 Paris Cedex 5, France*
[b] *Géomagnétisme, Institut de Physique du Globe de Paris, France*

Received 29 June 2006; received in revised form 30 October 2006; accepted 6 November 2006

Abstract

The geomagnetic field and secular variation exhibit asymmetrical spatial features which are possibly originating from an heterogeneous thermal control of the Earth's lower mantle on the core. The identification of this control in magnetic data is subject to several difficulties, some of which can be alleviated by the use of core surface flow models. Using numerical dynamos driven by heterogeneous boundary heat flux, we confirm that within the parameter space accessible to simulations, time average surface flows obey a simple thermal wind equilibrium between the Coriolis and buoyancy forces, the Lorentz, inertial and viscous forces playing only a secondary role, even for Elsasser numbers significantly larger than 1. Furthermore, we average the models over the duration of three vortex turnovers, and correlate them with a longer time average which fully reveals the signature of boundary heterogeneity. This allows us to quantify the possibility of observing mantle control in core surface flows averaged over a short time period. A scaling analysis is performed in order to apply the results to the Earth's core. We find that three vortex turnovers could represent between 100 and 360 years of Earth time, and that the heat flux heterogeneity at the core-mantle boundary could be large enough to yield an observable signature of thermal mantle control in a time average core surface flow within reach of the available geomagnetic data.

Keywords: Earth; Core; Dynamo; Geodynamo; Flows; Geomagnetism; Mantle; Thermal; Control; Coupling

1. Introduction

Over the last two decades many studies have been carried out to investigate possible intrinsically asymmetric spatial properties within the Earth's magnetic field. On the historical time scale, the secular variation (SV) of this field is quite heterogeneous (e.g. Bloxham and Gubbins, 1985; Jackson et al., 2000; Hulot et al., 2002), with a more active Atlantic hemisphere and a quieter Pacific hemisphere, and magnetic flux patches seemingly locked at remarkably stable spatial positions (Bloxham, 2002). It has also been suggested that the time average paleomagnetic (Gubbins and Kelly, 1993; Johnson and Constable, 1995) and archeomagnetic (Constable et al., 2000; Korte et al., 2005) fields show similar departures from axisymmetry as the modern historical field, although the robustness of such conclusions has been questioned by several authors (McElhinny et al., 1996; Carlut and Courtillot, 1998; Hongre et al., 1998) and is indeed difficult to assess without appropriate statistical tools (Hulot and Bouligand, 2005; Bouligand et al., 2005; Khokhlov et al., 2006).

The physical properties of the Earth's liquid core are however spatially homogeneous, and were the

* Corresponding author. Tel.: +33 144274796.
E-mail address: aubert@ipgp.jussieu.fr (J. Aubert).
URL: www.ipgp.jussieu.fr/~aubert (J. Aubert).

0031-9201/$ – see front matter © 2006 Elsevier B.V. All rights reserved.
doi:10.1016/j.pepi.2006.11.003

core-mantle boundary to impose homogeneous boundary conditions, no symmetry-breaking properties should arise in the time average behavior of the magnetic field created by the geodynamo, except possibly equatorial symmetry breaking properties which may arise spontaneously (Hulot and Bouligand, 2005; Bouligand et al., 2005). It is, therefore, generally thought that a longitudinal asymmetric signature within the geomagnetic field should reflect some spatially heterogeneous coupling at the CMB. Various coupling mechanisms have been proposed. Thermal control by the mantle, however, remains the most obvious and has indeed received much attention in the last decades (see for instance Hide, 1970; Jones, 1977; Bloxham and Gubbins, 1987). Given typical fluid velocities and heat diffusion constants at the base of the mantle, local temperature heterogeneities are likely to remain for millions of years, i.e. much longer than any time scale of core dynamics. Seen from the mantle, the rapidly mixed core is an isothermal boundary. Temperature anomalies in the mantle therefore translate into heat-flow anomalies (a colder mantle extracting more heat from the isothermal core). Since heat flow is continuous at the CMB, the core then "sees" the mantle as prescribing a steady and heterogeneous heat flow boundary condition.

Several difficulties hamper the identification of thermal mantle control in geomagnetic data. First, the signature of boundary heterogeneity is best seen when considering time averages (for instance Olson and Christensen, 2002; Bouligand et al., 2005) because transients usually mask the signal. Unfortunately, the needed averaging time is likely longer than the available geomagnetic time series. Autocorrelation functions of the geomagnetic field (Hulot and Le Mouël, 1994; Le Huy et al., 2000) indicate indeed that the signal loses memory of itself (a necessary condition for the removal of transients) on times of the order of several hundreds of years. A second difficulty is associated with the magnetic signature of thermal mantle control itself. Numerical dynamo models with heterogeneous heat flow at the outer boundary have shown that departures from the geocentric axial dipole are weak (Olson and Christensen, 2002) and difficult to distinguish from the statistical noise (Bouligand et al., 2005). The secular variation provides a clearer signature (Christensen and Olson, 2003) but it is difficult to formulate a simple theoretical link with the structure of boundary heterogeneity.

Core flows can be inverted at the core-mantle boundary (CMB) of the Earth from the historical magnetic field and SV observations (recently Hulot et al., 2002; Amit and Olson, 2004). Summarizing all the available information into a fluid dynamical framework, they tend to suffer less from the difficulties mentioned above. Their autocorrelation time is shorter (Le Huy et al., 2000), because the advection of momentum is much more turbulent than the advection of the magnetic field, as a result of the large ratio of magnetic diffusivity to viscosity in the Earth's core. Furthermore, a simple thermal wind theory is expected to connect them with CMB heat flow hetereogeneities (Bloxham and Gubbins, 1987; Bloxham and Jackson, 1990), although questions remain concerning the role of the Lorentz force, which will be addressed in the present study. Finally, they preserve the spatial asymmetry of the original data (Amit and Olson, 2006): the Atlantic/Pacific dichotomy, as well as stable vortices (specifically in the southern hemisphere). In addition heterogeneity is also present between the northern and southern hemispheres, with significant westward drift at mid-latitude of the southern hemisphere but nearly no drift at mid-latitude of the northern hemisphere (Pais and Hulot, 2000; Amit and Olson, 2006). In this line of work, several studies compared core flows models with the time average outcome of numerical convection models driven by heterogeneous thermal boundary conditions, especially focusing on the interaction of convection structures with the boundary heat flow pattern (Zhang and Gubbins, 1992, 1993; Gibbons and Gubbins, 2000).

Previous studies have shown that core flows also need time-averaging to reveal the mantle signature. A central question remains: how long should the time-average be in order to remove enough of the transients? We anticipate that this should be shorter than for the magnetic field, and the first goal of the present study is precisely to assess this. Amit and Olson (2006) used the historical geomagnetic SV data to infer a time-average flow model for the period 1840–1990. Is such an averaging interval enough to reveal the core flow driven by boundary heterogeneity? To address this question we focus on self-consistent numerical models of convective dynamo action with heterogeneous boundary heat flow, and produce two types of flows: snapshots, and averages over intermediate intervals which we argue would cover 100–360 years of real Earth time once properly rescaled. These flows are compared to the actual steady flow computed by averaging over the entire simulation time. A statistical analysis of the correlation coefficient between the intermediate flows and the steady flow then provides us with a quantitative way to assess the likeliness of revealing mantle control in time-average core surface flows. This study also provides an opportunity to investigate core surface fluid flows, in very much the same way as Olson and Christensen (2002) investigated the magnetic field. Finally it makes it possible to discuss more quantitatively the possibility that certain robust fea-

tures of SV inversion core flows could indeed be due to thermal control from the mantle.

2. Numerical model

2.1. Formulation

We model thermal convection and self-sustained dynamo action in a rotating spherical shell. A spherical coordinate system (r, θ, φ) with unit vectors $(\mathbf{e}_r, \mathbf{e}_\theta, \mathbf{e}_\varphi)$ is chosen. The magnetohydrodynamic equations for the velocity $\mathbf{u}$, magnetic induction $\mathbf{B}$, temperature T and pressure P are solved for a conducting and convecting Boussinesq fluid within a spherical shell between radii r_i and r_o, the aspect ratio r_i/r_o being fixed to 0.35 as for the liquid outer core of the Earth. The shell is rotating about the $\mathbf{e}_z$ axis of rotation. We adopt the dimensionless form chosen by Christensen and Aubert (2006), with a slight modification to account for a fixed heat flux boundary condition at the outer boundary:

$$\frac{\partial \mathbf{u}}{\partial t} + \mathbf{u}\cdot\nabla\mathbf{u} + 2\mathbf{e}_z \times \mathbf{u} + \nabla P = Ra_\kappa \frac{\mathbf{r}}{r_o} T + (\nabla + \mathbf{B}) \times \mathbf{B} + E\nabla^2\mathbf{u} \quad (1)$$

$$\frac{\partial \mathbf{B}}{\partial t} = \nabla \times (\mathbf{u} \times \mathbf{B}) + E_\lambda \nabla^2 \mathbf{B} \quad (2)$$

$$\frac{\partial T}{\partial t} + \mathbf{u}\cdot\nabla T = E_\kappa \nabla^2 T \quad (3)$$

$$\nabla \cdot \mathbf{u} = 0 \quad (4)$$

$$\nabla \cdot \mathbf{B} = 0 \quad (5)$$

The inverse of the rotation rate Ω^{-1} is chosen as time scale. The length scale is the shell thickness D. The magnetic induction is scaled by $(\rho\mu)^{1/2}\Omega D$, where ρ is the fluid density and μ the magnetic permeability of the fluid. The temperature is scaled by

$$\Delta T = \frac{q_0 D}{\rho C_p \kappa} \quad (6)$$

where q_0 is the homogeneous part of the heat flux per unit surface, C_p the specific heat of the fluid and κ is the thermal diffusivity. The dimensionless parameters are the Rayleigh number Ra_κ and the thermal, magnetic and viscous Ekman numbers E_κ, E_λ and E:

$$Ra_\kappa = \frac{\alpha g_o q_0}{\rho C_p \Omega^2 \kappa} \quad (7)$$

$$E_\kappa = \frac{\kappa}{\Omega D^2} \quad (8)$$

$$E_\lambda = \frac{\lambda}{\Omega D^2} \quad (9)$$

$$E_\lambda = \frac{\nu}{\Omega D^2} \quad (10)$$

Here α is the thermal expansion coefficient, g_o the gravity at the outer boundary, λ is the magnetic diffusivity and ν is the viscosity of the fluid. The reader may be more familiar with the Prandtl and magnetic Prandtl numbers $Pr = \nu/\kappa$ and $Pm = \nu/\lambda$ which will be reported in our Table 1 of numerical simulations.

The velocity field satisfies rigid boundary conditions. The magnetic field satisfies insulating boundary conditions. Although treating the inner core as an insulator is non-physical, the influence of inner-core conductivity is indeed thought to be insignificant (Wicht, 2002). The inner boundary has a constant and uniform temperature. A spatially heterogeneous heat flow is prescribed at the outer boundary, the influence of which we wish to investigate. Following Olson and Christensen (2002) the level of this heterogeneity is quantified by the parameter

$$q^* = \frac{q_{max} - q_{min}}{2q_0} \quad (11)$$

representing half the ratio of the peak-to-peak amplitude of the heterogeneity to the average heat flux q_0.

The numerical implementation MAGIC by Johannes Wicht is used in this study (Wicht, 2002).

2.2. Numerical data set, methods and outputs

Table 1 summarizes the different numerical calculations which have been performed. Cases q00 and q06 are reproductions of cases already published in Olson and Christensen (2002). Case T1 is similar to the "tomographic" dynamo of these authors. Our choice of values for q^* is subject to several constraints. Obviously q^* is bound to zero on the low side (no mantle control), whereas, dynamo action is lost for too large values of q^* (Olson and Christensen, 2002). We show in Section 3.1 that the product $q^* Ra_\kappa$ is the main scaling parameter for the amplitude of steady, boundary-driven flow. In Section 4, we estimate the values of q^* and Ra_κ in the Earth's core and show that numerical simulations can reach Earth-like values of $q^* Ra_\kappa$. We, therefore, use lower values of Ra_κ, and higher values of q^* than in the Earth's core, while maintaining Earth-like values of $q^* Ra_\kappa$.

In most calculations the heat flow heterogeneity has been reduced to a single spherical harmonic (denoted by Y_l^m as in Olson and Christensen (2002)) to facilitate the understanding of the results. For the real Earth a more complex boundary condition should obviously be used. The heat flow heterogeneity at the CMB is poorly known, and usually assumed to be correlated with seismic shear velocity at the base of the mantle (e.g. Olson

Table 1
Set of numerical models (see text for details)

Case	Pattern	q^*	Ra_κ	E_κ	Pm	Pr	U	U_{ave}	Pe	δ	Λ	τ_{ave}/τ_u
q00	None	0	0.225	3×10^{-4}	2	1	2.14×10^{-2}	0	71.3	–	5.4	497
q01	Y_2^2	0.1	0.225	3×10^{-4}	2	1	2.15×10^{-2}	1.80×10^{-3}	71.7	0.130	5.3	213
q02	Y_2^2	0.2	0.225	3×10^{-4}	2	1	2.15×10^{-2}	2.20×10^{-3}	71.7	0.079	5.2	215
q04	Y_2^2	0.4	0.225	3×10^{-4}	2	1	2.21×10^{-2}	3.89×10^{-3}	73.7	0.069	4.7	515
q04h	Y_2^2	0.4	0.45	3×10^{-4}	2	1	3.33×10^{-2}	1.15×10^{-2}	111.2	0.088	4.5	280
q06	Y_2^2	0.625	0.225	3×10^{-4}	2	1	2.21×10^{-2}	5.56×10^{-3}	73.7	0.061	4.7	589
Pr03	Y_2^2	0.625	0.75	10^{-3}	2	0.3	7.85×10^{-2}	2.90×10^{-2}	78.5	0.087	14.9	80
hh	Y_2^2	0.625	0.675	3×10^{-4}	2	1	4.18×10^{-2}	1.68×10^{-2}	139.3	0.056	5.4	238
ll	Y_2^2	0.625	0.0315	3×10^{-5}	2	1	3.00×10^{-3}	4.59×10^{-4}	100	0.062	12.2	50
lh	Y_2^2	0.625	0.18	3×10^{-5}	1	1	8.57×10^{-3}	2.52×10^{-3}	285.7	0.032	8.1	89
q08	Y_2^2	0.8	0.225	3×10^{-4}	2	1	2.30×10^{-2}	7.83×10^{-3}	76.7	0.060	3.6	307
Y21-2	Y_2^1	0.2	0.225	3×10^{-4}	2	1	2.17×10^{-2}	1.97×10^{-3}	72.2	0.141	5.1	364
Y21-1	Y_2^1	0.625	0.225	3×10^{-4}	2	1	2.17×10^{-2}	4.31×10^{-3}	72.3	0.129	5.4	290
Y21-3	Y_2^1	0.39	0.36	3×10^{-4}	2	1	2.88×10^{-2}	5.52×10^{-3}	96.1	0.120	4.8	404
Y21-4	Y_2^1	0.625	0.36	3×10^{-4}	2	1	2.90×10^{-2}	8.18×10^{-3}	96.7	0.112	4.8	119
Y21-5	Y_2^1	0.625	0.675	3×10^{-4}	2	1	4.75×10^{-2}	1.22×10^{-3}	158	0.085	0.9	130
T2	Tomo	0.2	0.225	3×10^{-4}	2	1	2.14×10^{-2}	1.13×10^{-3}	71.3	0.091	5.4	369
T1	Tomo	0.5	0.225	3×10^{-4}	2	1	2.14×10^{-2}	2.49×10^{-3}	71.3	0.097	5.7	357
T3	Tomo	0.31	0.36	3×10^{-4}	2	1	2.85×10^{-2}	5.07×10^{-2}	95.2	0.107	4.8	144
T4	Tomo	0.4	0.36	3×10^{-4}	2	1	2.88×10^{-2}	4.70×10^{-3}	96	0.065	4.7	251
T5	Tomo	0.93	0.36	3×10^{-4}	2	1	2.98×10^{-2}	7.5×10^{-3}	99.3	0.051	3.5	287
T6	Tomo	0.5	0.675	3×10^{-4}	2	1	4.44×10^{-2}	1.1×10^{-2}	148.1	0.071	2.4	138
S1	Y_2^2	0.625	2.25×10^{-4}	3×10^{-4}	2	1	3×10^{-5}	4.31×10^{-5}	0.1	0.693	0	Steady flow
S2	Tomo	0.5	2.25×10^{-4}	3×10^{-4}	2	1	1.414×10^{-5}	1.80×10^{-5}	0.047	0.57	0	Steady flow

and Christensen, 2002): regions of the mantle with high seismic shear velocity are supposedly colder than average, extracting more heat from the core. Note that this assumption allows to prescribe the pattern, but not the amplitude, of boundary heterogeneities. Note also that explaining seismic shear velocity variations in terms of temperature alone is quite a crude assumption because it entirely ignores possible contributions from chemical heterogeneities as well as possible phase transitions above the CMB. Obviously, it would be desirable to separate thermal and chemical contributions to the seismic anomalies. Such a decomposition has in fact been tentatively introduced by Trampert et al. (2004), but only with a sub-family of spherical harmonic components. Despite the lack of information, a multi-harmonic boundary condition should be included in order to render geophysically relevant non-linear effects. In cases T1–T6 and S2 (hereafter also labelled as tomographic cases) we have used the pattern of the seismic shear velocity model of Masters et al. (2000) at the base of the mantle. This pattern contains little energy after spherical harmonic degree 8 and is therefore truncated at this degree.

In cases S1 and S2 (hereafter also labelled as subcritical cases) the Rayleigh number has been set to a value below the critical value for convection onset. The fluid is then stably stratified and the system responds only to the lateral heat flow heterogeneity imposed at the outer boundary. Obviously cases S1 and S2 are not dynamos. All other cases but case Y21-5 produce a self-sustained magnetic field with a non-reversing axial dipole. Case Y21-5 presents a weaker axial dipole with excursions. The time-average magnetic field and secular variation produced by heterogeneous dynamos has been studied in detail by Olson and Christensen (2002), Christensen and Olson (2003) and is not within the general scope of the present study. However, for a crude estimate of the relative importance of the Lorentz force in the system, we have reported in Table 1 the value of the Elsasser number defined as:

$$\Lambda = \frac{1}{E_\lambda V}\left\langle \int_V \mathbf{B}^2 \, \mathrm{d}V \right\rangle_{\tau_{\mathrm{ave}}} \tag{12}$$

Angular brackets denote time-averaging. The averaging time τ_{ave} is the duration of the run. The shell volume is denoted by V.

In this study, the root-mean-squared, time average velocity in the shell is defined as

$$U = \sqrt{\left\langle \frac{1}{V}\int_V \mathbf{u}^2 \, \mathrm{d}V \right\rangle_{\tau_{\mathrm{ave}}}} \tag{13}$$

Due to the choice of $1/\Omega$ as time scale, U is a Rossby number of the flow. To quantify the importance of thermal advection versus diffusion of heat, we introduce the classical Péclet number

$$Pe = \frac{\tilde{U}D}{\kappa} \tag{14}$$

where we generally denote with a tilde the value of variables in the dimensional world (for the present instance $\tilde{U} = U\Omega D$). In the non-dimensional world, we have therefore

$$Pe = \frac{U}{E_\kappa} \tag{15}$$

Also derived from $\tilde{U}$ is the advection time, or vortex turnover time $\tilde{\tau}_u$:

$$\tilde{\tau}_u = \frac{D}{\tilde{U}} \tag{16}$$

In the non-dimensional world, we simply have

$$\tau_u = \frac{1}{U} \tag{17}$$

Numerical models are run until energetic equilibration. The steady flow is then extracted by a further calculation averaged over a time τ_{ave} ranging from 50 (for the most demanding calculations), to 500 vortex turnover times. The vortex turnover time is the fundamental time scale for mixing, and the steady flow therefore corresponds to a well-mixed thermal state where the effect of heterogeneous heat flow boundary conditions appears.

On a shorter time interval made of fewer vortex turnovers, average flows are associated with an incomplete thermal mixing. We now attempt to estimate the vortex turnover time in the Earth's core, in a manner consistent with (13) and (16). A conventional range of values for the velocity close to the CMB is 3×10^{-4} m/s to 5×10^{-4} m/s (Bloxham and Jackson, 1991; Eymin and Hulot, 2005). According to the numerical dynamos of Christensen and Aubert (2006), surface flow magnitudes have to be amplified by a factor 2–4 to get root-mean-squared flow velocities inside the core, yielding estimates of $U = 6 \times 10^{-4}$ to 2×10^{-3} m/s. The estimate for the vortex turnover hence ranges from 35 to 120 years. This range is consistent with the typical auto-correlation times computed from core surface flows inferred from the historical geomagnetic data (Le Huy et al., 2000). To determine the likeliness that core flows time averaged over historical time periods contain a signature of mantle control, we, therefore, define intermediate flows averaged over $3\tau_u$ time units of the simulation, and compare them to fully converged time-averages. For the real Earth, considering a duration of

three vortex turnovers corresponds to performing time averages over historical periods of 100–360 years. It must be stressed that our approach is equivalent to matching the non-dimensional time in numerical simulations to the actual time in the Earth's core through the advection, or vortex turnover time. We are well aware that this choice is quite uncommon, because the Reynolds number in numerical dynamos (which represents the amount of momentum advection with respect to viscous diffusion) has a typical value of a few hundreds and is very remote from Earth's core values of order 10^8 (Christensen and Aubert, 2006). The magnetic Reynolds number (which is the equivalent of the Reynolds number for magnetic advection) is more Earth-like in numerical dynamos, and this often motivates the choice to re-scale non-dimensional time to Earth's core time through the magnetic dipole decay time (see for instance Christensen and Tilgner (2004)). This is, however, of little use in the present study since we focus on flow and thermal features rather than on magnetic field features. We rather attempt to capture the mixing effect of three large-scale vortex turnovers, while the effect of smaller-scale, unresolved vortices is represented by an overestimated viscosity.

Flows will be examined on a spherical surface S located below the core-mantle boundary, at the top of the free stream, outside the viscous Ekman layer. The homogeneous dynamo drives a significant part of the zonal flow observed on S (Aubert, 2005). This part must be removed in order to avoid spurious positive correlations that are unrelated with our ability to retrieve mantle control. Since it is technically difficult to isolate the homogeneous dynamo zonal flow at all time scales, we simply use the non-axisymmetric velocity field $\mathbf{u}_{\rm na}$ and temperature field $T_{\rm na}$. The amplitude $U_{\rm ave}$ of the boundary-induced, steady flow is defined as:

$$U_{\rm ave} = \sqrt{\frac{1}{S}\int_S \langle \mathbf{u}_{\rm na}\rangle^2_{\tau_{\rm ave}}\ {\rm d}S} \tag{18}$$

We also define a thermal penetration depth δ as

$$\delta = \left(\frac{1}{S}\int_S \langle T_{\rm na}\rangle^2_{\tau_{\rm ave}}\ {\rm d}S\right)^{1/2}\left(\frac{1}{S}\int_S \left\langle \frac{\partial T_{\rm na}}{\partial r}\right\rangle^2_{\tau_{\rm ave}}\ {\rm d}S\right)^{-1/2} \tag{19}$$

The intermediate and steady flows will be compared through a standard vector correlation coefficient

$$C_{\rm int} = \frac{\int_S \langle \mathbf{u}_{\rm na}\rangle_{3\tau_u}\cdot\langle \mathbf{u}_{\rm na}\rangle_{\tau_{\rm ave}}\ {\rm d}S}{\sqrt{\int_S \langle \mathbf{u}_{\rm na}\rangle^2_{3\tau_u}\ {\rm d}S}\sqrt{\int_S \langle \mathbf{u}_{\rm na}\rangle^2_{\tau_{\rm ave}}\ {\rm d}S}} \tag{20}$$

Instantaneous correlation coefficients will also be computed using flow snapshots:

$$C = \frac{\int_S \mathbf{u}_{\rm na}\cdot\langle \mathbf{u}_{\rm na}\rangle_{\tau_{\rm ave}}\ {\rm d}S}{\sqrt{\int_S \mathbf{u}^2_{\rm na}\ {\rm d}S}\sqrt{\int_S \langle \mathbf{u}_{\rm na}\rangle^2_{\tau_{\rm ave}}\ {\rm d}S}} \tag{21}$$

Obviously, C and $C_{\rm int}$ are variable in time because snapshots and incomplete time averages are time-dependent. A statistical approach is therefore adopted. For each numerical model, 10 independent realizations of C and $C_{\rm int}$ are performed, in order to extract the mean and standard deviation of the correlation coefficients.

3. Results

3.1. The steady flow

In this study, the steady flow serves as a reference for detecting the signature of mantle control. In early studies of heterogeneous mantle control (Zhang and Gubbins, 1992, and followers) it was shown that a thermal wind balance between the buoyancy and Coriolis vorticities drives the flow at the top of the free stream. However, these studies used models of non-magnetic convection, which are unlikely to be relevant to the real core since the flow may change much in the presence of a magnetic field (Olson and Glatzmaier, 1996). The exact influence of the Lorentz force at the top of the core is not well-known. The hypothesis that it is weak is grounding the tangential geostrophy assumption (Le Mouël et al., 1985) that is commonly used in core flow inversion from geomagnetic SV data (Hulot et al., 2002). Here, we first clarify the role of the Lorentz force in the numerical models.

As in Christensen and Aubert (2006) we write the curled version of Eq. (1) to obtain an equation for the vorticity $\omega = \nabla\times\mathbf{u}$:

$$\frac{\partial\omega}{\partial t} + \nabla\times(\omega\times\mathbf{u}) - 2\frac{\partial\mathbf{u}}{\partial z} = \frac{Ra_\kappa}{r_{\rm o}}\nabla\times(T\mathbf{r}) + \nabla\times[(\nabla\times\mathbf{B})\times\mathbf{B}] + E\nabla^2\omega \tag{22}$$

The thermal wind balance holds when the Coriolis vorticity $-2\partial\mathbf{u}/\partial z$ is balanced by the buoyancy vorticity $Ra_\kappa/r_{\rm o}\nabla\times(T\mathbf{r})$. The two horizontal components of this balance are checked at the top of the free stream, for the steady flow, in Fig. 1. The azimuthal component shows a well-respected balance, dominated by the axisymmetric component. This is in agreement with the findings of Aubert (2005): the steady zonal flow in homogeneous dynamos is mainly a thermal wind. The meridional component reveals more the quality of the balance for non-axisymmetric flows driven by the heterogeneous boundary condition. The agreement, while being less

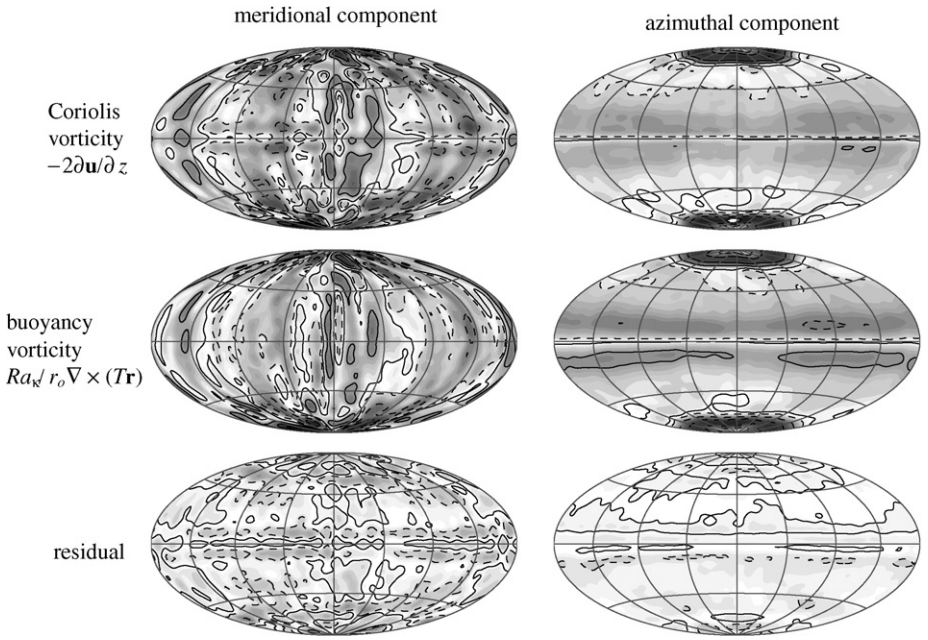

Fig. 1. Long-term (τ_{ave}) time average of case q04. Check of the meridional (contour interval 0.09, plain contours are positive values, dashed contours are negative values) and azimuthal (contour interval 0.03) thermal wind balance at depth 0.07. The residual represents the deviation of the vorticity balance from thermal wind. The root-mean-squared residual amplitude represents 33% (meridional) and 20% (azimuthal) of the root-mean-squared curled force amplitude.

satisfactory (especially near the equator where thermal wind is expected to fail) still shows a good degree of correlation with a low residual. The Lorentz force makes for most of this residual, while inertia and viscosity play a secondary role in this case (not shown here). At first glance it may seem surprising that the Lorentz force does not perturb the system from a thermal wind balance. However, one must bear in mind that the magnetic pressure, which represents a sizeable part of this force, does not enter the curled force balance (22), reducing the contribution of the Lorentz force, even when the Elsasser number Λ is clearly above 1 (for case q04 we have $\Lambda = 4.7$).

Now that we are confident that steady flows of the heterogeneous dynamos can reasonably be described in terms of thermal winds, we may propose a scaling for their amplitude, which will be useful to quantify their importance versus transient flows. The thermal wind balance writes

$$-2\frac{\partial \mathbf{u}}{\partial z} = \frac{Ra_\kappa}{r_o}\nabla\times(T\mathbf{r}) \tag{23}$$

The $\nabla\times$ operator acting on $T\mathbf{r}$ introduces a length scale in the lateral direction. The z-derivative on the left-hand-side contains radial and lateral length scales. In a thick spherical shell, both can be anticipated to be of the same order of magnitude. The left-hand side and right-hand side length scales therefore cancel in the scaling for U_{ave} which writes:

$$2U_{ave} \approx Ra_\kappa T_{ave} \tag{24}$$

Here T_{ave} is the typical amplitude of the temperature variations associated with the thermal wind U_{ave}. In the non-dimensional form introduced by (6), the Fourier law of heat conduction writes:

$$q = -\frac{\partial T}{\partial r} \tag{25}$$

Hence, a scaling for T_{ave} is obtained by using the thermal penetration depth δ and the amplitude of heat flux heterogeneity q^*:

$$T_{ave} \approx 2q^*\delta \tag{26}$$

Note that the factor 2 here is due to the fact that T_{ave} represents a peak-to-peak variation, while q^* is a zero-to-peak value. The scaling for U_{ave} writes

$$\frac{U_{ave}}{\delta} \approx q^* Ra_\kappa \tag{27}$$

The proposed scaling is checked in Fig. 2. For the Y_2^2 pattern (circles, diamonds and cross), U_{ave}/δ linearly grows with q^* and with Ra_κ, with a slope of 0.72, close to the theoretical slope 1. Moreover, a given value of the product $q^* Ra_\kappa$ yields a unique thermal wind amplitude. This response is checked against various values of Ra_κ, E_κ

and Pr. For Y_2^1 and tomographic patterns the linearity still mostly holds, with lower slopes of 0.45 (tomographic) and 0.33 (Y_2^1). Indeed these patterns contain equator-antisymmetric forcing components, which oppose the Proudman-Taylor constraint of the rotating system to set up a flow.

The Y_2^1 and tomographic patterns have, however, an additional peculiarity when compared to Y_2^2: looking for instance at cases T1 and T3 (or Y21-1 and Y21-3, T5 and T6) we see that it is possible to obtain slightly different thermal wind values (within a factor 2) for two sets of (q^*, Ra_κ), while maintaining a constant value for the product $q^* Ra_\kappa$. Due to the Proudman-Taylor constraint, equator-symmetric and antisymmetric patterns induce different responses. In the Y_2^2 cases the homogeneous (Ra_κ) and heterogeneous (q^*) forcings are both equator-symmetric, so the roles of q^* and Ra_κ can be swapped (for instance cases q04h and q08 yield almost exactly the same $U_{\rm ave}/\delta$). In the Y_2^1 and tomographic cases, the heterogeneous forcing is no longer equator-symmetric, and this breaks the symmetry between q^* and Ra_κ. Different behaviors of equator-symmetric and antisymmetric forcings were already observed by Gibbons and Gubbins (2000). While the symmetry-breaking between q^* and Ra_κ can influence the thermal wind amplitude, it certainly does not change its order of magnitude. We conclude that the response is still mostly linear.

Fig. 2 shows that, for a given flow pattern and as predicted by (27), the amplitude of the steady flow responds mostly linearly to the level of imposed mantle heterogeneity $q^* Ra_\kappa$ if we correct for the thermal penetration depth δ. The nonlinear part of the response is hidden in δ, which is crucially sensitive to advection and mixing of heat. To provide a scaling for δ, we first assimilate δ to a thermal boundary layer thickness (although the limitations of this hypothesis will be shown below). In a classical Rayleigh-Benard system without rotation, the dimensional $\tilde{\delta}$ correlates then with the thermal diffusion length $\sqrt{\kappa D/\tilde{U}}$. Due to the presence of a dominant Coriolis force, it is expected that core flows behave differently. It is possible to derive a scaling for the thermal boundary layer thickness in rotating dynamos from the extensive parameter space study of Christensen and Aubert (2006), starting from their scaling $Nu^* \propto (Ra_Q^*)^{0.5}$ tying their modified Nusselt Nu^* and Rayleigh Ra_Q^* numbers

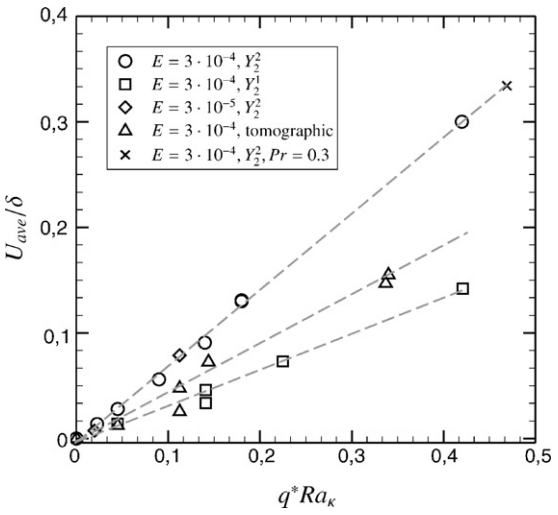

Fig. 2. Amplitude $U_{\rm ave}$ of the steady thermal wind, corrected for the thermal penetration depth δ as a function of the scaling parameter $q^* Ra_\kappa$. The three dashed lines represent the respective fits $U_{\rm ave}/\delta = 0.72,\ 0.45,\ 0.33\ q^* Ra_\kappa$ for cases with Y_2^2, tomographic and Y_1^2 heat flow patterns.

$$Nu^* = \frac{r_o}{r_i}\frac{q_{\rm adv}}{\rho C_p \Delta T \Omega D} \tag{28}$$

$$Ra_Q^* = \frac{r_o}{r_i}\frac{\alpha g_0 q_{\rm adv}}{\rho C_p \Omega^3 D^2} \tag{29}$$

Only the advective part $q_{\rm adv}$ of the total heat flux q_0 escaping from the core enters the formulas above. In their models the temperature difference ΔT is prescribed between the inner and the outer sphere of the shell. We have a different choice of boundary conditions, where ΔT is a variable while q_0 is prescribed. To adapt their result, we use Fourier's law to relate ΔT with q_0 using the thermal penetration depth $\tilde{\delta}$:

$$q_0 = \rho C_{\rm p} \kappa \frac{\Delta T}{2\tilde{\delta}} \tag{30}$$

Considering only sufficiently forced models so that $q_0 \approx q_{\rm adv}$ an expression for Nu^* as a function of δ follows:

$$Nu^* \approx \frac{r_o}{r_i}\frac{E_\kappa}{\delta} \tag{31}$$

and we also have

$$Ra_Q^* = \frac{r_o}{r_i} Ra_\kappa E_\kappa \tag{32}$$

so that the Christensen and Aubert (2006) scaling finally relates δ with control parameters:

$$\delta \propto \left(\frac{Ra_\kappa}{E_\kappa}\right)^{-0.5}. \tag{33}$$

In Fig. 3, a power-law fit for supercritical cases with Y_2^2 heat flow pattern yields $\delta = 1.1(Ra_\kappa/E_\kappa)^{-0.4}$, in reasonable agreement with (33). Assimilating δ to a thermal boundary layer thickness obviously fails to describe its sensitivity to q^* (circles aligned along a vertical). However q^* is bound by the need to maintain a dynamo (Olson

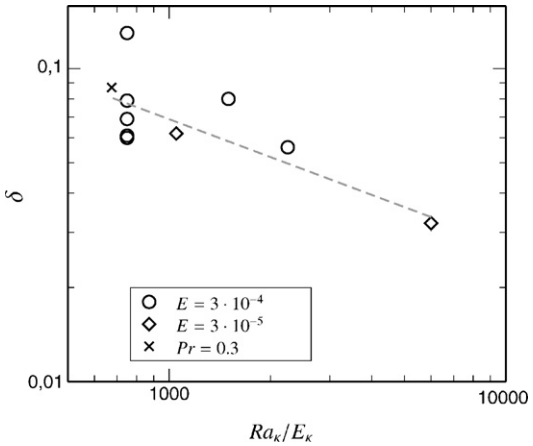

Fig. 3. Y_2^2 heat flow pattern. Scaling of the thermal penetration depth δ according to Christensen and Aubert (2006). The best-fit power law is $\delta = 1.1(Ra_\kappa/E_\kappa)^{-0.4}$.

and Christensen, 2002) and can certainly not influence δ on a range larger than that indicated on Fig. 3.

The advection of temperature alters the magnitude, but also the structure of the steady flow, especially when the boundary heterogeneity pattern has a complex spectral content such as in the tomographic cases T1 and S2. Fig. 4a shows the heat flow pattern used in these cases. In Fig. 4b we first show the pattern of sub-critical response (case S2) to this heat flow, with no underlying convection. The temperature field is simply a smoothed (due to thermal diffusion) image of the prescribed heat flow, and the resulting thermal wind is rather equatorially symmetric. Fig. 4c presents the supercritical response (case T1). For the purpose of comparison with Fig. 4b, the steady contribution from the homogeneous dynamo case q00 (which has the same parameters as case T1 except the value of q^*), which is entirely zonal, has been removed. The flow pattern is similar to that obtained by Olson and Christensen (2002, Fig. 9b), and Gibbons and Gubbins (2000, Fig. 4c). Here the temperature structure results from two effects: the imposed boundary heterogeneity as in Fig. 4b, but also the underlying thermal mixing, which drastically reduces the depth δ of penetration of the boundary condition, from one half of the shell in Fig. 4b to one tenth of the shell in Fig. 4c (see Table 1). The flow pattern driven by the mixed temperature heterogeneity is now quite asymmetric, with only two strong vortices (southern Atlantic and northern American) and quieter zones such as the southern Pacific.

Another interesting effect of temperature advection is the longitudinal angular shift between the imposed heat flow pattern and the flow vortices. Indeed a comparison between Fig. 4b and c reveals that the main African temperature patch and its associated vortex are

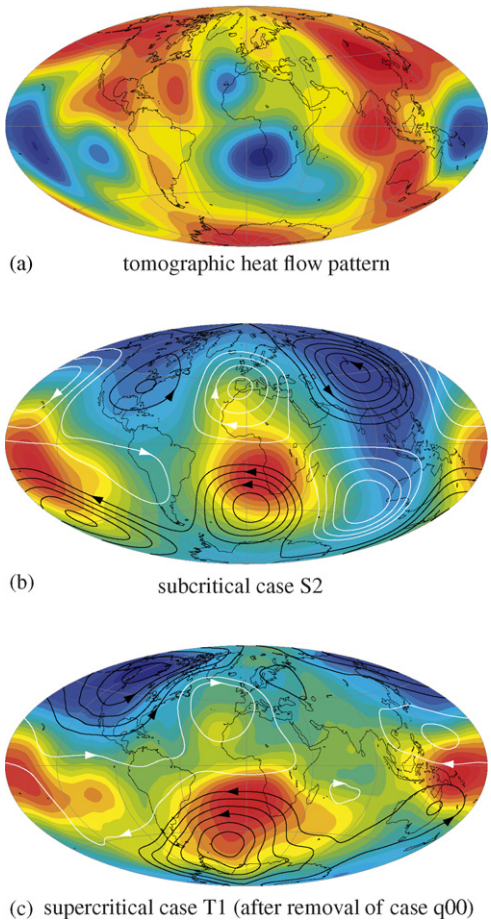

Fig. 4. (a) Heat flow pattern used in cases S2 and T1, derived from the Masters et al. (2000) seismic shear velocity model (larger than average outwards heat flux in red). (b and c) streamfunction representations of the steady flow at depth 0.07, plotted over the steady temperature field at the same depth. For (b), the sub-critical case S2 (contour interval 1.5×10^{-6}, 20 color contours from -0.07 to 0.07) and for (c) the supercritical case T1, after removal of the homogeneous steady flow and steady temperature field from case q00 (contour interval 0.0003, 20 color contours from -3.1 to -2.4).

displaced roughly 20° to the west when convection is present. Gibbons and Gubbins (2000) and Olson and Christensen (2002) have exhibited a dependence of this shift with the Ekman number. We argue here that the relevant parameter is the Peclet number of the flow (see (14)), because the shift crucially depends on temperature advection. To illustrate this, we use all cases with Y_2^2 heat flow pattern, including a sub-critical case. All control parameters are therefore varying. The westward shift is measured between the heat flux maxima/minima and the closest vortices, in both northern and southern hemispheres. This yields a set of eight results for each case, the mean and standard deviation of which are plotted versus *Pe* in Fig. 5. The sub-critical Y_2^2 case has almost no shift,

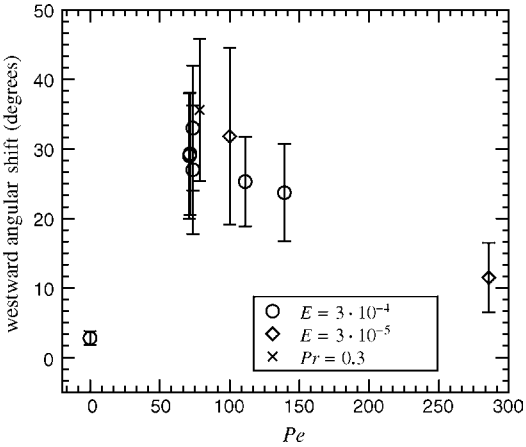

Fig. 5. Y_2^2 heat flow pattern. Westward longitudinal shift between the heat flow pattern and the streamfunction pattern, as a function of the Peclet number *Pe*. The error bars reflect the standard deviation of the angular shift in the set of 8 vortices (4 north, 4 south) created by a Y_2^2 heat flow pattern. The deviation is overestimated due to the asymmetric character of cyclones and anticyclones.

which strongly suggests that the shift is resulting from the advection of temperature patches by the underlying dynamo flow, away from the imposed heat flow location. As the Peclet number increases, the shift increases due to a coherent advection. The shift then reaches a maximum and decreases for large values of *Pe*, because advection becomes of smaller scale and less coherent. We, therefore, expect that the temperature patches reach zero shift with respect to the heat flux patches as mixing becomes complete in the large Peclet number limit which is relevant for the Earth's core.

3.2. The intermediate flows

Figs. 6 and 7 present streamfunctions representations of flows at the top of the free stream for cases q06 and q02, corresponding to high ($q^* = 0.625$) and low ($q^* = 0.2$) levels of mantle control, respectively, for a constant value of Ra_κ. In both cases a single harmonic Y_2^2 is used as boundary heterogeneity. Y_2^2 was chosen because it is the largest single harmonic in the mantle tomography model of Masters et al. (2000). In

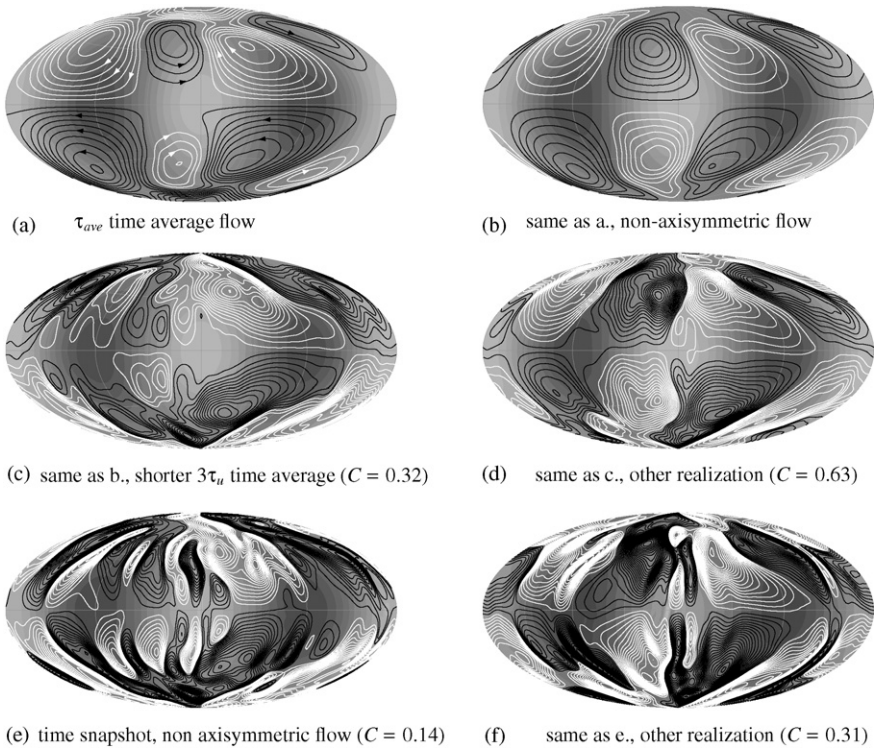

Fig. 6. Case q06 (high level of mantle control $q^* = 0.625$) streamfunction representations of flows at depth 0.07, plotted over heat flow pattern (larger than average outwards heat flow in light grey), (a) steady flow obtained by averaging over τ_{ave}. (b) Only the non-axisymmetric part of the flow, corresponding to the effect of the heterogeneous boundary condition, is selected as a reference for correlation. (c and d) Two realizations of intermediate averaging over a time $3\tau_u$ corresponding to three vortex turnover times (non-axisymmetric part of the flow). (e and f) Time snapshots from realizations (c and d), respectively. The vector correlation coefficient *C* with (b) is reported in (c, d, e and f). Contour interval in all plots is 0.0003.

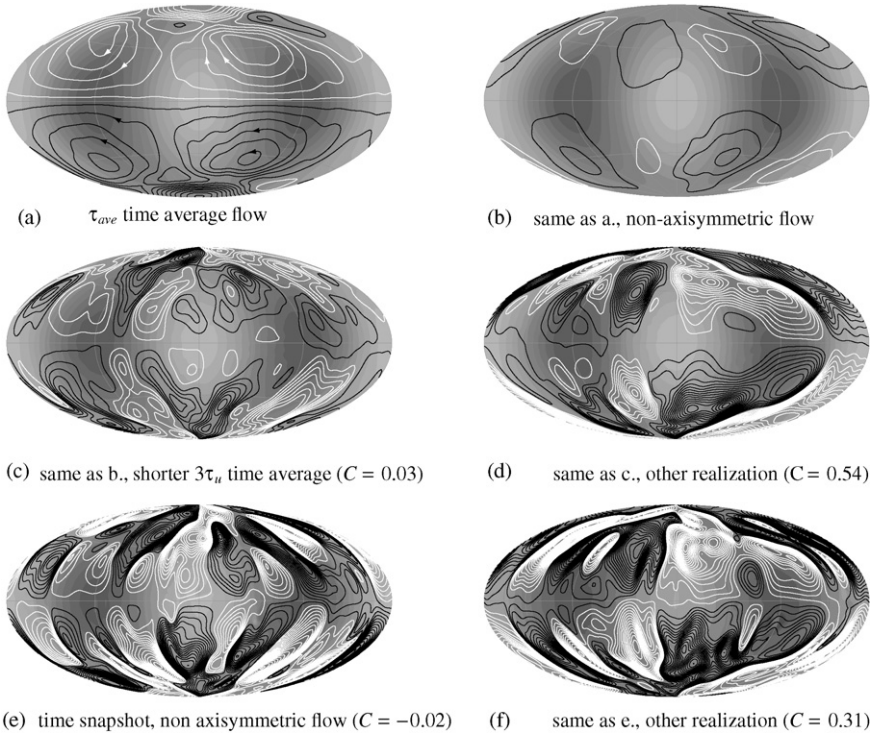

Fig. 7. Same as Fig. 6, for case q02 (low level of mantle control $q^* = 0.2$).

Figs. 6 and 7a, the steady flow pattern previously found by Olson and Christensen (2002) is recalled. In order to remove spurious correlations associated with the homogeneous dynamo, only the non-axisymmetric part of the flow (Figs. 6 and 7b) is taken as reference for subsequent analysis. A flow will be considered to carry a signature of mantle control if its non-axisymmetric part has a statistically significant correlation with this reference flow.

Figs. 6 and 7c and d show two intermediate flows obtained using time averaging over $3\tau_u$ units of time. These flows carry a significant transient part (see the higher density of streamlines compared to the reference flow (Figs. 6 and 7b) which is richer in smaller length scales. This transient flow is responsible for the time variability of the vector correlation coefficient C, which may vary from low (Figs. 6 and 7c) to high (Figs. 6 and 7d) values. In the case of high correlation, a qualitative visual check also indicates that the reference heterogeneity pattern and reference flow can indeed be seen in the intermediate flows. Comparing cases q06 and q02, we show that when the mantle control is large as in case q06, the correlation coefficient between the intermediate and reference flow is generally higher than when the mantle control is low as in case q02, which is an intuitive result. A somewhat more counter-intuitive and interesting result is revealed by case q02 in Fig. 7: the intermediate flow in Fig. 7d is much stronger in amplitude (by roughly a factor 10) than the steady flow in Fig. 7b, yet the two flows are highly correlated with $C = 0.54$. This shows that a weak level of mantle control can have a dramatic influence on the shape of the observable flow in this realization of intermediate time averaging. However, of course, an observer of the Earth core could be less fortunate and see a realization such as the one shown in Fig. 7c where the signature of mantle control has been lost ($C = 0.03$).

Figs. 6 and 7e and f present snapshots of flows captured within the intermediate time averaging of Figs. 6 and 7c and d, respectively. Snapshots are even richer in smaller length scales than intermediate averages. This underlines the importance of time-averaging, even over a short period of time such as $3\tau_u$: the resulting flows have higher correlation with the reference flow than snapshots, increasing significantly our chances to witness some mantle control.

3.3. Possibility of mantle control on intermediate flows

We anticipate that a key parameter to determine the correlation coefficient C is the relative amplitude A of the steady thermal wind with respect to the underlying

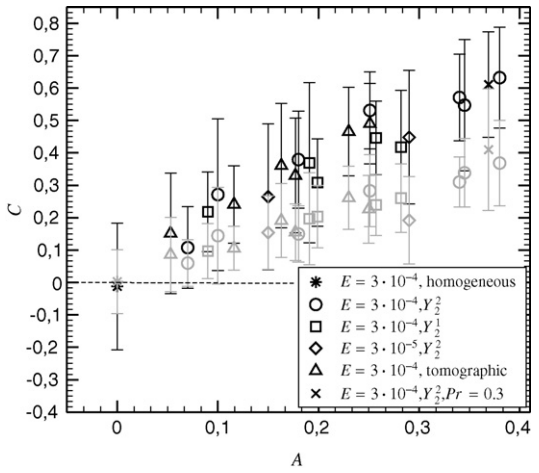

Fig. 8. Vector correlation coefficient C between steady thermal wind and transient flow at the outer surface of the model, as a function of the scaling parameter $A = U_{ave}/U$, describing the relative amplitude of the steady surface thermal wind and the underlying flow. Grey points are snapshots, black points are $3\tau_u$ intermediate time-averages. Points and error bars respectively represent the mean and standard deviation in a set of ten realizations.

dynamo flow, expressed as:

$$A = \frac{U_{ave}}{U} \tag{34}$$

where U_{ave} and U are respectively defined by (18) and (13). Fig. 8 shows a plot of C versus A, covering all cases in our data set. Points and error bars represent the mean and standard deviation of the correlation level in a set of ten realizations, for intermediate averages (black) and snapshots (grey). Generally we found positive correlation between intermediate and steady flows for all non-zero values of q^* which we investigated. The correlation C is increasing with A for a given heat flow pattern. Cases with different Ekman and Prandtl numbers, and with different heterogeneity patterns delineate the same trend curve, supporting the choice of A as a scaling parameter. Snapshots generally show about half the level of correlation seen for intermediate time averages.

4. Discussion

The novel approach of our study is to model time-average core flows from numerical dynamos with non-uniform boundary heat flow on two distinct time scales. On a long time scale representative of complete thermal mixing, a steady thermal wind arises, which is representative of the heterogeneous boundary heat flow pattern. The Lorentz, inertial and viscous forces have only a secondary influence. The thermal wind balance allowed us to propose and test a scaling law for this steady flow. In order to test the effect of an incomplete time-averaging, we have introduced the concept of intermediate flow, which we computed here for various simulations by taking averages over three vortex turnover times, presumably equivalent to 100–360 years in the Earth's core. Such intermediate flows are affected by both the steady flow and a transient flow from the underlying convective dynamo. We quantified the resemblance of steady and intermediate flow with a correlation coefficient, which we showed to be primarily dependent on the amplitude ratio of the two flows.

The generally positive character of the correlation between intermediate and steady flows suggests the possibility to observe thermal mantle control on the Earth's core on time scales related to flow advection. This is an encouraging perspective in light of the reliable SV inversion flow data, which have currently a timespan of roughly 150 years and could reach longer intervals when issues concerning geomagnetic data prior to 1840 are addressed, such as a re-evaluation of the magnetic field intensity (Gubbins et al., 2006). This is also consistent with the early suggestion of Bloxham and Gubbins (1987) that lateral temperature heterogeneities could be sufficient to force mantle-driven core convection. Here we may push the argument further by providing a quantification of this likeliness, and suggesting that the needed observation time is within the existing period of reliable historical geomagnetic data. To do this we estimate the relative amplitude $A = \tilde{U}_{ave}/\tilde{U}$ of the mantle-driven flow at the Earth's core surface and the underlying dynamo flow.

We may start by providing an estimate of the heat flow heterogeneity at the top of the Earth's core, from the mantle side of the CMB. Due to subducting plate material, lateral temperature heterogeneities there are thought to be quite considerable (Labrosse, 2002). Trampert et al. (2004) have attempted a separation of the thermal and chemical part of the seismic velocity heterogeneity. They found zero-to-peak lateral temperature variations of the order of 100 K. For the present estimation we will retain a peak-to-peak temperature variation of $\delta T = 200$ K. The thickness $\delta_m = 100$ km of the thermal boundary layer at the bottom of the mantle can be estimated using the thermal diffusion length $\delta_m = \sqrt{\kappa_m D_m/u_m}$, with the mantle velocity, thermal diffusivity and size being respectively taken as $u_m = 1$ cm/year, $D_m = 3000$ km and $K_m = 10^{-6}$ m^2/s (Schubert et al., 2001). Fourier's law then allows us to infer the heat flux heterogeneity across the core-mantle boundary:

$$\delta q = \rho_m C_{pm} \kappa_m \frac{\delta T}{\delta_m} \tag{35}$$

Using the mantle specific heat and density values $C_{pm} = 1000\,\mathrm{J\,K\,kg^{-1}}$ (Schubert et al., 2001) and $\rho_m = 5000\,\mathrm{kg/m^3}$ from PREM (Dziewonski and Anderson, 1981) we get $\delta q = 10\,\mathrm{mW/m^2}$. Compared to a reasonable value for the superadiabatic heat flow out of the Earth core of $q_0 = 15\,\mathrm{mW/m^2}$ (Labrosse, 2002), this represents a level of heterogeneity $q^* = \delta q/2q_0 = 30\%$.

On the core side the thickness $\tilde{\delta}$ of the thermal boundary layer is estimated using our best fit for (33). Using $D = 2200\,\mathrm{km}$, $\alpha = 10^{-5}\,1/\mathrm{K}$, $C_\mathrm{p} = 800\,\mathrm{J\,kg\,K^{-1}}$, and $\kappa = 5 \times 10^{-6}\,\mathrm{m^2/s}$ (Stacey, 1992), $\rho = 10^4\,\mathrm{kg/m^3}$ and $g_0 = 10\,\mathrm{m/s^2}$ (Dziewonski and Anderson, 1981), we get $Ra_\kappa = 7$, $E_\kappa = 10^{-14}$ and finally $\tilde{\delta} = 3$ m. Christensen and Aubert (2006) found a value of 10^6 for the Nusselt number Nu, which is equivalent to the ratio $D/\tilde{\delta}$. This is in agreement with our estimate for $\tilde{\delta}$. It differs strikingly from a thermal diffusion length estimate such as done previously for the mantle, which would yield $\tilde{\delta} \approx 100\,\mathrm{m}$, as previously used by Bloxham and Gubbins (1987). The point here is that rotating convection is quite different from Rayleigh-Bénard convection, and that Taylor columns have a tendency to break the conventional thermal boundary layer so as to shrink it towards the typical size of a viscous Ekman layer. This obviously appears only if the thickness of the thermal boundary layer is larger than that of the Ekman viscous boundary layer. The thickness of the Ekman layer is $DE^{1/2}$ (Greenspan, 1968). Using a core viscosity of $\nu = 10^{-6}\ \mathrm{m^2/s}$ (Stacey, 1992), we have $E = 2 \times 10^{-15}$, which gives an Ekman layer of thickness 10 cm. The thermal boundary layer is therefore expected to be still thicker than the Ekman layer, as already suggested by Christensen and Aubert (2006).

We next write the dimensional form of the thermal wind scaling (27) with its theoretical prefactor, and preserving its original form (23) as a force equilibrium:

$$2\Omega\tilde{U}_\mathrm{ave} = \alpha g_0 \frac{\delta q \tilde{\delta}}{\rho C_\mathrm{p} \kappa} \tag{36}$$

With the values previously used, we find $\tilde{U}_\mathrm{ave} = 5 \times 10^{-4}\mathrm{m/s}$. This is quite sizeable compared to our estimate $\tilde{U} = 6 \times 10^{-4}$ to $2 \times 10^{-3}\mathrm{m/s}$ for the root-mean-squared velocity inside the Earth's core. The amplitude ratio $A = \tilde{U}_\mathrm{ave}/\tilde{U} = 0.2 - 0.7$ is quite favourable, suggesting a level of correlation $C > 0.3$ between the intermediate and mantle-driven flow. Obviously we can only specify an order of magnitude for A, especially if we add uncertainties concerning the determination of U_ave which we have not included yet. Two factors might be underestimated and could yield an even stronger value for A. The peak-to-peak lateral temperature heterogeneity could be as large as 600 K (Trampert et al., 2004), and the penetration depth $\tilde{\delta}$ could also be larger, but not possibly much smaller than our estimate, since it already reaches down to the typical Ekman layer thickness. On the other hand, the prefactor for (27) lies between 0.33 and 0.72, depending on the boundary heat flow pattern, which could yield somewhat (but not by an order of magnitude) lower values for A. We conclude that the amplitude ratio lies in the range $0.1 < A < 1$, yielding a mean correlation level $C > 0.2$. This therefore suggests that the presence of a mantle signature in intermediate flows is quite likely.

A common drawback of scaling approaches is that we have to extrapolate a long way to reach Earth-like parameter values. This is not the case for scaling (27). For the Earth's core we have estimated $Ra_\kappa = 7$ and $q^* = 30\%$. The numerical models typically use the same q^*, and lower Ra_κ than in the Earth's core, but the key parameter to scale U_ave is the product $q^* Ra_\kappa \approx 2$, which is close to the range 0–0.5 explored by our models. There is more concern about scaling (33) for δ, in which the thermal Ekman number enters, with model values still remote from the Earth's core value $E_\kappa = 10^{-14}$. However, this scaling is derived from Christensen and Aubert (2006), who validated their approach over a broad parameter range. Finally, The Earth-like range of the output parameter A coincides with the explored range.

Our study suggests that core flows on centennial time scales are an important intermediate step between the geomagnetic data and their interpretation in terms of heterogeneous mantle control. We hope to motivate further work, both in the direction of core flow models and other coupling mechanisms between the core and the mantle.

Acknowledgements

Numerical calculations of this study were performed at the Service de Calcul Par-allele, IPGP, Paris, France. We are grateful to Peter Olson for stimulating discussions on this work. We also would like to thank two anonymous referees for comments which significantly improved the manuscript. This is IPGP contribution number 2180.

References

Amit, H., Olson, P., 2004. Helical core flow from geomagnetic secular variation. Phys. Earth Planet. Int. 147, 1–25.

Amit, H., Olson, P., 2006. Time average and time dependent parts of core flow. Phys. Earth Planet. Int. 155, 120–139, doi:10.1016/J.pepi.2005.10.006.

Aubert, J., 2005. Steady zonal flows in spherical shell dynamos. J. Fluid. Mech. 542, 53–67.

Bloxham, J., 2002. Time-independent and time-dependent behaviour of high-latitude flux bundles at the core-mantle boundary. Geophys. Res. Let 29 (18), 1854.

Bloxham, J., Gubbins, D., 1985. The secular variation of Earth's magnetic field. Nature 317, 777–781.

Bloxham, J., Gubbins, D., 1987. Thermal core-mantle interactions. Nature 325, 511–513.

Bloxham, J., Jackson, A., 1990. Lateral temperature variations at the core-mantle boundary deduced from the magnetic field. Geophys. Res. Let. 17, 1997–2000.

Bloxham, J., Jackson, A., 1991. Fluid flow near the surface of Earth's outer core. Rev. Geophys. 29, 97–120.

Bouligand, C., Hulot, G., Khokhlov, A., Glatzmaier, G.A., 2005. Statistical paleomagnetic field modeling and dynamo numerical simulation. Geophys. J. Int. 161, 603–626.

Carlut, J., Courtillot, V., 1998. How complex is the time-averaged geomagnetic field over the past 5 Myr? Geophys. J. Int. 134, 527–544.

Christensen, U., Aubert, J., 2006. Scaling properties of convection-driven dynamos in rotating spherical shells and application to planetary magnetic fields. Geophys. J. Int. 117, 97–114, doi:10.1111/j.l365-246X.2006.03009.x.

Christensen, U., Olson, P., 2003. Secular variation in numerical geodynamo models with lateral variations of boundary heat flux. Phys. Earth Planet. Int. 138, 39–54, doi:10.1016/S0031-9201(03)00064-5.

Christensen, U., Tilgner, A., 2004. Power requirement of the geodynamo from ohmic losses in numerical and laboratory dynamos. Nature 429, 169–171, doi:10.1038/nature02508.

Constable, C., Johnson, C., Lund, S., 2000. Global geomagnetic field models for the past 3000 years: transient or permanent flux lobes? Phil. Trans. Roy. Soc. A 358, 991–1008.

Dziewonski, A., Anderson, D., 1981. Preliminary reference Earth model PREM. Phys. Earth Planet. Int. 25, 297–356.

Eymin, C., Hulot, G., 2005. On core surface flows inferred from satellite magnetic data. Phys. Earth Planet. Int. 152, 200–220.

Gibbons, S., Gubbins, D., 2000. Convection in the Earth's core driven by lateral variation in the core-mantle boundary heat flux. Geophys. J. Int. 142, 631–642.

Greenspan, H.P., 1968. The Theory of Rotating Fluids. Breukelen Press.

Gubbins, D., Kelly, P., 1993. Persistent patterns in the geomagnetic field over the past 2.5 Myr. Nature 365, 829–832.

Gubbins, D., Jones, A.L., Finlay, C., 2006. Fall in Earth's magnetic field is erratic. Nature 312, 900–902.

Hide, R., 1970. On the Earth's core-mantle interface. Q. J. R. Meterol. Soc 96, 579–590.

Hongre, L., Hulot, G., Khokhlov, A., 1998. An analysis of the geomagnetic field over the past 2000 years. Phys. Earth Planet. Int. 106, 311–335.

Hulot, G., Bouligand, C., 2005. Statistical paleomagnetic field modeling and symmetry considerations. Geophys. J. Int. 161, 591–602.

Hulot, G., Le Mouël, J.-L., 1994. A statistical approach to the Earth's main magnetic field. Phys. Earth Planet. Int. 82, 167–183.

Hulot, G., Eymin, C., Langlais, B., Mandea, M., Olsen, N., 2002. Small-scale structure of the geodynamo inferred from Oersted and Magsat satellite data. Nature 416, 620–623.

Jackson, A., Jonkers, A.R.T., Walkers, M.R., 2000. Four centuries of geomagnetic secular variation from historical records. Phil. Trans. Roy. Soc. A 358, 957–990.

Johnson, C., Constable, C., 1995. The time averaged geomagnetic field as recorded by lava flows over the past 5 Myr. Geophys. J. Int. 112, 489–519.

Jones, G.M., 1977. Thermal interaction of the core and the mantle and long-term behaviour of the geomagnetic field. J. Geophys. Res. 82, 1703–1709.

Khokhlov, A., Hulot, G., Bouligand, C., 2006. Testing statistical paleomagnetic field models against directional data affected by measurement error. Geophys. J. Int. 167 (2), 635–648.

Korte, M., Genevey, A., Constable, C., Frank, U., Schnepp, E., 2005. Continuous geomagnetic field models for the past 7 millenia: 1. A new global data compilation. Geochem. Geophys. Geosyst. (G-cubed) 6, doi:10.1029/2004GC000800.

Labrosse, S., 2002. Hotspots, mantle plumes and core heat loss. Earth Planet. Sci. Lett. 199, 146–156.

Le Huy, M., Mandea, M., Le Mouël, J.-L., Pais, A., 2000. Time evolution of the fluid flow at the top of the core, geomagnetic jerks. Earth Planets Space 52, 163–173.

Le Mouël, J.-L., Jault, D., Gire, C., Madden, T., 1985. Motions of the core surface in the geostrophic approximation. Phys. Earth Planet. Int. 39, 270–287.

Masters, G., Laske, G., Bolton, H., Dziewonski, A., 2000. The relative behavior of shear velocity, bulk sound speed, and compressional velocity in the mantle: implications for chemical and thermal structure. In: Karato, S., Forte, A.M., Liebermann, R.C., Masters, G., Stixrude, L., (Eds.), Earth's Deep Interior, vol. 117, AGU Monograph, Washington D.C.

McElhinny, M., McFadden, P., Merrill, R., 1996. The time-averaged paleomagnetic field 0–5 mA. J. Geophys. Res. 101, 25007–25027.

Olson, P., Christensen, U., 2002. The time averaged magnetic field in numerical dynamos with non-uniform boundary heat flow. Geophys. J. Int. 151, 809–823.

Olson, P., Glatzmaier, G.A., 1996. Magnetoconvection and thermal coupling of the Earth's core and mantle. Phil. Trans. Roy. Soc. A 354, 1413–1424.

Pais, A., Hulot, G., 2000. Length of day decade variations, torsional oscillations and inner core superrotation: evidence from recovered core surface zonal flows. Phys. Earth Planet. Int. 118, 291–316.

Schubert, G., Turcotte, D., Olson, P., 2001. Mantle Convection in the Earth and planets. Cambridge University Press.

Stacey, F.D., 1992. Physics of the Earth. Brookfield Press.

Trampert, J., Deschamps, F., Resovsky, J., Yuen, D., 2004. Probabilistic tomography maps chemical heterogeneities throughout the lower mantle. Science 306, 853–856.

Wicht, J., 2002. Inner-core conductivity in numerical dynamo simulations. Phys. Earth Planet. Int. 132, 281–302.

Zhang, K., Gubbins, D., 1992. On convection in the Earth's core driven by lateral temperature variations in the lower mantle. Geophys. J. Int. 108, 247–255.

Zhang, K., Gubbins, D., 1993. Nonlinear aspects of core-mantle interaction. Geophys. Res. Let. 20, 2969–2972.

Geophys. J. Int. (2008) **172,** 945–956 doi: 10.1111/j.1365-246X.2007.03693.x

The magnetic structure of convection-driven numerical dynamos

Julien Aubert,[1] Jonathan Aurnou[2] and Johannes Wicht[3]

[1] *Dynamique des Fluides Géologiques, Institut de Physique du Globe de Paris,* 4 *place Jussieu,* 75252 *Paris cedex* 5, *France. E-mail: aubert@ipgp.jussieu.fr*
[2] *Department of Earth and Space Sciences, University of California, Los Angeles, USA*
[3] *Max-Planck Institute for Solar System Research, Katlenburg-Lindau, Germany*

Accepted 2007 November 21. Received 2007 November 15; in original form 2007 April 24

SUMMARY

The generation of a magnetic field in numerical simulations of the geodynamo is an intrinsically 3-D and time-dependent phenomenon. The concept of magnetic field lines and the frozen-flux approximation can provide insight into such systems, but a suitable visualization method is required. This paper presents results obtained using the Dynamical Magnetic Field line Imaging (DMFI) technique, which is a representation of magnetic field lines accounting for their local magnetic energy, together with an algorithm for the time evolution of their anchor points. The DMFI illustrations are consistent with previously published dynamo mechanisms, and allow further investigation of spatially and temporally complex systems. We highlight three types of magnetic structures: (i) magnetic cyclones and (ii) magnetic anticyclones are expelled by, but corotate with axial flow vortices; (iii) magnetic upwellings are amplified by stretching and advection within flow upwellings, and show structural similarity with helical plumes found in rotating hydrodynamic experiments. While magnetic anticyclones are responsible for the regeneration of a stable axial dipole, here we show that excursions and reversals of the dipole axis are caused by the emergence of magnetic upwellings, which amplify and transport a generally multipolar magnetic field from the inner to the outer boundary of the models. Geomagnetic observations suggest the presence of magnetic structures similar to those found in our models; thus, we discuss how our results may pertain to Earth's core dynamo processes. In order to make DMFI a standard tool for numerical dynamo studies, a public software package is available upon request to the authors (supplementary material is available at: http://www.ipgp.jussieu.fr/∼aubert/DMFI.html).

Key words: Dynamo: theories and simulations; Geomagnetic excursions; Geomagnetic induction; Reversals: process, timescale, magnetostratigraphy.

1 INTRODUCTION

The theoretical understanding of the geodynamo has been deeply influenced by Alfvén's frozen flux theorem (Alfvén 1943), which states that in a perfectly conducting fluid, magnetic field lines move with the medium, as if they were material lines frozen into it. In the wake of Alfvén's theorem, and before the availability of numerical dynamos, conceptual models (such as the Zeldovitch and Alfvén rope dynamos, for a review see Fearn *et al.* 1988) have been proposed to explain how, following frozen-flux theory, fluid motion could regenerate a pre-existing magnetic field, through the stretching, twisting and folding of magnetic field lines. In the Earth's liquid iron core, the dynamo process occurs in a highly, but not infinitely conducting fluid, where a frozen-flux approximation can be applied within certain limitations: Alfvén's theorem is considered as valid for larger length scales and timescales shorter than, say, a century (Roberts & Scott 1965; Roberts & Glatzmaier 2000).

Since the advent of numerical dynamos, a major goal is to understand their working mechanisms, and the frozen-flux approximation has proven to be a useful theoretical concept, providing a framework for the explanation of geomagnetic observations in terms of field line dynamics (e.g. Olson *et al.* 1999). Although the progress of computer graphics has permitted easier imaging of field lines, three major difficulties still remain: first, the limited applicability of the frozen-flux concept in a finitely conducting fluid complicates the interpretation. Fortunately, the magnetic Reynolds number, which measures the importance of magnetic diffusion in the dynamo process, is of comparable magnitude in Earth and in many dynamo simulations, $Re_m \approx 500$–1000 (e.g. Christensen & Tilgner 2004). The frozen-flux approximation is, therefore, expected to fail to a similar extent in numerical models and in the core. Magnetic field lines should, therefore, not only move with the fluid, but also diffuse due to Ohmic dissipation, adding another degree of complexity. Second, we face the problem of selecting the right field lines (through a choice of anchor points) that illustrate the relevant features of the dynamo process. If we depict too many lines the result will tend to resemble a 'bowl of spaghetti', blurring the interesting dynamic processes rather than highlighting them. Ideally, we concentrate on just a few field lines that happen to pass through the dynamically meaningful regions. Third, in a time-dependent system the time evolution

Table 1. Set of numerical models, and estimated parameters for the Earth's core. The magnetic Reynolds number Re_m and relative dipole strength $f_{\rm dip}$ are defined as in Christensen & Aubert (2006): $Re_m = UD/\lambda$, where U is the time average, root-mean-squared velocity in the shell, and $f_{\rm dip}$ is evaluated at the outer boundary of the shell as the time average, root-mean-squared amplitude of the dipole relative to the total magnetic field. Earth's core estimates are obtained from Jackson *et al.* (2000), Christensen & Tilgner (2004) and Christensen & Aubert (2006). The Prandtl number in the Earth's core can be either of order 10^{-2} (thermal convection) or much larger than one (chemical convection).

System	Driving	Ra^*	E	Pm	Pr	Re_m	Reversals?	$f_{\rm dip}$(stable)
C	Chemical	3	3×10^{-4}	3	1	514	Yes	0.23
T	Thermal	7	2×10^{-2}	10	1	110	Yes	0.35
Earth's core	Thermochemical	$\approx 10^{-5}$	$\approx 10^{-14}$	$\approx 10^{-6}$	?	≈ 1000	Yes	0.64 (in 1990)

of the anchor points has to be specified, in a way that ensures that the lines are being followed through time. The frozen-flux approximation requires us to follow material particles, but we risk missing effects related to Ohmic dissipation.

In this paper, we introduce the Dynamical Magnetic Field line Imaging technique (DMFI), which has been developed to represent the time evolution of relevant magnetic field lines in numerical dynamos, and thus provides visual support to the interpretation of their dynamics. The technique is not dependent on the applicability of the frozen-flux approximation, and allows us to image field line creation and dissipation, in addition to events related with advection and deformation. We first identify magnetic structures and highlight their relations with flow structures. This provides a visual confirmation of several previously published dynamo mechanisms. DMFI animations of Earth-like numerical dynamos are then used to highlight, for the first time, the field line mechanism of simulated polarity excursions and reversals.

2 MODELS AND TOOLS

2.1 Numerical models

We consider an electrically conducting, incompressible fluid in a spherical shell of aspect ratio 0.35, rotating about an axis $\mathbf{e}_z$ with constant angular velocity Ω. We solve the magnetic induction equation for the magnetic field $\mathbf{B}$ in the MHD approximation, the Navier–Stokes and thermo-chemical transport equations for the velocity field $\mathbf{u}$ and codensity C (which expresses the density anomaly resulting from a superadiabatic temperature, or excess concentration in light elements) in the Boussinesq approximation. The mechanical boundary conditions are of rigid type. The outer boundary is electrically insulating, while the inner boundary can be either conducting (in model T, see Table 1) or insulating (in model C). The influence of a change in the latter boundary condition is generally thought to be insignificant for Earth's core geometry (Wicht 2002). Our equation system is identical to that given in Christensen & Aubert (2006), except for the use of a codensity formulation for the Boussinesq buoyancy (Braginsky & Roberts 1995; Kutzner & Christensen 2002). The codensity C describes the combined effects of thermal and chemical buoyancies and follows a standard transport equation

$$\frac{\partial C}{\partial t} + \mathbf{u} \cdot \nabla C = \kappa \nabla^2 C + \beta. \qquad (1)$$

Here the thermal and chemical diffusivities are assumed to have the same value κ, representing the effects of the turbulent mixing that acts on the temperature and chemical concentration fields. The term β arises in the Boussinesq approximation to describe the cooling of the reference adiabatic thermal state, the non-zero divergence of the adiabatic thermal gradient, and the enrichment in light elements of the reference chemical state. We choose an end-member thermal model by setting $\beta = 0$ for simplicity, and using a constant temperature difference ΔT between the inner and outer boundary. For an end-member chemical model, we choose a negative uniform β, and adopt a fixed codensity at the inner boundary, and zero codensity flux at the outer boundary. The dimensionless control parameters of the

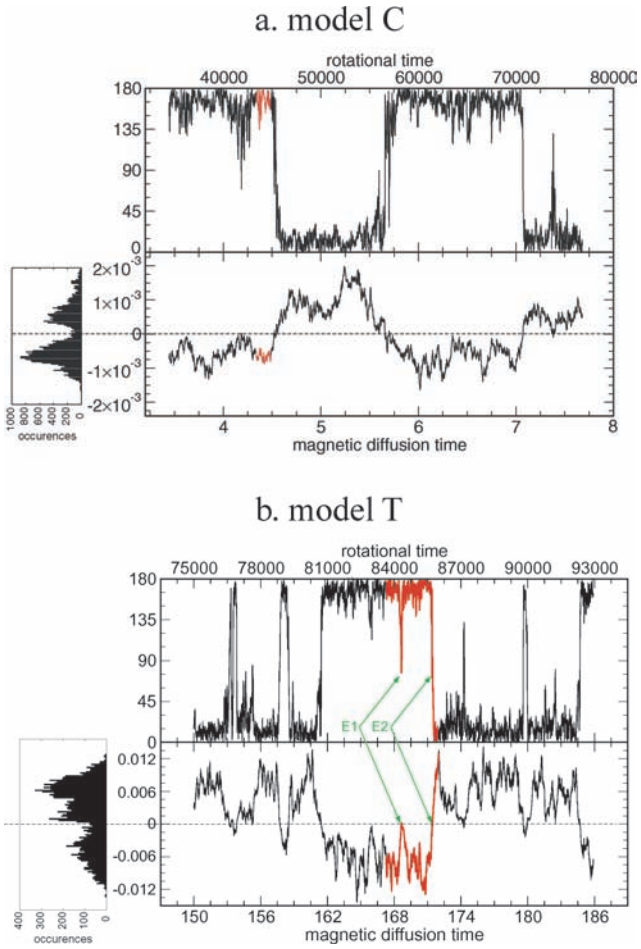

Figure 1. Dipole colatitude in degrees (upper panels), and g_1^0 axial dipole Gauss coefficient of the magnetic potential at the outer boundary (lower panels) as a function of time, for (a) model C and (b) model T. Histograms of the g_1^0 distribution are shown on the left-hand side. The red curves represent the time intervals imaged by DMFI in movies 1 (C) and 2 (T). Time is given in both units of the rotational time $1/\Omega$ (upper axis) and the magnetic diffusion time D^2/η (lower axis). The axial dipole gauss coefficient is given in units of $(\rho\mu)^{1/2}\Omega D$, where ρ and μ are, respectively, the fluid density and magnetic permeability.

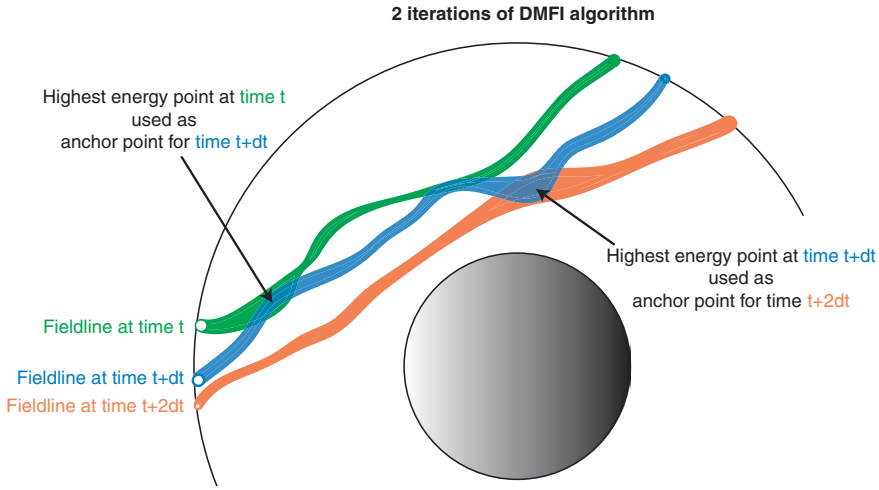

Figure 2. Sketch of the DMFI time-stepping algorithm used to choose dynamically evolving anchor points for the magnetic field lines. The algorithm is initialized with anchor points sampling the radial magnetic field patches at the external boundary of the shell. Subsequently, the anchors are floating and follow the points of maximum magnetic energy along each line (i.e. the points where the lines are thickest in DMFI representation).

system are the Ekman number $E = \nu/\Omega D^2$, Prandtl number $Pr = \nu/\kappa$, magnetic Prandtl number $Pm = \nu/\lambda$, and the Rayleigh number, which is given by $Ra^* = \alpha g_o \Delta T/\Omega^2 D$ and $Ra^* = g_o|\beta|/\Omega^3 D$ for thermal and chemical models, respectively. Here D is the spherical shell gap, g_o is the gravity at the outer boundary of the shell, α is the thermal expansion coefficient, ν and λ are, respectively, the viscous and magnetic diffusivities of the fluid. We use the new PARODY numerical implementation of the equations, written by Emmanuel Dormy and Julien Aubert. PARODY uses a spherical harmonics decomposition in the lateral direction, and a second-order finite differencing scheme in the radial direction, which makes it suitable for parallel computation on distributed memory clusters. PARODY has been benchmarked against other major implementations (Christensen *et al.* 2001).

Table 1 presents the input and output parameters of the models which we have analysed in this study, as well as values inferred for Earth's core conditions. Numerical models operate in a parameter range which is very remote from that of natural objects. As a result, the flow is much too viscous and short-timescale, small-scale phenomena are not simulated. Yet the structure of large-scale (more than 1000 km) and long-timescale (centennial to millennial) flow shows similarities with what is expected from the flow in the Earth's core (e.g. Amit & Olson 2006; Aubert *et al.* 2007), and, due to the relatively small value of the magnetic Reynolds number (which, incidentally, can be reached with numerical models), the magnetic induction should not feel the smaller flow scales (Christensen & Tilgner 2004). A comparison between the output of numerical models and the geomagnetic observations should, therefore, be limited to larger scales and longer timescales.

Time-series of the magnetic dipole tilt and axial dipole component are reported in Fig. 1. The control parameters in models C and T have been selected in the literature (respectively from Kutzner & Christensen 2002; Wicht 2005) for the similarity of some of the model outputs with what is known of the geomagnetic and palaeomagnetic field: a reasonably Earth-like magnetic Reynolds number Re_m (see Table 1 for definition) and the existence of well-defined stable and reversing polarity phases. More quantitatively, this corresponds to the existence of a bi-modal histogram of the g_1^0 axial dipole Gauss coefficient of the CMB magnetic potential (Valet & Meynadier 1993). As one increases the convective forcing, the onset of reversals is usually close to the point where the dipole part of the generated magnetic field ceases to dominate the magnetic spectrum (Olson & Christensen 2006). Within the parameter range currently accessible to numerical dynamos, it is, therefore, difficult to obtain reversals while maintaining a significant relative dipole strength $f_{\rm dip}$ during stable polarity phases, as observed for the Earth's core.

2.2 Outline of DMFI visualization

The DMFI algorithm relies on 15 floating anchor points seeded inside the fluid shell. The anchor points are not used as terminations of field lines. Rather, from each point we draw the field line corresponding to the magnetic field $\mathbf{B}$, and that corresponding to the magnetic field $-\mathbf{B}$. Using this method, we are able to draw field lines through our floating anchors, which terminate as they reach the outer boundary of the spherical shell (the outside potential field is not depicted). The field lines are rendered as tubes with a thickness which is proportional to the local magnetic energy $\mathbf{B}^2$ (Fig. 3a). Such a representation naturally depicts the most energetic field lines in the fluid interior and, thus, assigns less visual impact to lines which carry little magnetic energy.

Fig. 2 is a sketch of the time-stepping algorithm for floating anchor points: After rendering field lines at time t, the algorithm searches for the point of maximum magnetic energy along each line (the point where the line is thickest), and selects it as the new anchor point for time $t + \mathrm{d}t$. This ensures representation of the most energetic magnetic field structures. We have performed a simple test of the relevance of DMFI in Fig. 3(b). An isosurface of the magnetic energy has been represented at a level of 10 per cent of the maximal magnetic energy, which is also approximately eight times the mean magnetic energy. This isosurface encloses 25 per cent of the total energy in the shell, in 1.6 per cent of the shell volume. The magnetic energy distribution in the shell is volumetrically quite sparse, as previously noted by Kageyama & Sato (1997), and, thus, is accurately represented through the field lines chosen by the DMFI algorithm.

Our models C and T have been visualized using DMFI, and the results are presented in the supplementary movies 1 and 2 of this paper. The DMFI-imaged time intervals are marked in red in Fig. 1.

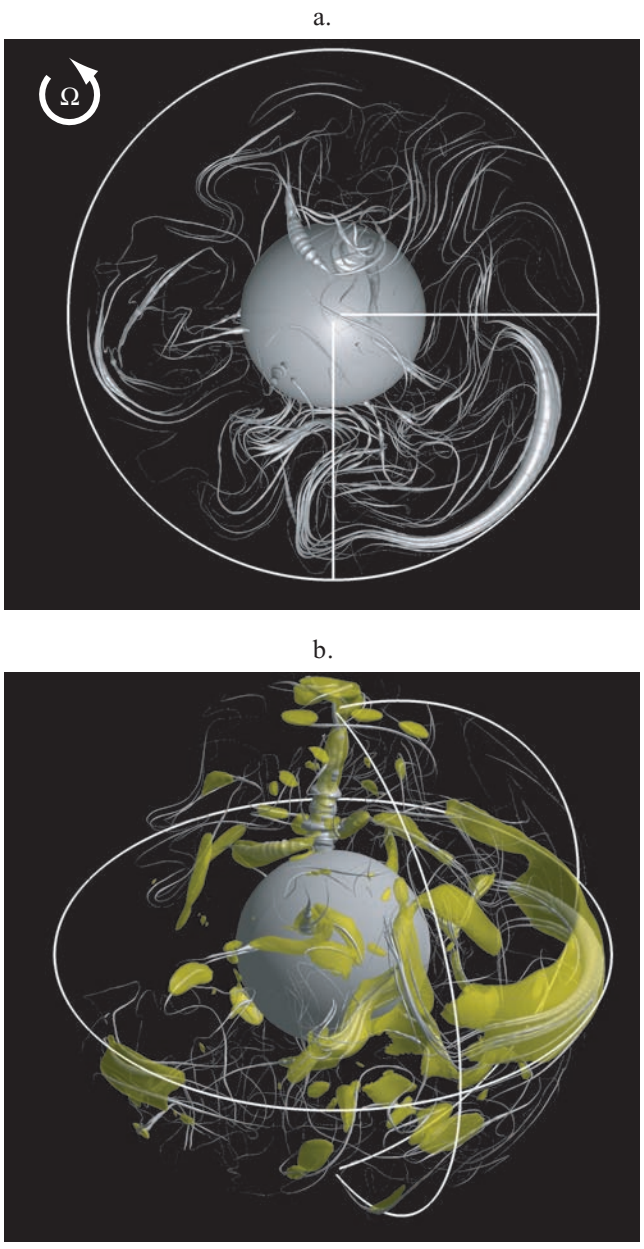

Figure 3. (a) Top view (the $\mathbf{e}_z$ vector is pointing towards the reader) of a DMFI snapshot in model C, at magnetic diffusion time 4.36078. Magnetic field lines are rendered with a thickness proportional to $\mathbf{B}^2$. Two meridians (at $\varphi = 0^\circ$ and $\varphi = 270^\circ$) and the equator are drawn in white. (b) Side view of same model. A magnetic energy isosurface (yellow) is drawn at 10 per cent of the maximal value, enclosing 25 per cent of the total magnetic energy in 1.6 per cent of the shell volume.

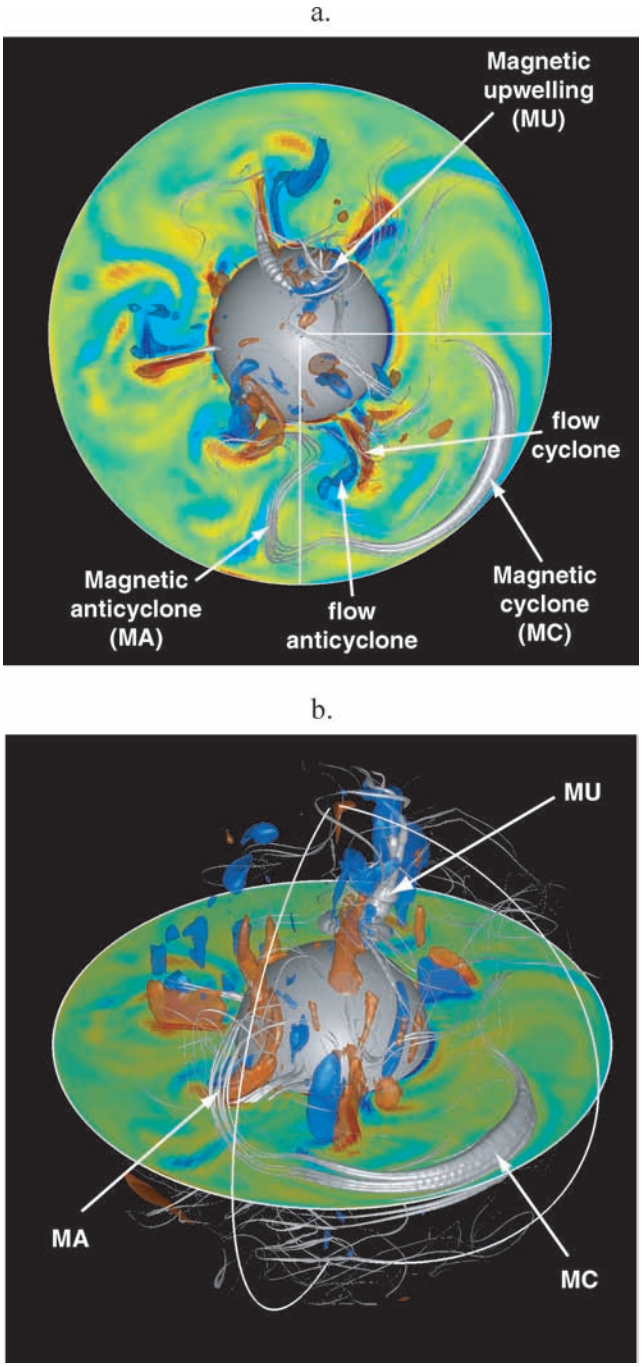

Figure 4. Top (a) and side (b) views of DMFI field lines in model C at magnetic diffusion time 4.36078, with same conventions as in Fig. 3. The equatorial plane is colour-coded with the axial vorticity $\omega_z = \boldsymbol{\omega} \cdot \mathbf{e}_z$ (colour map from -3, blue to +3, red, in units of Ω). Two volume isosurfaces of ω_z are represented at levels −1.5 (blue) and 1.5 (red).

3 RESULTS

3.1 Magnetic structures and time-dependent dynamo mechanisms

In this section, we examine the mechanisms governing the time evolution of magnetic field lines. The magnetic Reynolds number Re_m measures the relative importance of creation and advection with respect to diffusion and should be as Earth-like as possible for geophysical relevance. We therefore, choose to study model C in detail. This model is however quite intricate due to the small-scale character of magnetic structures and weak dipolarity. We therefore also use model T, which has larger scale structures and a more dipolar field morphology, to illustrate some aspects of the dynamo process. Note, however, that model T has a significantly lower Re_m.

Fig. 4 shows a coupled visualization of DMFI field lines and flow vortices, represented through the axial component $\omega_z = \boldsymbol{\omega} \cdot \mathbf{e}_z$ of the vorticity $\boldsymbol{\omega} = \nabla \times \mathbf{u}$. The Coriolis force organizes the

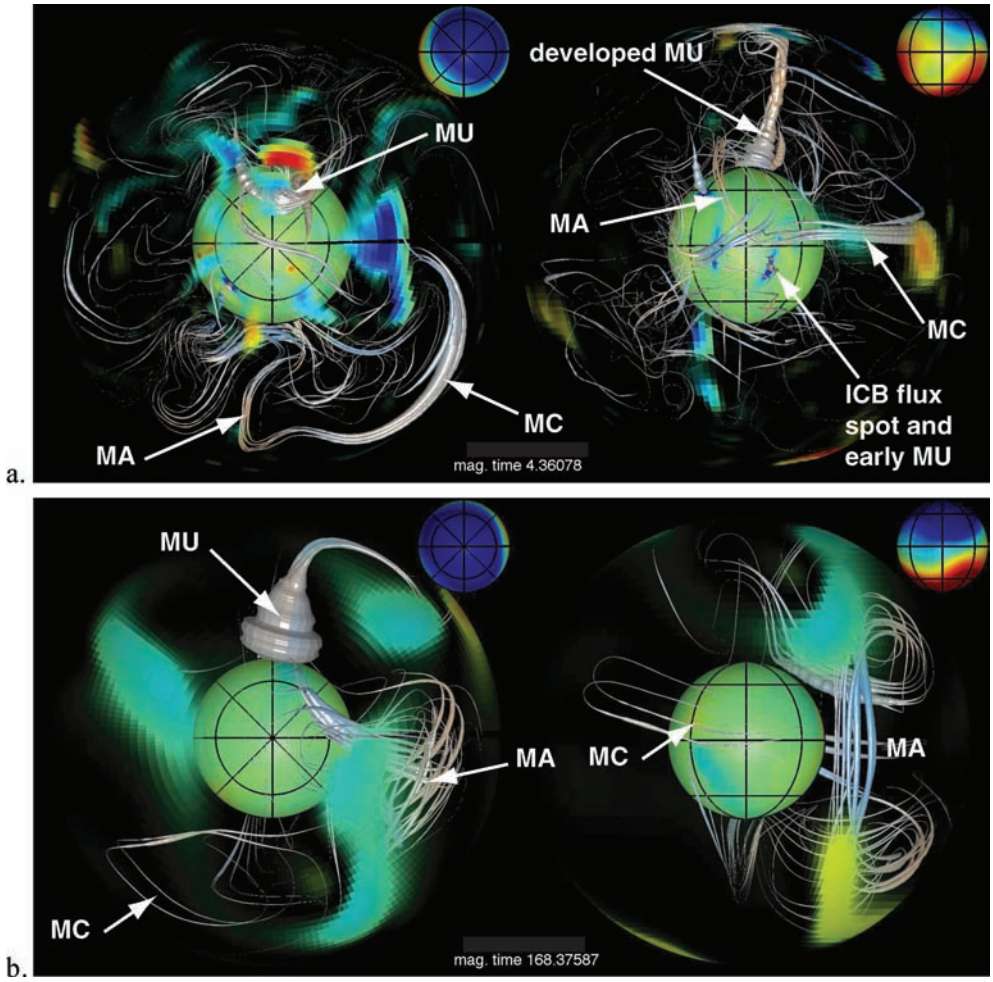

Figure 5. Snapshots from (a): DMFI movie 1 of model C and (b): movie 2 of model T. Left-hand panels: top view. Right-hand panels: side view. The inner (ICB) and outer (CMB) boundaries of the model are colour-coded with the radial magnetic field (a red patch denotes outwards oriented field). In addition, the outer boundary is made selectively transparent, with a transparency level that is inversely proportional to the local radial magnetic field. Field lines are also colour-coded in order to indicate $\mathbf{e}_z$-parallel (red) and antiparallel (blue) direction. The radial magnetic field as seen from the Earth's surface is represented in the upper-right inserts, in order to keep track of the current orientation and strength of the large-scale magnetic dipole. Colour maps for (a): ICB field from -0.12 (blue) to 0.12 (red), in units of $(\rho\mu)^{1/2}\Omega D$, CMB field from -0.03 to 0.03, Earth's surface field from $-2\ 10^{-4}$ to $2\ 10^{-4}$. For (b): ICB field from -0.72 to 0.72, CMB field from -0.36 to 0.36, Earth's surface field from $-1.8\ 10^{-3}$ to $1.8\ 10^{-3}$.

vortices into columns elongated along the $\mathbf{e}_z$ axis of rotation, due to the Proudman–Taylor constraint. The sparse character of the magnetic energy distribution results from the tendency of field lines to cluster at the edges of flow vortices due to magnetic field expulsion (Weiss 1966; Galloway & Weiss 1981). Since magnetic field lines correlate well with the flow structures in our models, we will subsequently visualize the magnetic field structure alone. The supporting movies of this paper (see Fig. 1 for time window and Figs 5–9 for extracts) present DMFI field lines, together with radial magnetic flux patches at the inner boundary (which we will refer to as ICB) and the selectively transparent outer boundary (CMB). We will first introduce the concept of a magnetic vortex, which is defined as a field line structure resulting from the interaction with a flow vortex. By providing illustrations of magnetic cyclones and anticyclones, DMFI provides a dynamic, field-line based visual confirmation of previously published dynamo mechanisms (Kageyama & Sato 1997; Olson *et al.* 1999; Sakuraba & Kono 1999; Ishihara & Kida 2002), and allows the extension of such descriptions to time-dependent, spatially complex dynamo regimes.

3.1.1 Magnetic cyclones

A strong axial flow cyclone (red isosurface in Fig. 4) winds and stretches field lines to form a magnetic cyclone. Fig. 6 relates DMFI visualizations of magnetic cyclones, as displayed in Figs 4 and 5, with a schematic view inspired by Olson *et al.* (1999). A magnetic cyclone can be identified by the anticlockwise motion of field lines clustered close to the equator, moving jointly with fairly stable high-latitude CMB flux patches concentrated above and below the centre of the field line cluster. Model C (movie 1, Fig. 5a) exhibits very large-scale magnetic cyclones (times 4.3617, 4.3811), which suggest an axial vorticity distribution biased towards flow cyclones. Inside these vortices, the uneven distribution of buoyancy along $\mathbf{e}_z$ creates a thermal wind secondary circulation (Olson *et al.* 1999), which is represented in red on Fig. 6. This secondary circulation concentrates CMB flux at high latitudes, giving rise to relatively long-lived (several vortex turnovers) flux patches similar to those found in geomagnetic field models. Simultaneously, close to the equatorial plane, the secondary circulation concentrates field lines into bundles and also pushes them towards the outer boundary, where

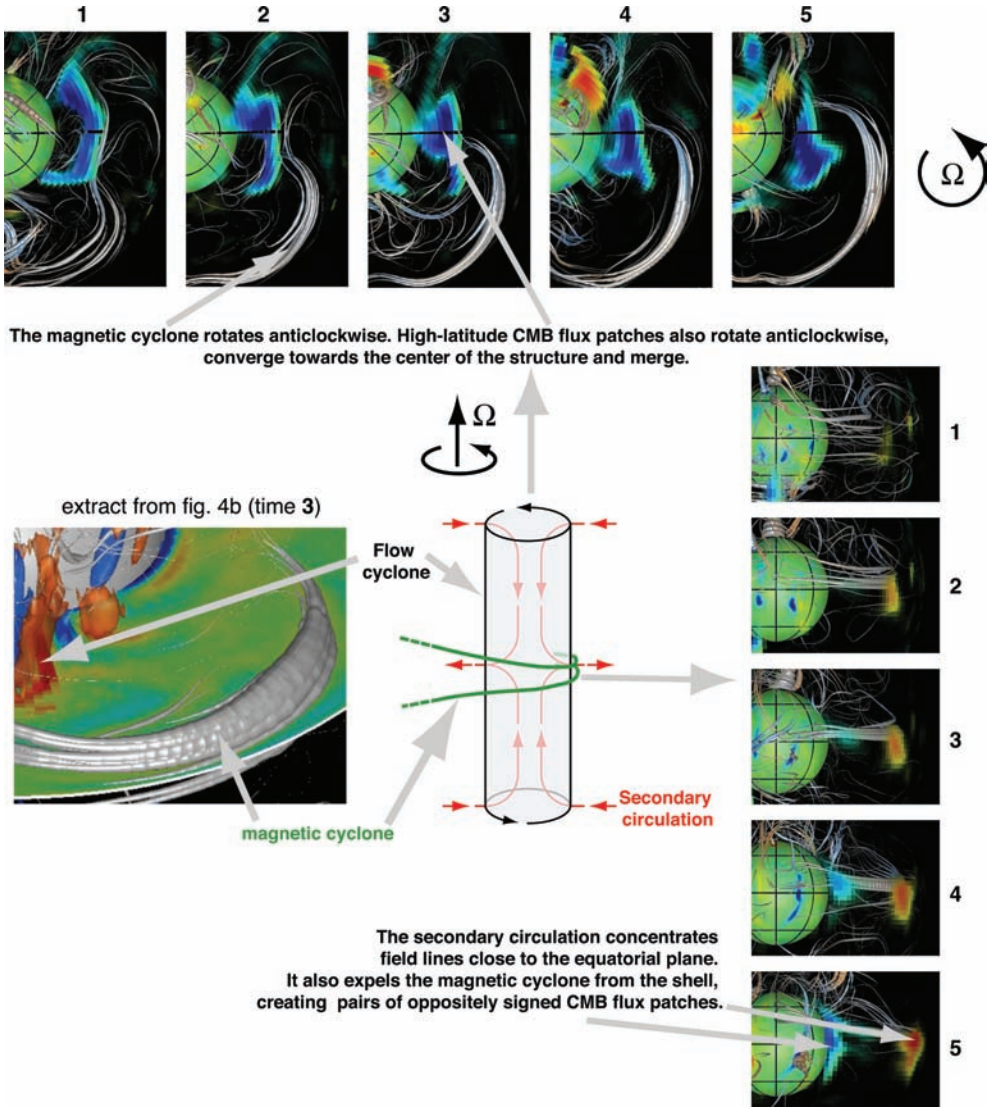

Figure 6. Schematic description of the generation of a magnetic cyclone, together with DMFI extracts from movie 1 (model C). The sequence snapshots 1–5 are taken from times 4.35982, 4.36030, 4.36078, 4.36127, 4.36187.

they are ultimately expelled from the shell, creating pairs of CMB patches with oppositely signed flux in a kinematic mechanism similar to that envisaged by Bloxham (1986). These low-latitude CMB flux features are rather short-lived (typically a vortex turnover) because there is no flow producing a dynamo cycle to sustain them; their decay involves significant Ohmic dissipation, in violation of the frozen-flux theorem.

3.1.2 Magnetic anticyclones

The magnetic anticyclones, which result from the magnetic field interaction with axial flow anticyclones (blue isosurfaces in Fig. 4) can be recognized through their characteristic shape illustrated on Fig. 7, underlying an alpha-squared dynamo mechanism (Olson *et al.* 1999). Since model C is biased towards flow cyclones, we rather use model T (movie 2 at time 168.375, Figs 5b and 7), for a clearer picture. An initial poloidal field is first wound by the anticyclone in the azimuthal (toroidal) direction. Flow anticyclones have the opposite secondary circulation to flow cyclones. The northern and southern toroidal parts of the line are, therefore, stretched away from the equatorial plane as the line winds into the anticyclone. This stretching regenerates a poloidal field line with the same polarity as the initial line. The flux from the newly generated poloidal field lines reaches the outer boundary, creating high-latitude CMB flux patches of normal polarity above and below the magnetic anticyclone. These patches are usually short-lived (less than a vortex turnover), because they are pushed away by a secondary circulation which has the exact opposite effect to that of magnetic cyclones.

3.1.3 Magnetic upwellings

Among the most remarkable structures highlighted by DMFI sequences, we define magnetic upwellings as energetic field lines generated within buoyancy-driven flow upwellings. These have previously received much less attention than magnetic vortices: their existence has been previously suspected from the analysis of poloidal field line dynamics during reversals (Wicht & Olson 2004), or through the appearance of tangent cylinder CMB flux patches closely related to helical flow upwelling plumes (Sreenivasan & Jones 2006). Here we provide the first description of their structure and dynamics. Models C and T show intermittent magnetic upwellings, either inside (Figs 5a and 8, times 4.3609, 4.4696 in movie

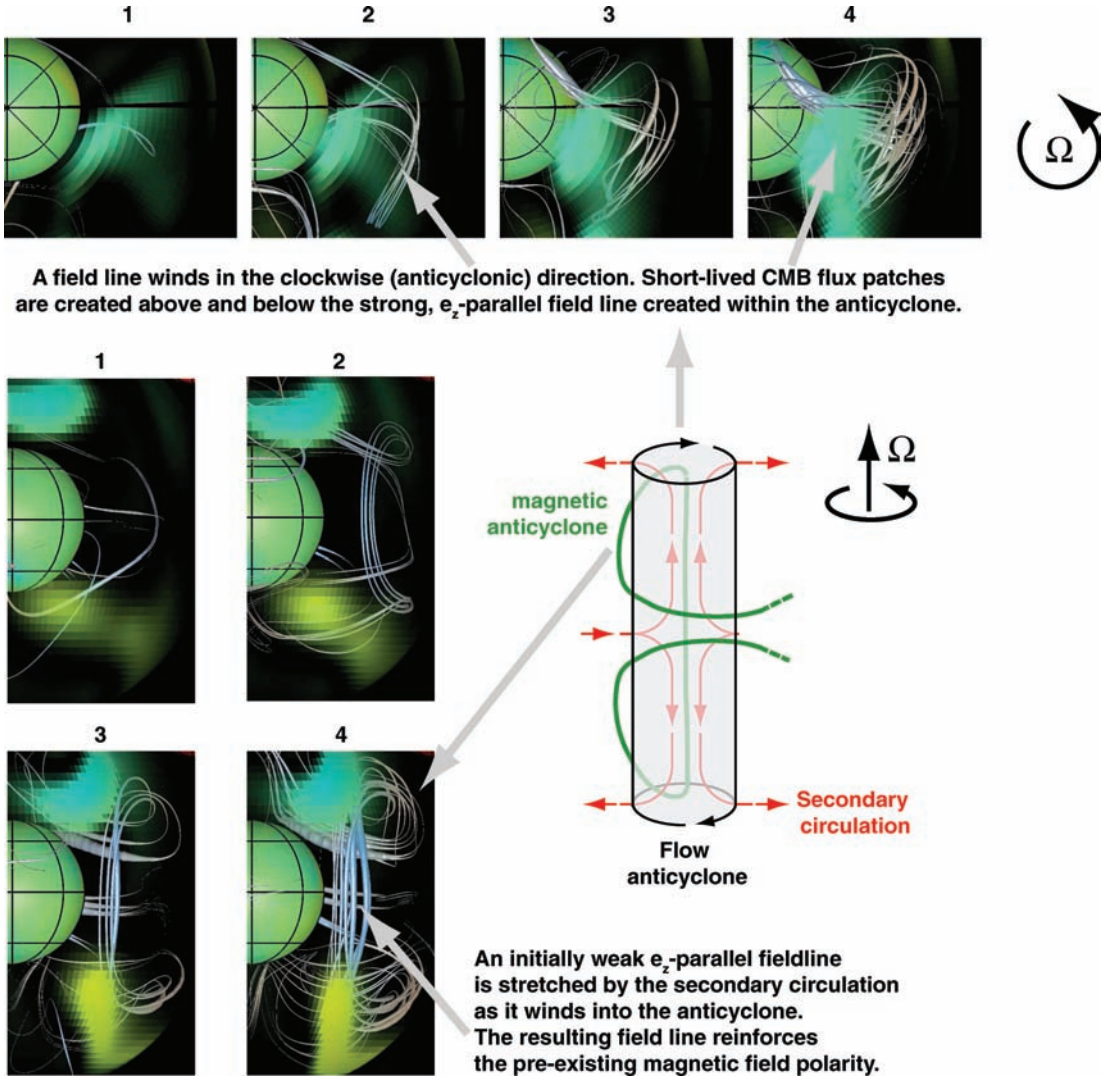

Figure 7. Schematic description of the generation of a magnetic anticyclone, together with DMFI extracts from movie 2 (model T). The sequence snapshots 1–4 are taken from times 168.366, 168.369, 168.373 and 168.376.

1) or outside the tangent cylinder (Figs 5b and 9, time 4.3575 in movie 1, 171.306 in movie 2). Inside the tangent cylinder, they are mostly parallel to, but not necessarily colinear with $\mathbf{e}_z$. Outside the tangent cylinder, they are mostly parallel to the cylindrical radial direction, and are found close to the equatorial plane.

Fig. 8 schematically describes our model mechanism for the creation of a polar magnetic upwelling. Thermal wind-driven plumes reside within the tangent cylinder (Aurnou *et al.* 2003; Aubert 2005). At the base of these upwellings, a converging flow concentrates the ICB magnetic flux into intense spots, which seed the magnetic field growth. The magnetic stretching $(\mathbf{B}\cdot\mathbf{e}_z)\partial(\mathbf{u}\cdot\mathbf{e}_z)/\partial z$ (which is part of the induction term in the magnetohydrodynamic induction equation) is responsible for the magnetic field amplification close to the ICB. The magnetic field line is subsequently advected towards the CMB, where the negative $\partial(\mathbf{u}\cdot\mathbf{e}_z)/\partial z$ de-amplifies the magnetic field. As a result, only a small part of the field **B** from the magnetic upwelling directly exits across the CMB. However, the stretching $\partial(\mathbf{u}\cdot\mathbf{e}_z)/\partial z$ also acts on the ambient vorticity field $\mathbf{2\Omega}$ to create anticyclonic helical flow, inducing a strong magnetic field **B** (Fig. 8a). When the helical plume axis is nearly colinear with the rotation axis, then **B** is purely azimuthal. In this situation, none of the induced magnetic flux should exit across the CMB. This can explain why CMB flux patches are not observed above magnetic upwellings which are aligned closely with the rotation axis (for instance in movie 1 at time 4.4706). However, strong CMB patches often arise while the helical plumes are migrating in cylindrical radius (Fig. 8, DMFI snapshot 3), when their axes are bending away from the axial direction (snapshot 4), or when they are unravelling (snapshot 5). Away from the rotation axis, the tops of the helical plumes efficiently push induced azimuthal flux across the CMB on the side of the plume at larger cylindrical radius, as shown schematically in Figs 8(b) and (c). This model predicts that high latitude flux patches will occur in oppositely signed pairs. However, qualitative review of the DMFI sequences (see Fig. 8) suggests that a bias may exist towards the polarity carried by the underlying magnetic upwelling. We hypothesize that some of the ambient field **B** reaches the CMB, in addition to the induced field due to the upwelling, **B**. This may be due to an asymmetric effect of the positive (amplifying) and negative (de-amplifying) upwelling along the upwelling path, or to the effect of magnetic diffusion.

Equatorial magnetic upwellings (Fig. 9) are created close to the equatorial part of the ICB, where the concentrated magnetic flux

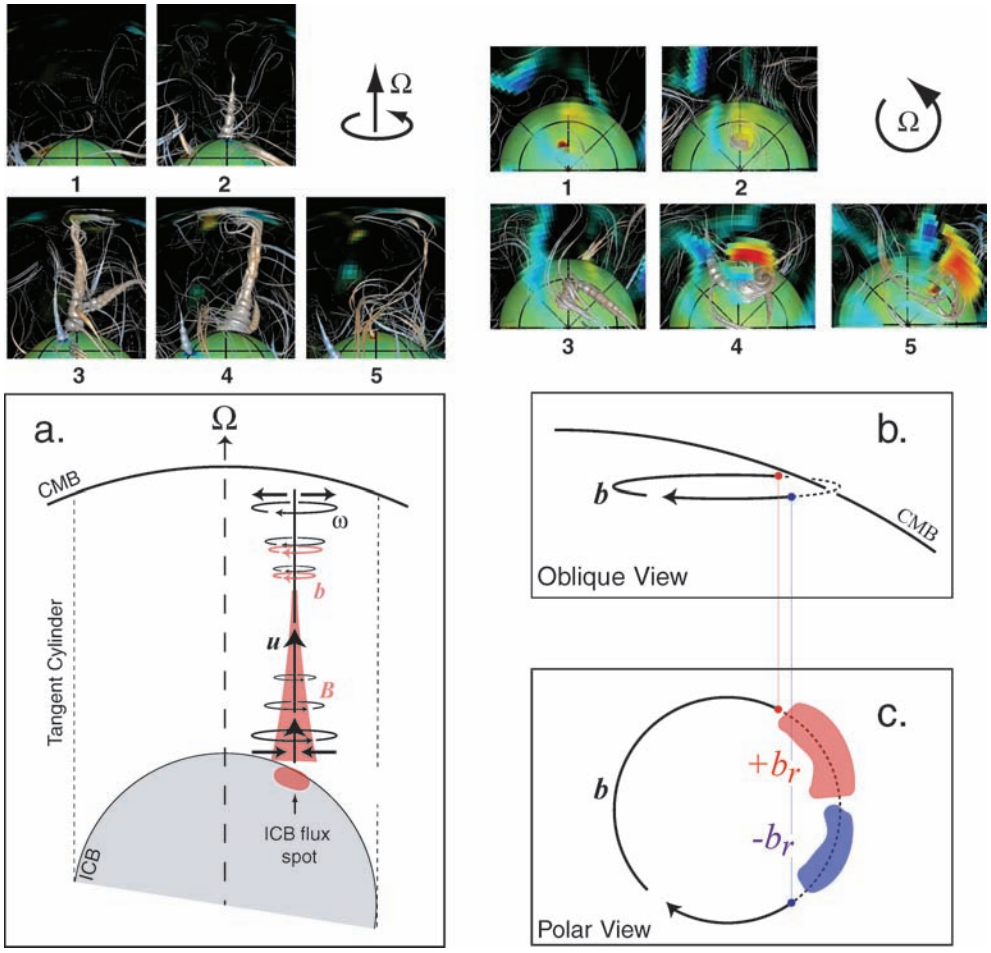

Figure 8. Mechanism for the generation of polar magnetic upwellings, together with DMFI images of model C (times 1–5, respectively, correspond to magnetic diffusion times 4.3584, 4.3589, 4.3598, 4.3608 and 4.3613). (a) Schematic side view of a polar magnetic upwelling. The converging flow beneath ICB upwellings concentrates magnetic flux patches into intense spots seeding the magnetic field growth. Stretching and advection inside the upwellings subsequently amplify the magnetic field bundle which rises in the $\mathbf{e_z}$ direction. Magnetic upwellings inside the tangent cylinder rise within helical flow plumes which are not colinear but parallel to the rotation axis. (b) Oblique close-up of the magnetic field induced by the helical flow plume, **b**, crossing the CMB within the tangent cylinder. (c) Top view of the induced field, **b**, and associated entering (blue) and exiting (red) CMB flux patches.

patches get near to the quasi-geostrophic columnar flow upwellings residing outside the tangent cylinder. The mechanism for their generation is largely the same as that of polar magnetic upwellings. However, they are not associated with helical flow plumes since the ambient vorticity field $\mathbf{2\Omega}$ is not stretched by cylindrical radial motion. Equatorial upwellings, therefore, lack the magnetic flux expulsion mechanism seen with polar upwellings, and have little to no observable signature at the CMB.

Helical plumes visualized using fluorescein dye (Fig. 10 and movie 3) in laboratory experiments of tangent cylinder convection (Aurnou *et al.* 2003) show a structure similar to that of magnetic upwellings imaged by DMFI in the tangent cylinder (DMFI sequence in Fig. 8). While dye is a passive tracer, the magnetic field should be seen as an active tracer, although Lenz's law predicts that it should minimize the disturbances caused to the flow. Both tracers are injected at the same location (ICB) and advected in a comparable manner by the two systems. This suggests that the flow inside a hydrodynamic helical plume in the experiment is similar to that found in the numerics, although helical plumes are typically more numerous (about 20 in the experiments of Aurnou *et al.* (2003)) when the magnetic field is absent (Sreenivasan & Jones 2005; Sreenivasan & Jones 2006). We note indeed that the vorticity and magnetic fields are both subject to stretching due to the upwelling $\partial(\mathbf{u}\cdot\mathbf{e}_z)/\partial z$. Close to the ICB, stretching the background vorticity field $\mathbf{2\Omega}$ and ambient magnetic field **B** in an upwelling plume [e.g. positive $\partial(\mathbf{u}\cdot\mathbf{e}_z)/\partial z$] will both create positive (cyclonic) axial vorticity and amplify **B**.

3.2 The mechanism of excursions and reversals

In our models, the bi-modal character of the g_1^0 axial dipole component histogram (Fig. 1), which is also present in the geomagnetic time-series (Valet & Meynadier 1993) suggests an attraction of the dynamo system towards a stable dipole either parallel or antiparallel with the axis of rotation. The field line loops found within magnetic anticyclones indeed provide a mechanism through which an existing predominantly axial dipole may be amplified and stabilized. However, the g_1^0 time-series in Fig. 1 also show that this attraction is frequently challenged by events breaking this polarity, leading to excursions and reversals of the dipole axis. These events may be linked to changes in the amplitude and distribution of CMB flux patches, as shown by Olson & Amit (2006) for the geomagnetic field. We now analyse the field line structure underlying these changes.

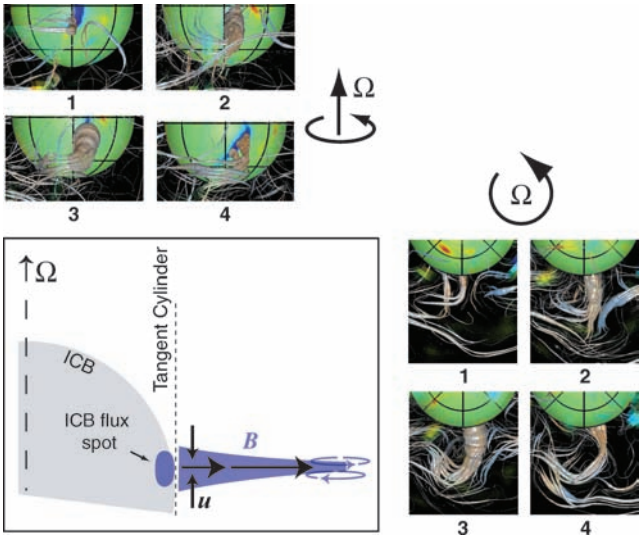

Figure 9. Mechanism for the generation of equatorial magnetic upwellings, together with DMFI images of model C (times 1–4, respectively, correspond to magnetic diffusion times 4.3563, 4.3569, 4.3573 and 4.3585). Same conventions as in Fig. 8.

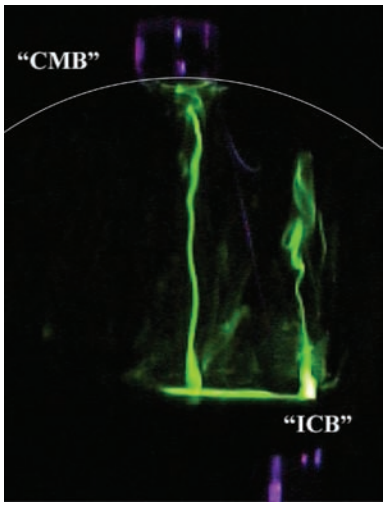

Figure 10. Sideview photograph of helical plumes in laboratory experimental simulations of tangent cylinder convection. Water is the working fluid; fluorescein dye marks the two plumes. Control parameters: flux Rayleigh number $Ra_F = 4.4 \times 10^9$; Ekman number $E = 4.3 \times 10^{-5}$, corresponding to a rotation period of $T = 7.0$ s, Prandtl number $Pr = 7$. Also, see supporting movie 3, made using a digital video camera in the rotating frame, which shows the formation and evolution of the helical plumes shown in this image over approximately 10 rotation periods. Further experimental details can be found in Aurnou *et al.* (2003).

The ICB magnetic field of our models generally has a much weaker axial dipole component than the CMB field (movies 1–2 and Fig. 5). Indeed the magnetic flux threading the ICB is influenced by chaotic concentration and mixing, while the CMB flux is ordered by magnetic anticyclones. The central observation brought by DMFI is that a polarity breaking event occurs when the ICB multipolar field is amplified and brought to the CMB by a coherent set of magnetic upwelling field lines. To illustrate this, we use model T which has a large-scale magnetic structure. Movie 2 contains two major polarity breaking events, both of which coincide with a large decrease of $|g_1^0|$ in Fig. 1. Event E1 occurs at magnetic diffusion time

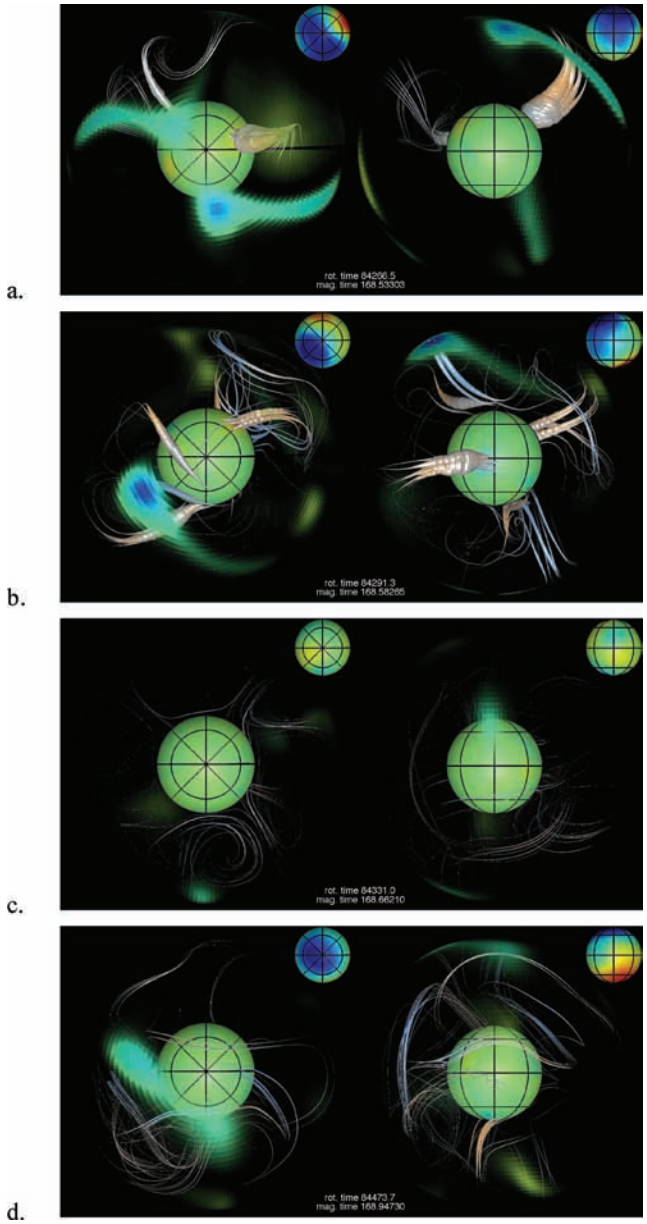

Figure 11. The steps involved in event E1, an excursion of the dipole axis occurring at time 168.52 in movie 2 (model T).

168.52 and leads to an excursion of the dipole axis. Event E2 occurs at time 171.32 and leads to a full reversal. The successive steps of these events are imaged in Figs 11 and 12. In movie 2, as well as Figs 11–12, the upper-right inserts indicate the magnetic field as it would be seen from the surface of the Earth. Moreover, the colour-coding of the field lines is important as it hints for their direction: field lines are red-tinted when directed upwards ($\mathbf{e}_z$-parallel), and blue-tinted when directed downwards ($\mathbf{e}_z$-antiparallel).

Event E1 starts with the rise of a magnetic upwelling in the northern hemisphere, within the tangent cylinder (Fig. 11a). Growing from an inverse (red) ICB flux spot, this structure has inverse polarity, and some of its flux exits at the CMB. The occurrence of this magnetic upwelling enriches the magnetic field inside the shell with an equatorial dipole component, which is then further amplified by equatorial magnetic upwellings (Fig. 11b). At time 168.583, the field lines of the original axial dipole (blue) co-exist with predominantly

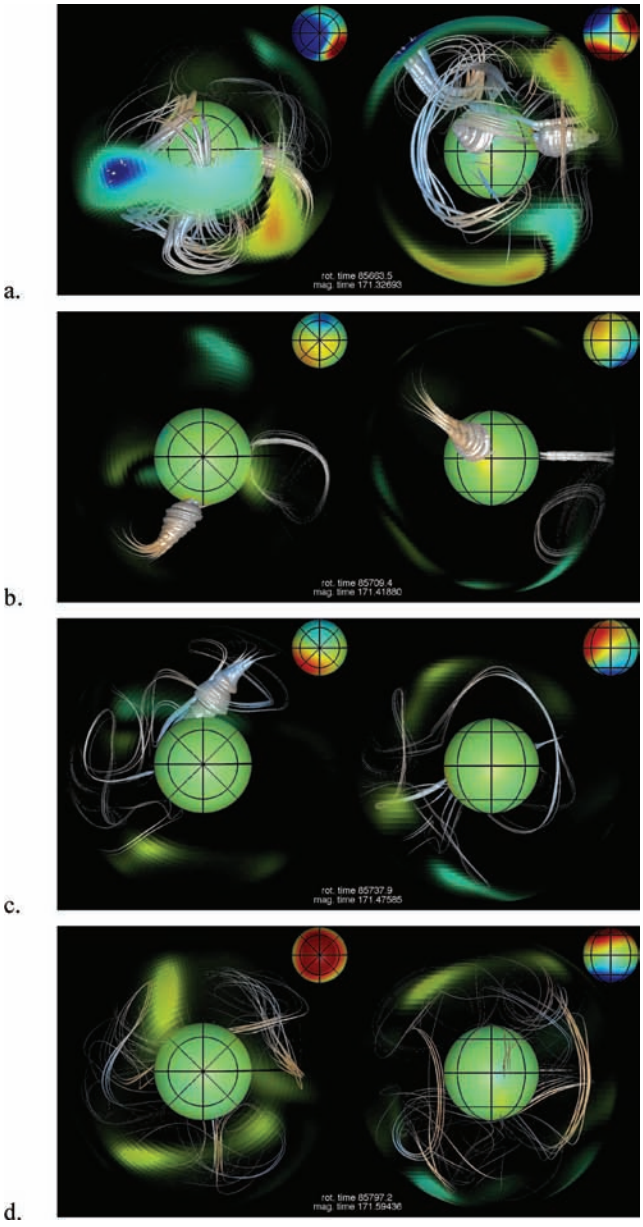

Figure 12. The steps involved in event E2, a full reversal of the dipole axis occurring at time 171.32 in movie 2 (model T).

equatorial field lines of inverse (red) polarity. In this context, faint magnetic anticyclones producing poloidal field lines of both polarities can be observed, which do not have a net effect on the regeneration of the axial dipole, which in turn collapses. The equatorial dipole component is also bound to collapse due to the intermittent character of the upwellings which maintain it. A low amplitude multipolar state, therefore, takes place in the whole shell, where again faint magnetic anticyclones of both polarities can be seen at different locations (Fig. 11c). After time 168.71 the normal polarity (blue) magnetic anticyclones take precedence, and regenerate an axial dipole in 0.2 magnetic diffusion times (Fig. 11d).

Event E2 starts with two equatorial magnetic upwellings, growing from ICB flux spots of opposite polarity, at the edges of adjacent axial vortices (Fig. 12a). The blue upwelling feeds a normal polarity (blue) magnetic anticyclone, while the red upwelling feeds an inverse polarity (red) magnetic anticyclone. At time 171.327 this competition between normal and inverse structures is felt at the CMB, as well as at the surface, through an axial quadrupole magnetic field. As in event E1, the axial dipole is not efficiently maintained by this configuration, leaving mostly equatorial field lines inside the shell, maintained by two equatorial magnetic upwellings (Fig. 12b), with slightly inverse (red) $\mathbf{e}_z$ orientation. Also similar to event E1, a competition between faint normal and inverse magnetic anticyclones can be observed (Fig. 12c) until time 171.5 where inverse structures take precedence and rebuild an axial dipole (Fig. 12d), thus completing the reversal sequence. The DMFI sequence for event E2 highlights the role of magnetic upwellings in a scenario which is broadly consistent with that proposed by Sarson & Jones (1999).

In the smaller-scale model C, the influence of magnetic upwellings on the dipole latitude and amplitude is not as clear-cut as in model T. Their appearance are, however, associated with tilting of the dipole axis as seen from the Earth's surface (see upper-right inserts in movie 1). Thus, we argue that two essential ingredients for the production of excursions and reversals in numerical dynamos are the existence of magnetic upwellings and a multipolar ICB magnetic field. This agrees with the models of Wicht & Olson (2004), in which the start of a reversal sequence was found to correlate with upwelling events inside the tangent cylinder.

4 DISCUSSION

Understanding the highly complex processes of magnetic field generation in the Earth's core is greatly facilitated by Alfvén's theorem and the frozen-flux approximation, provided one supplies an imaging method which is adapted to the intrinsically 3-D and time-dependent nature of the problem, and also takes into account diffusive effects. The DMFI technique used in the present study aims at achieving this goal, and highlights several magnetic structures: magnetic anticyclones are found outside axial flow anticyclones, and regenerate the axial dipole through the creation of magnetic loops characteristic of an alpha-squared dynamo mechanism. Magnetic cyclones are found outside axial flow cyclones, and concentrate the magnetic flux into bundles where significant Ohmic dissipation takes place. Our description of magnetic vortices confirms and illustrates previously published mechanisms, as presented for instance by Olson *et al.* (1999). By separating the influence of cyclones and anticyclones, we extend these views to more complex cases where there is a broken symmetry between cyclonic and anticyclonic motion. Furthermore, we present the first field line dynamic descriptions of magnetic upwellings, which are created by field line stretching and advection inside flow upwellings.

Our models show that the magnetic structures are robust features found at high (model T) as well as moderately low (model C) values of the Ekman number. This suggests that they pertain to the Earth's core. Since we only have access to the radial component of the magnetic field at the Earth's CMB, our description of the magnetic structure underlying CMB flux patches in the models is of particular interest. Inside the tangent cylinder, short-lived CMB patches of both polarities can be created by the expulsion of azimuthal flux within a magnetic upwelling. These patches are quickly weakened by the diverging flow on the top of the upwelling, therefore, they do not last more than a vortex turnover, which is equivalent to 60–300 yr in the Earth's core (Aubert *et al.* 2007). The observation of a tangent cylinder inverse flux patch in the present geomagnetic field (Olson & Aurnou 1999; Jackson *et al.* 2000; Hulot *et al.* 2002), although it is weakly constrained and not observed with all field regularizations

(Jackson 2003), could support the existence of short-lived magnetic upwellings in the Earth's core.

The origin of the ubiquitous high-latitude flux patches observed outside the tangent cylinder could be attributed to both magnetic anticyclones and cyclones. However, only cyclones can sustain long-lived (several vortex turnovers, centennial to millennial timescales) magnetic flux patches, such as observed in historical geomagnetic field models. In contrast, the sudden appearance of a mid-latitude reversed flux patch, as seen in present-day observations below the southern tip of Africa, could be attributed to a reverse magnetic anticyclone fed by an underlying equatorial magnetic upwelling (which itself does not have a CMB signature).

At low latitudes, magnetic cyclones tend to create oppositely signed pairs of flux patches, while the geomagnetic observations argue more for chains of intense equatorial flux spots of the same polarity (Jackson 2003). While this is an observation that the current generation of numerical models clearly fails to reproduce, we can infer that such an arrangement of flux spots could be caused by a meandering toroidal field line, such as observed for instance in movie 1 at time 4.41450. The meandering is caused by an arrangement of alternating flow cyclones and anticyclones. The expulsion of such a line, over a background poloidal field biased towards one polarity, could cause the observed flux spot chain, as proposed earlier by Finlay (2005).

In this study, we have provided the first field line-based description of the mechanisms of excursions and reversals. As already suggested by Wicht & Olson (2004), little or no dramatic changes in the fluid flow are needed to produce these phenomena: they occur when the multipolar magnetic field present at the ICB is amplified enough, and brought far enough by magnetic upwellings, thus disrupting the production of a normal dipolar field by magnetic vortices. This condition can be quantified by noting that the timescale for upwellings $\tau_U = D/U$ (where U is a typical radial velocity in the fluid) should be smaller than the timescale for the turnover of vortices $\tau_\omega = 1/\omega$ (where ω is a typical fluid vorticity). The ratio of the two timescales is a Rossby number $Ro_l = \tau_\omega/\tau_U$, which should, therefore, satisfy

$$Ro_l = \frac{U}{\omega D} \gg 1.$$

The inertial scaling for flow velocity in rotating convection and numerical dynamos (Aubert *et al.* 2001; Christensen & Aubert 2006) invokes an equilibrium between the curled inertia $\nabla \times ((\mathbf{u} \cdot \nabla)\mathbf{u})$ and curled Coriolis force $\nabla \times (2\Omega \mathbf{e}_z \times \mathbf{u})$. If we assume a columnar flow and denote as δ a typical length scale for the vortices, this writes:

$$\frac{U^2}{\delta^2} \approx \frac{\Omega U}{D}$$

and, since $\omega = U/\delta$,

$$\frac{\omega}{\Omega} = \frac{\delta}{D}.$$

The Rossby number Ro_l, therefore, relates to the classical Rossby number $Ro = U/\Omega D$ through $Ro_l = RoD/\delta$. This definition is similar to that of the local Rossby number introduced by Christensen & Aubert (2006), which was shown to be the main parameter controlling the occurrence of reversals in numerical dynamo models. It appears, therefore, plausible that the timescale competition between magnetic upwellings and magnetic vortices plays a key role in triggering polarity reversals in numerical dynamos.

We have shown that DMFI can accurately illustrate well-known macroscopic dynamo mechanisms. Furthermore, it facilitates the investigation of more complex spatio-temporal phenomena, such as the development of magnetic upwellings, and aids interpretation of the evolution of the geomagnetic field at the CMB. Through the release of a software package publicly available upon request to the authors, we hope to make it a standard tool for future dynamo studies.

ACKNOWLEDGMENTS

Julien Aubert acknowledges support from program DyETI of the *Institut National des Sciences de l'Univers*, France. Jonathan Aurnou thanks the U.S. NSF Geophysics Program for research support. We are grateful to H. Amit for useful discussions and comments, and to C. C. Finlay and C.A. Jones for insightful reviews. Numerical computations were performed at the *Service de Calcul Parallèle*, Institut de Physique du Globe de Paris, and at IDRIS, France. This is IPGP contribution 2315.

REFERENCES

Alfvén, H., 1943. On the existence of electromagnetic-hydrodynamic waves, *Ark. Mat. Astron. Fys.,* **29**(2), 1–7.

Amit, H. & Olson, P., 2006. Time average and time dependent parts of core flow, *Phys. Earth planet. Int.,* **155,** 120–139, doi:10.1016/J.pepi.2005.10.006.

Aubert, J., 2005. Steady zonal flows in spherical shell dynamos, *J. Fluid. Mech.,* **542,** 53–67.

Aubert, J., Brito, D., Nataf, H.-C., Cardin, P. & Masson, J.P., 2001. A systematic experimental study of spherical shell convection in water and liquid gallium, *Phys. Earth planet. Int.,* **128,** 51–74.

Aubert, J., Amit, H. & Hulot, G., 2007. Detecting thermal boundary control in surface flows from numerical dynamos, *Phys. Earth planet. Int.,* **160,** 143–156.

Aurnou, J., Andreadis, S., Zhu, L. & Olson, P., 2003. Experiments on convection in Earth's core tangent cylinder, *Earth planet. Sci. Lett.,* **212,** 119–134.

Bloxham, J., 1986. The expulsion of magnetic flux from the Earth's core, *Geophys. J. R. astr. Soc.,* **87**(2), 669–678.

Braginsky, S.I. & Roberts, P.H., 1995. Equations governing convection in Earths core and the geodynamo, *Geophys. Astrophys. Fluid Dyn.,* **79**(1–4), 1–97.

Christensen, U. & Aubert, J., 2006. Scaling properties of convection-driven dynamos in rotating spherical shells and application to planetary magnetic fields, *Geophys. J. Int.,* **117,** 97–114.

Christensen, U. & Tilgner, A., 2004. Power requirement of the geodynamo from ohmic losses in numerical and laboratory dynamos, *Nature,* **429,** 169–171, doi:10.1038/nature02508.

Christensen, U.R. *et al.*, 2001. A numerical dynamo benchmark, *Phys. Earth planet. Int.,* **128,** 25–34.

Fearn, D.R., Roberts, P.H. & Soward, A.M., 1988. Convection, stability and the dynamo, in *Energy, Stability and Convection,* pp. 60–324, eds Galdi, G. & Staughan, B., Longman Scientific and Technical, Harlow.

Finlay, C.C., 2005. Hydromagnetic waves in Earth's core and their influence on geomagnetic secular variation, *PhD thesis*, School of Earth and Environment, University of Leeds.

Galloway, D.J. & Weiss, N.O., 1981. Convection and magnetic-fields in stars, *Astrophys. J.,* **243**(3), 945–953.

Hulot, G., Eymin, C., Langlais, B., Mandea, M. & Olsen, N., 2002. Small-scale structure of the geodynamo inferred from Oersted and Magsat satellite data, *Nature,* **416,** 620–623.

Ishihara, N. & Kida, S., 2002. Dynamo mechanism in a rotating spherical shell: competition between magnetic field and convection vortices, *J. Fluid. Mech.,* **465,** 1–32.

Jackson, A., 2003. Intense equatorial flux spots on the surface of the earth's core, *Nature,* **424**(6950), 760–763.

Jackson, A., Jonkers, A.R.T. & Walkers, M.R., 2000. Four centuries of geomagnetic secular variation from historical records, *Phil. Trans. Roy. Soc. A,* **358,** 957–990.

Kageyama, A. & Sato, T., 1997. Velocity and magnetic field structures in a magnetohydrodynamic dynamo, *Phys. Plasmas,* **4,** 1569–1575.

Kutzner, C. & Christensen, U., 2002. From stable dipolar to reversing numerical dynamos, *Phys. Earth planet. Int.,* **131,** 29–45.

Olson, P. & Amit, H., 2006. Changes in Earth's dipole, *Naturwiss.,* **93**(11), 519–542.

Olson, P. & Aurnou, J., 1999. A polar vortex in the Earth's core, *Nature,* **402,** 170–173.

Olson, P. & Christensen, U.R., 2006. Dipole moment scaling for convection-driven planetary dynamos, *Earth planet. Sci. Lett.,* **250**(3–4), 561–571.

Olson, P., Christensen, U. & Glatzmaier, G.A., 1999. Numerical modelling of the geodynamo: mechanisms of field generation and equilibration, *J. geophys. Res.,* **104**(B5), 10 383–10 404.

Roberts, P.H. & Glatzmaier, G.A., 2000. A test of the frozen-flux approximation using a new geodynamo model, *Phil. Trans. R. Soc. Lond. A,* **358**(1768), 1109–1121.

Roberts, P.H. & Scott, S., 1965. On the analysis of the secular variation. i. A hydromagnetic constraint: theory., *J. Geomag. Geoelectr.,* **17,** 137–151.

Sakuraba, A. & Kono, M., 1999. Effect of the inner core on the numerical solution of the magnetohydrodynamic dynamo, *Phys. Earth planet. Int.,* **111**(1–2), 105–121.

Sarson, G.R. & Jones, C.A., 1999. A convection driven geodynamo reversal model, *Phys. Earth planet. Int.,* **111**(1–2), 3–20.

Sreenivasan, B. & Jones, C.A., 2005. Structure and dynamics of the polar vortex in the earth's core, *Geophys. Res. Lett.,* **32**(20), L20301.

Sreenivasan, B. & Jones, C.A., 2006. Azimuthal winds, convection and dynamo action in the polar regions of planetary cores, *Geophys. Astrophys. Fluid Dyn.,* **100**(4-5), 319–339.

Valet, J.P. & Meynadier, L., 1993. Geomagnetic field intensity and reversals during the past four million years., *Nature,* **336,** 234–238.

Weiss, N.O., 1966. The expulsion of magnetic flux by eddies, *Proc. R. Soc. Lond. A.,* **293**(1434), 310–328.

Wicht, J., 2002. Inner-core conductivity in numerical dynamo simulations, *Phys. Earth planet. Int.,* **132,** 281–302.

Wicht, J., 2005. Palaeomagnetic interpretation of dynamo simulations, *Geophys. J. Int.,* **162,** 371–380.

Wicht, J. & Olson, P., 2004. A detailed study of the polarity reversal mechanism in a numerical dynamo model, *Geophys. Geochem. Geosystems.,* **5**(3).

LETTERS

Thermochemical flows couple the Earth's inner core growth to mantle heterogeneity

Julien Aubert[1], Hagay Amit[2], Gauthier Hulot[2] & Peter Olson[3]

Seismic waves sampling the top 100 km of the Earth's inner core reveal that the eastern hemisphere (40° E–180° E) is seismically faster[1,2], more isotropic[2,3] and more attenuating[4] than the western hemisphere. The origin of this hemispherical dichotomy is a challenging problem for our understanding of the Earth as a system of dynamically coupled layers. Previously, laboratory experiments have established that thermal control from the lower mantle can drastically affect fluid flow in the outer core[5], which in turn can induce textural heterogeneity on the inner core solidification front[6]. The resulting texture should be consistent with other expected manifestations of thermal mantle control on the geodynamo, specifically magnetic flux concentrations[7,8] in the time-average palaeomagnetic field[9,10] over the past 5 Myr, and preferred eddy locations[11] in flows imaged below the core–mantle boundary by the analysis of historical geomagnetic secular variation[12]. Here we show that a single model of thermochemical convection and dynamo action can account for all these effects by producing a large-scale, long-term outer core flow that couples the heterogeneity of the inner core with that of the lower mantle. The main feature of this thermochemical 'wind' is a cyclonic circulation below Asia, which concentrates magnetic field on the core–mantle boundary at the observed location and locally agrees with core flow images. This wind also causes anomalously high rates of light element release in the eastern hemisphere of the inner core boundary, suggesting that lateral seismic anomalies at the top of the inner core result from mantle-induced variations in its freezing rate.

In the lower mantle, the double crossing of the post-perovskite phase transition detected by core-reflected seismic shear waves[13] directly constrains local temperature gradients. Heat flow from the core to the mantle is found[14] to be larger than average below Central America, where descending mantle currents induce regional heat flow anomalies of $\delta q = 40\ \mathrm{mW\ m^{-2}}$ or larger, and lower than average below the central Pacific. These results support a thermal interpretation of the largest scales present in seismic shear velocity maps[15], according to which fast regions correspond to cold deep subducted lithosphere[14,16] (as beneath Central America), and extract more heat from the core, while slow regions correspond to warm thermochemical piles[17,18] (as beneath the central Pacific), and extract less heat from the core. Cooling causes the inner core to grow at nominal rates of 0.3–0.9 mm $\mathrm{yr^{-1}}$ (ref. 19), corresponding to 100 km of solidification within the past 100–300 Myr. As the large-scale lower mantle structure has changed little during that time[18], a connection between its present-day pattern and the upper inner core heterogeneous properties is plausible.

The following numerical simulation shows how thermal mantle heterogeneity simultaneously affects the time-average outer core magnetic field structure, core flow, and the asymmetric structure of the inner core. We use the same model of Boussinesq convection and dynamo action in a rotating spherical shell as in a previous study[11], except for the use of a co-density formulation[20] to describe both thermal and chemical buoyancy sources in the outer core in terms of a single co-density variable C (see Methods). We assume that the thermal and chemical perturbations have the same effective diffusivity κ because of turbulent mixing. At the core–mantle boundary, we assume zero chemical mass flux, so the mass anomaly flux $f = -\kappa \partial C/\partial r$ there (which combines thermal and chemical contributions) is related to the heat flow q through $f = \alpha q/C_p$, where r is the radial coordinate, and α and C_p are respectively the thermal expansivity and the specific heat of the liquid outer core. Thermal mantle control is modelled by imposing a heterogeneous heat flow pattern proportional to lowermost mantle seismic shear velocity anomalies[15] (Supplementary Fig. 1), superimposed on a uniform background heat flow, as in earlier studies[7,8]. The seismically inferred amplitude[13,14] $\delta q = 40\ \mathrm{mW\ m^{-2}}$ of the lateral heat flow variation corresponds to a mass anomaly flux variation $\delta f = 5 \times 10^{-10}\ \mathrm{kg\ m^{-2}\ s^{-1}}$, using[21] $\alpha = 10^{-5}\ \mathrm{K^{-1}}$ and $C_p = 800\ \mathrm{J\ kg^{-1}\ K^{-1}}$. This is of the same order of magnitude as the estimated homogeneous part of the mass anomaly flux in the core[21] $f_o = 2 \times 10^{-10}\ \mathrm{kg\ m^{-2}\ s^{-1}}$, expressed per unit surface at the core–mantle boundary. Accordingly, we specify $\delta f/f_o = 1$ in our model. At the inner core boundary, the co-density C is set to a constant value, and f is free to react to the convection. This thermodynamically consistent boundary condition (see Supplementary Information) allows for a spatially variable release of heat and light elements, and implies[20] lateral variations in the inner core growth rate, which is fastest where outer core downwellings bring relatively cold and chemically depleted liquid close to the inner core boundary. The simulation parameters are chosen so that the model produces a self-sustained magnetic field with dipole reversals. Because of the great disparity in the timescales of outer core and mantle dynamical processes, we consider only the time-average behaviour of the model. The flow is then dominated by a thermochemical wind balance[11] between the pressure gradient and the Coriolis and buoyancy forces.

The most prominent non-axisymmetric feature of the resulting thermochemical wind (Fig. 1) is a cyclonic (anticlockwise on a north polar view) flow column, parallel to the rotation axis, extending from the outer to the inner boundary, just outside the inner core tangent cylinder. The column is located below Asia, and is driven by mantle-induced lateral temperature gradients between the cold sub-Asian region and warmer African and Pacific regions. Two additional columns are located below the Pacific and Atlantic oceans. Strong helical polar vortices are generated inside the northern and southern parts of the tangent cylinder. The Asian cyclone is visible in the flow at the top of the free stream (Fig. 2d), and locally concentrates[22] the outer boundary radial magnetic field (Fig. 2b). Similar signatures are found

[1]Dynamique des Fluides Géologiques, [2]Géomagnétisme, Institut de Physique du Globe de Paris, Université Paris-Diderot, INSU/CNRS, 4, Place Jussieu, 75252, Paris cedex 05, France. [3]Department of Earth and Planetary Sciences, Johns Hopkins University, Baltimore, Maryland 21218, USA.

in the time-average core flow (Fig. 2c) and palaeomagnetic field (Fig. 2a), showing that these patterns could indeed result from the presence of such a cyclone in the Earth's outer core. Our model (Fig. 2b, d) further shows that the second persistent palaeomagnetic flux lobe below north America (Fig. 2a) is associated with a similar long-term cyclone, suggesting that the anticyclonic flow inferred in this region from historical geomagnetic secular variation (Fig. 2c) may be a transient. This interpretation is supported by changes in the instantaneous rotation direction of this vortex[12], occurring between 1840 and 1990.

The thermochemical wind flows efficiently extract heat and light elements from the equatorial belt of the inner boundary (Fig. 2e), while the polar vortex circulations in the tangent cylinder suppress the buoyancy extraction, yielding lower-than-average mass anomaly flux in the polar regions. Our model thus confirms the likelihood of a faster inner-core growth in the equatorial region, in line with earlier predictions[6,23]. It also predicts an extra mass anomaly flux release and locally faster inner-core growth below southeastern Asia, where the sub-Asian cyclone brings colder, chemically depleted material from the outer boundary towards the inner boundary. This maximum coincides with the maximum perturbation in the isotropic seismic velocity of the upper inner core[2] (Fig. 2e), which is also representative of the large-scale pattern of anisotropic[2,3] and first-order attenuation[4] properties. This result is weakly sensitive to the time-average mass anomaly flux partition between the inner and outer boundaries, as shown (Fig. 2f) by a simulation in which the inner-boundary mass anomaly flux is increased from 50% to 80% of the total, to better match current estimates (see Methods).

Solidification texturing appears to be the most likely micromechanism for explaining seismic heterogeneity below the inner core boundary, because the alternative process, deformational texturing, is too slow, typically requiring 1 Gyr timescales[23]. Solidification experiments reveal the importance of interstitial solute flow rate in controlling fabric development in hexagonal-close-packed alloys[24]. Slower freezing rates result in more widely spaced dendritic platelets with greater sensitivity to the solute flow direction, and produce a more textured solid through preferential *c*-axis orientation, whereas faster freezing rates inhibit this effect and result in a solid with more random platelet orientation. Seismic waves that sample the top of the inner core will therefore have anisotropic wave speed and attenuation in the more textured slow-growing regions, and will be more isotropic, faster on average and more attenuated[25] (due to scattering by an increased number of grain boundary crossings) in the less-textured fast-growing regions. If inner core textures are controlled by the processes just described, then the heterogeneous crystallization predicted by our dynamo model qualitatively agrees with the ensemble of seismic data[25]. Our results therefore strongly suggest that the upper inner core has inherited its seismic heterogeneity through mantle-induced lateral variations in its growth rate.

Our interpretation requires a small inner core rotation with respect to the lower mantle over the past 100–300 Myr. Subject to a long term magnetic torque $\bar{\Gamma}_B$, viscous torque $\bar{\Gamma}_v$ and gravitational

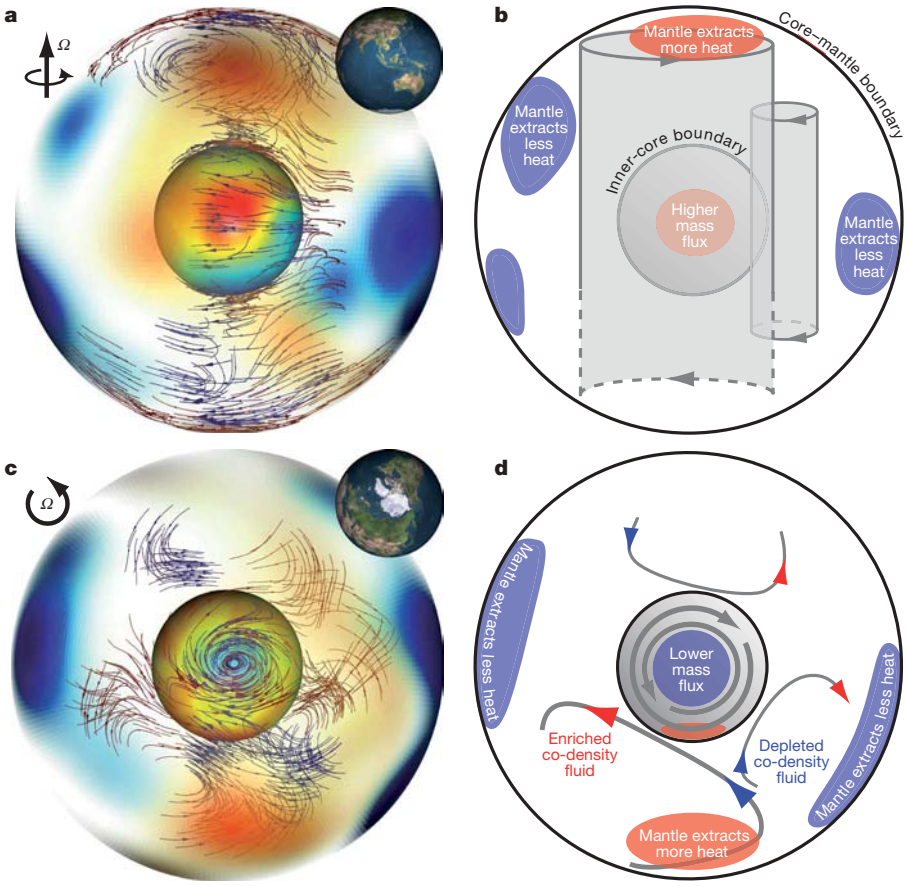

Figure 1 | Time-average flow structure of model case I. Parameters for this case are given in Methods. **a**, **c**, Equatorial and polar visualizations, respectively, of the time-average flow. Insets at upper right indicate the viewing angle. Insets at upper left show the rotation axis direction. The outer boundary is made selectively transparent and colour-coded according to the imposed outwards heat flow (a red patch, such as the dominant positive anomaly below Asia, means a larger-than-average heat flow; see also Supplementary Fig. 1). The inner boundary is colour-coded according to the mass anomaly flux $f = -\kappa\partial C/\partial r$ extracted from the inner core (colour scheme as in Fig. 2e). Within the shell, flow streamlines are represented and colour-coded according to the local velocity along the cylindrical radius (blue streamlines represent downwellings). **b**, **d**, Explanatory diagrams of the equatorial and polar views **a**, **c**. Red and blue arrowheads in **d** respectively represent flow up- and downwellings.

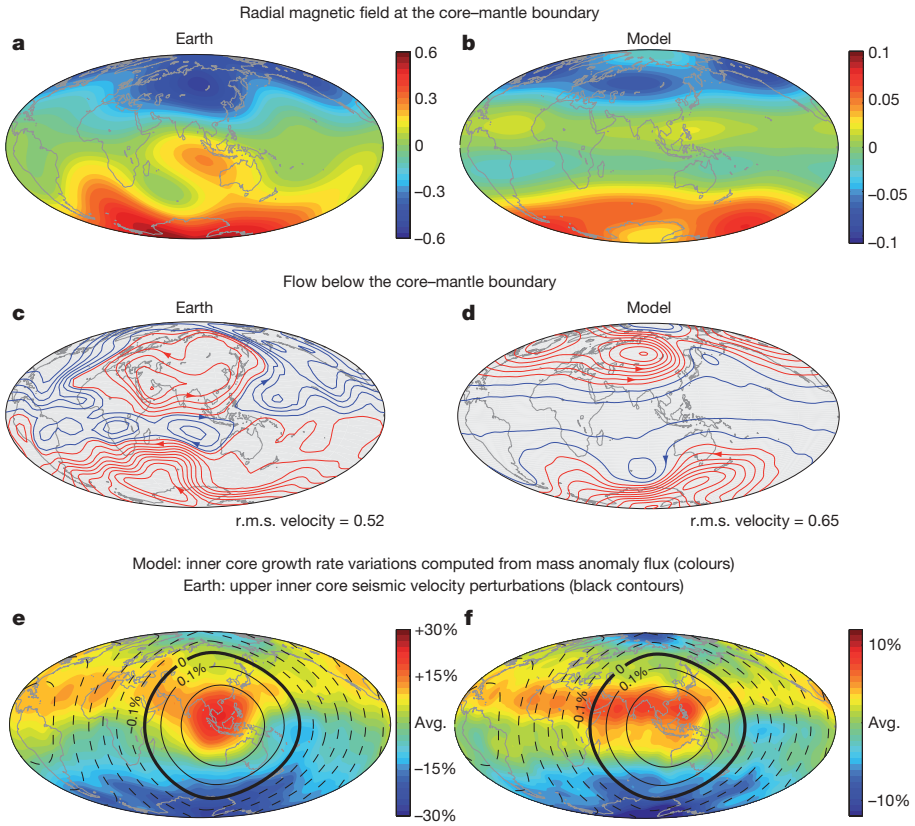

Figure 2 | Comparison between model and observations. a, Time-average palaeomagnetic field model[10] at the core–mantle boundary over the normal polarity periods of the past 5 Myr. **b**, Time-average magnetic field at the outer boundary for case I, taken over the stable polarity periods of 0.7 Myr, and filtered to spherical harmonic degree and order 5. In **a** and **b**, the amplitude (colour scale) is normalized relative to the values predicted by a systematic scaling study[21] (the predicted magnetic field strength in the Earth's core is 1 mT, see Supplementary Information). **c**, Streamlines of the time-average flow below the core–mantle boundary, obtained from geomagnetic secular variation inversions[12], for the period 1840–1990. **d**, Streamlines of the time-average flow at the top of the free stream for case I. In **c** and **d**, the root-mean-squared velocity is normalized relative to the values predicted by thermal wind scaling[11] (the predicted flow amplitude for the core is 15.8 km yr^{-1}, see also Supplementary Information). **e**, Colour map of relative anomalies of the mass anomaly flux extracted from the inner boundary for case I (or, equivalently, of inner-core growth rate anomalies). The black contours show an upper inner core seismic velocity perturbation model[2] expanded to spherical harmonic degree and order 1, the pattern of which is representative of anisotropic[2,3] and attenuation[4] seismic properties. **f**, Same as **e**, for case II (see Methods).

torque with coupling constant Γ_G, the inner core can be expected to reach a steady rotation rate[26] $\bar{\omega} = (\bar{\Gamma}_B + \bar{\Gamma}_v)/\tau\Gamma_G$, where τ is the relaxation time of the inner core towards its hydrostatic shape. The observation[27] of a 6-yr gravitational oscillation in length-of-day data implies that $\tau > 5$ yr and $\Gamma_G = 3 \times 10^{20}$ N m. Numerical dynamo simulations[26] with gravitational coupling further show that in the long term, the system tends to minimize $\bar{\Gamma}_B$, and that when the viscous torque is taken into account, both magnetic and gravitational torques independently counteract the viscous torque which entrains the inner core rotation. These results suggest that $\bar{\Gamma}_B + \bar{\Gamma}_v$ is only a fraction of the typical turbulent viscous torque, which we estimate by assuming a relative zonal flow velocity of the same order of magnitude (10^{-4} m s^{-1}) as at the core surface[12]. Using equation (9) of ref. 28, this yields $\bar{\Gamma}_v = 2 \times 10^{12}$ N m, and a maximum inner core rotation of only 8° in 100 Myr, compatible with our results. On decadal timescales, additional torsional oscillations are expected to disrupt the steady Taylor state of the outer core. For a 60-yr periodicity, magnetic torque fluctuations much larger than $\bar{\Gamma}_B$ can then cause the inner core to oscillate at a maximum angular velocity of[29] 0.1° yr^{-1}, within the range of present seismic inferences[30]. Both processes would only smear, but not erase, the mantle signature on the inner core.

METHODS SUMMARY

We solve for fluid motion, thermochemical transport and magnetic induction in a spherical shell of aspect ratio $r_i/r_o = 0.35$, rotating with constant angular velocity Ω. The non-dimensional Navier–Stokes and induction equations are identical to those presented in an earlier study[11]. The boundary conditions are rigid for the velocity field, and insulating for the magnetic field. The thermochemical buoyancy described by the co-density field C obeys the following evolution equation:

$$\frac{\partial C}{\partial t} + \mathbf{u}\cdot\nabla C = \frac{E}{\mathrm{Pr}}\nabla^2 C + S_T - S_\chi \qquad (1)$$

Here $\mathbf{u}$ is the flow velocity field, and S_T and S_χ are respectively the volumetric thermal buoyancy source and chemical buoyancy sink terms. In model cases I and II, the relevant dimensionless parameters are set as follows: the Ekman number is $E = \nu/\Omega D^2 = 3 \times 10^{-4}$, where $D = r_o - r_i$ is the shell gap and ν is the fluid viscosity. The Prandtl number is $\mathrm{Pr} = \nu/\kappa = 1$, and the magnetic Prandtl number is $\mathrm{Pm} = \nu/\lambda = 2$, where λ is the magnetic diffusivity. The Rayleigh number based on the homogeneous mass anomaly flux[21] f_o imposed at the outer boundary is $\mathrm{Ra}_Q = g_o f_o/\rho\Omega^3 D^2$, where ρ is the fluid density and g_o is the gravity at the outer boundary. Model case I (Figs 1 and 2b, d, e) has $S_T + S_\chi = 0$ and $\mathrm{Ra}_Q = 2 \times 10^{-4}$. Model case II (Fig. 2f) has $S_T + S_\chi = -2.1 \times 10^{-3}$ and $\mathrm{Ra}_Q = 8.1 \times 10^{-5}$.

Full Methods and any associated references are available in the online version of the paper at www.nature.com/nature.

Received 9 November 2007; accepted 12 May 2008.

1. Niu, F. L. & Wen, L. X. Hemispherical variations in seismic velocity at the top of the Earth's inner core. *Nature* **410**, 1081–1084 (2001).
2. Tanaka, S. & Hamaguchi, H. Degree one heterogeneity and hemispherical variation of anisotropy in the inner core from PKP(BC)-PKP(DF) times. *J. Geophys. Res.* **102**, 2925–2938 (1997).
3. Yu, W. C. & Wen, L. X. Inner core attenuation anisotropy. *Earth Planet. Sci. Lett.* **245**, 581–594 (2006).
4. Cao, A. & Romanowicz, B. Hemispherical transition of seismic attenuation at the top of the Earth's inner core. *Earth Planet. Sci. Lett.* **228**, 243–253 (2004).

5. Sumita, I. & Olson, P. A laboratory model for convection in Earth's core driven by a thermally heterogeneous mantle. *Science* **286,** 1547–1549 (1999).
6. Bergman, M. I., Macleod-Silberstein, M., Haskel, M., Chandler, B. & Akpan, N. A laboratory model for solidification of Earth's core. *Phys. Earth Planet. Inter.* **153,** 150–164 (2005).
7. Olson, P. & Christensen, U. The time averaged magnetic field in numerical dynamos with non-uniform boundary heat flow. *Geophys. J. Int.* **151,** 809–823 (2002).
8. Gubbins, D., Willis, A. P. & Sreenivasan, B. Correlation of Earth's magnetic field with lower mantle thermal and seismic structure. *Phys. Earth Planet. Inter.* **162,** 256–260 (2007).
9. Johnson, C. L. & Constable, C. G. The time averaged geomagnetic field as recorded by lava flows over the past 5 Myr. *Geophys. J. Int.* **122,** 489–519 (1995).
10. Kelly, P. & Gubbins, D. The geomagnetic field over the past 5 million years. *Geophys. J. Int.* **128,** 315–330 (1997).
11. Aubert, J., Amit, H. & Hulot, G. Detecting thermal boundary control in surface flows from numerical dynamos. *Phys. Earth Planet. Inter.* **160,** 143–156 (2007).
12. Amit, H. & Olson, P. Time average and time dependent parts of core flow. *Phys. Earth Planet. Inter.* **155,** 120–139 (2006).
13. Lay, T., Hernlund, J., Garnero, E. J. & Thorne, M. S. A post-perovskite lens and D'' heat flux beneath the central Pacific. *Science* **314,** 1272–1276 (2006).
14. van der Hilst, R. *et al.* Seismostratigraphy and thermal structure of Earth's core-mantle boundary region. *Science* **315,** 1813–1817 (2007).
15. Masters, G., Laske, G., Bolton, H. & Dziewonski, A. in *Earth's Deep Interior: Mineral Physics and Tomography from the Atomic to the Global Scale* (eds Karato, S., Forte, A., Liebermann, R. C., Masters, G. & Stixrude, L.) 63–87 (AGU Monogr. Vol. 117, American Geophysical Union, Washington DC, 2000).
16. van der Hilst, R., Widiyantoro, S. & Engdahl, E. R. Evidence for deep mantle circulation from global tomography. *Nature* **386,** 578–584 (1997).
17. McNamara, A. K. & Zhong, S. J. Thermochemical structures beneath Africa and the Pacific Ocean. *Nature* **437,** 1136–1139 (2005).
18. Torsvik, T. H., Smethurst, M. A., Burke, K. & Steinberger, B. Large igneous provinces generated from the margins of the large low-velocity provinces in the deep mantle. *Geophys. J. Int.* **167,** 1447–1460 (2006).
19. Labrosse, S., Poirier, J. P. & Le Mouel, J. L. The age of the inner core. *Earth Planet. Sci. Lett.* **190,** 111–123 (2001).
20. Braginsky, S. I. & Roberts, P. H. Equations governing convection in Earth's core and the geodynamo. *Geophys. Astrophys. Fluid Dyn.* **79,** 1–97 (1995).
21. Christensen, U. & Aubert, J. Scaling properties of convection-driven dynamos in rotating spherical shells and application to planetary magnetic fields. *Geophys. J. Int.* **117,** 97–114 (2006).
22. Olson, P., Christensen, U. & Glatzmaier, G. A. Numerical modelling of the geodynamo: Mechanisms of field generation and equilibration. *J. Geophys. Res.* **104,** 10383–10404 (1999).
23. Yoshida, S., Sumita, I. & Kumazawa, M. Growth model of the inner core coupled with the outer core dynamics and the resulting elastic anisotropy. *J. Geophys. Res.* **101,** 28085–28103 (1996).
24. Bergman, M. I., Agrawal, S., Carter, M. & Macleod-Silberstein, M. Transverse solidification textures in hexagonal close-packed alloys. *J. Cryst. Growth* **255,** 204–211 (2003).
25. Cormier, V. Texture of the uppermost inner core from forward and back scattered seismic waves. *Earth Planet. Sci. Lett.* **258,** 442–453 (2007).
26. Buffett, B. A. & Glatzmaier, G. A. Gravitational braking of inner-core rotation in geodynamo simulations. *Geophys. Res. Lett.* **27,** 3125–3128 (2000).
27. Mound, J. E. & Buffett, B. A. Detection of a gravitational oscillation in length-of-day. *Earth Planet. Sci. Lett.* **243,** 383–389 (2006).
28. Aurnou, J. & Olson, P. Control of inner core rotation by electromagnetic, gravitational and mechanical torques. *Phys. Earth Planet. Inter.* **117,** 111–121 (2000).
29. Dumberry, M. Geodynamic constraints on the steady and time-dependent inner core axial rotation. *Geophys. J. Int.* **170,** 886–895 (2007).
30. Souriau, A. in *Treatise on Geophysics* Vol. 1, *Seismology and Structure of the Earth* (eds Dziewonski, A. & Romanowicz, B.) 655–693 (Elsevier, 2007).

Supplementary Information is linked to the online version of the paper at www.nature.com/nature.

Acknowledgements J.A. was supported by the SEDIT programme of CNRS-INSU. H.A. was supported by a Marie Curie intra-European grant. Numerical calculations were performed at the Service de Calcul Parallèle, IPGP, and at IDRIS, France. We thank S. Tanaka for providing published data, and V. Cormier for discussions. This is IPGP contribution 2369.

Author Information Reprints and permissions information is available at www.nature.com/reprints. Correspondence and requests for materials should be addressed to J.A. (aubert@ipgp.jussieu.fr).

METHODS

We consider an electrically conducting, incompressible fluid in a spherical shell between radii r_i and r_o. The aspect ratio is $r_i/r_o = 0.35$, as in the Earth's core. The shell is rotating about an axis $\mathbf{e}_z$ with constant angular velocity Ω. We model thermal and chemical convection in the Boussinesq approximation, and define the deviation temperature field T' and light element molar fraction field χ' with respect to the adiabatic temperature and well-mixed molar fraction. Both buoyancy effects are grouped into a co-density (or density anomaly) field[20] C such that:

$$C = \alpha\rho T' + \Delta\rho\chi' \quad (1)$$

Here α is the thermal expansion coefficient, ρ is the fluid density, and $\Delta\rho$ is the density difference between light elements and pure iron. The temperature and molar fraction fields are assumed to have the same diffusivity κ, due to turbulent mixing in the outer core. This allows us to write a single transport equation for the co-density C, which is solved numerically in a non-dimensional form, together with the magnetic induction equation for the solenoidal magnetic field $\mathbf{B}$ in the magnetohydrodynamic approximation, and the Navier–Stokes and thermochemical transport equations for the incompressible velocity field $\mathbf{u}$, and pressure P:

$$\frac{\partial\mathbf{u}}{\partial t} + \mathbf{u}\cdot\nabla\mathbf{u} + 2\,\mathbf{e}_z\times\mathbf{u} + \nabla P = \mathrm{Ra}_Q\frac{\mathbf{r}}{r_o}C + (\nabla\times\mathbf{B})\times\mathbf{B} + E\nabla^2\mathbf{u} \quad (2)$$

$$\frac{\partial\mathbf{B}}{\partial t} = \nabla\times(\mathbf{u}\times\mathbf{B}) + \frac{E}{\mathrm{Pm}}\nabla^2\mathbf{B} \quad (3)$$

$$\frac{\partial C}{\partial t} + \mathbf{u}\cdot\nabla C = \frac{E}{\mathrm{Pr}}\nabla^2 C + S_T - S_\chi \quad (4)$$

$$\nabla\cdot\mathbf{u} = 0 \quad (5)$$

$$\nabla\cdot\mathbf{B} = 0 \quad (6)$$

Time is scaled with the inverse of the rotation rate Ω^{-1}. Length is scaled with the shell gap $D = r_o - r_i$. The velocity is scaled with ΩD. The magnetic induction is scaled with $(\rho\mu)^{1/2}\Omega D$, where μ is the magnetic permeability of the fluid. The co-density is scaled with $|f_o|/\Omega D$, where f_o is the amplitude of the spherically symmetric part of the mass anomaly flux $\mathbf{f} = -\kappa\nabla C$ imposed at the outer boundary of the model.

At both boundaries, the boundary conditions for velocity are rigid, and insulating for the magnetic field. Although treating the inner core as an insulator is non-physical, the influence of inner-core conductivity is insignificant[31], except for inner-core differential rotation, which is however not allowed in the present simulations.

At the outer boundary of the model, the mass anomaly flux is prescribed with an homogeneous part f_o and an heterogeneous part proportional to the lower mantle seismic shear wave tomography[15] SB4L18 (see Supplementary Fig. 1), truncated at spherical harmonic degree and order 9, and scaled to have a peak-to-peak magnitude of $\delta f = f_o$. At the inner boundary, the co-density is fixed (see Supplementary Information for a justification of this condition).

The Ekman number is $E = \nu/\Omega D^2 = 3\times10^{-4}$, where ν is the fluid viscosity. The Prandtl number is $\mathrm{Pr} = \nu/\kappa = 1$, and the magnetic Prandtl number is $\mathrm{Pm} = \nu/\lambda = 2$, where λ is the magnetic diffusivity. The Rayleigh number based on mass anomaly flux[21] is $\mathrm{Ra}_Q = g_o f_o/\rho\Omega^3 D^2$, where g_o is the gravity at the outer boundary. In equation (4), S_T is a source term representing the cooling over time of the reference adiabatic thermal state, and S_χ is a sink term representing the enrichment over time of the reference chemical state. Adjusting $S_T + S_\chi$ influences the relative strength of the inner-boundary and outer-boundary originated mass anomaly fluxes on time average. Simulations are carried out for two cases with approximately equal convective power: case I (Figs 1 and 2b, d, e), where $S_T + S_\chi = 0$ and $\mathrm{Ra}_Q = 2\times10^{-4}$, for which scaling laws already exist in the literature[11,21], and a geophysically more relevant[32] case II (Fig. 2f) where $S_T + S_\chi = -2.1\times10^{-3}$ and $\mathrm{Ra}_Q = 8.1\times10^{-5}$. In case II, the inner-boundary originated mass anomaly flux represents 80% of the total.

The numerical implementation MAGIC[31] is used in this study. A Chebyshev polynomials expansion is used in the radial direction with 65 radial grid points. A spherical harmonics expansion is used in the lateral directions, up to maximum degree and order 85.

The model is time-averaged during 4.4 magnetic diffusion times D^2/λ. Using $D = 2{,}200$ km and $\lambda \approx 1\ \mathrm{m^2\,s^{-1}}$ for iron in the Earth's core[33], this is equivalent to a period of about 700 kyr. The time-average magnetic field is taken during the run periods of stable dipole.

31. Wicht, J. Inner-core conductivity in numerical dynamo simulations. *Phys. Earth Planet. Inter.* **132**, 281–302 (2002).
32. Lister, J. R. & Buffett, B. A. The strength and efficiency of thermal and compositional convection in the geodynamo. *Phys. Earth Planet. Inter.* **91**, 17–30 (1995).
33. Secco, R. A. & Shloessin, H. H. The electrical resistivity of solid and liquid Fe at pressures up to 7 GPa. *J. Geophys. Res.* **94**, 5887–5894 (1989).

Modelling the paleo-evolution of the geodynamo

Julien Aubert[1], Stéphane Labrosse[2], and Charles Poitou[3]

[1]*: Dynamique des Fluides Géologiques,* [3]*: Paléomagnétisme, Institut de Physique du Globe de Paris, Université Paris-Diderot, INSU/CNRS, 4 Place Jussieu, 75252, Paris cedex 05, France.* aubert@ipgp.jussieu.fr, http://www.ipgp.jussieu.fr/~aubert

[2]*: Laboratoire des sciences de la Terre, Ecole normale supérieure de Lyon, Université de Lyon, CNRS UMR 5570, 46 Allée d'Italie, 69364 Lyon Cedex 07, France.*

Summary

Although it is known that the geodynamo has been operating for at least 3.2 Gyr, it remains difficult to infer the intensity, dipolarity and stability (occurrence of reversals) of the Precambrian magnetic field of the Earth. In order to assist the interpretation of paleomagnetic data, we produce models for the long-term evolution of the geodynamo by combining core thermodynamics with a systematic scaling analysis of numerical dynamos with aspect ratios and buoyancy source distributions relevant to Earth in the Precambrian. Two end-member models of heat flow evolution at the core-mantle boundary are used, respectively terminating at present heat flows of 11 TW (high-power scenario) and 3 TW (low power scenario). The resulting models suggest that the geodynamo has been above the threshold for dynamo action for ages younger than 3.8 Gyr, and has lied close to the transition to polarity reversals throughout its history. In the Precambrian, we predict a dynamo with similar dipolarity and less frequent reversals than at present times, due to conditions of generally lower convective forcing. The dipole moment time series predicted by both scenarios are in equally good agreement with the paleomagnetic data during that epoch. Specifically, before the appearance of the inner core (which both scenarios predict to have occurred less than 2 Gyr ago), a thermal dynamo driven only by secular cooling can produce a dipole moment of strength compatible with the data, thus precluding an interpretation of the oldest paleomagnetic records as evidence of the inner core presence. The moment of inner core nucleation cannot be detected in the dipole moment series because of the mutually cancelling effects of a sudden power increase and a deeper-seated dynamo. For more recent times (less than 0.5 Gyr ago), the low-power scenario is unable to predict a dipole moment of sufficient strength, because it implies the presence of a stably stratified fluid layer in the upper outer core which decreases the magnitude of the dipole field seen at the surface. Our preferred evolution model is therefore of the high-power type, and predicts a monotonous increase of the dipole moment from about 5 10^{22} A.m^2 3 Gyr ago to 8 10^{22} A.m^2 at present. In the last 0.5 Gyr also, we find that it is unlikely that mantle heat flow fluctuations may have caused superchrons by temporarily switching the geodynamo to a non-reversing state without shutting it down altogether.

Key words: Earth's core, Dynamo theory, Geomagnetic field, Geomagnetic reversals,

1 Introduction

Paleomagnetic records can be used in order to shed light onto the past of the Earth's dynamo. However, with increasing age, rock sequences are likely to be affected by weathering, alteration, and metamorphism, thus destroying the pristine information on the early magnetic field. Although the situation constantly improves with newer samples and better techniques, especially regarding paleointensity determinations (see Valet, 2003, for a review), uncertainties remain concerning the key characteristics of the geodynamo in the Precambrian (Dunlop & Yu, 2004). A first quantity of interest is the dipole moment. The oldest (3.2 Gyr before present) reliable paleomagnetic record to date (Tarduno et al., 2007) reveals that the virtual dipole moment (VDM) was possibly as large as its present value of 8 10^{22} A.m^2, although the consideration of the cooling rate effect may lead to a twofold decrease in the determined VDM. As a result, the debate concerning the long-term evolution of the VDM remains lively (Dunlop & Yu, 2004), though there are suggestions (Macouin et al., 2004) of a long-term average monotonous increase from 3 10^{22} A.m^2 at 1000-2000 Myr to 8 10^{22} A.m^2 at present times. In addition, although it has been proposed (Stevenson et al., 1983; Hale, 1987) that the power increase subsequent to inner core nucleation and onset of chemical convection in the core could cause a sudden increase in the dipole moment, it appears that until now, the paleomagnetic data scatter has prevented a proper resolution of this feature. A second quantity of interest is the dipolarity of the field, which can be assessed (McFadden et al., 1991) through the analysis of latitude dependence in paleosecular variation (PSV). Following this line, Smirnov & Tarduno (2004) proposed that the dipolarity should have been higher some 2.5 Gyr ago. However, the existence of antipodal directions, which would be a clear evidence of high dipolarity (Dunlop & Yu, 2004), is lacking in their data, and more generally, there are considerable issues with this method (Hulot & Gallet, 1996), including the difficulty to separate the dipolarity effect from the secular variation effect in the PSV. The paleosecular variation can indeed also be used to study the intrinsic variability of the geomagnetic pole, as recently done by Biggin et al. (2008), who found evidence of a more stable dynamo 2.4-2.8 Gyr ago. This led to the suggestion that a third quantity of interest, the reversal frequency of the geodynamo, was lower at that time than at present. The same conclusion was reached for the last 500 Myr (Eide & Torsvik, 1996) through direct magnetostratigraphic analysis, which is obviously a more robust method when data is available, but some contrary indications of high reversal frequency have also been reported for the same period (Pavlov & Gallet, 2001). It should be noted however that the strongest signal on the reversal frequency curve is related to the irregular occurrence of superchrons (see for instance Pavlov & Gallet, 2005), where reversal frequency goes down to zero. A last important paleomagnetic result is the timing of

the oldest known reversal, which occurred 2.7 Gyr ago (Strik et al., 2003), though there are some indications of reversals occurring at 3.2 Gyr ago (Tarduno et al., 2007).

As none of the debate presented above is currently settled, the goal of this study is to gain insight from the comparison of paleomagnetic data with synthetic time evolution models for the dipolarity, intensity and stability of the Precambrian Earth dynamo. Since a few years, a scaling theory (Christensen & Tilgner, 2004; Christensen & Aubert, 2006; Olson & Christensen, 2006) is available to predict the main characteristic quantities of the present-day geodynamo and planetary dynamos. The central control variable in almost all scalings is the convective buoyancy flux, which is equivalent to convective power available for the dynamo. Thus, in order to achieve scaling predictions relevant to the Precambrian Earth dynamo, one needs a time series of the dynamo power, which can be evaluated from core thermodynamics and Earth cooling histories (e. g. Labrosse, 2003; Lister, 2003). Furthermore, the results of Christensen & Tilgner (2004); Christensen & Aubert (2006); Olson & Christensen (2006) need to be extended to cases where the outer core aspect ratio varies, and where the partitioning between the inner-boundary and outer-boundary originated buoyancies also varies. In section 2 we introduce the numerical dynamo model which we use for our systematic parameter space study. The numerical results are presented in section 3.1. Then we turn to the investigation of various Earth cooling histories, and how they relate to the dynamo power (section 3.2). Finally we produce our time evolution model for paleomagnetic observables (section 3.3) and discuss the results in light of the paleomagnetic observations and geophysical constraints (section 4).

2 Model.

2.1 Outline

We consider an electrically conducting, incompressible fluid in a self-gravitating spherical shell between radii r_i and r_o. The shell is rotating about an axis $\mathbf{e}_z$ with an angular velocity Ω, and convecting thermally and chemically. We study the Earth's core at various stages of its existence, hence the rotation rate, aspect ratio $\chi = r_i/r_o$ and thermo-chemical buoyancy partitioning are variable over geological times, but can be assumed to be constant control parameters over timescales relevant for core dynamics. We define the deviation temperature field T' and light element molar fraction field ξ' with respect to the isentropic temperature and well-mixed molar fraction, and, within the Boussinesq approximation, both buoyancy effects are grouped into a co-density (or density anomaly) field (Braginsky & Roberts, 1995) C such that:

$$C = \alpha\rho T' + \Delta\rho\xi' \tag{1}$$

Here α is the thermal expansion coefficient, ρ is the fluid density, and $\Delta\rho$ is the density difference between the light components that contribute to chemical convection and pure iron. The temperature and molar fraction fields are assumed to have the same diffusivity κ, due to turbulent mixing in the outer core. This allows us to write a single transport equation for the co-density C, which is solved numerically in a dimensionless form, together with the magnetic induction equation for the solenoidal magnetic field $\mathbf{B}$ in the magnetohydrodynamic approximation, and the Navier-Stokes and thermo-chemical transport equations for the incompressible velocity field $\mathbf{u}$, and pressure P:

$$\frac{\partial \mathbf{u}}{\partial t} + \mathbf{u}\cdot\nabla\mathbf{u} + 2\,\mathbf{e}_z\times\mathbf{u} + \nabla P = Ra_Q\,\frac{\mathbf{r}}{r_o}C + (\nabla\times\mathbf{B})\times\mathbf{B} + E\nabla^2\mathbf{u} \tag{2}$$

$$\frac{\partial \mathbf{B}}{\partial t} = \nabla\times(\mathbf{u}\times\mathbf{B}) + \frac{E}{Pm}\nabla^2\mathbf{B} \tag{3}$$

$$\frac{\partial C}{\partial t} + \mathbf{u}\cdot\nabla C = \frac{E}{Pr}\nabla^2 C + S_{T/\xi} \tag{4}$$

$$\nabla\cdot\mathbf{u} = 0 \tag{5}$$

$$\nabla\cdot\mathbf{B} = 0 \tag{6}$$

Here $\mathbf{r}$ is the radius vector. Time is scaled with the inverse of the rotation rate Ω^{-1}. Length is scaled with the shell gap $D = r_o - r_i$. Velocity is scaled with ΩD. Magnetic induction is scaled by $(\rho\mu)^{1/2}\Omega D$, where ρ is the fluid density and μ the magnetic permeability of the fluid. The Ekman number E , magnetic Prandtl and Prandtl numbers Pm and Pr are defined as:

$$E = \frac{\nu}{\Omega D^2} \tag{7}$$

$$Pm = \frac{\nu}{\lambda} \tag{8}$$

$$Pr = \frac{\nu}{\kappa} \tag{9}$$

Here ν, λ are respectively the viscous and magnetic diffusivities of the fluid. In the present study, the co-density boundary conditions relevant to thermo-chemical convection are treated in the following way: at the inner-core boundary, the release of latent heat and light elements correspond to a positive mass anomaly flux F_i (expressed in kilograms per second), which we consider uniform and imposed on the long term by global core thermodynamics. The dimensional form of F_i writes:

$$F_i = -\int_{S_i} \kappa\nabla C\cdot\mathbf{dS} \tag{10}$$

where S_i is the inner boundary surface. Similarly, at the outer boundary, we consider that the mantle imposes a uniform mass anomaly flux (which in fact corresponds to a heat flux without chemical contributions). The dimensional form of F_o writes:

$$F_o = -\int_{S_o} \kappa\nabla C\cdot\mathbf{dS} \tag{11}$$

Here S_o is the outer boundary surface. Note that F_o is defined with respect to the adiabatic heat flux carried out at the outer boundary (this is the reference state of the Boussinesq system). Hence, F_o can be either positive or negative, but in any case the total mass anomaly flux $F = F_i + F_o$ must be positive for convection to occur. The co-density is scaled with $F/4\pi D^3\Omega$. The Rayleigh number based on mass anomaly flux, Ra_Q, which appears in (2) is therefore defined as:

$$Ra_Q = \frac{g_o F}{4\pi\rho\Omega^3 D^4} \tag{12}$$

Here g_o is gravity at radius $r = r_o$. The present formulation is slightly different from, but equivalent to that in Christensen & Aubert (2006), where a Rayleigh number based on advected buoyancy flux Ra_Q^* was introduced. For sufficiently supercritical convection the conversion from their formalism to ours can be achieved through

$$Ra_Q \approx \frac{r_o r_i}{D^2} Ra_Q^*, \tag{13}$$

The reason for introducing this change of formulation is that Ra_Q^* is singular in the case where the inner core is not present.

The fraction of inner-boundary originated buoyancy $f_i = F_i/F$ has been variable throughout the Earth's core history, it is therefore a control parameter of the present study. More explicit dimensionless forms of the co-density boundary conditions (10) and (11) write:

$$\frac{\partial C}{\partial r}(r_i) = -\frac{f_i}{r_i^2}\frac{Pr}{E} \tag{14}$$

$$\frac{\partial C}{\partial r}(r_o) = -\frac{1-f_i}{r_o^2}\frac{Pr}{E} \tag{15}$$

In general, we have $F_i \neq F_o$, which leads to a necessary time evolution of the Boussinesq base state (decrease in temperature, enrichment in light elements). Since we presently consider a time-independent basic state, a volumetric correction term $S_{T/\xi}$ arises in (4), such that the mass anomaly budget of the spherical shell vanishes (Braginsky & Roberts, 1995; Kutzner & Christensen, 2002). This constrains the dimensional form of the volume source (or sink) term $S_{T/\xi}$ present in equation (4) to obey $\frac{4}{3}\pi(r_o^3 - r_i^3)S_{T/\xi} = F_o - F_i$, hence the dimensionless form of $S_{T/\xi}$ writes:

$$S_{T/\xi} = 3\frac{(1-2f_i)}{r_o^3 - r_i^3} \tag{16}$$

The other boundary conditions at both boundaries are of rigid type for velocity, and insulating for the magnetic field (the effect on inner-core conductivity on the long-term behavior of dynamo simulations has been found to be negligible, as shown by Wicht, 2002). The numerical implementation PARODY-JA is used in this study

(see Aubert et al., 2008, for details). The numerical scheme is of finite-differencing type in the radial direction with up to 120 grid points, and uses a spherical harmonic decomposition in the lateral directions up to degree and order 106. No particular symmetry along longitude was assumed.

Table 1 gives details on the 43 models which we have integrated for this study. These models explore the new parameter space axes relative to χ and f_i. The aspect ratio goes down to $\chi = 0.01$, where the inner core is practically non-existent in the simulation. This situation is meant to simulate the core before or at the inner core nucleation time. The geophysically relevant buoyancy driving mode is therefore secular cooling ($f_i = 0$), which, in our formalism, corresponds to no buoyancy at the inner boundary, a positive volumetric source term, and a fixed heat flow at the outer boundary. Several models have been computed at $\chi = 0.05$, where f_i has been set to 0, 0.5, and 1. These cases correspond to a system where the inner core has just nucleated, and the buoyancy driving is therefore a mix of secular cooling and chemical convection. Finally, models with $\chi = 0.35$ were also needed for comparison with present Earth. Core thermodynamics predict that the main buoyancy source of the present-day geodynamo (in terms of available power) is chemical convection (Lister & Buffett, 1995). For that reason, cases with $f_i = 0$, $\chi = 0.35$ are left out of the present study. However, the uncertainties pertaining to the determination of core-mantle boundary (CMB) heat flow (Lay et al., 2008) and core adiabat leave some room for the determination of f_i. Here we use the published runs from Christensen & Tilgner (2004); Christensen & Aubert (2006); Olson & Christensen (2006), which have been performed with fixed temperature boundary conditions. In our formalism, this is roughly equivalent to $f_i = 0.5$ (see figure 1). In addition, we have included models with $f_i = 1$, and also with $f_i = 2, 10$, describing situation of dominant chemical convection where the CMB heat flow is respectively just adiabatic, or below the adiabat. In the latter case, a stably stratified layer exists at the top of the outer core.

We define several outputs, which are all averaged over times much longer than core flow time scales (but shorter than geological time scales for Earth's mantle variations), and over the full volume of the spherical shell or the surface of the outer boundary. Most of these bear the same definitions as in Christensen & Aubert (2006): the root-mean-squared velocity inside the shell Ro, r.m.s. magnetic field amplitude inside the shell Lo, mean harmonic degree in the velocity field $\bar{l}$, ohmic dissipation fraction of the convective power f_{ohm}, ratio b_{dip} of the mean field strength inside the shell Lo to the dipole strength on the outer boundary B_{dip}, and ratio f_{dip} of B_{dip} to the r.m.s amplitude of the magnetic field at the outer boundary truncated at spherical harmonic degree 12. Parameters with definitions which are proper to this study are the following: the convective power density p is the ratio of the convective power defined in Christensen & Aubert (2006) to the shell volume $V = 4\pi(r_o^3 - r_i^3)/3$. The magnetic dissipation time τ_{diss} is defined as in Christensen & Tilgner (2004), by dividing the magnetic energy by the power dissipated through ohmic losses. However, in that study τ_{diss} was normalized by the dipole diffusion

	E	Ra_Q	Pr	Pm	χ	f_i	Ro	Lo	b_{dip}	f_{dip}	$\bar{l}$	τ_{diss}/τ_{mag}	p	f_{ohm}
	$3\,10^{-5}$	$1.80\,10^{-6}$	1	1	0.05	0.5	$5.03\,10^{-3}$	$3.22\,10^{-3}$	9.56	0.74	10.0	$7.90\,10^{-4}$	$8.32\,10^{-7}$	0.23
	$3\,10^{-5}$	$4.50\,10^{-6}$	1	2	0.01	0	$3.83\,10^{-3}$	$1.19\,10^{-2}$	4.61	0.67	16.3	$9.56\,10^{-4}$	$1.79\,10^{-6}$	0.62
	$3\,10^{-5}$	$4.50\,10^{-6}$	1	1	0.01	0	$4.28\,10^{-3}$	$1.18\,10^{-2}$	3.56	0.81	16.6	$1.88\,10^{-3}$	$2.09\,10^{-6}$	0.58
	$3\,10^{-5}$	$9.00\,10^{-6}$	1	1	0.01	0	$5.98\,10^{-3}$	$1.17\,10^{-2}$	4.03	0.78	20.1	$9.46\,10^{-4}$	$4.20\,10^{-6}$	0.52
	$3\,10^{-5}$	$9.00\,10^{-7}$	1	2	0.05	1	$4.99\,10^{-3}$	$3.91\,10^{-3}$	16.0	0.66	7.0	$6.94\,10^{-4}$	$6.24\,10^{-7}$	0.27
	$3\,10^{-5}$	$1.80\,10^{-6}$	1	2	0.05	1	$6.81\,10^{-3}$	$4.24\,10^{-3}$	24.0	0.48	8.1	$4.01\,10^{-4}$	$1.36\,10^{-6}$	0.25
	$3\,10^{-5}$	$9.00\,10^{-7}$	1	2	0.05	0.5	$3.56\,10^{-3}$	$2.80\,10^{-3}$	13.7	0.63	7.8	$7.31\,10^{-4}$	$3.26\,10^{-7}$	0.25
	10^{-4}	$6\,10^{-5}$	1	5	0.01	0	$1.21\,10^{-2}$	$2.24\,10^{-2}$	7.19	0.53	13.3	$4.23\,10^{-4}$	$2.63\,10^{-5}$	0.45
	10^{-4}	$6\,10^{-5}$	1	2	0.01	0	$1.20\,10^{-2}$	0	n/a	n/a	14.5	0	$2.65\,10^{-5}$	0
	10^{-4}	$3\,10^{-5}$	1	5	0.05	1	$2.22\,10^{-2}$	$1.27\,10^{-2}$	36.0	0.32	6.0	$3.34\,10^{-4}$	$2.59\,10^{-5}$	0.18
	10^{-4}	$3\,10^{-5}$	1	5	0.05	0.5	$1.32\,10^{-2}$	$1.95\,10^{-2}$	9.23	0.53	8.1	$6.09\,10^{-4}$	$1.66\,10^{-5}$	0.38
T	10^{-4}	$1.5\,10^{-5}$	1	10	0.05	0	$5.19\,10^{-3}$	$1.88\,10^{-2}$	7.17	0.49	9.2	$8.17\,10^{-4}$	$3.98\,10^{-6}$	0.54
C	10^{-4}	$1.5\,10^{-5}$	1	10	0.05	1	$1.20\,10^{-2}$	$1.76\,10^{-2}$	13.3	0.47	7.4	$3.98\,10^{-4}$	$1.21\,10^{-5}$	0.32
	10^{-4}	$1.5\,10^{-5}$	1	10	0.05	0.5	$8.44\,10^{-3}$	$1.99\,10^{-2}$	9.36	0.49	7.6	$6.03\,10^{-4}$	$7.59\,10^{-6}$	0.43
	10^{-4}	$3\,10^{-5}$	1	2	0.05	0	$8.64\,10^{-3}$	$1.64\,10^{-2}$	4.66	0.62	12.6	$1.51\,10^{-3}$	$1.02\,10^{-5}$	0.43
	10^{-4}	$3\,10^{-5}$	1	2	0.05	1	$2.38\,10^{-2}$	$5.63\,10^{-3}$	40.4	0.32	6.1	$4.08\,10^{-4}$	$2.54\,10^{-5}$	0.07
	10^{-4}	$3\,10^{-5}$	1	2	0.05	0.5	$1.60\,10^{-2}$	$1.29\,10^{-2}$	7.93	0.68	7.1	$9.56\,10^{-4}$	$1.68\,10^{-5}$	0.25
	10^{-4}	$6\,10^{-5}$	1	2	0.05	0.5	$2.06\,10^{-2}$	$1.71\,10^{-2}$	7.23	0.64	8.1	$6.65\,10^{-4}$	$3.56\,10^{-5}$	0.30
	10^{-4}	$6\,10^{-5}$	1	2	0.05	0	$1.54\,10^{-2}$	$8.53\,10^{-3}$	10.4	0.53	14.1	$4.63\,10^{-4}$	$2.43\,10^{-5}$	0.11
	10^{-4}	$6\,10^{-5}$	1	2	0.05	1	$3.22\,10^{-2}$	$5.93\,10^{-3}$	44.1	0.28	6.2	$2.81\,10^{-4}$	$5.09\,10^{-5}$	0.06
	10^{-4}	$3\,10^{-5}$	1	5	0.01	0	$8.36\,10^{-3}$	$1.95\,10^{-2}$	6.64	0.50	11.5	$6.93\,10^{-4}$	$1.12\,10^{-5}$	0.49
	10^{-4}	$3\,10^{-5}$	1	5	0.05	0	$8.00\,10^{-3}$	$1.99\,10^{-2}$	6.55	0.52	11.7	$7.66\,10^{-4}$	$1.02\,10^{-5}$	0.50
	10^{-4}	$1.5\,10^{-5}$	1	10	0.01	0	$5.33\,10^{-3}$	$1.89\,10^{-2}$	7.20	0.44	9.1	$7.60\,10^{-4}$	$4.40\,10^{-6}$	0.53
	10^{-4}	$3\,10^{-5}$	1	10	0.01	0	$7.83\,10^{-3}$	$2.27\,10^{-2}$	7.68	0.48	11.5	$4.57\,10^{-4}$	$1.13\,10^{-5}$	0.50
	10^{-4}	$3\,10^{-5}$	1	10	0.05	0	$7.58\,10^{-3}$	$2.23\,10^{-2}$	7.39	0.48	11.9	$4.80\,10^{-4}$	$1.04\,10^{-5}$	0.50
	10^{-4}	$3\,10^{-5}$	1	10	0.05	1	$1.83\,10^{-2}$	$1.90\,10^{-2}$	19.0	0.38	7.0	$2.71\,10^{-4}$	$2.59\,10^{-5}$	0.25
	10^{-4}	$3\,10^{-5}$	1	10	0.05	0.5	$1.20\,10^{-2}$	$2.23\,10^{-2}$	10.2	0.50	8.8	$3.99\,10^{-4}$	$1.68\,10^{-5}$	0.37
	10^{-4}	$4\,10^{-4}$	1	5	0.01	0	$3.63\,10^{-2}$	$2.40\,10^{-2}$	47.8	0.17	13.7	$1.05\,10^{-4}$	$2.09\,10^{-4}$	0.26
	10^{-4}	10^{-4}	1	5	0.01	0	$1.70\,10^{-2}$	$2.34\,10^{-2}$	11.0	0.50	12.4	$3.04\,10^{-4}$	$4.65\,10^{-5}$	0.38
	10^{-4}	$1.5\,10^{-4}$	1	5	0.01	0	$2.26\,10^{-2}$	$2.26\,10^{-2}$	19.2	0.30	11.5	$2.14\,10^{-4}$	$7.26\,10^{-5}$	0.32
	10^{-4}	$1.5\,10^{-4}$	1	5	0.05	0	$2.21\,10^{-2}$	$2.05\,10^{-2}$	18.8	0.33	13.1	$1.98\,10^{-4}$	$6.81\,10^{-5}$	0.30
	10^{-4}	$2.5\,10^{-4}$	1	5	0.01	0	$2.92\,10^{-2}$	$2.06\,10^{-2}$	46.9	0.18	13.5	$1.28\,10^{-4}$	$1.26\,10^{-4}$	0.26
	10^{-4}	10^{-4}	1	2	0.05	0.5	$2.80\,10^{-2}$	$1.74\,10^{-2}$	8.31	0.54	7.6	$4.72\,10^{-4}$	$6.17\,10^{-5}$	0.26
	10^{-4}	$2\,10^{-4}$	1	2	0.05	0.5	$4.14\,10^{-2}$	$1.72\,10^{-2}$	18.3	0.38	7.2	$2.73\,10^{-4}$	$1.27\,10^{-4}$	0.18
	$3\,10^{-4}$	$1.80\,10^{-5}$	1	3	0.35	10	$2.28\,10^{-2}$	$3.52\,10^{-3}$	14.3	0.73	6.9	$1.03\,10^{-3}$	$2.96\,10^{-5}$	0.02
	$3\,10^{-4}$	$2.48\,10^{-5}$	1	3	0.35	10	$2.64\,10^{-2}$	$1.61\,10^{-3}$	38.1	0.49	7.2	$7.75\,10^{-4}$	$4.20\,10^{-5}$	0.04
	$3\,10^{-4}$	$3.15\,10^{-5}$	1	3	0.35	10	$2.92\,10^{-2}$	$2.30\,10^{-3}$	70.0	0.35	7.6	$6.61\,10^{-4}$	$5.45\,10^{-5}$	0.07
	$3\,10^{-4}$	$4.50\,10^{-5}$	1	3	0.35	10	$3.34\,10^{-2}$	$6.78\,10^{-3}$	60.0	0.40	8.0	$5.81\,10^{-4}$	$8.00\,10^{-5}$	0.04
	$3\,10^{-4}$	$7.20\,10^{-5}$	1	3	0.35	10	$4.01\,10^{-2}$	$1.17\,10^{-2}$	106.3	0.27	8.3	$5.03\,10^{-4}$	$1.31\,10^{-4}$	0.10
	$3\,10^{-4}$	$1.08\,10^{-4}$	1	3	0.35	10	$4.87\,10^{-2}$	$1.61\,10^{-2}$	161.7	0.22	8.4	$4.44\,10^{-4}$	$2.30\,10^{-4}$	0.14
	$3\,10^{-4}$	$4.50\,10^{-4}$	1	3	0.35	2	$4.61\,10^{-2}$	$1.59\,10^{-2}$	85.8	0.20	9.0	$4.80\,10^{-4}$	$2.02\,10^{-4}$	0.13
	$3\,10^{-4}$	$9.41\,10^{-4}$	1	3	0.35	1	$4.82\,10^{-2}$	$2.83\,10^{-2}$	20.2	0.40	10.1	$5.52\,10^{-4}$	$2.95\,10^{-4}$	0.24
	$3\,10^{-4}$	$1.05\,10^{-3}$	1	3	0.35	1	$5.14\,10^{-2}$	$2.78\,10^{-2}$	28.2	0.32	10.0	$5.09\,10^{-4}$	$3.29\,10^{-4}$	0.23

Table 1
Numerical models and results (see text for details). Models C and T are visualized in figure 2.

time. Here we choose to normalize this quantity by the standard magnetic diffusion time $\tau_{mag} = D^2/\lambda$, in order to account for the variation in the shell gap D throughout geological time.

2.2 *Generalized relationship between convective power and mass anomaly flux / Rayleigh number*

Here we derive a general relation between the convective power density p and the Rayleigh number Ra_Q. Buffett et al. (1996) demonstrated that under the assumption of good mixing (sufficiently supercritical convection), the total dissipation Φ of the dynamo is proportional to the sum of the inner- and outer- boundary originated mass anomaly fluxes:

$$\Phi = \Phi_i + \Phi_o = F_i(\psi_i - \overline{\psi}) + F_o(\overline{\psi} - \psi_o) \tag{17}$$

Here ψ is the gravitational potential such that the gravity vector is $\mathbf{g} = -\nabla\psi$, and ψ_i, ψ_o, $\overline{\psi}$ are respectively the inner boundary, outer boundary, and mean values of the gravitational potential. The physical meaning of (17) is that the dissipation results from taking mass anomaly at a given gravitational potential, and redistributing it at the mean gravitational potential, which is where the good mixing assumption enters.

In the present context of radial gravity, the gravitational potential is expressed as $\psi = r^2 g_o/2r_o + cst$. The expression for $\overline{\psi}$ is (Buffett et al., 1996):

$$\overline{\psi} = \frac{3g_o}{10r_o}\left(\frac{r_o^5 - r_i^5}{r_o^3 - r_i^3}\right) \tag{18}$$

Expanding (17) with the help of (18), and making use of the fact that the conservation of energy, when averaged over times long relatively to core flow time scales, yields $pV = \Phi$, we obtain after some algebra the following proportionality relationship between the dimensional power per unit volume p and the total mass anomaly flux F:

$$p = \gamma \frac{g_o F}{4\pi D^2} \tag{19}$$

with

$$\gamma = \frac{3(r_o - r_i)^2}{2(r_o^3 - r_i^3)r_o}\left[f_i\left(\frac{3}{5}\frac{r_o^5 - r_i^5}{r_o^3 - r_i^3} - r_i^2\right) + (1 - f_i)\left(r_o^2 - \frac{3}{5}\frac{r_o^5 - r_i^5}{r_o^3 - r_i^3}\right)\right] \tag{20}$$

The dimensionless form of (19) therefore writes:

$$\frac{p}{\rho\Omega^3 D^2} = \gamma Ra_Q \tag{21}$$

Equations (20,21) are the generalizations to arbitrary buoyancy distributions of the relationships obtained in appendix A of Christensen & Aubert (2006). They are tested in figure 1 versus our numerical data. The agreement between theoretical and numerical values of p/Ra_Q becomes good as the supercriticality of convection increases. Cases with a strong stable density stratification (i.e $f_i >> 1$) need a stronger level of mixing to approach the theoretical line. This is simply a consequence of the fact that convection does not fill the entire shell in these cases. For a

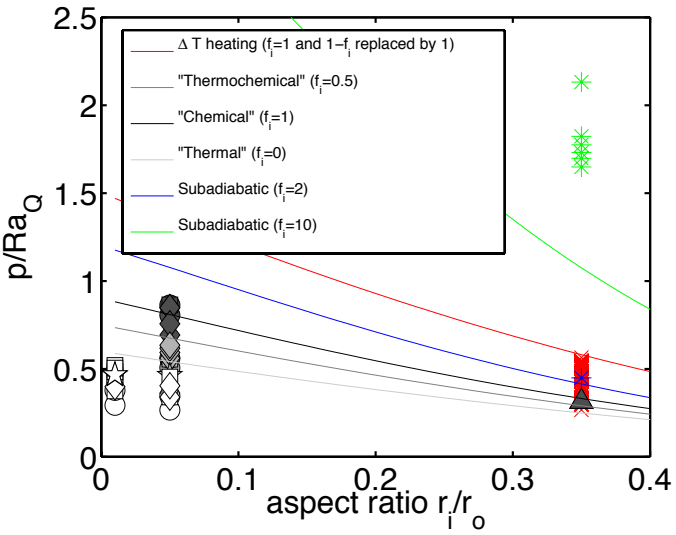

Fig. 1. Test of the perfect mixing theoretical p/Ra_Q relationship with numerical data. Symbols represent the numerical data, and lines represent the theoretical prediction of equations (20,21). Red color: Christensen & Aubert (2006) data points. Our theory applies to their choice of fixed temperature boundary conditions provided f_i and $1 - f_i$ are replaced by 1 in equation (20). White symbol filling and light grey line: cases of secular cooling with $f_i = 0$. Medium-grey symbol filling and line: cases of thermo-chemical convection with $f_i = 0.5$. Dark-grey symbol filling and black line: cases of purely chemical convection with $f_i = 1$. Blue symbols and lines: cases where the shell is stably stratified at the outer boundary (sub-adiabatic system) with $f_i = 2$. Green symbols: same as blue, for $f_i = 10$. For symbol shape definitions see figure 3.

given level of convection supercriticality, the mass anomaly, while indeed produced at the inner boundary, therefore fails to be redistributed at the mean gravitational potential of the shell to a greater extent.

For the scaling relationships to be presented in the next section, the use of p instead of Ra_Q as a basic scaling parameter is motivated by several important reasons. First, the theory underlying these scalings (Christensen & Aubert, 2006) relies on convective power arguments, while Ra_Q is merely an approximate proxy for convective power. In our present study, where we vary the buoyancy partition f_i and the aspect ratio r_i/r_o, the use of Ra_Q as a basic scaling parameter does not capture the geometrical and buoyancy distribution effects contained in (20), thus resulting in a larger scatter that the use of p corrects for. Another advantage of using p instead of Ra_Q is that p is a geophysical parameter which is constrained by thermodynamic studies of the Earth's core (e.g Lister, 2003, see section 3.2). Finally, expressing the scalings with p leads to a useful internal consistency relationship to be detailed in section 3.3.

2.3 Statistics of least-squares fits

In section 3.1, we obtain power laws of the form $y = ax^b$ from numerical data. The problem reduces to getting a linear least squares fit of the form $\ln y = \ln a + b \ln x$. Let $e_i = \ln \hat{y}_i - \ln y_i$ be the error between the fitted value (hat) and actual value for sample i. An estimator for the variance of the errors is therefore

$$\sigma^2 = \frac{1}{N-2} \sum_{i=1}^{N} e_i^2 \tag{22}$$

While σ can be seen as a measure of the error for the scaling prefactor $\ln a$, it is possible to estimate the error for the scaling exponent b through the following formula:

$$\sigma_b^2 = \frac{1}{N-2} \sum_{1}^{N} \left[\left(\frac{\ln y_i - \ln a}{\ln x_i} \right) - b \right]^2 \tag{23}$$

In the scalings presented in section 3.1, we usually have $\sigma_b << b$, while σ is comparable to $|\ln a|$. We therefore present the best-fit laws $y = ax^b$ together with their 3σ lines $y = (a/e^{3\sigma})x^b$ and $y = ae^{3\sigma}x^b$, which theoretically enclose 99.7% of the data if the distribution of errors e_i is normal. The internal consistency of the scalings is also discussed in the light of the results for σ_b.

3 Results.

3.1 Results from numerical dynamos.

We first present (Figure 2) images from two models with a small inner core ($r_i/r_o = 0.05$, see table 1 for other parameters). Model C is driven by inner-boundary originated buoyancy (chemical convection, $f_i = 1$), and model T is driven by volumetric heating and outer-boundary originated buoyancy (secular cooling, $f_i = 0$). Convection sets up where the thermo-chemical gradients are most unstable: one single convection cell near the inner boundary for C, five cells extending from mid-shell to the outer boundary for T. DMFI visualization (Aubert et al., 2008) reveals that the magnetic field is generated according to the classical macroscopic alpha-squared mechanism (Olson et al., 1999), although model C additionally has an enhanced toroidal field production by zonal flow near the outer boundary. Both models are dipole-dominated, with magnetic dipoles of similar relative strengths (C and T respectively have $f_{dip} = 0.47, 0.49$). They are typically less dipolar than similar models with $\chi = 0.35$ (see figure 6). In model T, the lower dipolarity can be explained by shallow convection columns which enhance magnetic flux expulsion and thus enrich the outer boundary power spectrum in multipolar content. In model C, the

small inner core surface over which the buoyancy is distributed favors the occurrence of magnetic upwellings (Aubert et al., 2008) which reduce the dipolarity by frequently disrupting the magnetic dipole. In both models, the absence of the inner core favors a global axisymmetric poloidal circulation, which, at a given instant in time, concentrates magnetic field at one pole and disperses it at the other pole (in the snapshots presented in figure 2, flux concentration is occurring at the south pole for model C and the north pole for model T). It should finally be noted that in thermal models, the absence of buoyancy at the inner-core boundary decouples the inner core from the convection and dynamo processes, with two consequences: first, thermal models with $r_i/r_o = 0.05$ or $r_i/r_o = 0.01$ yield almost the same results, which are presumably those which would be obtained from a case where $r_i = 0$. Second, the relationship between reverse magnetic flux patch locations and inner core size (Stanley et al., 2007) does not hold if secular cooling drives the dynamo.

Figure 3 presents a plot of the Rossby numbers Ro versus the dimensionless convective power p. The best fit and 3σ lines have equations

$$Ro = (0.69, 1.31, 2.49)\ p^{0.42} \tag{24}$$

When cast into a $p-Ro$ space, the Christensen & Aubert (2006) scaling is virtually unchanged by the addition of the new data points with variable inner core size and buoyancy distribution, with a scatter which is also unchanged. In the dipole-dominated regime ($f_{dip} > 0.35$), the same remarks hold for the Lorentz number Lo scaling (figure 4), which obeys:

$$Lo/f_{ohm}^{0.5} = (0.62, 1.17, 2.22)\ p^{0.34} \tag{25}$$

We deduce that the convective power p is the primary scaling parameter for magnetic and velocity field amplitude, and integrates the relevant dependencies on inner core size and buoyancy distributions for our present purposes. We further check (figure 5) the relation between the magnetic dissipation time τ_{diss} and the magnetic Reynolds number $Rm = RoPm/E$ (Christensen & Tilgner, 2004):

$$\tau_{diss}/\tau_{mag} = (0.11, 0.26, 0.65)\ Rm^{-1.0} \tag{26}$$

For this last scaling, the newer runs cause a significantly larger scatter than that obtained by Christensen & Tilgner (2004). We attribute this to the rather small size (26 models) and limited parameter space extent of the data set used in that study, and conclude that the aspect ratio and buoyancy distribution have little influence on this scaling.

For an extrapolation of the three scalings presented above to Earth's core conditions, the scaling prefactors need to be determined. Here we derive a useful internal consistency relationship tying these prefactors. We first define the dimensional values B_{rms} and V_{rms} for Lo and Ro, expand them using (24,25) and also recall the

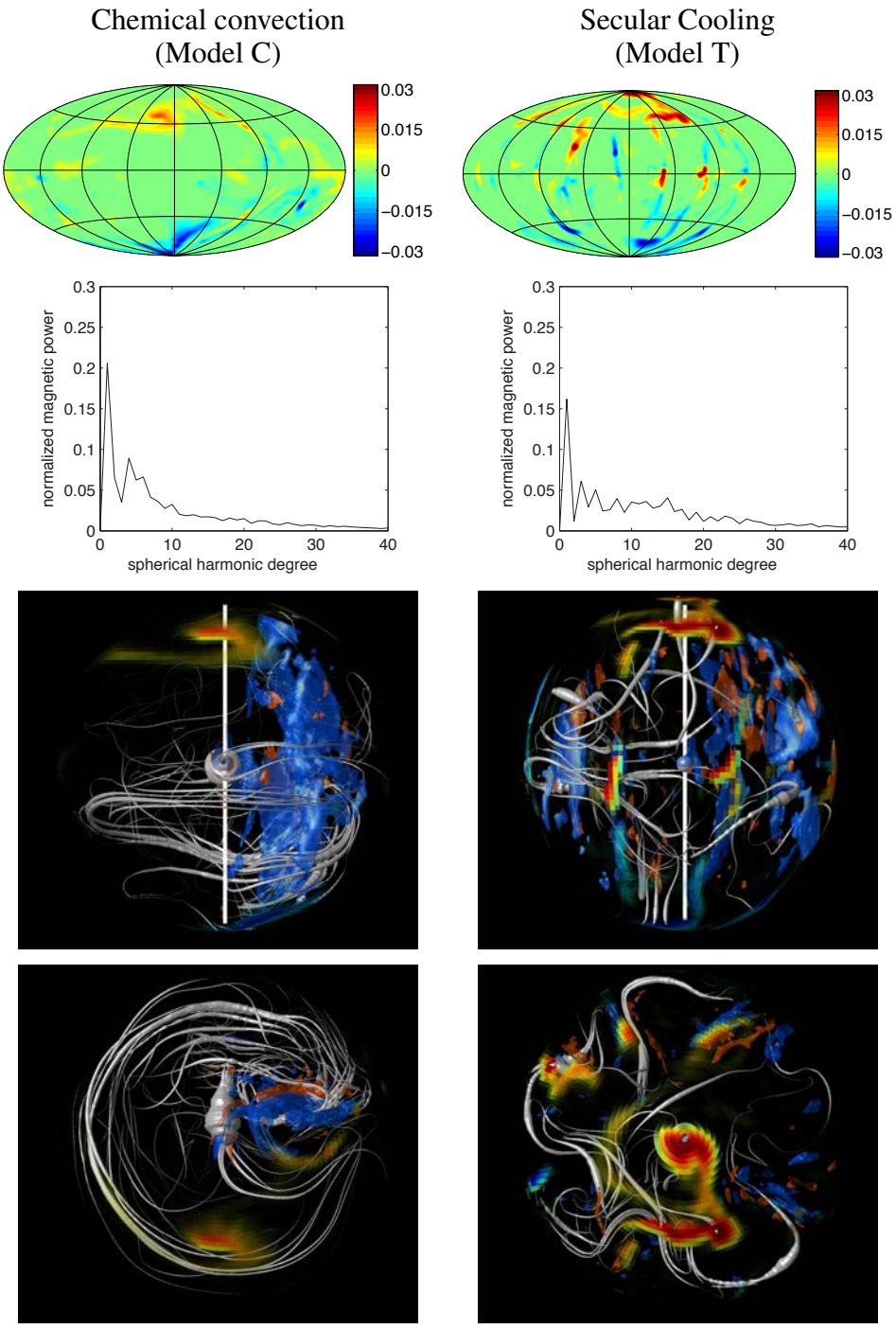

Fig. 2. Magnetic field and flow morphologies from a chemically-driven model (C, $f_i = 1$), and a model driven by secular cooling (T, $f_i = 0$). See table 1 for other parameters. From top to bottom: hammer projections of the radial magnetic field at the outer boundary, harmonic degree spectrum of the power normalized by the total power, DMFI equatorial and polar visualizations. The DMFI images present magnetic field tubes (grey) with thicknesses normalized by the local magnetic energies, as well as two isosurfaces of the axial vorticity $\omega_z = (\nabla \times \mathbf{u}) \cdot \mathbf{e}_z$, with levels -0.54 (blue) and 0.54 (red) for model C, and ± 0.18 for T. The outer boundary is color coded with the radial magnetic field, with similar color scheme as on the hammer projections. The thick white line is the rotation axis. For other details on DMFI imaging see Aubert et al. (2008).

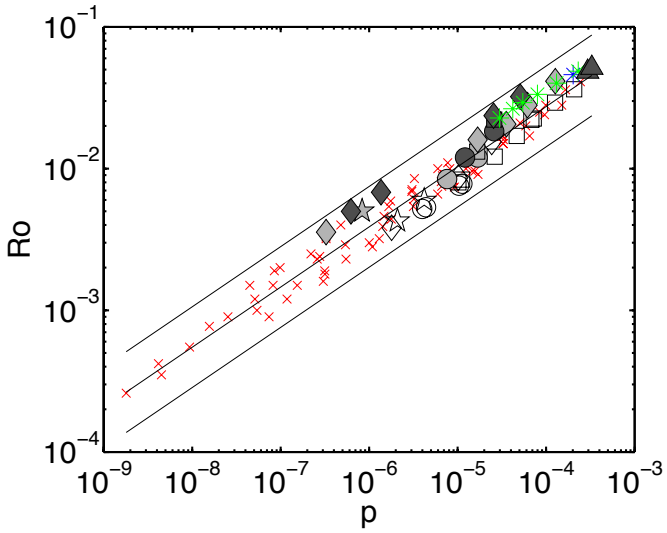

Fig. 3. Dimensionless r.m.s. velocity, or Rossby number Ro as a function of the dimensionless convective power p. Red crosses are the Christensen & Aubert (2006) data points. Other symbol colors are defined in figure 1. Symbol shapes are as follows: small aspect ratio models ($\chi < 0.05$) have circles for $Pm = 10$, squares for $Pm = 5$, diamonds for $Pm = 2$, pentagrams for $Pm = 1$. Present aspect ratio ($\chi = 0.35$) additional models (triangles and stars) have $Pm = 3$. Our dataset is filtered to exclude the non-dynamo run.

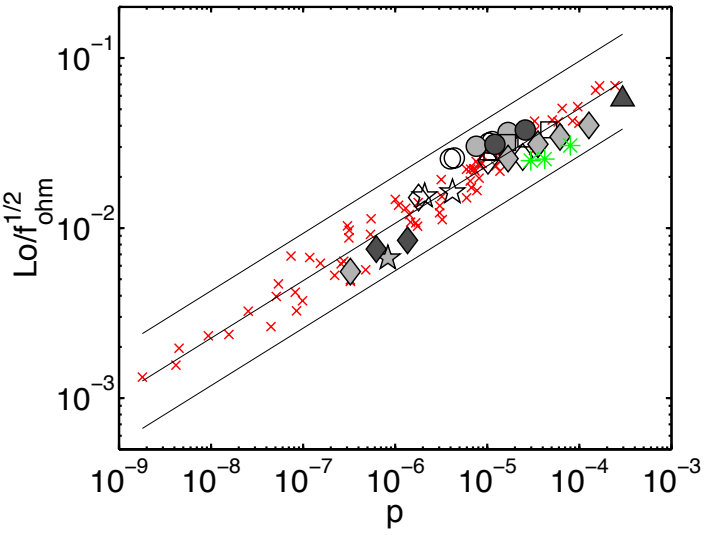

Fig. 4. Dimensionless magnetic field, or Lorentz number Lo, corrected with the ohmic dissipation fraction $f_{ohm}^{0.5}$, as a function of the dimensionless convective power p. Symbols as in figure 3. Our dataset is filtered to exclude dynamos with a dipole fraction $f_{dip} \leq 0.35$.

definition of τ_{diss}:

$$B_{rms} = Lo(\rho\mu)^{1/2}\Omega D = c_1 f_{ohm}^{0.5} p^{0.34}(\rho\mu)^{1/2}\Omega D, \tag{27}$$

$$\tau_{diss} = c_2 Rm^{-1} D^2/\lambda \quad \text{with} \quad Rm = U_{rms}D/\lambda \tag{28}$$

$$U_{rms} = (\Omega D)Ro = c_3 p^{0.42}\Omega D \tag{29}$$

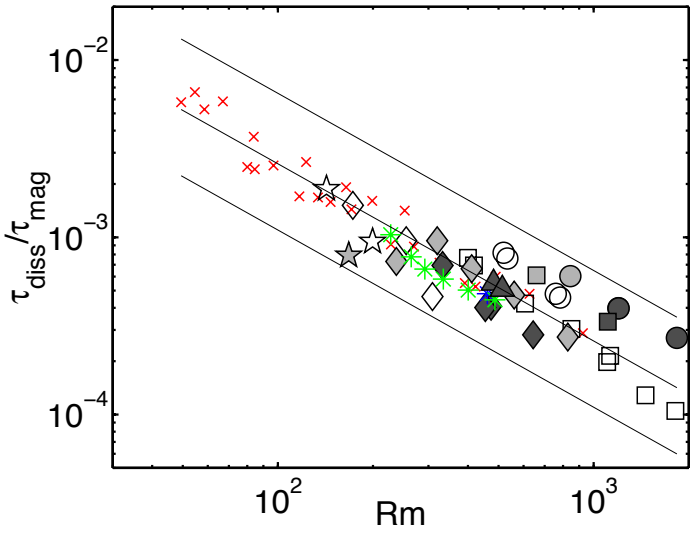

Fig. 5. Magnetic dissipation time τ_{diss}, normalized by the standard magnetic diffusion time τ_{mag}, as a function of the magnetic Reynolds number Rm. Symbols as in figure 3, except the red crosses which represent the Christensen & Tilgner (2004) models. Our dataset is filtered to exclude the non-dynamo run.

Here the c_i coefficients are scaling prefactors, to be chosen within the 3σ range of each scaling. In the case of the geodynamo, where the magnetic diffusivity is much larger than the viscous diffusivity, we expect most of the convective power $\rho\Omega^3 D^2 pV$ to be dissipated through ohmic losses (i.e. $f_{ohm} \approx 1$), hence:

$$\rho\Omega^3 D^2 p = \frac{B_{rms}^2}{2\mu}\frac{1}{\tau_{diss}} \tag{30}$$

The dimensionless version of (30) writes:

$$1 = \frac{c_1^2 c_3}{2c_2} p^{0.1} \tag{31}$$

This reveals a good consistency of the scalings: for instance, the dependency in λ vanishes as it should, thanks to the scaling exponent -1 in (28). However consistency is not perfect, as witnessed by the residual power 0.1 at which p appears. As in the next section, p will be assumed to vary over geological time, this will prevent (31) to be exactly satisfied with time-independent values for c_{1-3}. This problem can be related to the standard error in the least-squares determination of each exponent. Following the procedure delineated in section 2.3, we obtained standard exponent errors of $\sigma_{b1} = 0.0169$, $\sigma_{b2} = 0.0639$, and $\sigma_{b3} = 0.0178$ for the Lo, τ_{diss} and Ro scalings, respectively. The error on the exponent of the ohmic dissipation, in the right-hand-side of (31), is therefore:

$$\sigma_b = 2\sigma_{b1} + 0.42\sigma_{b2} + \sigma_{b3} = 0.078 \tag{32}$$

As σ_b is comparable with the residual power 0.1 present in (31), we conclude that this inconsistency reflects the inherent error introduced by data scatter in the least-

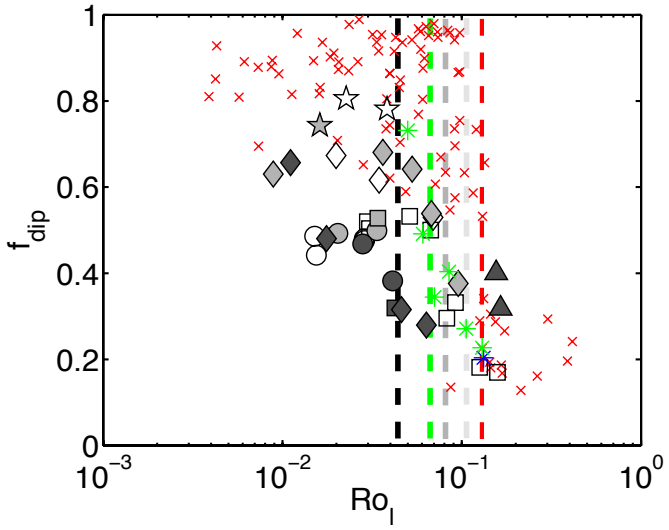

Fig. 6. dipolar fraction f_{dip} as a function of the local Rossby number $Ro_l = Ro\ \bar{l}/\pi$. Symbols as in figure 3. The dashed lines delineate the transition point from stable to reversing dynamos: red dashes for the $\chi = 0.35$ models from Christensen & Aubert (2006), green for $\chi = 0.35$ and $f_i > 1$, light grey for $\chi = 0.01 - 0.05$ and $f_i = 0$, medium grey for $\chi = 0.01 - 0.05$ and $f_i = 0.5$, black for $\chi = 0.01 - 0.05$ and $f_i = 1$. Our dataset is filtered to exclude the non-dynamo run.

squares fitting procedure used to derive the three scalings. This error remains small however, and can be compensated (as will be done in section 3.3) by choosing a set of c_{1-3} that minimizes the deviations caused by $p^{0.1}$ (typically 20%).

The control parameter $Ro_l = Ro\ \bar{l}/\pi$ was identified in Christensen & Aubert (2006) as the main parameter governing the dipolarity and stability versus reversals of numerical dynamo models. Here we follow the same approach (figure 6). We find that the critical local Rossby number for reversals Ro_{lc} is located in a narrow range $Ro_{lc} = 0.04 - 0.12$. In the dipole-dominated regime ($f_{dip} > 0.35$), figure 6 shows again that the absence of the inner core generally decreases the dipolarity, as already explained in figure 2.

We then analyze (figure 7) the ratio b_{dip}, which determines the relative strength of the internal field and the dipole field at the outer boundary. Since, as shown by figure 6, the geodynamo is likely to have had a dipolarity lower or equal to the present-day value throughout its history, we restrict the data to the range $0.4 < f_{dip} < 0.7$. In this range, we find little variability of b_{dip} with the convective power (or Ro_l), whereas the main source of variability comes from f_i and χ. This can be attributed to depth variations of the dynamo region, the dipole seen at the surface being reduced in the case of a deeper dynamo. Indeed chemical models (deeper dynamos) have a markedly larger b_{dip} value than thermal models (shallow dynamos, see figure 2). The highest b_{dip} values are obtained for models with $f_i > 1$, where the extent of the dynamo region is restricted even further by a stably stratified layer at the top of the shell (see for instance Christensen, 2006). In section 3.3, a model

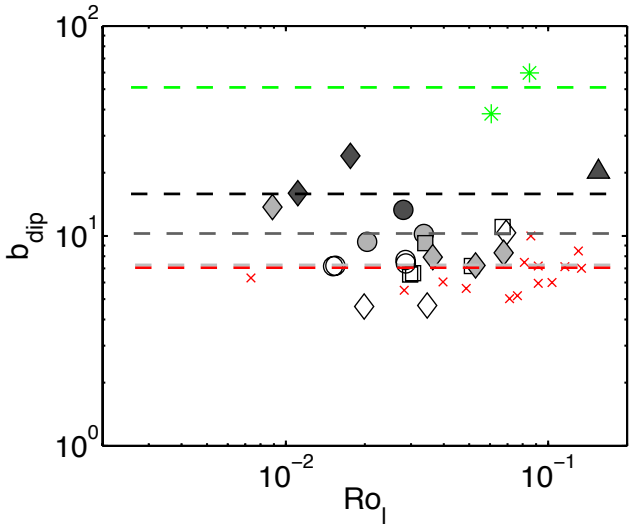

Fig. 7. ratio b_{dip} of the r.m.s magnetic field inside the shell to the dipole field at the outer boundary, as a function of the local Rossby number Ro_l. Symbols as in figure 3. The dashed lines locate the predictions of model (33), with same color conventions as in figure 6. Our dataset is filtered to retain dynamos with a dipole fraction $0.4 < f_{dip} < 0.7$.

will be needed for b_{dip} in order to estimate the dipole moment at any point in the geological history. We adopt the simplest possible linear dependency:

$$b_{dip} = 7.3(1-\chi)(1+f_i) \tag{33}$$

The last scaling which we check (figure 8) is the relationship (Olson & Christensen, 2006) between the local Rossby number Ro and the dynamo control parameters p, Ek, Pm, Pr. As there does not currently exist a physical rationale to exclude some control parameters, the powers in this last scaling were obtained by an approach of empirical scatter minimization. We confirm (figure 8.a) the scaling relationship obtained by Olson & Christensen (2006):

$$Ro_l = (0.34, 0.68, 1.35) p^{0.48} E^{-0.32} Pr^{0.19} Pm^{-0.19} \tag{34}$$

Unlike in the previous scalings, there appears an additional dependence on the aspect ratio χ, which we resolve by adopting the following relationship, yielding a smaller data scatter (figure 8.b):

$$\frac{Ro_l}{(1+\chi)} = (0.33, 0.54, 0.89) p^{0.48} E^{-0.32} Pr^{0.19} Pm^{-0.19} \tag{35}$$

Note that factoring out a $(1+\chi)$ dependence also slightly reduces the scatter in the critical Ro_{lc} values obtained from figure 6. We therefore propose the following model for Ro_{lc}:

$$\frac{Ro_{lc}}{(1+\chi)} \approx 0.04 - 0.1 \tag{36}$$

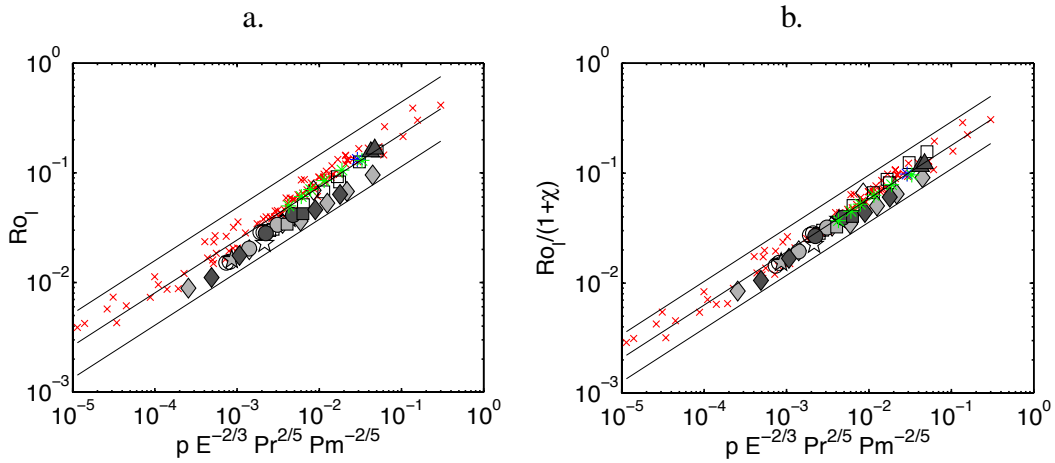

Fig. 8. Local Rossby number Ro_l as a function of the combination $pE^{-2/3}Pr^{2/5}Pm^{-2/5}$ proposed in Olson & Christensen (2006). a: without a dependence in χ, b: with a dependence in χ. Symbols as in figure 3. Our dataset is filtered to exclude the non-dynamo run.

3.2 Core thermodynamics and cooling models.

The previous section shows how time-average properties of the past geodynamo can be estimated from the convective power. The assumed time scale for this time average is long (say a million years) compared to core flow time scales, but short compared to any geological evolution time scale of the Earth. The geological evolution of dynamo properties can be obtained from our scaling laws if we have a long-term evolution model for the convective power, which we now derive from core thermodynamics (see the recent studies from Labrosse, 2003; Lister, 2003, and references therein). The fundamental inputs which are needed is an history of core-mantle heat flow $Q_{cmb}(t)$, of the radioactive core heating $Q_r(t)$, and the heat flow down the isentropic temperature gradient at the CMB Q_a (hereafter denoted as adiabatic heat flow), which is assumed constant over time. In what follows, we use the simple parametrization of Lister (2003) which holds if the inner core volume is small relative to the outer core volume ($\chi^3 << 1$):

The entropy budget of the system, when time-averaged over time scales much longer than core flow time scales, but shorter than geological time scales, gives an expression for the total dynamo dissipation Φ as a function of the fundamental inputs listed above. The part Φ_i of the dissipation that originates from mass anomaly flux at the inner boundary is then

$$\Phi_i = (Q_{cmb} - Q_r)(\epsilon_L + \epsilon_B) \tag{37}$$

Where ϵ_L and ϵ_B are respectively the thermodynamic efficiencies of latent heat and

light element release, which are given by

$$\epsilon_L = \frac{3\mathcal{L}(1-\overline{e}(\phi))\chi}{2+3(\mathcal{L}+\mathcal{B}-C)\chi} \tag{38}$$

$$\epsilon_B = \frac{3\mathcal{B}\chi}{2+3(\mathcal{L}+\mathcal{B}-C)\chi} \tag{39}$$

The values of the thermodynamic parameters $\mathcal{L}, \mathcal{B}, C$, $\overline{e}(\phi)$ and ϕ are given in table 2. The part Φ_o of the dissipation that originates from mass anomaly flux at the outer boundary is

$$\Phi_o = (Q_{cmb} - Q_a)\epsilon_S \tag{40}$$

Where ϵ_S is the thermodynamic efficiency of thermal convection, given by

$$\epsilon_S = e^{\phi}\overline{e}(\phi) - 1 \tag{41}$$

The dimensionless, total volumetric power p can be obtained through the time average conservation of energy $\rho\Omega^3 D^2 pV = \Phi_i + \Phi_o$, where V is the shell volume. Once the dissipations Φ_i and Φ_o are known, it is straightforward to retrieve the associated mass anomaly fluxes F_i and F_o from equation (17), which finally yield $f_i = F_i/(F_i + F_o)$. Note that for strongly sub-adiabatic cases, (17) may not hold because of incomplete mixing, which in this case might lead to an underestimation of f_i.

Once the inner core is present, the evolution of the inner core aspect ratio χ is constrained by the heat capacity for solidification $\mathcal{M}$ (value in table 2) through the equation:

$$\mathcal{M}\frac{\mathrm{d}}{\mathrm{d}t}\left[\chi^2 + (\mathcal{L}+\mathcal{B}-C)\chi^3\right] = -(Q_{cmb} - Q_r) \tag{42}$$

Equation (42) can be integrated backwards in time from present (Labrosse et al., 2001) until the inner core age a (Here time is measured before present, therefore $a > 0$).

In the present study, we neglect the radioactive heating in the core throughout the Earth's history, i.e. $Q_r = 0$, as recent experiments (Hirao et al., 2006) of potassium partitioning between iron and silicates suggest that present potassium radioactivity amounts for a heat production of about 0.2 TW, which is quite low when compared to typical Q_{cmb} values. Radioactivity was obviously stronger in the past (in the case of potassium, the power is double every 1.26 Gyr backwards), but this would amount to typically 1.5 TW at the beginning of the Earth's history, which again is quite low compared to estimated Q_{cmb} at that time.

The value of the adiabatic heat flow Q_a is uncertain and debated. Following Stacey & Loper (2007); Labrosse et al. (2007); Lay et al. (2008), we adopt $Q_a = 6$ TW for a central value and allow for an uncertainty range of 1 TW above and below this value. This would correspond to a central value of the upper outer core thermal conductivity of about 50 W/m/K at the top of the core (Labrosse, 2003).

Parameter	Meaning	Value	Reference
$Q_{cmb}(t)$	Earth's cooling model	variable	see section 3.2
Q_a	Adiabatic heat flow at the CMB	6 TW	see section 3.2
Q_r	radiogenic heating in the outer core	0 W	see section 3.2
$\mathcal{M}$	Heat capacity for solidification	9.2 10^{29} J	Lister (2003)
$\mathcal{L}$	Latent heat effect	2.1	Lister (2003)
$\mathcal{B}$	Buoyancy effect	0.86	Lister (2003)
$\mathcal{C}$	Compositional effect	-0.8	Lister (2003)
ϕ	Adiabatic decay parameter	0.256	Lister (2003)
$\overline{e}(\phi)$	Adiabatic decay integral	0.8595	Lister (2003)
r_o	Outer core radius	3480 km	
$\Omega(t)$	Earth's rotation rate	variable	see section 3.3
λ	Outer core magnetic diffusivity	1.3 m^2/s	Secco & Shloessin (1989)
ν	Outer core viscosity	10^{-6} m^2/s	de Wijs et al. (1998)
κ	Outer core thermo-chemical diffusivity (assumed to be the same as thermal diffusivity)	5 10^{-6} m^2/s	Stacey & Loper (2007); Labrosse et al. (2007); Lay et al. (2008)
ρ	Outer core density	10^4 kg/m^3	Dziewonski & Anderson (1981)

Table 2
Parameters used in the thermodynamic, core cooling (section 3.2, upper panel), and paleomagnetic (section 3.3, lower panel) models.

We now turn to the central unknown of our analysis, the history of the heat flow at the CMB $Q_{cmb}(t)$. Since there are many uncertainties involved in the determination of Earth cooling models, as well as in our present modelling effort, our goal is not to propose a definitive model for the geologic evolution of the geodynamo, which would be based on a definitive model for $Q_{cmb}(t)$. Rather, we focus on two end-member scenarios representing the variety of geophysical situations which can be expected based on the uncertainties (figure 9). The first one, which we label as the high-power scenario, was proposed by Labrosse et al. (2007). It is motivated by the large (about 10 TW) present heat flows at the CMB deduced from post-perovskite seismological studies (Hernlund et al., 2005; Lay et al., 2006), from geochemical constraints and from the present crystallization of a basal magma ocean in the lower mantle. As indicated by figure 9.a, it yields a typical dynamo power of 2.7 TW at present. The second, low power scenario is motivated by the fact that the scaling of ohmic dissipation in numerical dynamos (Christensen & Tilgner, 2004) favors a low present dissipation of about 0.2-0.5 TW. Using the thermodynamic analysis presented above, this implies that the top of the Earth's core is presently

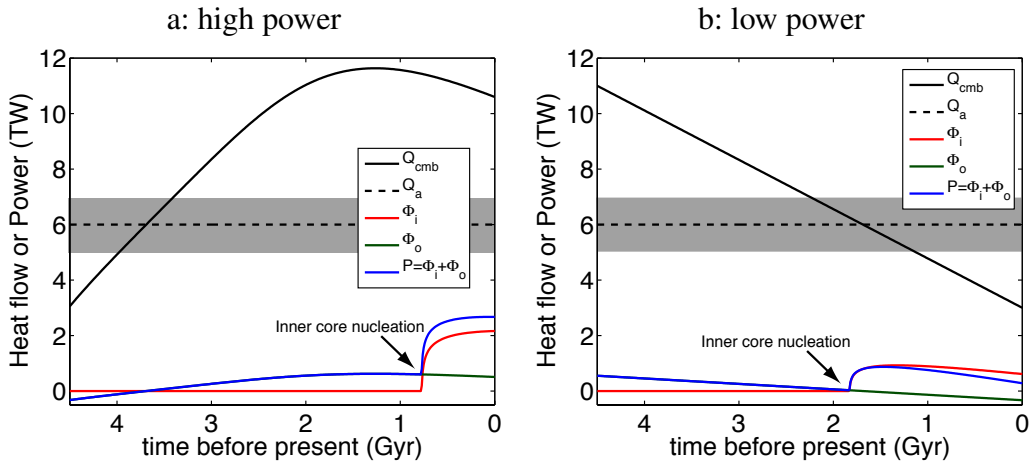

Fig. 9. High- (a) and Low- (b) power models for: heat flow from the core to the mantle Q_{cmb}, adiabatic heat flow Q_a, inner- and outer- boundary originated dissipations Φ_i,Φ_o, and total power $P = \Phi_i + \Phi_o$ as functions of the time before present. The greyed area represents the uncertainty range for the adiabatic heat flow. The inner core nucleates at $a \approx 1.8$ Gyr before present in the low power scenario, and $a \approx 0.8$ Gyr before present in the high-power scenario.

sub-adiabatic ($Q_{cmb} < Q_a$, see figure 9.b). A variety of idealized, constant rate cooling histories can be built, which cross the adiabat at an age b. Plausible models are such that $b \leq a$ (Labrosse et al., 1997), because if $b > a$ then convection stops in the Earth's core between the adiabat crossing and the nucleation of the inner core. This is not acceptable since a conducting core would not cool fast enough to subsequently nucleate an inner core before present. Our second scenario is built according to this constraint, taking an initial core-mantle boundary heat flow of $Q_{cmb} = 11$ TW, and a present value $Q_{cmb} = 3$ TW, corresponding to a present dynamo power of about 0.3 TW.

3.3 Time evolution models for paleomagnetic observables.

We now combine the dynamo scaling study from section 3.1 with the thermodynamic elements from section 3.2 in order to evaluate the main properties of the past geodynamo. At any point in time, the power p can be accessed from the analysis of the previous section. The Prandtl and magnetic Prandtl numbers are set according to the diffusivity values listed in table 2. In order to determine the Ekman number E, the rotation rate of the Earth is needed. We use the length-of-day model (LOD) of Varga et al. (1998), according to which the LOD has piecewise linearly increased from 19 hours 2.5 Gyrs ago to 20.8 hours 0.64 Gyr ago, and to 24 hours today. As there is no constraint on earlier length of day, we backward continue the 2.5-0.5 Gyr trend, thus yielding an initial length of day of 17 hours. It should be mentioned that the length-of-day variation should not exceed a factor 2 in any case, which has a weak impact on the scalings where the Ekman number is present.

We next turn to the choice of the scaling prefactors c_{1-3} in equations (27,28,29), under the constraint (31) of internal consistency. Using the central values for the prefactors c_i as a starting point, we obtain $p^{0.1}c_1^2c_3/2c_2 \approx 0.3$ throughout time. We therefore need to adjust the prefactors c_i within the 3σ error range, increasing $c_{1,3}$ and decreasing c_2. This under-determined problem requires further assumptions. As the central value $c_3 = 1.31$ already produces quite large U_{rms} values in the high-power scenario (up to 1.8 mm/s, at the upper end of admissible core velocities (Christensen & Aubert, 2006)), we choose not to increase c_3 further. We also take an end-member model approach and look for the smallest magnetic field which can be produced by the high-power scenario, and the largest magnetic field which can be produced by the low-power scenario. The relevance of this choice will appear later, when we analyze the model predictions for the dipole moment. The largest magnetic field is obtained with $c_1 = 2.22$ (at the upper end of the admissible range), and $c_2 = 0.16$ is then obtained from (31). The smallest magnetic field is obtained with $c_1 = 1.65$ and $c_2 = 0.11$ (note that in this case, it is impossible to bring c_1 down to 0.62, at the lower end of the admissible range). Our predictions for U_{rms} (or the magnetic Reynolds number Rm), B_{rms} and the local Rossby number Ro_l are reported in figures 10.b,c,d. We note that the model for B_{rms} implicitly assumes that the dynamo has been dipole-dominated throughout Earth's history. This is reasonable since our models show that Ro_l, the parameter controlling the breakdown of dipolarity (figure 6) , has been below its present-day value throughout Earth's history (figure 10.d).

Having obtained end-member models for the paleo-evolution of the internal core magnetic field B_{rms}, we finally compute models for the true dipole moment

$$M = \frac{4\pi r_o^3}{\sqrt{2}\mu}\frac{B_{rms}}{b_{dip}} \tag{43}$$

For the determination of b_{dip}, we use the simple model (33), the time evolution of which is presented in figure 11.a. The resulting true dipole moment is compared with virtual dipole moment values from the IAGA paleointensity database (Perrin & Schnepp, 2004; Biggin et al., in press) on figure 11.b.

We define a normalized misfit δ between model values $\hat{m}_i$ and data m_i:

$$\delta = \sqrt{\frac{1}{N}\sum^{N}\frac{(\hat{m}_i - m_i)^2}{\hat{m}_i^2}} \tag{44}$$

Restricting the test to the Precambrian (more than 500 Myr ago), the high and low power models respectively yield almost the same values $\delta = 0.59, 0.55$. This underlines the large extent of our uncertainty concerning the extraction of cooling history information from paleointensities. If we now include the full dataset of figure 11.b, the high-power model yields $\delta = 0.46$, a markedly better fit than the low power model which has $\delta = 2.0$. Indeed the low-power model is strongly sub-

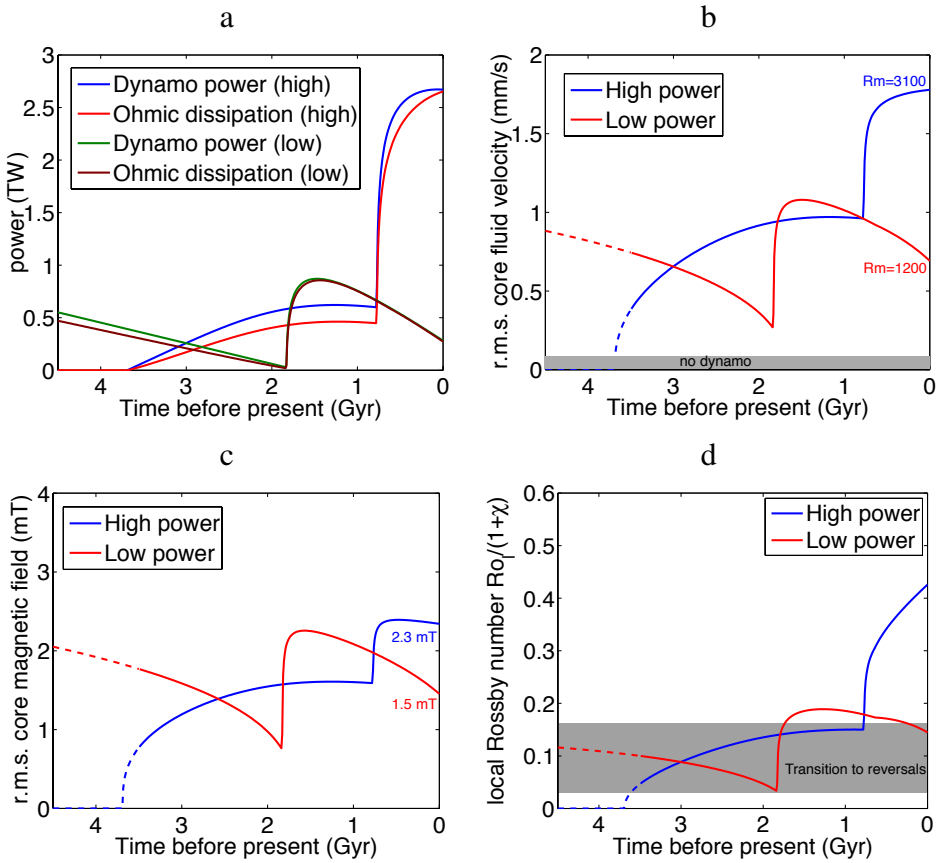

Fig. 10. a: dynamo power and ohmic dissipation (respectively left-hand-side and right-hand-side of the internal consistency relationship (30), both multiplied by the shell volume V). For the high- and low- power scenario we respectively use $(c_1, c_2, c_3) = (1.65, 0.11, 1.31)$ and $(c_1, c_2, c_3) = (2.22, 0.16, 1.31)$. The lack of scaling exponent consistency in (31) causes a maximal relative misfit of 20% through time. b: r.m.s core velocity U_{rms}, with indications of the equivalent magnetic Reynolds numbers Rm at present, and a rough delineation of the dynamo onset which would correspond to $Rm \approx 40$ (Christensen & Aubert, 2006). c: r.m.s. core magnetic field B_{rms}. d: local magnetic Reynolds number Ro_l (corrected by $1+\chi$). For this last scaling the central value 0.54 from (35) is used, and the 3σ uncertainty range is propagated to the location of the critical value Ro_{lc} for reversals obtained from (36) (grey zone). In b,c,d, the dashes represent the epoch with no available paleomagnetic samples.

adiabatic at recent-times ($f_i = 3.6$), which implies the presence of a stably stratified fluid layer in the upper outer core, thus decreasing the relative dipole intensity (large b_{dip} values, see figure 11.a).

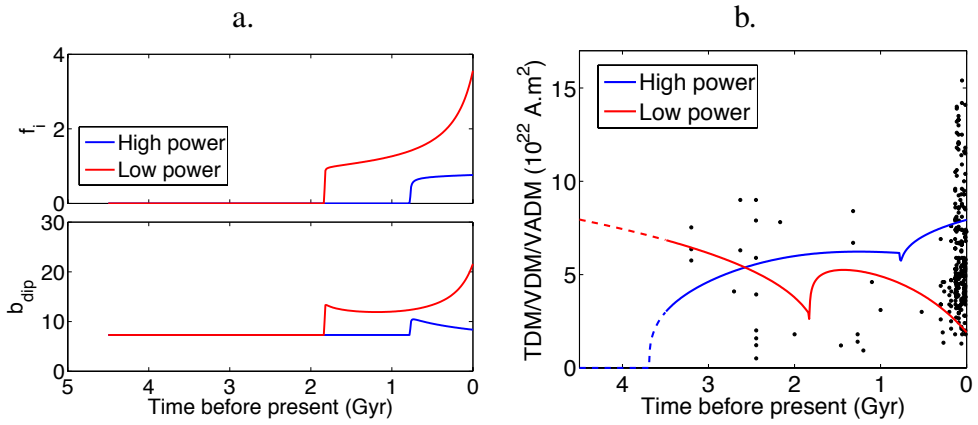

Fig. 11. a: time evolutions for f_i, obtained from (17), and for b_{dip}, obtained from (33). b: Time evolution models for the true dipole moment (TDM) M, with the same choice of scaling prefactors as in figure 10. The black dots represent the virtual dipole moment (VDM), or virtual axial dipole moment (VADM) values from the IAGA paleomagnetic database (Perrin & Schnepp, 2004; Biggin et al., in press). Only VDM/VADM data obtained from Thellier-Thellier-type experiments using pTRM consistency checks (Thellier & Thellier, 1959) were selected for robustness. Samples with an age of less than 10 Myr, of unknown or transitional polarity, or with VDM standard deviation greater than 20% of the mean were also excluded, thus reducing the data set to 242 reliable points, 24 of which corresponding to the Precambrian.

4 Discussion.

We first analyze the tighter constraints provided by the more recent (less than 500 Myr ago) data on our cooling scenarios. The maximum field predicted by the low-power scenario is still too low to fit the recent dipole moment data, a fact which leads us to prefer the high-power dynamo estimates for recent times. However, the dipole moments which we have presented for the high-power scenario are minimal estimates, and they correspond to quite large velocities inside the core, about 1.8 mm/yr, corresponding to a magnetic Reynolds number of about 3100 (see figure 10.a). Although not completely unrealistic, this seems rather extreme compared to surface flow velocities of about 5 mm/yr, corresponding to a magnetic Reynolds number of about 800 (Christensen & Tilgner, 2004). Keeping the same core cooling model, if we lower our estimates for the velocity field (by lowering the prefactors c_3), the internal consistency (30) imposes to raise our estimate for the minimum magnetic field (prefactor c_1), thus producing a worse fit to the recent paleointensities. An appropriate cooling model for the Earth's core would therefore need to terminate between the high and the low-power models, in order to provide the best fit to all observations. Our prediction for the present CMB heat flow would then lie at the lower bound of the range 7.5-15 TW proposed in recent seismological studies (Hernlund et al., 2005; Lay et al., 2006; van der Hilst et al., 2007).

Due to the small number and large scatter of paleomagnetic results from the Pre-

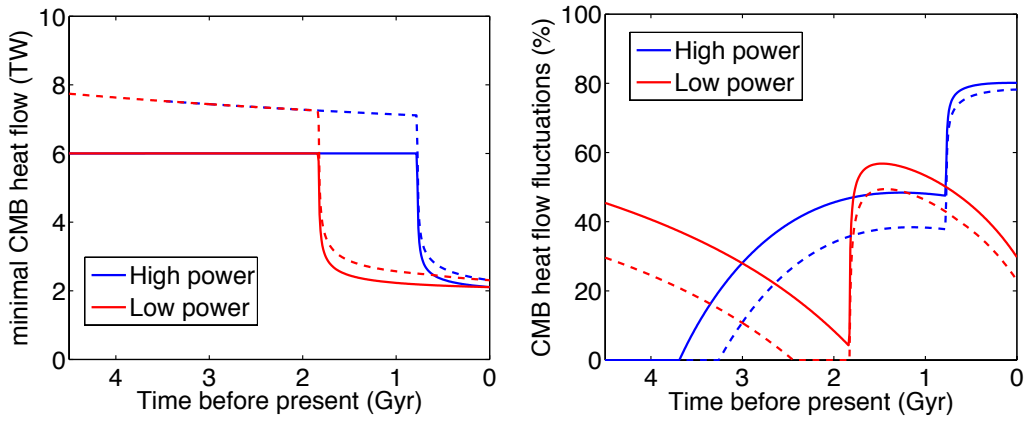

Fig. 12. Minimal CMB heat flow (left: absolute, right: relative to CMB heat flow) needed to get a dynamo (solid lines) and reversals (dashed lines).

cambrian, we have seen that our analysis fails to distinguish between the high and the low power scenarios during that epoch. We therefore discuss here the common features of both models. Not surprisingly, figure 10.b shows that the dynamo has operated above the typical value of the critical magnetic Reynolds number $Rm_c \approx 40$ (Christensen & Aubert, 2006) throughout the period 3.2 Gyr to present. As shown by Labrosse et al. (2007), it is possible though that intense initial radioactive decay in the mantle has blanketed the early core thermally, in such a way that the dynamo could not operate prior to 3.8-3.9 Gyr ago. This effect is integrated in the high-power scenario, but not in our idealized linear cooling model used in the low-power scenario.

Mantle dynamics can cause sizeable temporal fluctuations of the CMB heat flow (see for instance Nakagawa & Tackley, 2005), which would superimpose to the long-term geological trend which we used to produce our models. To simulate the effect of these fluctuations, we compute in figure 12 the minimal CMB heat flow required to get a dynamo. Here it is assumed that $Rm_c = 40$, but this value has a negligible effect on the result, which can be determined by simply writing down the condition $p \geq 0$. If the goal is to maintain a working dynamo throughout the Precambrian, then the low-power scenario appears to impose quite drastic restrictions on the amplitude of allowed fluctuations, especially near the inner core nucleation time, when the dynamo is very close to shut down. In contrast, the high-power scenario allows for fluctuations of 30% and larger throughout the period 3.2 Gyr ago to present.

Our results suggest that for a given convective forcing (more precisely, for a given local Rossby number), the absence of an inner core reduces the dipolarity. All forcing conditions being equal, the earlier geodynamo could therefore have been less dipolar than at present. However, inferring the dipolarity of the past geodynamo implies to weigh the effects of the geometry at given forcing, and of the forcing variations, a smaller Ro_l implying a possibly more stable and more dipolar dynamo (see figure 6). As, in both models, Ro_l has been generally lower than its present

value throughout Earth's history (figure 10.d), it is possible that 3-2.5 Gyr ago, the effects related to the absence of the inner core and to a lower Ro_l might have compensated to yield a dynamo with about present-day dipolarity, in line with the findings of Roberts & Glatzmaier (2001); Smirnov & Tarduno (2004).

In figure 10.d, both scenarios predict that the geodynamo has lied close to the transition towards polarity reversals throughout the Earth's history. This fact provides an a-posteriori justification for our use of scaling laws relevant to the dipole-dominated regime, even though the dynamo has been in a reversing state. Both scenarios predict that Ro_l was lower 2-3.2 Gyr ago than at present. Indeed, at this time, the dynamo had low thermal power, and the chemical buoyancy source was not present yet. This result is in good qualitative agreement with the conclusions of Biggin et al. (2008), who reported a trend towards less reversals some 2.4-2.8 Gyr ago than in recent times. It also agrees with the prediction of Coe & Glatzmaier (2006) that reversals must have been less common in the distant geological past. The picture is less clear for the last 1 Gyr, where the cooling rate variation (which determines p) is in competition with the variation in the length-of-day (which determines E) for the determination of Ro_l variations. More precise core cooling models will be required to determine whether reversals are becoming more frequent (as is the case in the high-power scenario) or less frequent (low-power scenario).

As for the onset of dynamo action, the same analysis of sensitivity to fluctuations can be done for the onset of reversals (figure 12), assuming for instance that the critical local Rossby number for reversals is $Ro_{lc}/(1+\chi) = 0.07$. The thermal dynamo which pertained to the early Earth conditions would have needed about 1-2 TW superadiabatic CMB heat flow to reverse. Here both scenarios are compatible with the oldest timing for reversals, which is in the range 2.7-3.2 Gyr (Strik et al., 2003; Tarduno et al., 2007). At recent-times, the amount of fluctuations needed to shut down reversals is very close to that needed to shut down the dynamo altogether, a fact which does not support the likeliness of mantle-induced superchrons in the last 500 Myr.

Models of the true dipole moment M presented in figure 11.b are both in equally good agreement with the Precambrian paleointensity data. In any case, our simulations show that core convection driven by secular cooling alone (before the appearance of the inner core) has no difficulties generating a magnetic field with strength comparable to the present field. As a consequence, the suggestion (Dunlop, 2007) that old paleomagnetic samples such as those analyzed by Tarduno et al. (2007) provide evidence that the inner core was already present before 3.2 Gyr ago should be discarded. Our two end-member models rather argue in favor of an inner core younger than 2 Gyr. The time evolution of M differs remarkably from that of the r.m.s core magnetic field B_{rms} (figure 10.c), due to the evolution of the conversion factor b_{dip} (figure 11.a). An interesting effect is the attenuation in M of the sudden B_{rms} increase associated with the nucleation of the inner core. Indeed, at this time, the dynamo also becomes deeper-seated, hence an increase in b_{dip} which compen-

sates the B_{rms} increase. The prospect of observing the signature of inner core nucleation through a sudden increase of the paleointensity at the surface of the Earth, following the suggestion of Hale (1987), is therefore reduced. The cooling scenario presented by Labrosse et al. (2007), which serves as a basis for the high-power model, predicts a monotonous increase of the dipole moment from 5 10^{22} A.m^2 3 Gyr ago to 8 10^{22} A.m^2 at present. The dipole moment 3.2 Gyr ago is therefore on par with present-day values, as suggested by Tarduno et al. (2007).

A striking feature of the paleomagnetic record is the large dispersion of virtual dipole moments (see figure 11.b), with, for instance, fluctuations from about 2 10^{22} to 15 10^{22} A.m^2 in the last 500 Myr, occurring over very short (million year) time scales. These are unlikely to be explained by magnetohydrodynamic processes taking place in dynamo models, where the magnetic field has typically smaller (and faster) fluctuations (see for instance Olson, 2008), with epochs of low dipole moment representing only rare events associated with reversals. Moreover, these are also too short to represent a response of the dynamo to changing mantle conditions, and, even if this was the case, the CMB heat flow would have to come very close to the minimal 2 TW required to get a dynamo (figure 12) in order to cause such large magnetic field fluctuations. Refinements in the knowledge of core-mantle boundary heat flow variations, in dynamo theory, and in variability analyses of paleomagnetic samples, will be needed in order to conclude regarding the physical nature of these variations.

Acknowledgements

We thank U. R. Christensen for providing the numerical data relative to published dynamo models. J.A. was supported by CNRS and programs Programme National de Planétologie (PNP) and Structure et Dynamique de l'Intérieur de la Terre (SEDIT) of the French Institut National des Sciences de l'Univers (INSU). S. L. was supported by program ANR BEGDy from French Agence Nationale de la Recherche. Numerical calculations were performed at the MésoCentre de Calcul et de données (MCCD) of IPGP, and at IDRIS, France. This is IPGP contribution XXXX.

References

Aubert, J., Aurnou, J., & Wicht, J., 2008. The magnetic structure of convection-driven numerical dynamos, *Geophys. J. Int.*, **172**, 945–956.

Biggin, A. J., Strik, G. H. M. A., & Langereis, C. G., in press, 2008. The intensity of the geomagnetic field in the late-archaean: new measurements and an analysis of the updated IAGA palaeointensity database, *Earth Planets Space*.

Biggin, A. J., Strik, G. H. M. A., & Langereis, C. G., 2008. Evidence for a very-long-term trend in geomagnetic secular variation, *Nature Geosci.*, **1**(6), 395–398.

Braginsky, S. I. & Roberts, P. H., 1995. Equations governing convection in Earths core and the geodynamo, *Geophys. Astrophys. Fluid Dyn.*, **79**(1-4), 1–97.

Buffett, B., Huppert, H., Lister, J., & Woods, A., 1996. On the thermal evolution of the Earth's core, *J. Geophys. Res.*, **101**(B4), 7989–8006.

Christensen, U. & Aubert, J., 2006. Scaling properties of convection-driven dynamos in rotating spherical shells and application to planetary magnetic fields, *Geophys. J. Int.*, **117**, 97–114.

Christensen, U. & Tilgner, A., 2004. Power requirement of the geodynamo from ohmic losses in numerical and laboratory dynamos, *Nature*, **429**, 169–171, doi: 10.1038/nature02508.

Christensen, U. R., 2006. A deep dynamo generating Mercury's magnetic field, *Nature*, **444**(7122), 1056–1058.

Coe, R. S. & Glatzmaier, G. A., 2006. Symmetry and stability of the geomagnetic field, *Geophys. Res. Lett.*, **33**(21).

de Wijs, G., Kresse, G., Vocadlo, L., Dobson, D., Alfe, D., Gillan, M., & Price, G., 1998. The viscosity of liquid iron at the physical conditions of the Earth's core, *Nature*, **392**(6678), 805–807.

Dunlop, D. & Yu, Y., 2004. Intensity and polarity of the geomagnetic field during Precambrian time, in *Timescales of the paleomagnetic field*, edited by Channell, JET and Kent, DV and Lowrie, W and Meert, JG, vol. 145, pp. 85–100, AGU Monograph.

Dunlop, D. J., 2007. Palaeomagnetism - A more ancient shield, *Nature*, **446**(7136), 623+.

Dziewonski, A. & Anderson, D., 1981. Preliminary reference Earth model PREM, *Phys. Earth Planet. Int.*, **25**, 297–356.

Eide, E. A. & Torsvik, T. H., 1996. Paleozoic supercontinental assembly, mantle flushing, and genesis of the kiaman superchron, *Earth Plan. Sci. Let.*, **144**, 389–402.

Hale, C. J., 1987. Paleomagnetic data suggest link between the Archean-Proterozoic boundary and inner-core nucleation, *Nature*, **329**(6136), 233–237.

Hernlund, J. W., Thomas, C., & Tackley, P. J., 2005. Phase boundary double crossing and the structure of Earth's deep mantle, *Nature*, **434**, 882–886, doi:10.1038/nature03472.

Hirao, N., Ohtani, E., Kondo, T., Endo, N., Kuba, T., Suzuki, T., & Kikegawa, T., 2006. Partitioning of potassium between iron and silicate at the core-mantle boundary, *Geophys. Res. Lett.*, **33**(8).

Hulot, G. & Gallet, Y., 1996. On the interpretation of virtual geomagnetic pole (VGP) scatter curves, *Phys. Earth Planet. Int.*, **95**(1-2), 37–53.

Kutzner, C. & Christensen, U., 2002. From stable dipolar to reversing numerical dynamos, *Phys. Earth Planet. Int.*, **131**, 29–45.

Labrosse, S., 2003. Thermal and magnetic evolution of the Earth's core, *Phys. Earth Planet. Int.*, **140**, 127–143.

Labrosse, S., Poirier, J. P., & Le Mouël, J. L., 1997. On cooling of the earth's core,

Phys. Earth Planet. Int., **99**, 1–17.
Labrosse, S., Poirier, J. P., & Le Mouel, J. L., 2001. The age of the inner core, *Earth Planet. Sci. Let.*, **190**(3-4), 111–123.
Labrosse, S., Hernlund, J. W., & Coltice, N., 2007. A crystallizing dense magma ocean at the base of the Earth's mantle, *Nature*, **450**(7171), 866–869.
Lay, T., Hernlund, J., Garnero, E. J., & Thorne, M. S., 2006. A post-perovskite lens and D" heat flux beneath the central pacific, *Science*, **314**(5803), 1272–1276.
Lay, T., Hernlund, J., & Buffett, B. A., 2008. Core-mantle boundary heat flow, *Nature Geosci.*, **1**(1), 25–32.
Lister, J. R., 2003. Expressions for the dissipation driven by convection in the Earth's core, *Phys. Earth Planet. Int.*, **140**(1-3), 145–158.
Lister, J. R. & Buffett, B. A., 1995. The strength and efficiency of thermal and compositional convection in the geodynamo, *Phys. Earth Planet. Int.*, **91**(1-3), 17–30.
Macouin, M., Valet, J., & Besse, J., 2004. Long-term evolution of the geomagnetic dipole moment, *Phys. Earth Planet. Int.*, **147**(2-3), 239–246.
McFadden, P. L., Merrill, R. T., McElhinny, M. W., & Lee, S. H., 1991. Reversals of the earths magnetic-field and temporal variations of the dynamo families, *J. Geophys. Res.*, **96**(B3), 3923–3933.
Nakagawa, T. & Tackley, P. J., 2005. Deep mantle heat flow and thermal evolution of the earth's core in thermochemical multiphase models of mantle convection, *Geophys. Geochem. Geosystems.*, **6**, doi:10.1029/2005GC000967.
Olson, P., 2008. Gravitational dynamos and the low frequency geomagnetic secular variation, *Proc. Nat. Acad. Sci.*, **104**(51), 20159–20166.
Olson, P. & Christensen, U. R., 2006. Dipole moment scaling for convection-driven planetary dynamos, *Earth Plan. Sci. Let.*, **250**(3-4), 561–571.
Olson, P., Christensen, U., & Glatzmaier, G. A., 1999. Numerical modelling of the geodynamo: mechanisms of field generation and equilibration, *J. Geophys. Res.*, **104**(B5), 10383–10404.
Pavlov, V. & Gallet, Y., 2001. Middle Cambrian high magnetic reversal frequency (Kulumbe River section, northwestern Siberia) and reversal behaviour during the Early Palaeozoic, *Earth Plan. Sci. Let.*, **185**(1-2), 173–183.
Pavlov, V. & Gallet, Y., 2005. A third superchron during the Early Paleozoic, *Episodes*, **28**(2), 78–84.
Perrin, M. & Schnepp, E., 2004. IAGA paleointensity database: distribution and quality of the data set, *Phys. Earth Planet. Int.*, **147**(2-3), 255–267, Joint Meeting of the European-Geophysical-Society/American-Geophysical-Union and European-Union-of-Geoscience, Nice, FRANCE, APR 06-11, 2003.
Roberts, P. & Glatzmaier, G., 2001. The geodynamo, past, present and future, *Geophys. Astrophys. Fluid Dyn.*, **94**(1-2), 47–84.
Secco, R. A. & Shloessin, H. H., 1989. The electrical resistivity of solid and liquid Fe at pressures up to 7 GPa, *J. Geophys. Res.*, **94**, 5887–5894.
Smirnov, A. & Tarduno, J., 2004. Secular variation of the Late Archean Early Proterozoic geodynamo, *Geophys. Res. Let.*, **31**(16).
Stacey, F. D. & Loper, D. E., 2007. A revised estimate of the conductivity of iron

alloy at high pressure and implications for the core energy balance, *Phys. Earth Planet. Int.*, **161**(1-2), 13–18.

Stanley, S., Zuber, M. T., & Bloxham, J., 2007. Using reversed magnetic flux spots to determine a planet's inner core size, *Geophys. Res. Lett.*, **34**(19).

Stevenson, D. J., Spohn, T., & Schubert, G., 1983. Magnetism and thermal evolution of the terrestrial planets, *Icarus*, **54**(3), 466–489.

Strik, G., Blake, T., Zegers, T., White, S., & Langereis, C., 2003. Palaeomagnetism of flood basalts in the Pilbara Craton, Western Australia: Late Archaean continental drift and the oldest known reversal of the geomagnetic field, *J. Geophys. Res.*, **108**(B12).

Tarduno, J. A., Cottrell, R. D., Watkeys, M. K., & Bauch, D., 2007. Geomagnetic field strength 3.2 billion years ago recorded by single silicate crystals, *Nature*, **446**(7136), 657–660.

Thellier, E. & Thellier, O., 1959. Sur l'intensité du champ magnétique terrestre dans le passé historique et géologique, *Annales de Geophysique*, pp. 285–376.

Valet, J. P., 2003. Time variations in geomagnetic intensity, *Reviews of Geophysics*, **41**(1), 1004.

van der Hilst, R., De Hoop, M. V., Wang, P., Shim, S.-H., Ma, P., & Tenorio, L., 2007. Seismostratigraphy and thermal structure of Earth's core-mantle boundary region, *Science*, **315**, 1813–1817.

Varga, P., Denis, C., & Varga, T., 1998. Tidal friction and its consequences in palaeogeodesy, in the gravity field variations and in tectonics, *J. Geodynamics*, **25**(1-2), 61–84.

Wicht, J., 2002. Inner-core conductivity in numerical dynamo simulations, *Phys. Earth Planet. Int.*, **132**, 281–302.